

**DEVELOPMENT OF SILICON/CARBON NANOCOMPOSITE ANODES  
FROM SIMPLE PRECURSORS FOR LITHIUM-ION BATTERIES**

by

ALI ANSARI HAMEDANI



Submitted to the Graduate School of Engineering and Natural Sciences in partial  
fulfillment of the requirements for the degree of Doctor of Philosophy

Sabancı University

December 2021

DEVELOPMENT OF SILICON/CARBON NANOCOMPOSITE ANODES FROM  
SIMPLE PRECURSORS FOR LITHIUM-ION BATTERIES

APPROVED BY:

[Redacted Signature]

[Redacted Signature]

[Redacted Signature]

[Redacted Signature]

[Redacted Signature]

DATE OF APPROVAL: 11/12/2021



ALI ANSARI HAMEDANI 2021 ©

All Rights Reserved

# DEVELOPMENT OF SILICON/CARBON NANOCOMPOSITE ANODES FROM SIMPLE PRECURSORS FOR LITHIUM-ION BATTERIES

ALI ANSARI HAMEDANI

Materials Science and Engineering, Ph.D. Dissertation, December 2021

Supervisor: Prof. Dr. Clewa W. Ow-Yang

Co-supervisor: Asst. Prof. Dr. Serap Hayat Soytaş

Keywords: Lithium-ion Batteries, Electrode Materials, Silicon, Silicon/Carbon Nanocomposites, Metallothermic Reduction

## ABSTRACT

Silicon is an attractive material for the anode in lithium-ion batteries due to its low delithiation potential (0.4 V), high gravimetric and volumetric capacity, and abundance in nature. However, the use of silicon-based anode imposes challenges in the performance of lithium-ion batteries that can lead to their poor capacity retention. These challenges include (1) pulverization of silicon under significant volume expansion and contraction during alloying and dealloying with lithium, (2) instability of the interphase formed between silicon and electrolyte, and (3) low electrical conductivity of silicon. Reducing the size of silicon particles to the nanoscale has been proven to prevent particle pulverization. However, the other issues can be addressed by making composites of silicon nanoparticles and carbon. Nevertheless, it is still challenging to produce nanoscale silicon and its well-dispersed nanocomposites in carbon using a cost-effective and scalable method. In this dissertation, we focus our research on fabricating nanoscale silicon materials from simple precursors. First, the synthesis of silicon nanoparticles from a silicon dioxide mineral through salt-mediated magnesiothermic reduction was investigated. Then, electrospinning of a hybrid solution prepared by mixing various silicon precursors and polyacrylonitrile as a carbon source was explored. Finally, low-temperature aluminothermic reduction of silicon dioxide-carbon nanocomposite fibers was investigated. The electrochemical performance of the developed silicon nanostructures and silicon-carbon nanocomposite fibers was validated.

# LİTYUM-İYON PİLLER İÇİN ÖNCÜL MALZEMELERDEN SİLİSYUM/KARBON NANOKOMPOZİT ANOTLARIN GELİŞTİRİLMESİ

ALI ANSARI HAMEDANI

Malzeme Bilimi ve Mühendislik , Doktora Tezi, Aralık 2021

Danışman: Prof. Dr. Cleva W. Ow-Yang

Eş-danışman: Dr. Öğr. Üyesi Serap Hayat Soytaş

Anahtar Kelimeler: Lityum-iyon Piller, Elektrot Malzemeleri, Silisyum,  
Silisyum/Karbon Nanokompozitler, Metalotermik İndirgeme

## ÖZET

Silisyum, düşük lityasyon potansiyeli, yüksek gravimetrik ve hacimsel kapasitesi ve doğadaki bolluğu nedeniyle lityum iyon pillerdeki anot için ilgi çekici bir malzemedir. Bununla birlikte, silisyum esaslı malzemelerin anot olarak kullanımı, lityum-iyon pillerin performansında, hızlı kapasite kaybına yol açabilecek zorluklar getirir. Bu zorluklar, (1) lityum ile tersinir alaşım oluşturma sırasında önemli hacim genleşme ve daralma nedeniyle silisyumun parçalanarak yapısının bozulması, (2) silisyum ve elektrolit arasında oluşan ara fazın kararsızlığı ve (3) silisyumun düşük elektriksel iletkenliği olarak sıralanabilir. Silisyum parçacık boyutunu nano ölçeğe indirmenin hacimsel genleşmenin etkisini azaltarak parçacık kararlılığını korumaya yardımcı olduğu kanıtlanmıştır. Bununla birlikte, diğer sorunlar ancak silisyum nanoyapılar ile karbon nanokompozitler yapılarak giderilebilir. Nano ölçekli silisyumun, karbon matrisi içinde iyi dağılmış nanokompozitlerinin uygun maliyetli ve ölçeklenebilir bir yöntem kullanılarak üretimi halen zorlu bir iştir. Bu tezde, araştırmamızı basit öncülerden nano ölçekli silisyum malzemeler üretmeye odakladık. İlk olarak, bir silisyum dioksit mineralinden tuz-aracılı magnezyotermik indirgeme yoluyla silisyum nanoparçacıkların sentezi araştırılmıştır. Daha sonra, çeşitli silisyum öncüleri ile karbon kaynağı olarak poliakrilonitril karıştırılarak hazırlanan hibrit bir çözeltinin elektrodeleme ile nanokompozit fiberlerin üretimi incelenmiştir. Son olarak, silisyum-karbon hibrit nanofiberlerin düşük sıcaklıkta alüminotermik indirgenmesi araştırılarak geliştirilen silisyum nanoyapıların ve silisyum-karbon nanokompozit fiberlerin elektrokimyasal performansları doğrulanmıştır. Sonuç olarak, silisyumun tuz-aracılı magnezyotermik indirgenme kullanılarak birbirine paralel üç farklı reaksiyon yoluyla silisyum nanoparçacıklar üretilebildiği, ve karbon ve silisyum öncülerinden başlanıldığında karbon içine gömülü silisyum nanokristallerin homojen olarak dağılmış olduğu karbon-silisyum nanokompozitlerinin elde edilebildiği gösterildi.

## Acknowledgments

I would like to thank the help of my advisors Prof. Dr. Cleva W. Ow-Yang and Asst. Prof. Dr. Serap Hayat Soytaş, whose help during my Ph.D. program was crucial. This work was funded by the Scientific and Technological Research Council of Turkey (TÜBİTAK) under project number 114M216. Also, I would like to appreciate the financial support of the Faculty of Engineering and Natural Sciences at Sabanci University during my Ph.D. studies. Furthermore, the internal jury members of my dissertation, Prof. Dr. Serhat Yeşilyurt, and Assoc. Prof. Dr. Fevzi Çakmak Cebeci, attended progress meetings of this dissertation and provided their invaluable feedback since the proposal. Also, I would like to appreciate the feedback of the external jury members, Assoc. Prof. Dr. Rezan Demir-Çakan and Asst. Prof. Dr. Billur Deniz Karahan. I would like to mention that I found the unconditional professional help from Prof. Dr. Mehmet Ali Gülgün as a significant factor in my Ph.D. journey. I also consider the fruitful discussions and occasional consultations with Dr. Alp Yürüm as assets.

I would like to appreciate the help I received from team members: Dr. Hasan Kurt, Dr. Guliz Inan Akmehmet, Dr. Sirous Khabbaz Abkenar, Zeki Semih Pehlivan, Arzu Ergene, Mahdiah Shakoorioskooie, and Ece Günay.

Dr. Ali Tufani and Dr. Shayan Mehraeen were great friends and generously shared their lab experiences with me. This means a lot to me. Sharing the labs and occasional discussions with Dr. Adnan Taşdemir and Dr. Buse Bulut Köpüklü was also a great experience that I would like to acknowledge. I should thank two other friends, Vahid Charkhesht and Farid Sayar Irani, who shared their time for discussions and gave me feedback about my presentations whenever I asked them. Among other colleagues, I would like to thank Dr. Mohammad Hadi Khaksaran, Dr. Sorour Semsari Parapari, Mohammad Jafarpour, Dr. Pozhhan Mokhtari, Farzad Rokhsartalab, Dr. Ferdows Afghah, Kosar Hasannejad, Ekin Berksun, and former L068 office colleagues.

Sabanci University members, Mrs. Sinem Aydin, Dr. Daniel Lee Calvey, Mr. Turgay Gonul, Ms. Burcin Yildiz, Mr. Suleyman Çelik, and other SUNUM members were helpful since my earliest days.

Last but not least, I will always be grateful for receiving unconditional emotional support from my family. My parents and my sisters' family managed to do great work in supporting each other in my physical absence.

Ali Ansari Hamedani



*In memory of my uncle*

*Amoo Mahmood*



# TABLE OF CONTENTS

CHAPTER 1: Introduction .....	19
1.1 Preface and Hypothesis.....	19
1.2 Methodology .....	21
1.3 Roadmap of Chapters.....	21
CHAPTER 2: Literature Review .....	23
2.1 Historical perspective .....	23
2.1.1 Silicon as an anode material in LIBs .....	23
2.1.2 Nanostructured silicon anodes in LIBs .....	26
2.2 Synthesis methods of silicon nanostructures .....	31
2.2.1 Synthesis through gas-phase CVD (pyrolysis of SiH <sub>4</sub> ) .....	32
2.2.2 Synthesis through chemical reduction .....	33
2.2.3 Metallothermic reduction.....	33
2.3 Carbon nanofibers.....	41
2.3.1 Electrospinning polymeric precursors .....	41
2.3.2 Carbonization of polyacrylonitrile (PAN) fibers .....	43
2.4 Composites of silicon/carbon nanofibers.....	45
2.4.1 Addition of preformed silicon nanoparticles to the CNF polymer precursor .....	45
2.4.2 Addition of silicon precursors to the CNF polymer precursor .....	46
2.5 From Active Electrode Materials to Cells .....	50
2.5.1 Binders .....	50
2.5.2 Electrolytes .....	52
2.5.3 Other components and half-cell assembly .....	56
CHAPTER 3: Characterization Methods.....	57
3.1 Materials Characterizations Methods .....	57
3.1.1 Thermogravimetric and differential thermal analysis (TG-DTA) .....	57

3.1.2 Fourier-transformed infrared spectroscopy .....	58
3.1.3 Raman spectroscopy .....	60
3.1.4 Liquid proton nuclear magnetic resonance ( <sup>1</sup> H NMR) spectroscopy .....	62
3.1.5 X-ray diffraction (XRD) .....	63
3.1.6 Specific surface area by gas adsorption (BET method).....	65
3.1.7 Field-emission scanning electron microscopy (FE-SEM).....	66
3.1.8 Transmission electron microscopy (TEM) .....	68
3.1.9 X-ray photoelectron spectroscopy (XPS) .....	69
3.2 Electrochemical Characterization Methods .....	70
3.2.1 Characterization of a battery half-cell .....	70
3.2.2 Chronopotentiometry .....	72
3.2.3 Cyclic Voltammetry.....	73
3.2.4 Electrochemical Impedance Spectroscopy (EIS).....	73
CHAPTER 4: Magnesiothermic Reduction of SiO <sub>2</sub> .....	75
4.1 Introduction.....	76
4.2 Experimental Section .....	78
4.2.1 Materials synthesis.....	78
4.2.2 Materials characterizations .....	79
4.2.3 Electrochemical characterizations .....	80
4.3 Results and Discussion .....	82
4.3.1 Results.....	82
4.3.2 Discussion.....	90
4.4 Conclusion .....	97
4.5 Supporting Information.....	98
4.5.1 XRD patterns .....	98
4.5.2 N <sub>2</sub> adsorption-desorption .....	99
4.5.3 Estimation of equivalent spherical particle size .....	100

4.5.4 Supplementary micrographs .....	101
4.5.5 Maximum temperature calculation without NaCl .....	102
4.5.6 Maximum temperature calculation with NaCl.....	108
4.5.7 References of Supporting Information .....	114
CHAPTER 5: Synthesis of Carbon-SiO <sub>2</sub> Composite Fibers .....	115
5.1 Introduction.....	115
5.2 Experimental.....	115
5.2.1 Copolymer nanofibers.....	115
5.2.2 Homopolymers and producing blend nanofibers.....	116
5.2.3 Hybrid nanofibers .....	118
5.3 Results.....	119
5.3.1 Copolymer nanofibers.....	119
5.3.2 Homopolymers and producing blend nanofibers.....	122
5.3.3 Hybrid nanofibers .....	128
5.4 Discussion.....	132
CHAPTER 6: Metallothermic Reduction of Carbon-SiO <sub>2</sub> Structures.....	135
6.1 Introduction.....	136
6.2 Materials and Methods.....	138
6.2.1 Synthesis of Active Materials .....	138
6.2.2 Materials Characterizations .....	139
6.2.3 Electrochemical Characterizations .....	140
6.3 Results.....	141
6.4 Discussion.....	148
6.5 Conclusions.....	150
6.6 Supporting Information.....	151
CHAPTER 7: Summary and Further Studies .....	155
References.....	158

## LIST OF FIGURES

- Figure 1.1. A more uniform distribution of Si nanoparticles along the carbon fiber length is expected to minimize localized volumetric changes in expansion and contraction during charge-discharge cycling..... 20
- Figure 2.1. Evolution of the specific energy and energy density of LIBs (cell level) from 1991 to 2015, following their commercialization. Reprinted with permission from Placke, T., Kloepsch, R., Dühnen, S., & Winter, M. (2017). Lithium-ion, lithium metal, and alternative rechargeable battery technologies: the odyssey for high energy density. *Journal of Solid State Electrochemistry*, 21(7), 1939-1964. doi:10.1007/s10008-017-3610-7 ..... 24
- Figure 2.2. (a) Degradation of film and particle silicon structures during cycling, (b) Advantages of nanowires directly grown on the surface of current-collector. Reprinted with permission from Chan, C. K., Peng, H., Liu, G., McIlwrath, K., Zhang, X. F., Huggins, R. A., & Cui, Y. (2008). High-performance lithium battery anodes using silicon nanowires. *Nature Nanotechnology*, 3(1), 31-35. doi:10.1038/nnano.2007.411 27
- Figure 2.3. Synthesis and characterization of an interconnected Si hollow nanosphere electrode. (A) Schematic of hollow sphere synthesis. (B) Typical cross-sectional SEM image of hollow Si nanospheres. (C) SEM side view of the same sample of hollow Si nanospheres. (D) SEM image of hollow Si nanospheres (E) TEM image of interconnected hollow Si spheres, (F) Energy-dispersive X-ray spectroscopy (EDS) of a hollow Si sphere. Adapted with permission from Y. Yao, M. T. McDowell, I. Ryu, H. Wu, N. A. Liu, L. B. Hu, W. D. Nix, Y. Cui, *Nano Lett.* 2011, 11, 2949-2954,..... 28
- Figure 2.4. Schematic of synthesis steps: (a) PS nanoparticles, (b) PS@SiO<sub>2</sub>, (c) Hollow SiO<sub>2</sub>, (d) Hollow Si, and (e) Hollow Si@C. Adapted with permission from Ashuri, M., He, Q., Liu, Y., Zhang, K., Emani, S., Sawicki, M. S., . . . Shaw, L. L. (2016). Hollow Silicon Nanospheres Encapsulated with a Thin Carbon Shell: An Electrochemical Study. *Electrochimica Acta*, 215, 126-141. doi:http://dx.doi.org/10.1016/j.electacta.2016.08.059 ..... 29
- Figure 2.5. Schematic illustration showing the synthesis of mesoporous silicon nanofibers (m-SiNFs). From D. J. Lee, H. Lee, M.-H. Ryou, G.-B. Han, J.-N. Lee, J. Song, J. Choi, K. Y. Cho, Y. M. Lee, J.-K. Park, *ACS Appl. Mater. Interfaces* 2013, 5, 12005-12010. <https://doi.org/10.1021/am403798a>..... 30
- Figure 2.6. Si particles with different internal architectures: (a) solid and hollow particles, (b) solid core-shell structures, (c) hollow core-shell structures, and (d) yolk-shell structures. Reprinted with permission from Ashuri, M., He, Q., & Shaw, L. L. (2015). Silicon as a potential anode material for Li-ion batteries: where size, geometry, and structure matter. *Nanoscale*, 8(1), 74-103. doi:http://dx.doi.org/10.1039/C5NR05116A ..... 30
- Figure 2.7. Synthesis of nanostructured silicon through different routes. .... 31
- Figure 2.8. Ellingham diagram for the formation of oxides based on their standard free energy of formation over temperature. Reprinted with permission from Oar-Arteta, L., Wezendonk, T., Sun, X., Kapteijn, F., & Gascon, J. (2017). Metal organic frameworks

- as precursors for the manufacture of advanced catalytic materials. *Materials Chemistry Frontiers*, 1(9), 1709-1745. doi:10.1039/c7qm00007c ..... 35
- Figure 2.9. Schematic of mass transfer and periodic structure formation at SiO<sub>2</sub>/Mg interface (a) Si accumulation on the SiO<sub>2</sub> surface, as a result, MgO of ‘resistance’ to Si diffusion; (b) simultaneous formation of a new MgO/Mg<sub>2</sub>Si pair of layers. Reproduced with permission from Gutman, I., Gotman, I., & Shapiro, M. (2006). Kinetics and mechanism of periodic structure formation at SiO<sub>2</sub>/Mg interface. *Acta Materialia*, 54(18), 4677-4684. doi:http://doi.org/10.1016/j.actamat.2006.05.048 ..... 37
- Figure 2.10. A schematic illustration of the Si nanocrystal formation in molten salts based on the reduction of SiO<sub>2</sub> by electrons solvated in the liquid phase. Reprinted with permission from Liu, X., Giordano, C., & Antonietti, M. (2012). A molten-salt route for synthesis of Si and Ge nanoparticles: chemical reduction of oxides by electrons solvated in salt melt. *Journal of Materials Chemistry*, 22(12), 5454-5459. doi:http://dx.doi.org/10.1039/C2JM15453F ..... 38
- Figure 2.11. Schematic of the heat scavenger-assisted Mg-MRR. Reprinted with permission from Favors, Z., Wang, W., Bay, H. H., Mutlu, Z., Ahmed, K., Liu, C., . . . Ozkan, C. S. (2014). Scalable Synthesis of Nano-Silicon from Beach Sand for Long Cycle Life Li-ion Batteries. *Scientific Reports*, 4, 5623. doi:http://doi.org/10.1038/srep05623 ..... 39
- Figure 2.12. Typical set-up of an electrospinning apparatus. Reprinted with permission from Bhardwaj, N., & Kundu, S. C. (2010). Electrospinning: A fascinating fiber fabrication technique. *Biotechnology Advances*, 28(3), 325-347. doi:https://doi.org/10.1016/j.biotechadv.2010.01.004 ..... 42
- Figure 2.13. Processes during stabilization of polyacrylonitrile (PAN) fibers. Reprinted with permission from Rahaman, M. S. A., Ismail, A. F., & Mustafa, A. (2007). A review of heat treatment on polyacrylonitrile fiber. *Polymer Degradation and Stability*, 92(8), 1421-1432. doi:https://doi.org/10.1016/j.polymdegradstab.2007.03.023 ..... 44
- Figure 2.14. The removal of hydrogen and nitrogen during carbonization. Reprinted with permission from Rahaman, M. S. A., Ismail, A. F., & Mustafa, A. (2007). A review of heat treatment on polyacrylonitrile fiber. *Polymer Degradation and Stability*, 92(8), 1421-1432. doi:https://doi.org/10.1016/j.polymdegradstab.2007.03.023 ..... 44
- Figure 2.15. Cross-linking of PVA upon addition of hydrolyzed TEOS. (A) FTIR spectra of as-spun PVA, silica, and PVA–silica composites. (B) Enlarged version shows the Si–O–C peak which is generated because of the interaction between –OH groups of PVA and surface silanols of silica resulting in possible production of (C) suggested structure. Reprinted with permission from Pirzada, T., Arvidson, S. A., Saquing, C. D., Shah, S. S., & Khan, S. A. (2012). Hybrid Silica–PVA Nanofibers via Sol–Gel Electrospinning. *Langmuir*, 28(13), 5834-5844. doi:10.1021/la300049j. Copyright 2012 American Chemical Society ..... 47
- Figure 2.16. PAN and hydrolyzed TEOS form hydrogen bonds (not covalent bonds). Reprinted with permission from Pirzada, T., Arvidson, S. A., Saquing, C. D., Shah, S. S., & Khan, S. A. (2014). Hybrid Carbon Silica Nanofibers through Sol–Gel Electrospinning. *Langmuir*, 30(51), 15504-15513. doi:10.1021/la503290n ..... 48
- Figure 2.17. The battery value-chain showing how the inactive components are added to the active materials at each level. Reprinted with permission from Placke, T., Kloepsch, R., Dühnen, S., & Winter, M. (2017). Lithium ion, lithium metal, and alternative

rechargeable battery technologies: the odyssey for high energy density. <i>Journal of Solid State Electrochemistry</i> , 21(7), 1939-1964. doi:10.1007/s10008-017-3610-7 .....	51
Figure 2.18. Schematic potential diagram showing the mismatch between the electrochemical stabilities of electrolyte and the redox potentials of most anode and cathode materials used in modern LIBs. GR, LFP, LCO, NMC, LMNO, and LCP stand for graphite, lithium iron phosphate, lithium cobalt oxide, lithium nickel manganese cobalt oxide, lithium manganese nickel oxide, and lithium cobalt phosphate, respectively. Adapted with permission from Winter, M., Barnett, B., & Xu, K. (2018). Before Li Ion Batteries. <i>Chemical Reviews</i> , 118(23), 11433-11456. doi:http://dx.doi.org/10.1021/acs.chemrev.8b00422 .....	53
Figure 2.19. Schematic of the anode solid electrolyte interphase (SEI) formation process showing (a) graphene layers surrounded by electrolyte salts and solvents above 1.4 V vs. Li/Li <sup>+</sup> , (b) propylene carbonate (PC) intercalation with lithium-ions into graphene layers resulting in exfoliations below 0.9 V vs. Li/Li <sup>+</sup> and (c) stable SEI formation in ethylene carbonate (EC)-based electrolyte below 0.9 V vs. Li/Li <sup>+</sup> ; plane side with thinner SEI and edge side with thicker SEI. Originally appeared in An, S. J., Li, J., Daniel, C., Mohanty, D., Nagpure, S., & Wood, D. L. (2016). The state of understanding of the LIB graphite solid electrolyte interphase (SEI) and its relationship to formation cycling. <i>Carbon</i> , 105, 52-76. doi:https://doi.org/10.1016/j.carbon.2016.04.008 .....	55
Figure 3.1. Separation of electronic, vibrational, and rotational energy levels for a molecule.....	59
Figure 3.2. Energy levels in Raman spectroscopy that shows (a) Elastic scattering, (b) Stokes scattering (leaving photon with lower energy), and (c) anti-Stokes scattering (leaving photon with higher energy).....	61
Figure 3.3. Scattering of X-rays by the atoms in a crystalline solid with an interplanar spacing of d.....	64
Figure 3.4. (a) An SEM specimen in which the X-ray excitation happens in a spreading volume in the bulk of the specimen, and (b) a thin TEM specimen in which the X-ray excitation region (interaction volume) is of the same size as the probe-size diameter. .	67
Figure 3.5. (a) The schematic view of the photoelectron spectrometer with a hemispherical electron energy analyzer, (b) energy level diagram for a sample in good electrical contact to the XPS spectrometer. Reprinted with permission from Greczynski, G., & Hultman, L. (2020). X-ray photoelectron spectroscopy: Towards reliable binding energy referencing. <i>Progress in Materials Science</i> , 107, 100591. doi:https://doi.org/10.1016/j.pmatsci.2019.100591 .....	70
Figure 3.6. The schematic illustration of a half-cell that is used to test the electrochemical performance of the active materials. (The casings are not shown for simplicity). .....	71
Figure 3.7. Schematic representation of the profiles of the electrochemical potential of electrons and Li <sup>+</sup> ions. It is reprinted with permission. Originally appeared in Weiss, M., Ruess, R., Kasnatscheew, J., Levartovsky, Y., Levy, N. R., Minnmann, P., . . . Janek, J. (2021). Fast Charging of Lithium-Ion Batteries: A Review of Materials Aspects. <i>Advanced Energy Materials</i> , 11(33), 2101126. doi:https://doi.org/10.1002/aenm.202101126.....	72

Figure 3.8. Kramers-Kronig fitting residuals are low, and it indicates time-invariance of the conditions and correctness of further proceeding to fit an equivalent circuit model to the spectra. ....	74
Figure 4.1. Schematic of the LIB half-cell architecture: (a) the entire cell test assembly, (b) inside of the half-cell consisting of (1) stainless steel current collector, (2) lithium metal chip, (3) liquid electrolyte, (4) separator, (5) liquid electrolyte, (6) negative electrode, and (7) copper foil current collector.....	81
Figure 4.2. Thermograms of the reactants without and with heat moderation. ....	82
Figure 4.3. XRD patterns of SiO <sub>2</sub> reduced (a) without the presence of NaCl and (b) in the presence of NaCl.....	83
Figure 4.4. Crystallite size of the silicon material obtained under different reduction conditions and duration.....	84
Figure 4.5. Morphology revealed by SEM imaging of (a) the mineral SiO <sub>2</sub> , (b) the product of synthesis without NaCl, and (c) the product of synthesis with NaCl. Representative bright-field TEM micrographs of the Si particles synthesized (d) without NaCl and (e) with the presence of NaCl. The insets in (d) and (e) are FFT analyses of the corresponding images. ....	85
Figure 4.6. (a) Cycling performance of the two types of half-cells; (b) potential profile of the first cycles; cyclic voltammetry of the Si electrolyte Li half-cells (under 0.1 mV s <sup>-1</sup> scan rate) (c) for the porous Si network, and (d) for individual particles; (e) first cyclic voltammograms of the Si electrolyte Li half-cells, and (f) the rate performance of half-cells after undergoing 10 CV cycles. ....	88
Figure 4.7. Nyquist plots of the half-cells in the lithiated state (5 mV) with active material synthesized (a) without NaCl (active material with a porous network) and (c) with NaCl (individual particles) along with their corresponding resistance values, respectively (b), (d); corresponding equivalent circuits in the inset figures.....	89
Figure 4.8. Physical model of NaCl-mediated MRR of SiO <sub>2</sub> to produce Si nanoparticles, with the 3 reaction pathways indicated described in detail in the text. ....	92
Figure 4.9. (a) The XRD pattern of the ball-milled and cleaned SiO <sub>2</sub> mineral used as the silicon source. Phase analysis shows the single crystalline phase of cristobalite (PDF 82-0512). The crystallinity of this powder was calculated to be 34.3%. (b) XRD patterns of as reduced samples synthesized with NaCl. The non-indexed sharp peaks represent NaCl (PDF 88-2300). To observe the peaks, we had to zoom the vertical axis. (c), (d) XRD patterns of the samples synthesized after HCl washing step for no NaCl and NaCl-containing samples respectively. (e), and (f) XRD patterns of the samples synthesized after HF washing step for no NaCl and NaCl-containing samples respectively. ....	98
Figure 4.10. N <sub>2</sub> adsorption-desorption isotherms for the Si products and the starting SiO <sub>2</sub> mineral.....	99
Figure 4.11. Bright-field TEM micrographs of the silicon particles synthesized (a) without NaCl and (e) with the presence of NaCl (lower magnification compared to Figure 4.5).....	101
Figure 5.1. The monomers used for copolymerization.....	116
Figure 5.2. Homopolymerization of VTES .....	117

Figure 5.3. IR spectra of the synthesized (a) poly(AN- <i>co</i> -TMSPMA) and (b) poly(AN- <i>co</i> -VTES) copolymers. ....	119
Figure 5.4. <sup>1</sup> H NMR spectra of the synthesized (a) poly(AN- <i>co</i> -TMSPMA) and (b) poly(AN- <i>co</i> -VTES) copolymers. ....	121
Figure 5.5. Morphology of the fibermats made from (a) poly(AN- <i>co</i> -TMSPMA) and (b) poly(AN- <i>co</i> -VTES) copolymers. ....	121
Figure 5.6. The IR spectra of VTES and PVTES .....	122
Figure 5.7. <sup>1</sup> H NMR spectra of the VTES and (bulk-polymerized) PVTES .....	123
Figure 5.8. (a) Electrospun PAN-PVTES 1:1 fiber mat and, (b) its dark-field TEM micrograph after carbonization ,and (c) its corresponding elemental maps for carbon, silicon, and oxygen (scale bars show 200 nm). ....	124
Figure 5.9. The IR spectra of TMSPMA and pTMSPMA.....	124
Figure 5.10. <sup>1</sup> H NMR of TMSPMA and pTMSPMA (NMR in deuterated chloroform). ....	125
Figure 5.11. (a) Electrospun PAN-pTMSPMA 1:1 fiber mat, and (b) its TEM micrograph after carbonization (scale bar shows 100 nm), and (c) its STEM-EDS elemental distribution maps of carbon, silicon, and oxygen (scale bar shows 50 nm). ....	126
Figure 5.12. Raman spectrum of carbonized fibermat synthesized from electrospun PAN-pTMSPMA 1:1 .....	126
Figure 5.13. Cyclic voltammogram (under 0.1 mV s <sup>-1</sup> ) of the half-cell made of C-SiO <sub>2</sub> derived from PAN-pTMSPMA mixture (in 0.005- 3V cut-off voltage window) .....	127
Figure 5.14. (a) The galvanostatic charge-discharge (under 500 mA g <sup>-1</sup> ) and (b) the rate performance of the half-cell made of C-SiO <sub>2</sub> derived from PAN-pTMSPMA mixture (in 0.005- 3V cut-off voltage window) .....	127
Figure 5.15. Micrograph of the fibers produced through different PAN-SiO <sub>2</sub> hybrids	128
Figure 5.16. The comparison between the IR spectra of the different PAN-SiO <sub>2</sub> hybrids with different nominal SiO <sub>2</sub> content .....	129
Figure 5.17. Thermogravimetric analysis of the hybrid PAN-SiO <sub>2</sub> materials under air (10 K min <sup>-1</sup> heating rate) .....	129
Figure 5.18. The X-ray diffraction pattern and Raman spectra of the carbonized hybrid structures .....	130
Figure 5.19. Cyclic voltammogram (under 0.1 mV s <sup>-1</sup> ) of the half-cell made of C-SiO <sub>2</sub> derived from PAN-SiO <sub>2</sub> with nominal 30wt.% SiO <sub>2</sub> (in 0.005- 3V cut-off voltage window) .....	131
Figure 5.20. (a) The galvanostatic charge-discharge (under 500 mA g <sup>-1</sup> ) and (b) the rate performance of the half-cell made of C-SiO <sub>2</sub> derived from PAN-SiO <sub>2</sub> with nominal 30wt.% SiO <sub>2</sub> (in 0.005- 3V cut-off voltage window) .....	131
Figure 5.21. Comparison of the long-term retention of specific capacities of lithiation (discharge) for free-standing C-SiO <sub>2</sub> fibermats from different hybrid PAN-SiO <sub>2</sub> compositions (in 0.005- 3V cut-off voltage window). The current rates are shown on the plot. ....	132

Figure 6.1. (a) SEM micrograph of PAN-SiO <sub>x</sub> hybrid nanofibers, (b) FTIR spectrum of PAN-SiO <sub>x</sub> nanofibers and pure PAN, and (c) TGA of PAN-SiO <sub>x</sub> nanofibers under air. ....	141
Figure 6.2. (a) SEM micrograph, (b) XRD pattern, (c) TGA (under air atmosphere), and (d) Raman spectrum of carbonized C-SiO <sub>2</sub> fibers. ....	142
Figure 6.3. (a) SEM micrograph, (b) XRD pattern, (c) TGA (under air atmosphere), and (d) Raman spectrum of reduced C-Si/SiO <sub>x</sub> fibers.....	144
Figure 6.4. XRD patterns of carbonized fibers and the ones reduced via magnesiothermic and aluminothermic reduction.....	145
Figure 6.5. XPS spectra of O1s and Si2p of carbonized hybrid nanofibers (a) before and (b) after aluminothermic reduction. ....	146
Figure 6.6. (a) Cyclic voltammograms (CV), (b) Nyquist plots vs. cycle numbers of CV, (c) the resistances extracted from fitting an equivalent circuit model (inset) vs. cycle numbers of CV (R <sub>s</sub> : equivalent series resistance, R <sub>int</sub> : interfacial resistance, R <sub>SEI</sub> : SEI resistance, R <sub>CT</sub> : charge-transfer resistance), (d) the voltage profiles of the selected cycles, and (e) cycling performance of the C-Si/SiO <sub>x</sub> material as the working electrode. ....	147
Figure 6.7. XRD phase analysis of (a) as-reduced powder, and (b) after washing with distilled water.....	151
Figure 6.8. FTIR spectra of carbonized fibers before and after aluminothermic reduction. ....	152
Figure 6.9. STEM-EDS mapping of elemental distribution on a C/Si short fiber.....	152
Figure 6.10. XPS survey spectra of carbonized fibers and their spectra after aluminothermic reduction. ....	153
Figure 6.11. The galvanostatic charge-discharge cycling of the C-SiO <sub>2</sub> (before aluminothermic reduction).....	153
Figure 6.12. The first 5 cycles of an electrode containing Si nanoparticles at 200 mA g <sup>-1</sup> current rate. ....	154

## LIST OF TABLES

Table 4.1. Quantitative phase analysis of the XRD patterns in Figure 4.3.....	83
Table 4.2. Nanoparticle properties extracted from N <sub>2</sub> adsorption-desorption and microscopy data. ....	86
Table 4.3. Summary of particle characteristics for generating the physical model.....	91
Table 4.4. Specific heat capacity coefficients for Si and MgO .....	104
Table 4.5. Specific heat capacity coefficients for NaCl .....	110



## CHAPTER 1: **Introduction**

### **1.1 Preface and Hypothesis**

One of the ways to increase the energy that can be stored in lithium-ion batteries (LIBs) is to utilize electrode materials with higher lithium (Li) intake with respect to state-of-the-art electrode materials. To this end, in the negative electrode of LIBs, the common widely used graphite material could be substituted with silicon-based materials. However, using pure silicon has been shown to be challenging for cyclability. The mechanism of lithium intake in graphite is stacking the Li atoms in between its graphene sheets, known as intercalation, while for silicon, it is an alloying reaction. Compared to intercalation-type electrode materials, alloying-type Li storage materials experience larger volume expansion and contraction upon alloying and dealloying reactions. For silicon, this volume expansion can lead to an up to 280% increase in volume (Obrovac & Chevrier, 2014). Such a high alloying-induced strain can lead to pulverization of the silicon particle and their loss of electrical contact to the current collector and eventual degradation of capacity upon cycling.

Pulverization of particles can be avoided by decreasing the size of silicon particles below a critical value because the crack propagation is only spontaneous above a certain crack size (Meyers & Chawla, 2008; G. Zhu, Chao, Xu, Wu, & Zhang, 2021). It has been experimentally shown that crystalline silicon particles with diameters below 150 nm do not pulverize during lithiation-delithiation cycles (X. H. Liu et al., 2012). However, from an electrode level point of view, the larger specific surface area of silicon nanoparticles compared to bulk silicon leads to a higher degree of interfacial interactions between the material and the liquid electrolyte in the first few cycles (G.

Zhu et al., 2021). This type of interaction, introduced in section 2.5.2, can drastically decrease the number of mobile Li-ions in the electrolyte and decrease the energy stored in the battery. Therefore, the surface of silicon nanostructures must be protected using a coating or matrix material that is stable in the liquid electrolyte.

To protect the surface of silicon nanoparticles, they can get embedded in a carbon nanofiber matrix, but they tend to agglomerate during processing to decrease their surface energy by reducing their surface-to-volume ratio. The agglomerated silicon nanoparticles experience localized expansions and contractions along the axis of the carbon nanofiber (as shown in Figure 1.1), resulting in a loss in the capacity of the electrode in the subsequent cycles. A structure of fine silicon nanoparticles homogeneously dispersed in a CNF matrix, as shown in Figure 1.1, is expected to show superior capacity retention compared to a structure with aggregates of silicon nanoparticles, as it promotes more even volume expansion-contraction.

## Si-decorated carbon nanofibers as anodes of Li-ion batteries

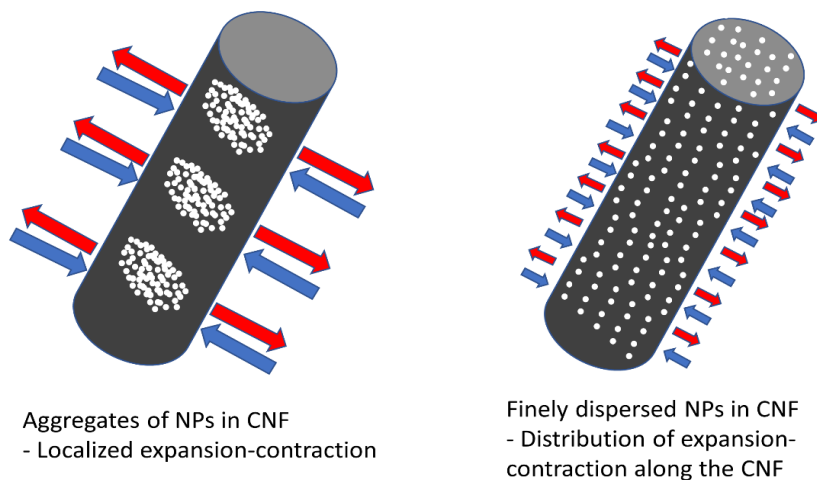


Figure 1.1. A more uniform distribution of Si nanoparticles along the carbon fiber length is expected to minimize localized volumetric changes in expansion and contraction during charge-discharge cycling

## 1.2 Methodology

I first produced an electrospun hybrid fiber mat made of polyacrylonitrile (PAN) and siloxane oligomers via hydrolysis of TEOS to obtain the structure with fine silicon nanoparticles homogeneously dispersed in a CNF matrix, inspired by the sol-gel synthesis of biomaterials (Maçon et al., 2015). The hybrid nanofiber mat, in which polyacrylonitrile and TEOS are known to be mixed at the molecular level (Novak, 1993), was used as a precursor for the subsequent steps.

The precursor fibers were stabilized and carbonized through heat treatment recipes known for producing carbon nanofibers (CNFs) from PAN. Simultaneously the embedded siloxane oligomer was undergoing condensation to form  $\text{SiO}_2$ . The resulting structure was a fiber mat composed of a fine mixture of amorphous carbon and  $\text{SiO}_2$  (C- $\text{SiO}_2$ ).

The C- $\text{SiO}_2$  fiber mats produced were subjected to metallothermic reduction reaction (MRR), aiming for the reduction of  $\text{SiO}_2$  to silicon. The fibers obtained at the end of this step were short fibers of C-Si/ $\text{SiO}_x$ .

The short fibers produced were applied as the working electrode in LIB half-cells to measure their specific capacity and charge-discharge cycling stability.

## 1.3 Roadmap of Chapters

In this dissertation, I demonstrate the implementation of a combination of principles and methods such as sol-gel and polymer chemistry, electrospinning, and metallothermic reduction reaction (MRR) to produce silicon-carbon composite anodes for LIBs. In Chapter 2, a literature review of silicon-based anodes in LIBs, production methods of silicon nanostructures, carbon nanofibers, silicon-carbon hybrid materials, a summary of the battery components other than the active materials (such as binders, electrolytes, and additives) is presented. In Chapter 3, the details of characterization methods are introduced. Chapter 4 includes my study on how to perform the magnesiothermic reduction of a sample  $\text{SiO}_2$  material, the reaction mechanism yielding

silicon nanoparticles, and the electrochemical characterization of the silicon nanoparticle product. In chapter 5, the production of C-SiO<sub>2</sub> precursor fibers is discussed. Chapter 6 reports my study in which the aluminothermic reduction is applied to C-SiO<sub>2</sub> fibermat product and the electrochemical characterization of the resulting composite. Finally, a summary and suggestions for further work are presented in Chapter 7.



## CHAPTER 2: Literature Review

### 2.1 Historical perspective

SONY commercialized the first lithium-ion battery (LIB) in 1991. In the first version of the lithium-ion batteries, the anode was made of carbon coke. However, after 1994 almost all commercial LIBs have been using graphite as the active material of their negative electrode (Asenbauer et al., 2020). Only recently (in September 2021), Sila Nanotechnologies developed the first commercial battery with silicon anode.

#### 2.1.1 Silicon as an anode material in LIBs

The total energy stored by the movement of  $n$  charged species (with elemental charge  $q$ ) in a battery with an average potential difference of  $V_{\text{avg}}$  would be  $E_{\text{cell}} = (n)(q)(V_{\text{avg, cell}}) = (C_{\text{cell}})(V_{\text{avg, cell}})$ , in which  $C_{\text{cell}}$  (also known as the capacity of the cell) is the amount of charge that can move between the cathode and anode and is depending on the nature of the electrode active materials that have been used. The theoretical gravimetric ( $\text{mAh g}^{-1}$ ) and volumetric ( $\text{mAh cm}^{-3}$ ) capacities of the cell ( $C_{\text{cell}}$ ), in terms of the capacity of the cathode ( $C_{m,c}$  or  $C_{v,c}$ ) and capacity of the anode ( $C_{m,a}$  or  $C_{v,a}$ ), respectively, can be written as:

$$C_{\text{cell}}(\text{in mAhg}^{-1}) = \frac{1}{\frac{1}{C_{m,a}} + \frac{1}{C_{m,c}}} \quad \text{Equation 2.1}$$

and

$$C_{\text{cell}}(\text{in mAh cm}^{-3}) = \frac{1}{\frac{1}{C_{v,a}} + \frac{1}{C_{v,c}}} \quad \text{Equation 2.2}$$

In both cases, the amount of  $C_{\text{cell}}$  increases with the increasing capacity of active materials, which is the motivation for the quest for finding active materials with high specific/volumetric capacity. Moreover, the amount (weight and volume) of inactive components in each cell should be minimized to achieve higher energy density. Figure 2.1 shows that through optimizations of these parameters, the energy density and specific energy of commercial LIBs (in the cell level) have reached  $\sim 700 \text{ Wh L}^{-1}$  and  $\sim 250 \text{ Wh kg}^{-1}$ , respectively.

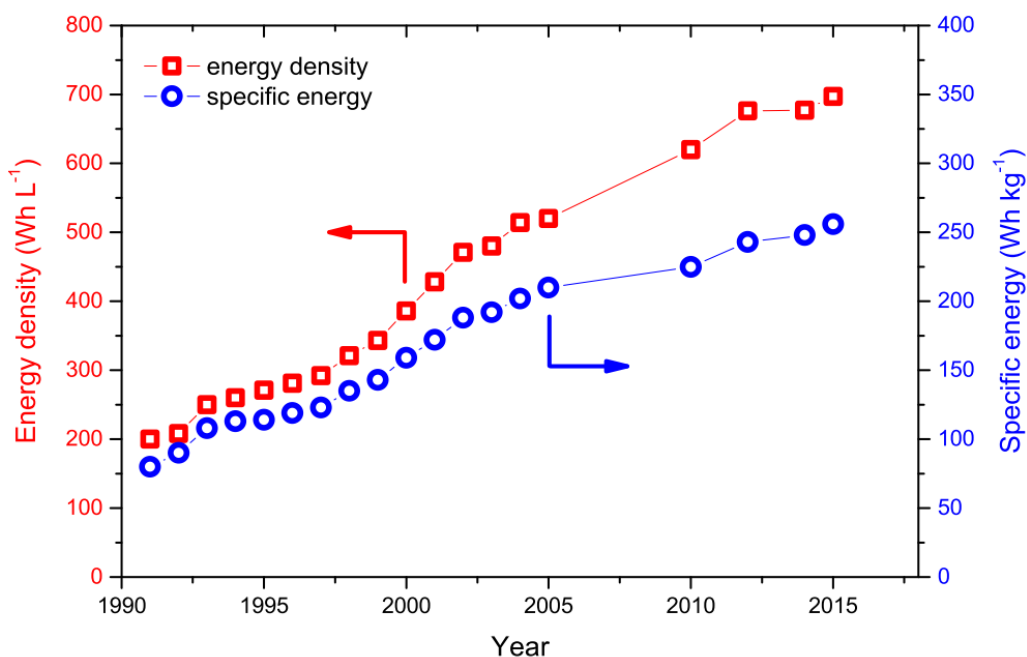


Figure 2.1. Evolution of the specific energy and energy density of LIBs (cell level) from 1991 to 2015, following their commercialization. Reprinted with permission from Placke, T., Kloepsch, R., Dühnen, S., & Winter, M. (2017). Lithium-ion, lithium metal, and alternative rechargeable battery technologies: the odyssey for high energy density. *Journal of Solid State Electrochemistry*, 21(7), 1939-1964. doi:10.1007/s10008-017-3610-7

For the cathode materials, the specific capacity values are limited to a maximum value of  $\sim 200 \text{ mAh g}^{-1}$  in the case of  $\text{LiNi}_{0.8}\text{Mn}_{0.1}\text{Co}_{0.1}\text{O}_2$  (NMC-811) (Placke, Kloepsch, Dühnen, & Winter, 2017). This means that if the energy density improvement is to be achieved through increasing charge-storage capacity, the capacity of the anode should be increased.

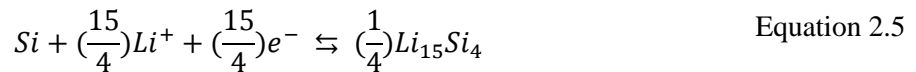
The anode active material in the state-of-the-art LIBs has been graphite that works based on the intercalation of Li between its graphene planes (Placke et al., 2017). The specific capacity of graphite is calculated according to the following equation:



$$\begin{aligned} \text{Specific Capacity} &= \frac{(1)F}{\text{wt. of } 6 \text{ mol } C} = \frac{(1)(F)}{6(M_C)} \\ &= \frac{(1)(26.80148 * 10^3 \text{ mAh mol}^{-1})}{6(12.0107 \text{ g mol}^{-1})} = 372 \text{ mAh g}^{-1} \end{aligned} \quad \text{Equation 2.4}$$

If we consider the density of graphite as  $2.266 \text{ g cm}^{-3}$ , the volumetric capacity is calculated as  $843 \text{ Ah L}^{-1}$ . The average delithiation potential of graphite is  $0.2\text{-}0.1 \text{ V}$  (Obrovac & Chevrier, 2014).

On the other hand, metals and metalloids such as Mg, Sb, Sn, and Si can host Li ions with alloying-dealloying reactions. Theoretically, the capacities of the alloy-type negative electrodes can reach extremely high values, both gravimetrically and volumetrically. However, due to their significant volume expansions and contractions during alloying and dealloying reactions, the long-term stability of these electrodes is challenging (Obrovac & Chevrier, 2014). Among alloy-type negative electrode materials, silicon has attracted scientific and practical interest in the development of high energy-density LIBs. It is the second most abundant element in the earth's crust (Ashuri, He, & Shaw, 2015). It has a relatively low dealloying potential ( $0.4 \text{ V}$ ), which does not significantly decrease the average cell voltage. It has a high theoretical specific capacity of  $3579 \text{ mAh g}^{-1}$  and volumetric capacity of  $2194 \text{ Ah L}^{-1}$ , forming  $Li_{15}Si_4$  alloy with lithium:



$$\begin{aligned} \text{Specific Capacity} &= \frac{(15/4)F}{\text{wt. of } 1 \text{ mol } Si} = \frac{\left(\frac{15}{4}\right)(F)}{M_{Si}} \\ &= \frac{\left(\frac{15}{4}\right)(26.80148 * 10^3 \text{ mAh mol}^{-1})}{(28.0855 \text{ g mol}^{-1})} = 3579 \text{ mAh g}^{-1} \end{aligned} \quad \text{Equation 2.6}$$

Therefore, the implementation of silicon anode in a commercial LIB cell has a great potential to take specific energy and energy density to the next level. For example, in a hypothetical cell stack with  $LiCoO_2$  as a cathode, substituting graphitic carbon with silicon can increase the volumetric cell energy by up to  $34 \%$  (Obrovac & Chevrier,

2014). However, the alloy-type anode materials undergo a significant volume expansion once alloyed with Li. The electrochemical reaction of Si with Li at room temperature results in  $\text{Li}_{15}\text{Si}_4$  alloy (Obrovac & Christensen, 2004). Compared to 4 moles of crystalline Si, the volume of 1 mole of crystalline  $\text{Li}_{15}\text{Si}_4$  will be 280% bigger, i.e.

$$\frac{V_{(1 \text{ mole } \text{Li}_{15}\text{Si}_4)} - V_{(4 \text{ moles } \text{Si})}}{V_{(4 \text{ moles } \text{Si})}} = 2.80 \quad \text{Equation 2.7}$$

Such a high volume-expansion has detrimental consequences at all levels. At the subparticle level, this expansion leads to pulverization of alloy particles, electrical contact loss, and cell failure. At the particle level, the electrolyte decomposition product on the surface of the electrode materials (also known as *solid electrolyte interphase (SEI)*) can get disrupted in each cycle, and hence its thickness continues to increase. At the electrode level, the binder might not be able to endure the volume expansion, and loss of electrical contact could happen. Also, at the cell level, such a volume expansion can cause cell bulging, separator failure, and current collector distortion (Obrovac & Chevrier, 2014).

### 2.1.2 Nanostructured silicon anodes in LIBs

It is known that decreasing the size of materials (including silicon) to the nanoscale (below the critical value) prevents crack propagation because of the lower density of lattice defects in the nanostructures (G. Zhu et al., 2021). Therefore, the nanostructured silicon materials show more promise in their cycling stability.

The most important achievements in nanostructuring silicon-based lithium-ion battery anodes are explained from a chronicle perspective by Zuo et al. up to 2016 (Zuo, Zhu, Müller-Buschbaum, & Cheng, 2017). Pioneer works done between 1990 and 2000 mainly focused on the synthesis of silicon and carbon composites by embedding silicon in graphite or an amorphous carbon matrix through mechanical milling or chemical vapor deposition (CVD) (Wilson, Way, Dahn, & Buuren, 1995; Zuo et al., 2017). From 2001 to 2005, the main strategies to circumvent the degradation of performance of silicon-based anodes were decreasing the particle size of silicon to form nanoparticles (zero-dimensional (0-D)), and synthesis of composites of silicon with active and inactive buffer matrices.

From 2006 to 2010, the research on silicon with one-dimensional (1-D) nanostructures like nanowires (NW) and nanotubes (NT) and also three-dimensional (3-D) porous structures emerged (Chan et al., 2008; S. Zhang et al., 2010). It was

previously found that the amorphous thin-film silicon electrodes showed stable capacity retention over cycling; however, the amount of active material that could be loaded was insufficient for practical uses. Increasing the thickness of the electrode and using the bulk micron-sized particles both led to poor cycling because of the pulverization of the silicon upon expansion-contraction (Figure 2.2(a)). On the other hand, silicon nanowires could accommodate large strains without getting pulverized (Figure 2.2). The main drawback of the Si NW and Si NT structures was the low mass-loading of the anodes that prevented their practical application (Zuo et al., 2017). This was the reason for the emergence of the studies for the synthesis of 3-D porous silicon structures through magnesiothermic reduction (Hai, Grigoriants, & Gedanken, 2009). Removal of byproducts of magnesiothermic reduction left void spaces in the structure that could accommodate the large volume expansion of the silicon during lithiation.

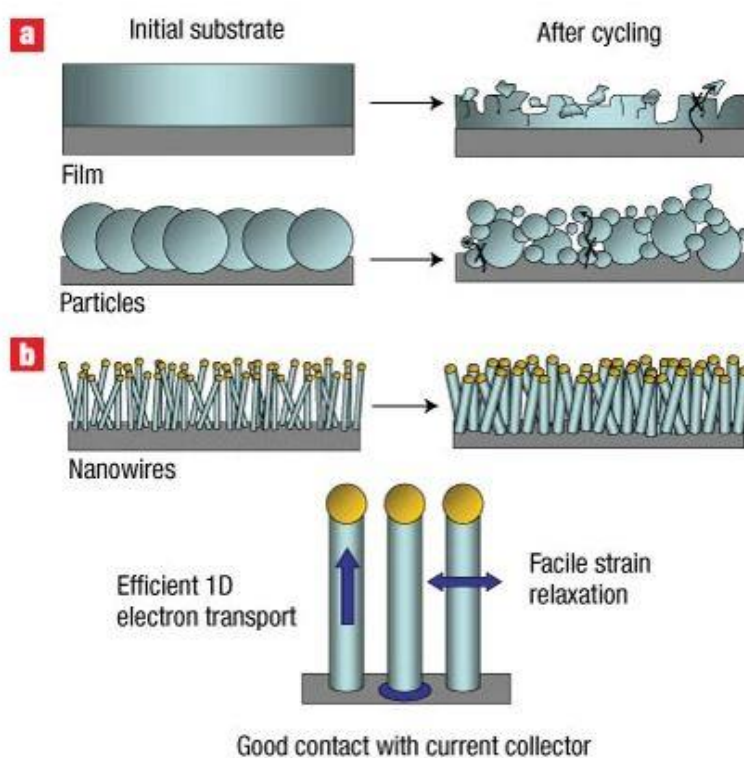


Figure 2.2. (a) Degradation of film and particle silicon structures during cycling, (b) Advantages of nanowires directly grown on the surface of current-collector. Reprinted with permission from Chan, C. K., Peng, H., Liu, G., McIlwrath, K., Zhang, X. F., Huggins, R. A., & Cui, Y. (2008). High-performance lithium battery anodes using silicon nanowires. *Nature Nanotechnology*, 3(1), 31-35. doi:10.1038/nano.2007.411

Due to poor control on the pore size of 3-D porous structures prepared using magnesiothermic reduction, from 2010 to 2016, the state-of-the-art studies (pioneered by Yi Cui's group at Stanford University) were focused on making engineered void spaces in the nanostructures (N. Liu et al., 2014; N. Liu et al., 2012; Hui Wu & Cui, 2012; Yao et al., 2011). The purpose of the void spaces in the structures was to accommodate the volume expansion of silicon. In a study of Cui's group, interconnected silicon hollow nanospheres were developed (Figure 2.3) (Yao et al., 2011). Silica particles ( $R \sim 175$  nm) were coated onto a stainless steel substrate, followed by CVD deposition of Si. The  $\text{SiO}_2$  core was then removed by HF etching. The electrode thickness was  $\sim 12$   $\mu\text{m}$ . The empty interior space in the spheres was expected to buffer the volume expansion of silicon. The selected area electron diffraction pattern shows the amorphous nature of the sample (Figure 2.3 (E) inset). The electrodes with interconnected silicon hollow nanospheres achieved the high initial discharge capacity of  $2725$   $\text{mAh g}^{-1}$  with less than 8% capacity degradation every hundred cycles for 700 total cycles.

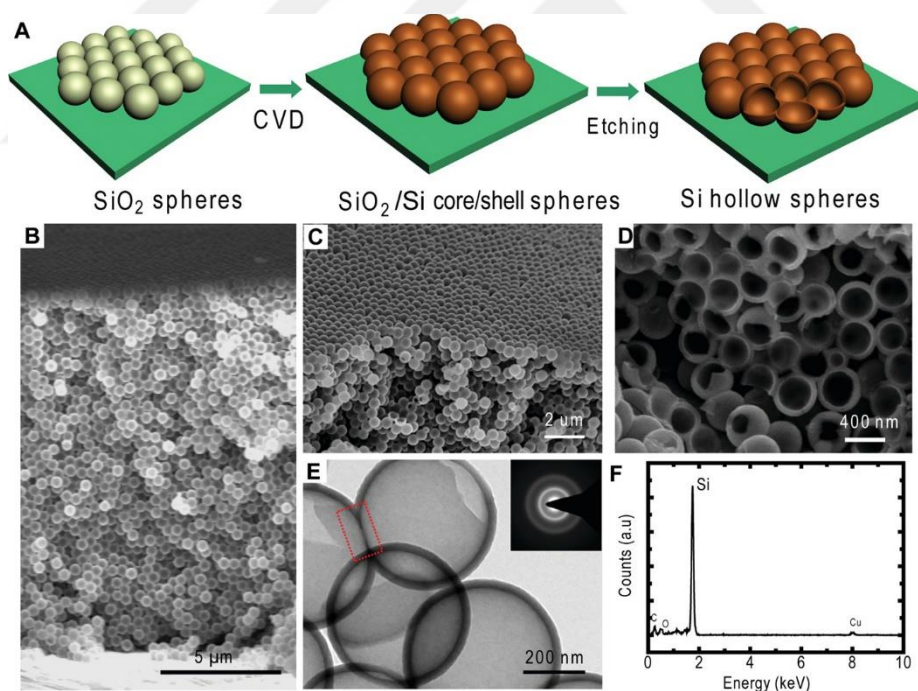


Figure 2.3. Synthesis and characterization of an interconnected Si hollow nanosphere electrode. (A) Schematic of hollow sphere synthesis. (B) Typical cross-sectional SEM image of hollow Si nanospheres. (C) SEM side view of the same sample of hollow Si nanospheres. (D) SEM image of hollow Si nanospheres (E) TEM image of interconnected hollow Si spheres, (F) Energy-dispersive X-ray spectroscopy (EDS) of a hollow Si sphere. Adapted with permission from Y. Yao, M. T. McDowell, I. Ryu, H. Wu, N. A. Liu, L. B. Hu, W. D. Nix, Y. Cui, *Nano Lett.* 2011, 11, 2949-2954,

In another study, Ashuri et al. synthesized a powder form of core-shell hollow silicon nanospheres through a multi-step synthesis route using polystyrene nanoparticles as templates (Figure 2.4) (Ashuri et al., 2016). The hollow Si@C structure exhibited better electrochemical cycle stability than both micro-sized and nano-sized silicon anodes. It delivered a stable specific capacity of 700 mAh g<sup>-1</sup> after 100 cycles at a current density of 2 A g<sup>-1</sup> and 800 mAh g<sup>-1</sup> after 120 cycles at a current density of 1 A g<sup>-1</sup>.

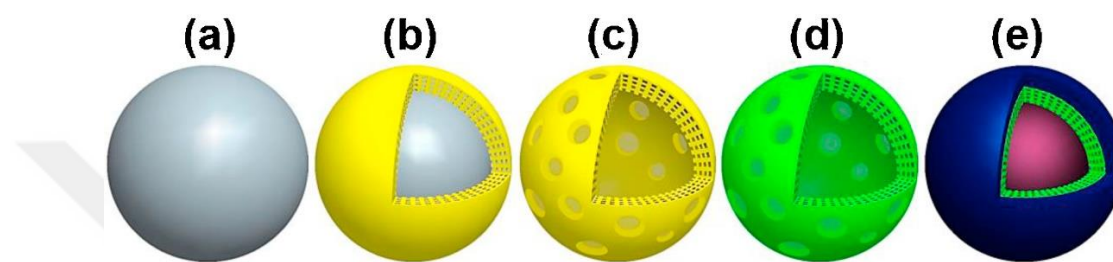


Figure 2.4. Schematic of synthesis steps: (a) PS nanoparticles, (b) PS@SiO<sub>2</sub>, (c) Hollow SiO<sub>2</sub>, (d) Hollow Si, and (e) Hollow Si@C. Adapted with permission from Ashuri, M., He, Q., Liu, Y., Zhang, K., Emani, S., Sawicki, M. S., . . . Shaw, L. L. (2016). Hollow Silicon Nanospheres Encapsulated with a Thin Carbon Shell: An Electrochemical Study. *Electrochimica Acta*, 215, 126-141. doi:<http://dx.doi.org/10.1016/j.electacta.2016.08.059>

Another architecture was mesoporous silicon nanofibers (m-SiNFs) which were synthesized by adding preformed colloidal silica nanoparticles to a polyacrylic acid (PAA) solution as the carrier polymer and template. The mixture was electrospun, and the resulting nanofiber was calcined to remove the carrier PAA and reduced to silicon by magnesiothermic reduction (Figure 2.5) (Lee et al., 2013). In this case, the mesoporosity (pores with diameters less than 20 nm) served to buffer the expansion-contraction of the silicon primary particles.

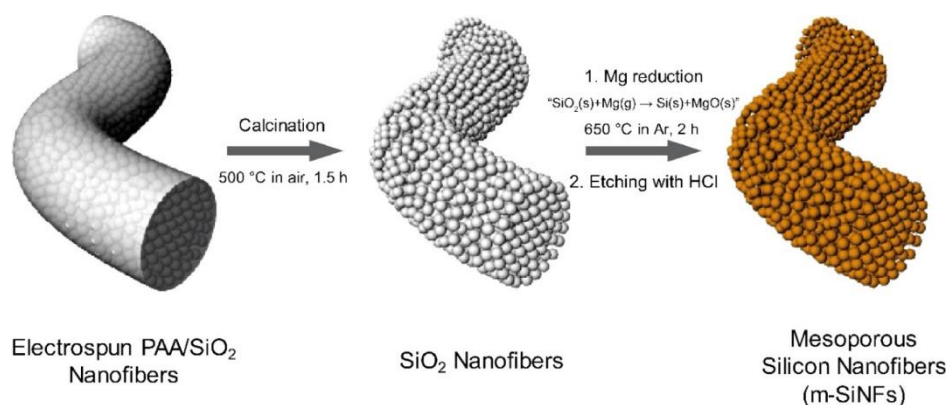


Figure 2.5. Schematic illustration showing the synthesis of mesoporous silicon nanofibers (m-SiNFs). From D. J. Lee, H. Lee, M.-H. Ryou, G.-B. Han, J.-N. Lee, J. Song, J. Choi, K. Y. Cho, Y. M. Lee, J.-K. Park, *ACS Appl. Mater. Interfaces* 2013, 5, 12005-12010. <https://doi.org/10.1021/am403798a>

The design to accommodate the strain induced by volume expansion-contraction of silicon during alloying-dealloying led to the synthesis of different engineered nanostructures such as hollow particles, hollow core-shell, and yolk-shell structures (Figure 2.6) (Ashuri et al., 2015; Lu, Chen, Pan, Cui, & Amine, 2018). However, the multi-step synthesis routes, low scalability of the production methods, and using template and carrier materials that do not eventually remain in the structure can lead to an increase in cost (Adelhelm, 2018). To this end, it was necessary to develop simpler and more facile methods to synthesize silicon nanoparticles and nanostructures.

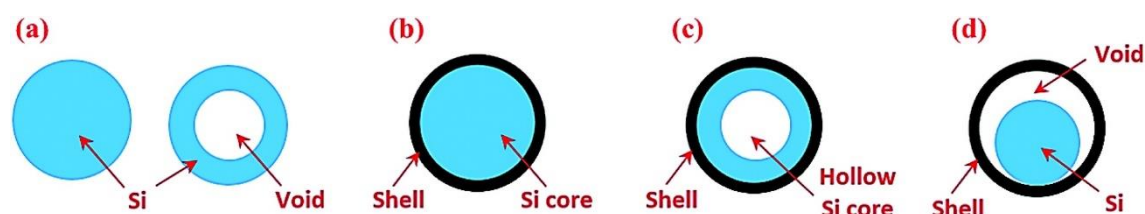


Figure 2.6. Si particles with different internal architectures: (a) solid and hollow particles, (b) solid core-shell structures, (c) hollow core-shell structures, and (d) yolk-shell structures. Reprinted with permission from Ashuri, M., He, Q., & Shaw, L. L. (2015). Silicon as a potential anode material for Li-ion batteries: where size, geometry, and structure matter. *Nanoscale*, 8(1), 74-103. doi:<http://dx.doi.org/10.1039/C5NR05116A>

Since 2016, the synthesis of polycrystalline mesoporous silicon networks and templated structures has been achieved through metallothermic reduction of oxide precursors and subsequent etching of the byproducts, thanks to low-temperature strategies realized in the metallothermic reduction (J. Entwistle, Rennie, & Patwardhan,

2018; Gao et al., 2018; Jia et al., 2020). These chemical synthesis procedures are explained in section 2.2.3.

## 2.2 Synthesis methods of silicon nanostructures

Depending on the state of precursors, the synthesis mechanism of silicon nanoparticles varies. In this section, their synthesis routes are introduced. Figure 2.7 shows a summary of the existing methods for the production of Si nanostructures.

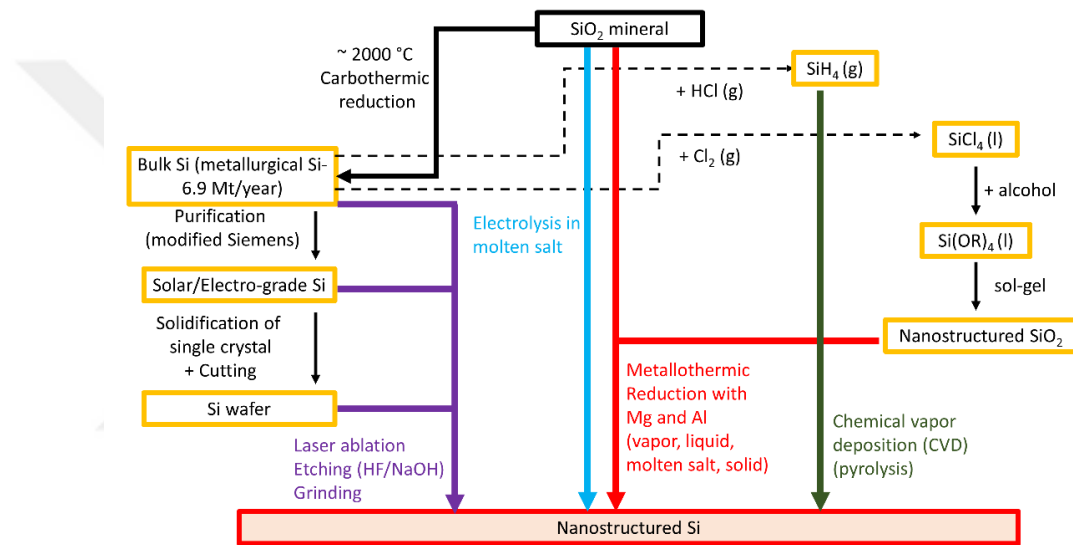
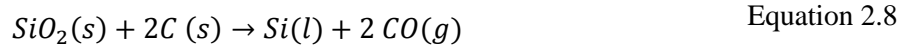


Figure 2.7. Synthesis of nanostructured silicon through different routes.

Carbothermic reduction is a chemical reduction method that produces the largest share of all industrial silicon products (6.9 Mt/year). It is the initial stage of industrial silicon extraction from SiO<sub>2</sub> minerals, and its product is known as bulk metallurgical grade silicon (J. Entwistle et al., 2018). This process consists of heating the mineral in electric arc furnaces, where an electric arc is produced using carbon electrodes. The reaction is expressed as follows:



For the reaction above to proceed (negative  $\Delta G$ , driving force), the temperature has to exceed  $2000^{\circ}\text{C}$  (N. Liu, Huo, McDowell, Zhao, & Cui, 2013), which is higher than the melting temperature of the Si product ( $1414^{\circ}\text{C}$ ). Therefore, the Si product melts, and there will be no chance of direct synthesis of porous particles and nanoparticles (J. Entwistle et al., 2018). The metallurgical grade Si is widely used in semiconductor and alloy metallurgy and is further purified depending on the final products (Tan, Jiang, & Chen, 2021). Any intermediate produced from metallurgical silicon can be used as a precursor of nanostructured silicon that is synthesized through top-down methods such as Laser ablation, HF/NaOH etching, and grinding. However, the top-down methods are energy-intensive, expensive, and generate massive contaminating emissions (Tan et al., 2021).

Electrolysis of  $\text{SiO}_2$  minerals in molten salt is another route for the production of silicon nanostructures. The molten salt (e.g.,  $\text{CaCl}_2$ ) is used as a medium to transfer oxygen ions, while the electron should be provided by an external power source. The temperature at which this process is performed is determined by the melting temperature of the salt mixture used, and for the case of  $\text{CaCl}_2$ , temperatures are typically as high as  $850^{\circ}\text{C}$  (Yasuda et al., 2013). The production yield and efficiency of this method limit its commercial application compared to carbothermic reduction (Tan et al., 2021).

Through the reaction of metallurgical silicon with HCl and  $\text{Cl}_2$ ,  $\text{SiH}_4$  and  $\text{SiCl}_4$ , which are the intermediate products of silicon nanostructure synthesis, are produced.  $\text{SiH}_4$  is the main silicon precursor used in the chemical vapor deposition (CVD) process (N. Liu et al., 2013).  $\text{SiCl}_4$  is further reacted with alcohols to produce organometallic silicon compounds of silicon such as tetraethoxysilane (TEOS), which are the precursors used in the sol-gel process to produce nanostructured  $\text{SiO}_2$ . The sol-gel-derived nanostructures of  $\text{SiO}_2$  can also be reduced to silicon nanostructures if their structures are preserved during the reduction. Temperature control during reduction reactions is critical to preserve the formed nanostructure (J. Entwistle et al., 2018). In the following sections, CVD and metallothermic reduction are discussed in more detail.

### **2.2.1 Synthesis through gas-phase CVD (pyrolysis of $\text{SiH}_4$ )**

If SiH<sub>4</sub> (monosilane) gas is heated to temperatures higher than 415°C (under an inert atmosphere) it undergoes thermal decomposition to form solid silicon particles and hydrogen gas (Ulvestad et al., 2020). The formed silicon particles can be tailored to become semi-crystalline or amorphous depending on the synthesis conditions (Andersen et al., 2014). Such a thermal decomposition has been documented in different reactor types such as fluidized bed reactors (FBR)(Wyller et al., 2016), centrifugal chemical vapor deposition reactors (C-CVDR)(Ulvestad et al., 2020), and Free Space Reactors (FSR)(Andersen et al., 2014).

The thermal decomposition (pyrolysis) reaction is:



Particles synthesized through this method are spherical with diameters in the range of 100 nm to 500 nm, and the method is claimed to be cost-effective and up-scalable in large-scale facilities (Andersen et al., 2014). The produced particles have an amorphous structure, which requires annealing under air and argon to achieve crystallinity. However, their use as LIB anode showed that the long-term cycle life of the electrodes made with amorphous silicon nanoparticles was superior to the crystallized counterparts (Ulvestad et al., 2020). Although this method has advantages for scale-up, the toxicity of the precursor gas (SiH<sub>4</sub>) and the fact that SiH<sub>4</sub> must be synthesized separately does not make it suitable for large-scale production.

### **2.2.2 Synthesis through chemical reduction**

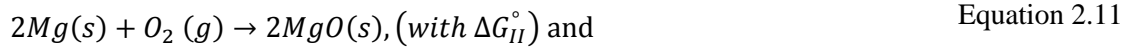
As discussed above, the carbothermic chemical reduction method produces bulk silicon. Therefore, multi-step and expensive techniques, such as CVD (Andersen et al., 2014), and Laser ablation (N. Liu et al., 2013), should be applied to produce nanostructured products. Here, metallothermic reduction methods are presented as simpler and less expensive alternatives.

### **2.2.3 Metallothermic reduction**

Metallothermic reduction reaction (MRR) that typically uses a reactive metal, such as magnesium (Mg) and aluminum (Al), has shown great potential to produce Si nanostructures at lower temperatures than conventional carbothermic reduction.

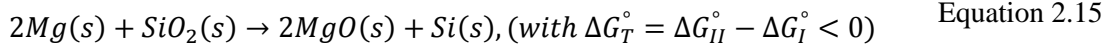
### 2.2.3.1 Underlying Thermodynamics

The thermodynamic driving force required for a reaction to be spontaneous can be quantified using the Gibbs free energy ( $\Delta G$ ) of that reaction. Suppose we plot the change in standard Gibbs free energy for consumption of 1 mole  $O_2$ . In that case, we obtain the Ellingham diagram (Figure 2.8), which shows the temperature dependence of the stability of oxides and can be used to evaluate their ease of reduction. For example, if we consider oxidation of Si and Mg, we obtain the following equations:



$$\Delta G_{II}^\circ < \Delta G_I^\circ \quad \text{Equation 2.12}$$

If we consider the summation of these reactions, the final reaction will have a negative Gibbs free energy change, which means that there is a driving force for Mg (or any element located below Si in the Ellingham diagram) to break the Si-O bonds in  $SiO_2$  and release elemental Si.



In addition to the thermodynamic driving force ( $\Delta G < 0$ ), the kinetics of the reaction should be taken into account to predict whether the reaction will occur at an acceptable rate. For this reason, MRRs with magnesium are usually carried out at temperatures between 550°C and 800°C, although they have negative Gibbs free energy change for the entire temperature range up to 1000°C (Chen, Fan, Dhanabalan, Chen, & Wang, 2011; X. Liu, Giordano, & Antonietti, 2012). Since the reaction temperatures are well below the melting point of the produced silicon (1414°C), nanoparticles and porous forms of silicon can be synthesized without difficulty.

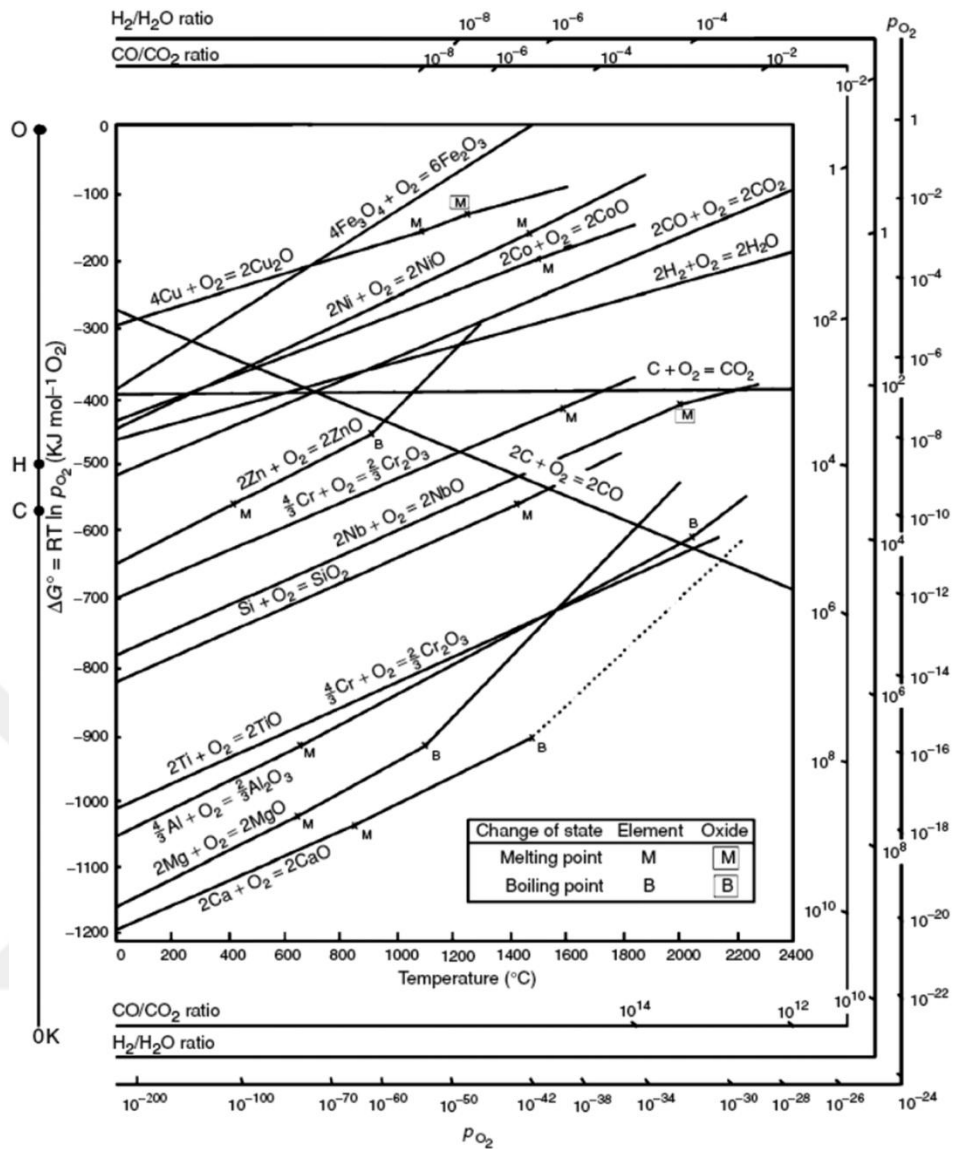
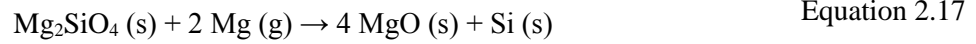


Figure 2.8. Ellingham diagram for the formation of oxides based on their standard free energy of formation over temperature. Reprinted with permission from Oar-Arteta, L., Wezendonk, T., Sun, X., Kapteijn, F., & Gascon, J. (2017). Metal organic frameworks as precursors for the manufacture of advanced catalytic materials. *Materials Chemistry Frontiers*, 1(9), 1709-1745. doi:10.1039/c7qm00007c

### 2.2.3.2 Mg-MRR through the gas-phase mechanism

Mg is known to have a high vapor pressure at elevated temperatures (e.g. 1 Pa at 428 $^\circ\text{C}$ ) (N. Liu et al., 2013). In other words, it undergoes sublimation even before reaching its melting temperature (650 $^\circ\text{C}$ ). Therefore, magnesiothermic reduction has been generally carried out in a sealed and closed vessel to prevent Mg vapor from escaping from the system (Chen et al., 2011; N. Liu et al., 2013; Richman, Kang, Brezesinski, & Tolbert, 2008).

According to Wynnyckyj and Bhogeswara Rao, the gas-phase magnesiothermic reduction of SiO<sub>2</sub> starts with the surface adsorption of Mg vapor on the SiO<sub>2</sub> (Wynnyckyj & Bhogeswara Rao, 1976), followed by reduction reactions as:



According to Equation 2.17, the absence of enough Mg (g) in the system can lead to residual Mg<sub>2</sub>SiO<sub>4</sub> (s) in the final product. Namely, in a sealed container, the lower the set temperature, the higher the chance of having Mg<sub>2</sub>SiO<sub>4</sub> (s) in the final product since the vapor pressure of Mg(g) decreases. Xie et al (Xie et al., 2014) confirmed that residual Mg<sub>2</sub>SiO<sub>4</sub> (s) could be reduced by increasing the reaction set temperature from 700°C to 900°C. They argued that increasing the reaction set temperature increases Mg-vapor pressure, and this consumes the residual Mg<sub>2</sub>SiO<sub>4</sub>. In another study (also in a closed vessel), Chen et al. showed that the formation of Mg<sub>2</sub>SiO<sub>4</sub> at lower temperatures could be compensated by increasing the Mg/SiO<sub>2</sub> ratio in the reactants (Chen et al., 2011).

### 2.2.3.3 Diffusion-controlled magnesiothermic reduction reaction Mg-MRR

Gutman et al. observed periodic layered structure of reaction products (MgO and Mg<sub>2</sub>Si) in the magnesiothermic reduction of SiO<sub>2</sub> in the temperature range of 400 – 640°C and proposed a diffusion-controlled mechanism based on thermodynamics and kinetics principles (Gutman, Gotman, & Shapiro, 2006). Their thermodynamics calculation and experimental observations showed that in their magnesiothermic reduction trials, first, a MgO layer forms at the interface of SiO<sub>2</sub>/Mg. Since the diffusivity of Mg in the MgO is much higher compared to that of Si, there will be the accumulation of Si at the SiO<sub>2</sub>/MgO interface. When the Mg concentration exceeds a critical concentration (due to diffusion), it promotes the formation of the Mg<sub>2</sub>Si phase. The formation of Mg<sub>2</sub>Si on the SiO<sub>2</sub> surface is not energetically favorable, which leads to the formation of another layer of MgO between the newly formed Mg<sub>2</sub>Si and SiO<sub>2</sub> surface. Therefore, a new MgO/Mg<sub>2</sub>Si pair forms, and the layered structure grows as depicted in Figure 2.9.

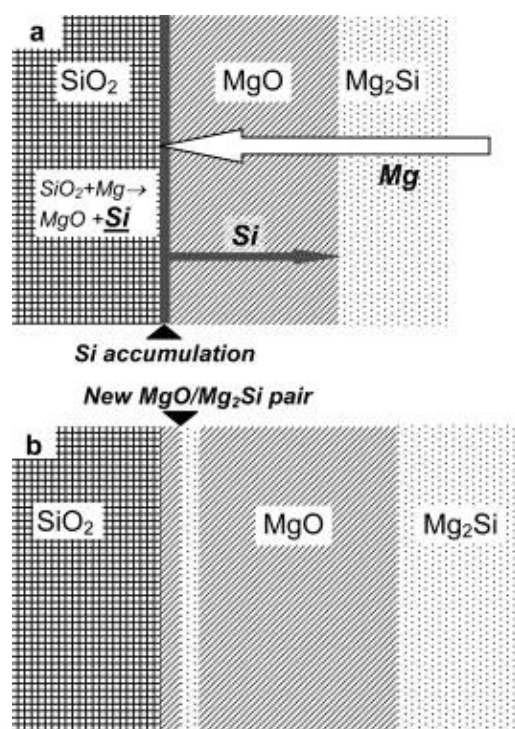


Figure 2.9. Schematic of mass transfer and periodic structure formation at SiO<sub>2</sub>/Mg interface (a) Si accumulation on the SiO<sub>2</sub> surface, as a result, MgO of 'resistance' to Si diffusion; (b) simultaneous formation of a new MgO/Mg<sub>2</sub>Si pair of layers. Reproduced with permission from Gutman, I., Gotman, I., & Shapiro, M. (2006). Kinetics and mechanism of periodic structure formation at SiO<sub>2</sub>/Mg interface. *Acta Materialia*, 54(18), 4677-4684. doi:<http://doi.org/10.1016/j.actamat.2006.05.048>

#### 2.2.3.4 Mg-MRR through solvated electrons in liquid salt

Liu et al. showed that the mechanism of reducing SiO<sub>2</sub> by Mg in molten salts (eutectic mixtures of LiCl/KCl and NaCl/MgCl<sub>2</sub>) is through the solvated electrons, as shown in Figure 2.10. The top image in Figure 2.10 a reaction vessel of molten salts containing spatially separated SiO<sub>2</sub> and Mg particles is shown. In the bottom left SiO<sub>2</sub> particles are surrounded by electrons from ionization of Mg. In the bottom middle solvated electrons attack the SiO<sub>2</sub> particle meanwhile removing the O<sup>2-</sup> from the SiO<sub>2</sub> network, leading to the crushing of the particle and formation of Si. And at bottom right optimization of surface energy results in the formation of spherical Si particles. In their study, they obtained silicon with crystallite sizes in the 5 nm- 35 nm range (X. Liu et al., 2012). They showed that the size of the crystallites of the produced silicon nanoparticles increases with increasing the solubility of Mg in the halide salt, i.e. larger crystallites of silicon were observed in NaCl/MgCl<sub>2</sub> eutectic mixture compared to LiCl/KCl. They introduced the idea of controlling the primary particle size (crystallite size) of the synthesized silicon nanoparticles and thereby controlling their optical properties.

Iwadate et al. showed that the yield of Si was higher in a LiCl-MgCl<sub>2</sub> melt, in which the Mg solubility was higher, than in NaCl-MgCl<sub>2</sub> melt (Iwadate, Ohgane, & Ohkubo, 2018). Iwadate and Liu's works indicated that reduction in Mg solubility at lower temperature decrease both the crystallite size and the yield of reduction in molten salt systems.

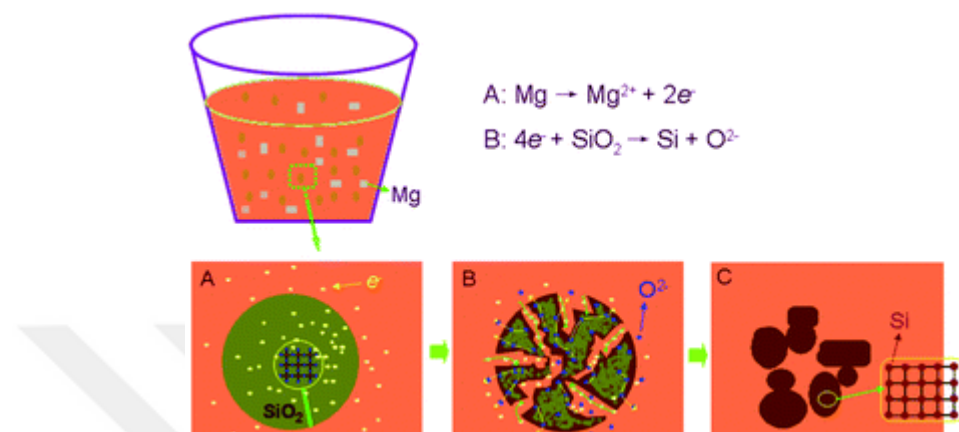


Figure 2.10. A schematic illustration of the Si nanocrystal formation in molten salts based on the reduction of SiO<sub>2</sub> by electrons solvated in the liquid phase. Reprinted with permission from Liu, X., Giordano, C., & Antonietti, M. (2012). A molten-salt route for synthesis of Si and Ge nanoparticles: chemical reduction of oxides by electrons solvated in salt melt. *Journal of Materials Chemistry*, 22(12), 5454-5459. doi:<http://dx.doi.org/10.1039/C2JM15453F>

### 2.2.3.5 Heat-scavenging

According to Luo et al., the heat produced during the magnesiothermic reduction of SiO<sub>2</sub> with the gas phase mechanism (Equation 2.19) (for Mg (g),  $\Delta H = -586.7$  kJ/mol<sub>SiO<sub>2</sub></sub>, or 9.8 kJ/g<sub>SiO<sub>2</sub></sub>) is high enough to cause sintering of the Si particle products (Luo et al., 2013).



They showed that although their set temperature for the synthesis was 650°C, the actual temperature experienced by the magnesiothermic reduction products could exceed 1300°C. Exposure to such high temperatures could collapse the porosity and increase the crystallite size. This study showed the necessity of heat moderation during magnesiothermic reduction to produce nanostructured silicon materials. As previously discussed, before the work by Luo et al., molten salts were used as the reaction medium in magnesiothermic reduction of SiO<sub>2</sub> to produce silicon nanoparticles (X. Liu et al.,

2012). It is deduced that the heat transfer rate in the molten eutectic salt medium was high enough to prevent sintering silicon products and loss of porosity. Luo et al. used NaCl as a heat-scavenger because of its abundance, relatively low melting point (801°C), and high enthalpy of melting at the melting point ( $\Delta H_m$ , 801°C = 28.2 kJ mol<sup>-1</sup>) and found that for a set temperature of 650°C, the observed reaction temperature in the presence of NaCl as a heat scavenger was between 840°C to 1100°C, while in its absence it was higher than 1300°C (Luo et al., 2013). They showed that silicon synthesized in the presence of heat-scavengers showed ~ 295 m<sup>2</sup> g<sup>-1</sup> of BET surface area and a pore volume of ~ 1.2 cm<sup>3</sup> g<sup>-1</sup> with 22 nm diameter particles. On the other hand, in the absence of heat-scavengers, they obtained a silicon structure with dense morphology with a surface area of ~ 5.2 m<sup>2</sup> g<sup>-1</sup> BET and a pore volume of ~ 0.01 cm<sup>3</sup> g<sup>-1</sup>. During magnesiothermic reduction of SiO<sub>2</sub> in the presence of NaCl, the reaction temperature rises above the set temperature due to the exothermic nature of the reaction. Then the heat is transferred to NaCl and consumed by its fusion, which prevents the further rise of temperature, as shown in Figure 2.11 (Favors et al., 2014). In the molten salt route, the set temperature is always higher than the melting temperature of the medium (eutectic salt mixture), while in the heat-scavenging, the salt added to the reactant is only expected to lower the maximum temperature.

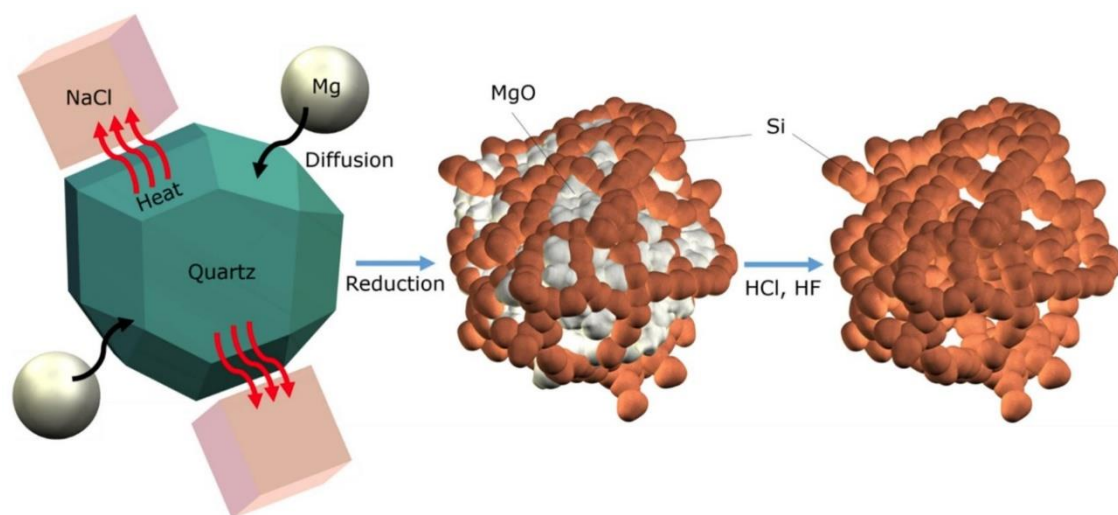


Figure 2.11. Schematic of the heat scavenger-assisted Mg-MRR. Reprinted with permission from Favors, Z., Wang, W., Bay, H. H., Mutlu, Z., Ahmed, K., Liu, C., . . . Ozkan, C. S. (2014). Scalable Synthesis of Nano-Silicon from Beach Sand for Long Cycle Life Li-ion Batteries. Scientific Reports, 4, 5623. doi:<http://doi.org/10.1038/srep05623>

### 2.2.3.6 Low-temperature MRR through bi-functional molten salts

The role of molten salts in the MRR of silicon precursors had been established as a kinetic controller until Lin et al. showed that  $\text{AlCl}_3$  could also take part in the MRR reaction (N. Lin, Han, Zhou, et al., 2015). Therefore,  $\text{AlCl}_3$  and its mixtures with other salts are known as bi-functional molten salts (Song et al., 2018). Crystalline silicon could be produced at temperatures as low as  $200^\circ\text{C}$  when  $\text{AlCl}_3$  is used as a bi-functional molten salt. It was argued that with proper recycling of byproducts, low-temperature MRR could be seen as a sustainable method to produce silicon nanoparticles, even from micron-sized silicon precursors (N. Lin, Han, Zhou, et al., 2015). The drawback of the process is the moisture sensitivity of  $\text{AlCl}_3$ , which causes the formation of corrosive species when exposed to moisture (Song et al., 2018).

According to the the initial crystallographic phase characterizations (N. Lin, Han, Zhou, et al., 2015), low-temperature magnesiothermic reduction reaction (LTMRR) and low-temperature aluminothermic reduction reaction (LTARR) are, respectively:



The mechanism of LTMRR includes initial reduction of  $\text{AlCl}_3$  by Mg to form nascent Al ( $\text{Al}^*$ ) and  $\text{MgCl}_2$ , reduction of  $\text{SiO}_2$  to Si by the active  $\text{Al}^*$ , and the reaction of remaining  $\text{AlCl}_3$  and  $\text{MgCl}_2$  to form eutectic  $\text{MgAl}_2\text{Cl}_8$  salt (N. Lin, Han, Wang, et al., 2015).

The mechanism of LTARR in the molten salts was the formation of metallic Al and the release of highly active electrons that attack the Si-O bonds of  $\text{SiO}_2$  to liberate silicon (Gao et al., 2018). Song et al. proposed a ligand-promoted reduction mechanism in which the activated  $\text{AlCl}^*$  produced from the ligand dissociation reacts with oxygen atoms on the  $\text{SiO}_2$  surface (Song et al., 2018).

## 2.3 Carbon nanofibers

Carbon nanofibers (CNFs) refer to carbon fibers with a diameter less than 1  $\mu\text{m}$  (B. Zhang, Kang, Tarascon, & Kim, 2016). They are used in structural applications when weight is a concern, thanks to their strength-to-weight ratio. Also, due to their excellent mechanical strength, they are used as reinforcements in polymer-matrix composites. Moreover, their high electrical conductivity and mechanical strength are applied in energy-storage applications when used as support materials for electrodes. They can be used as a host for silicon nanoparticles in the electrode material, providing both mechanical strength and electrical conductivity. (T. H. Hwang, Y. M. Lee, B.-S. Kong, J.-S. Seo, & J. W. Choi, 2012; Zhou, Wan, & Guo, 2013; J. Zhu, Wang, Fan, Mei, & Lu, 2016). Generally, carbon fibers are produced through 3 main routes:

(I) CVD, which is an old process for the production of carbon filaments during which they are grown from hydrocarbon gas on metallic catalysts (Fe, Co, or Ni) in the temperature range 700-1200 K. Hence, the CVD-derived carbon fiber product is also known as vapor-grown carbon fiber (VGCF). Due to the high graphitization temperatures used, they possess excellent electrical conductivities; however, the cost of their production is relatively high (B. Zhang et al., 2016).

(II) traditional spinning that includes mechanical ejection of a polymer solution into a coagulation bath or air that leads to the formation of the polymeric fibers. Through subsequent stabilization and carbonization under tension, stiff carbon fibers are produced. Such fibers typically have a diameter of larger than 5  $\mu\text{m}$  that does not fall into the category of nanofibers (B. Zhang et al., 2016).

(III) Electrospun carbon nanofibers that are produced through a 2-step process: (a) electrospinning a polymeric precursor; and (b) a carbonization process in which the polymer transforms into an amorphous carbon form. The electrospinning and subsequent carbonization of polyacrylonitrile (PAN) are explained in sections 2.3.1 and 2.3.2.

### 2.3.1 Electrospinning polymeric precursors

Electrospinning is a facile and scalable method for the fabrication of polymeric nanofibers. As shown in Figure 2.12, the set-up is typically composed of: (a) a syringe

pump for controlling the flow rate of a polymer solution; (b) a spinneret for extruding the polymer solution; (c) a collector on which the fibers are collected; (d) a high-voltage source for applying an electric field between the spinneret and the collector.

When the polymer solution is dispensed, and high-voltage is applied, the electrostatic force from the electric field ( $E = \frac{Voltage}{Distance}$ ) overcomes the surface tension of the polymer solution, and a jet is ejected from the spinneret. After the formation of the initial jet, it splits into multiple tiny jets as the electrostatic repulsion between the charged jet becomes stronger due to solvent evaporation. The jets go through a spiral motion caused by the electrically driven bending instability forming ultrathin nanofibers. The nanofibers generally accumulate in a random orientation on the collector (B. Zhang et al., 2016). The size and morphology of the fibers produced through electrospinning depend on the solution properties i.e. concentration, chemical composition and solvent volatility or electrospinning process parameters i.e. flow rate, voltage and spinneret to collector distance (Teo, 2015; Yördem, Papila, & Menceloğlu, 2008).

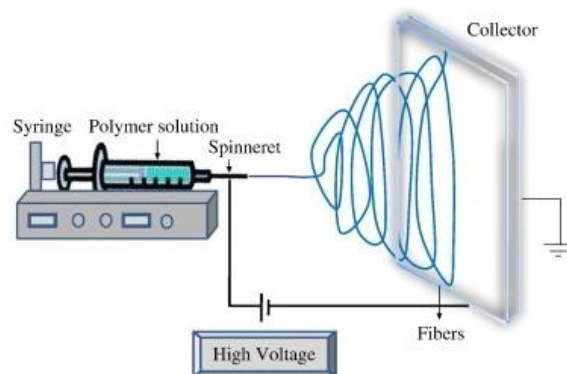


Figure 2.12. Typical set-up of an electrospinning apparatus. Reprinted with permission from Bhardwaj, N., & Kundu, S. C. (2010). Electrospinning: A fascinating fiber fabrication technique. *Biotechnology Advances*, 28(3), 325-347. doi:<https://doi.org/10.1016/j.biotechadv.2010.01.004>

Various polymers have been used as precursors to produce electrospun carbon nanofibers (B. Zhang et al., 2016). Precursor polymers can be divided into two categories based on their function in the resulting CNFs: (a) the host precursors such as polyacrylonitrile (PAN), poly(vinyl pyrrolidone) (PVP), polyimide (PI), and polyvinyl

alcohol (PVA) are the scaffold for the nanofibers, which are transformed into carbon through a heat treatment in an inert atmosphere; (b) the guest precursors such as polymethylmethacrylate (PMMA) and polystyrene (PS) are used as a sacrificial phase which decomposes during the heat treatment promoting pore formation.

Polyacrylonitrile (PAN) has been the most preferred host precursor to produce CNFs for energy storage applications due to its advantages such as high carbon yield (> 50 wt.%), excellent mechanical properties of the resulting CNFs (B. Zhang et al., 2016), and tunable diameter size by adjusting electrospinning parameters (Yördem et al., 2008). Moreover, PAN-derived CNF contains nitrogen that has been found beneficial in energy storage applications, possibly due to the improvement of electrical conductivity (Weihaan, Linchao, Ying, & Yan, 2016).

### **2.3.2 Carbonization of polyacrylonitrile (PAN) fibers**

#### **2.3.2.1 Mechanism of stabilization**

A two-step heating process is applied, namely stabilization (in air) and carbonization (in inert atmospheres), to transform the electrospun PAN fibers into carbon fibers. Stabilization is performed at a temperature between 200 and 280°C to maintain the fiber structure during the subsequent high-temperature carbonization. During stabilization, the oxygen promotes dehydrogenation by elimination of water (dehydrogenation). Then, the dangling nitrile groups react with their neighboring counterparts and undergo cyclization to form C-N bonds and C=C double bonds leading to a thermodynamically stable ladder structure. This structure has been found to show higher thermal stability (compared to PAN precursor) and withstands subsequent transformation-driven shrinkage (B. Zhang et al., 2016). As shown in Figure 2.13, the order of cyclization and dehydrogenation does not affect the final ladder-like structure (Rahaman, Ismail, & Mustafa, 2007).

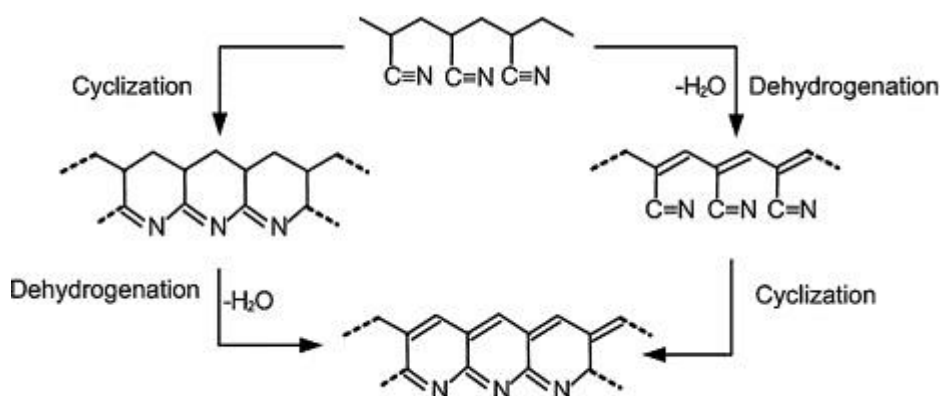


Figure 2.13. Processes during stabilization of polyacrylonitrile (PAN) fibers. Reprinted with permission from Rahaman, M. S. A., Ismail, A. F., & Mustafa, A. (2007). A review of heat treatment on polyacrylonitrile fiber. *Polymer Degradation and Stability*, 92(8), 1421-1432. doi:<https://doi.org/10.1016/j.polyimdegradstab.2007.03.023>

### 2.3.2.2 Mechanism of carbonization

During the carbonization process, performed in an inert atmosphere (Ar, N<sub>2</sub>, etc.), more dehydrogenation and denitrogenation, i.e. elimination of non-carbon atoms, take place, as shown in Figure 2.14. If the material is heated up to 3000°C, long-range order of a graphitic structure can be obtained, which is called graphitization. However, graphitization is not applied to CNF/nanoparticle composites for energy storage applications because it can lead to the growth and separation of metal/metal oxides embedded in the CNFs (B. Zhang et al., 2016).

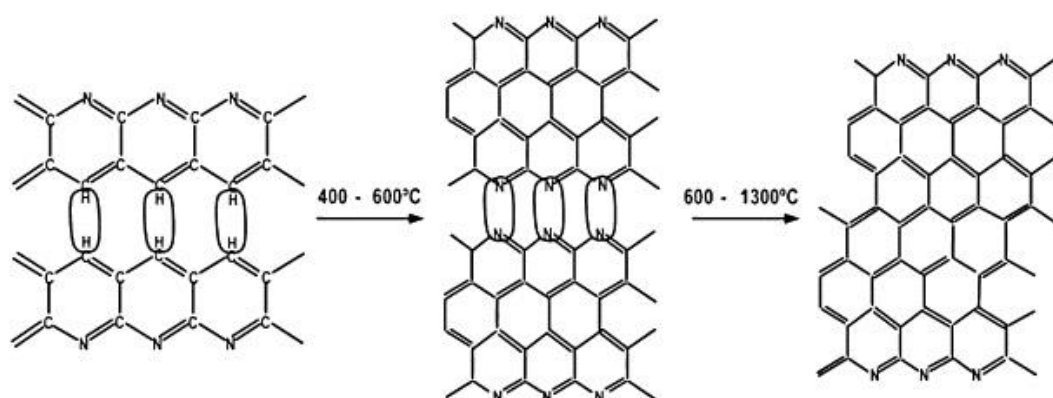


Figure 2.14. The removal of hydrogen and nitrogen during carbonization. Reprinted with permission from Rahaman, M. S. A., Ismail, A. F., & Mustafa, A. (2007). A review of heat treatment on polyacrylonitrile fiber. *Polymer Degradation and Stability*, 92(8), 1421-1432. doi:<https://doi.org/10.1016/j.polyimdegradstab.2007.03.023>

## 2.4 Composites of silicon/carbon nanofibers

In section 2.1.1 we introduced some of the challenges with using silicon anodes. They can be summarized as (a) pulverization due to large-volume expansion-contraction during cycling, (b) unstable SEI that keeps consuming the mobile Li-ions of the electrolyte during cycling, and (c) low electrical conductivity of silicon that makes the charge-transfer sluggish (Ashuri et al., 2015). As discussed previously, the nanostructured silicon can address the pulverization problem during cycling. However, the larger specific surface area of nanostructures makes the SEI formed on them bulkier per unit mass (and per unit volume) of the active material. Combined with the low electrical conductivity, this leads to having a cell with high resistance against the transfer of Li ions across the SEI. Embedding nanostructured silicon in a conductive carbon matrix has a great potential to address this issue. A carbon matrix can facilitate the electron transfer, and the SEI formed on the composite will be more stable than the one formed on silicon nanoparticles. Thanks to their scalability of production and tunable electrical conductivity, carbon nanofibers are attractive candidate materials to host electrochemically active particles (B. Zhang et al., 2016). Silicon can be incorporated into carbon nanofibers by two methods: (a) adding preformed silicon nanoparticles to the CNF polymer precursor and (b) adding a silicon precursor to the CNF polymer precursor. The addition of silicon to sacrificial (guest) polymeric precursors is beyond the scope of this thesis, and we only discuss the addition of silicon into host polymer precursors.

### 2.4.1 Addition of preformed silicon nanoparticles to the CNF polymer precursor

The most straightforward method of synthesizing Si/CNFs nanocomposites is to incorporate the preformed particles into the polymer precursor solution followed by its electrospinning. However, the direct addition of solid nanoparticles often leads to agglomeration of nanoparticles (Ji, Jung, Medford, & Zhang, 2009; Z.-L. Xu, Zhang, & Kim, 2014) as the high-surface area nanoparticles tend to minimize their interfacial energy by forming aggregates (Tjong & Chen, 2004). To address this issue, Wang et al. used a surfactant and reached capacity retention of 58% over 100 cycles at 100 mA g<sup>-1</sup> (final capacity of 870 mAh g<sup>-1</sup> for a composite containing 60 wt.% Si NPs) (M.-S. Wang, Song, Wang, & Fan, 2015). Xu et al. studied the surface-modification of silicon nanoparticles before adding them into an aqueous solution of PVA and obtained ~ 74%

capacity retention over 50 cycles at 100 mA g<sup>-1</sup> (final capacity of 735 mAh g<sup>-1</sup> for a composite containing 41 wt.% Si NPs) (Z.-L. Xu et al., 2014). Although anodes prepared using modified silicon nanoparticles and dispersing agents exhibited improved cyclic performance, the dispersion efficiency and cycling stability were not satisfactory for practical applications. Therefore, methods to homogeneously disperse silicon nanostructures in a carbon network should be further explored.

#### **2.4.2 Addition of silicon precursors to the CNF polymer precursor**

In the carbon-metal/metal oxide composite materials used for electrochemical applications, a high degree of mixing between carbon and inorganic particles has a beneficial effect on the electrochemical properties of the resulting devices. The reason is attributed to the larger interface available for charge transfer between the phases (Zhenhui Liu et al., 2018).

The organic-inorganic co-networks of sol-gel hybrid materials are known to be indistinguishable above the nanoscale (Maçon et al., 2015). One of the methods to obtain carbon-silicon (oxide) composites with a high degree of mixing between co-networks is to synthesize a hybrid of a polymer and silicon (oxide) precursor. If the carbon-precursor polymer is pre-formed before the hybrid synthesis and has no covalent bonding to the silicon (oxide) network, the hybrid material is categorized as type I hybrid (Novak, 1993). The earliest attempt to make submicron electrospun hybrid polymer silica nanofibers was a study in which a SiO<sub>2</sub> sol, made of hydrolyzed tetraethyl orthosilicate (TEOS), was added to a pre-formed polyvinyl alcohol (PVA) solution (Pirzada, Arvidson, Saquing, Shah, & Khan, 2012). It was found that Si-OH groups formed covalent bonds with the pre-formed PVA polymer, characterized by FTIR analysis, as schematically shown in Figure 2.15. This finding indicated a covalent bonding between the organic and inorganic co-networks, which is categorized as a type II hybrid material (Novak, 1993). The study by Pirzada et al. showed that the PVA undergoes cross-linking upon exposure to the sol of TEOS, leading to increased viscosity upon aging the solutions, which resulted in the formation of larger diameter fibers (Pirzada et al., 2012).

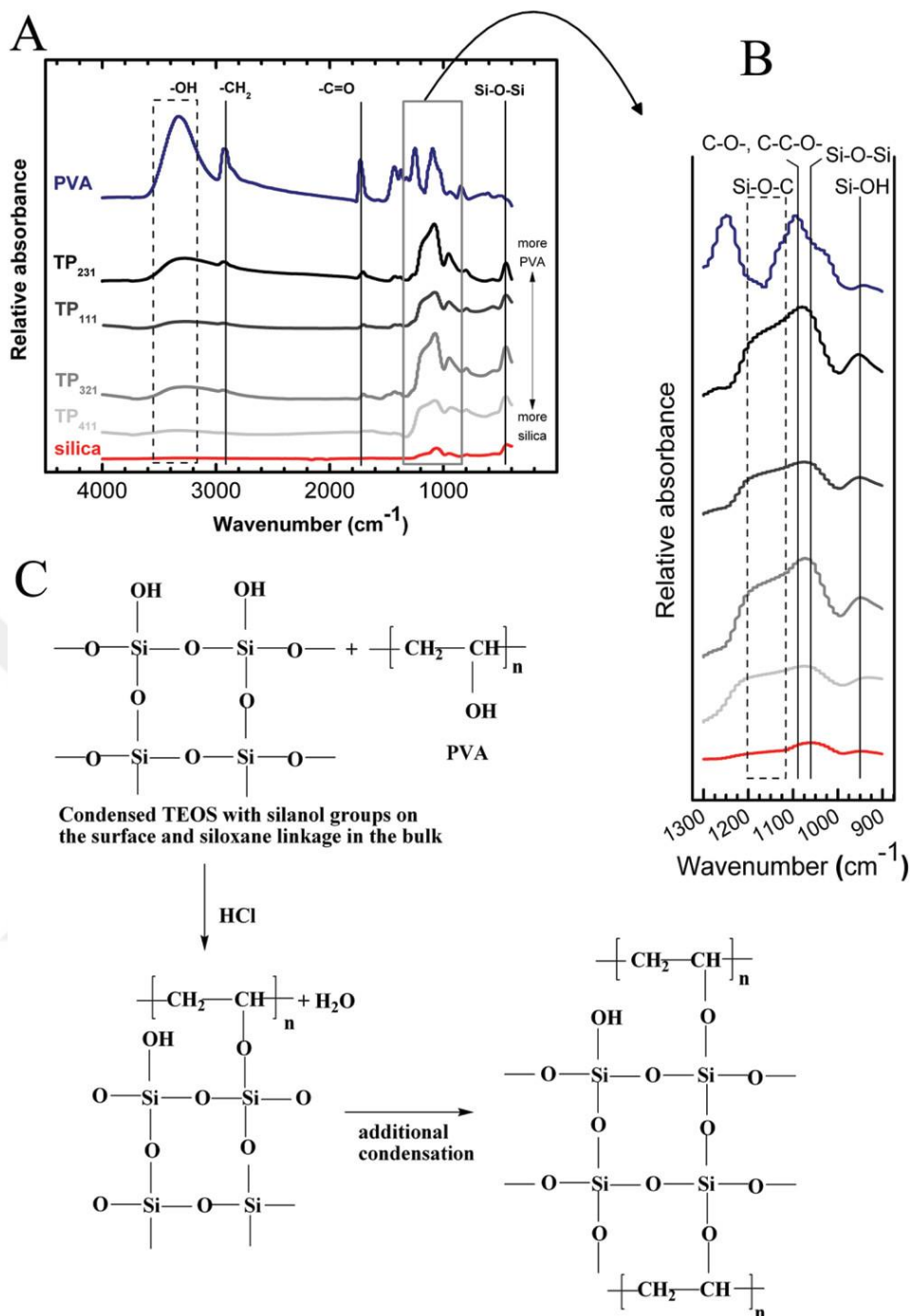


Figure 2.15. Cross-linking of PVA upon addition of hydrolyzed TEOS. (A) FTIR spectra of as-spun PVA, silica, and PVA-silica composites. (B) Enlarged version shows the Si-O-C peak which is generated because of the interaction between -OH groups of PVA and surface silanols of silica resulting in possible production of (C) suggested structure. Reprinted with permission from Pirzada, T., Arvidson, S. A., Saquing, C. D., Shah, S. S., & Khan, S. A. (2012). Hybrid Silica-PVA Nanofibers via Sol-Gel Electrospinning. *Langmuir*, 28(13), 5834-5844. doi:10.1021/la300049j. Copyright 2012 American Chemical Society

This issue was not observed in their later study, in which they used polyacrylonitrile (PAN) instead of PVA (Pirzada, Arvidson, Saquing, Shah, & Khan, 2014). They did not observe any covalent bonding between PAN and the TEOS and suggested that possible intermolecular interaction is via hydrogen bonding, as shown in Figure 2.16. The diameter of fibers is directly related to the viscosity of the solution. The diameter of PVA-SiO<sub>2</sub> fibers increased upon aging of the precursor solutions before electrospinning due to the cross-linking effect. On the other hand, diameter and viscosity control was achieved more easily in the case of PAN-SiO<sub>2</sub> hybrid (Pirzada et al., 2012, 2014). Under the acidic conditions, TEOS was polycondensed to form a SiO<sub>2</sub> linear framework instead of SiO<sub>2</sub> colloidal particles because the rate of condensation was slow relative to the rate of hydrolysis. Hence, the composite nanofiber was composed of a continuous PAN phase and homogeneously dispersed SiO<sub>2</sub> domains. After the carbonization under an inert atmosphere, PAN transformed to carbon, and the hydrolyzed TEOS completely condensed to SiO<sub>2</sub> (Tai, Gao, Tan, Sun, & Leckie, 2014).

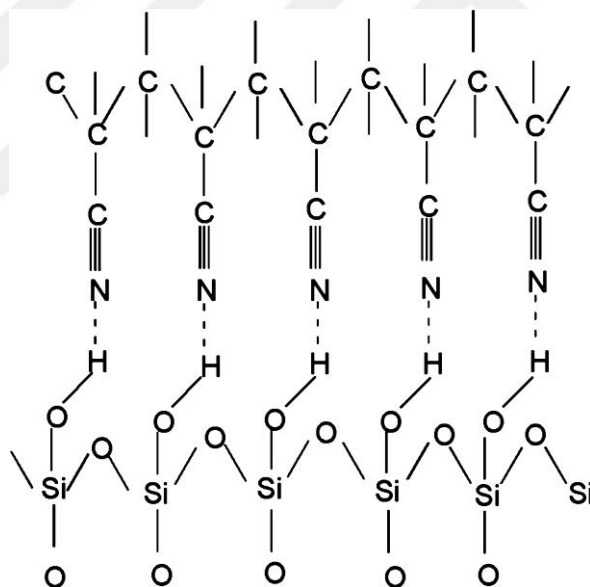


Figure 2.16. PAN and hydrolyzed TEOS form hydrogen bonds (not covalent bonds). Reprinted with permission from Pirzada, T., Arvidson, S. A., Saquing, C. D., Shah, S. S., & Khan, S. A. (2014). Hybrid Carbon Silica Nanofibers through Sol-Gel Electrospinning. *Langmuir*, 30(51), 15504-15513. doi:10.1021/la503290n

Magnesiothermic reduction (explained in section 2.2.3) can be applied to reduce SiO<sub>2</sub> to Si in the C-SiO<sub>2</sub> composites. However, if the SiO<sub>2</sub> phase is embedded and close to amorphous carbon, the magnesiothermic reduction reaction (MRR) bears the challenge of forming an inactive amorphous SiC phase. Briefly, it has been shown that

the formation of amorphous SiC at the interface of carbon and SiO<sub>2</sub> is thermodynamically more favorable compared to reduction to separate carbon and silicon phases (Ahn, Kim, Pyo, Lee, & Yoo, 2016). To address the SiC formation issue, control of temperature using heat-scavenging NaCl salt has been confirmed to be effective for the reduction of SiO<sub>2</sub> particles grown on the surface of reduced-graphene oxide (Kannan, Kim, Yang, & Kim, 2016). However, if the degree of mixing of a C-SiO<sub>2</sub> nanocomposite material is on the molecular scale, the larger interface between the carbon and SiO<sub>2</sub> phases makes the temperature control even more critical.

The reduction temperature can be further lowered using aluminothermic reduction in the presence of AlCl<sub>3</sub> at set temperatures less than 350°C to eliminate the formation of the SiC phase (LTAAR as explained in section 2.2.3.6). Apart from MRR and LTAAR, in-cell lithiation reduction of SiO<sub>2</sub> and SiO<sub>x</sub> (x < 2) has recently been investigated (J. E. Entwistle et al., 2020; Lepoivre, Larcher, & Tarascon, 2016). Briefly, it has been shown that prolonged lithiation of the SiO<sub>2</sub>-containing electrodes at low-potentials of ~ 2 mV leads to an increase in the specific capacity of the electrode in subsequent cycles (Lepoivre et al., 2016). Through comparison of the increased specific capacities and the irreversible capacities obtained at different potentiostatic lithiation times in the activation cycles, Lepoivre and Blanco have proposed that the following reaction is responsible for the in-cell lithiation reduction of SiO<sub>2</sub> (Blanco, Renman, Vullum-Bruer, & Svensson, 2020; Lepoivre et al., 2016):



However, they did not show any materials characterization confirmation that the reduction mechanism is what they proposed (probably due to the amorphous nature of the reaction products). Later Entwistle showed the formation of Si-Si bonds (corresponding to a 2.35 Å bond length) in the electrodes subjected to prolonged potentiostatic lithiation using total X-ray scattering methods (X-ray Pair Distribution Function) (J. E. Entwistle et al.). In none of these studies, the by-products of in-cell lithiation reduction of SiO<sub>2</sub> cannot be removed, making this method less attractive from a practical point of view.

## 2.5 From Active Electrode Materials to Cells

Problems related to the electrochemical behavior of silicon anodes have been addressed by several strategies including nanostructuring, introducing porosity and making Si-C nanocomposite, as detailed in the previous sections. While going from the active material to the cell level, as schematically illustrated in Figure 2.17, several inactive components are introduced, which have a significant role in the performance of the battery. Binders and electrolyte additives offer some of the most promising solutions for unlocking the full potential of silicon-based anodes.

### 2.5.1 Binders

Polyvinylidene fluoride (PVDF) is the conventional binder used in electrode preparation for LIBs (for cathode materials and graphite) because of its acceptable adhesion, hydrophobicity and high level of electrochemical and thermal stability. However, the weak van der Waals interaction between silicon-based active materials and PVDF is not enough to keep particles intact during significant volume expansion (Magasinski et al., 2010). In addition, since PVDF does not support a stable SEI formation, excessive growth of SEI isolates the silicon particles, causing loss of electrical contact, which results in low coulombic efficiency in each cycle. As this process is repeated over cycles, silicon anodes with PVDF binders show very poor capacity retention (Obrovac & Chevrier, 2014).

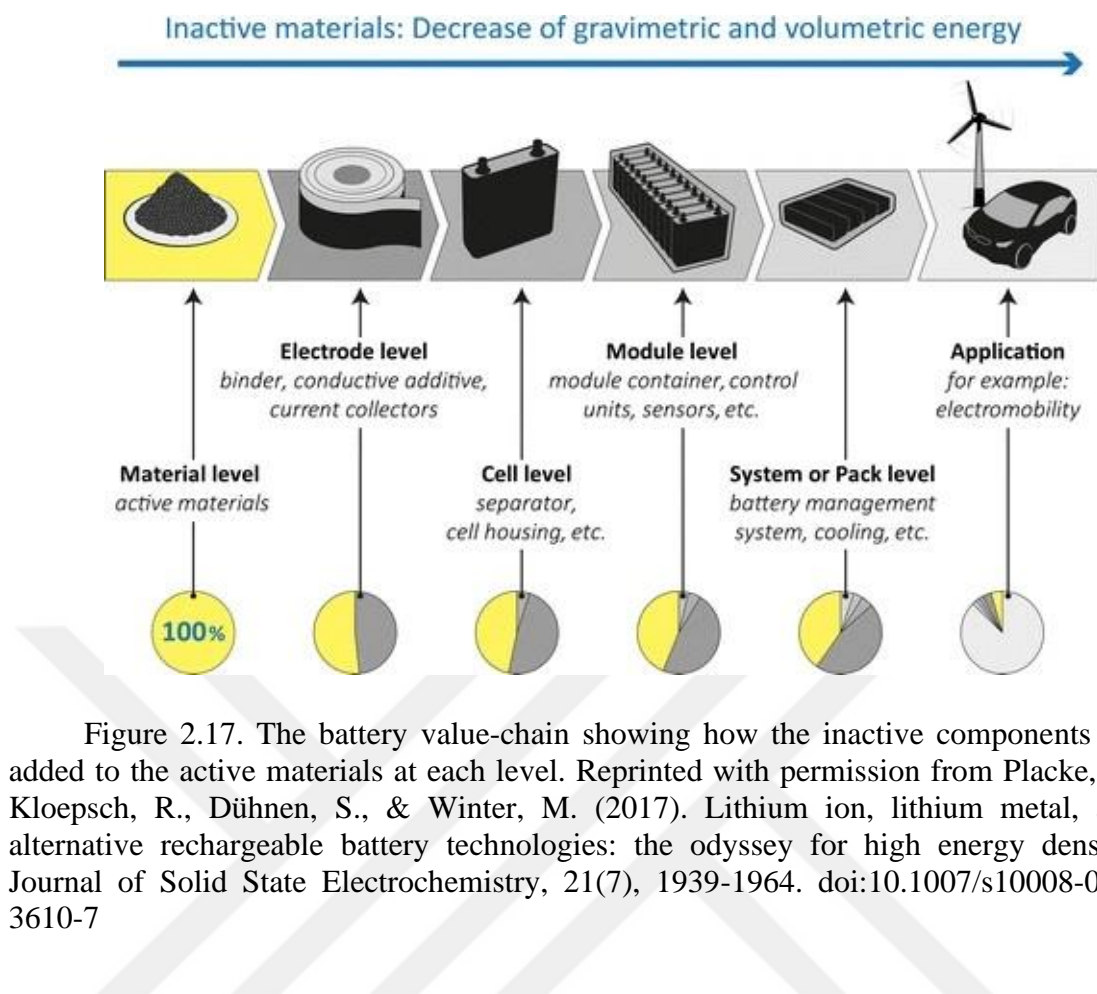


Figure 2.17. The battery value-chain showing how the inactive components are added to the active materials at each level. Reprinted with permission from Placke, T., Kloepsch, R., Dühnen, S., & Winter, M. (2017). Lithium ion, lithium metal, and alternative rechargeable battery technologies: the odyssey for high energy density. *Journal of Solid State Electrochemistry*, 21(7), 1939-1964. doi:10.1007/s10008-017-3610-7

It is found that if hydrogen bonding interactions exist between the silicon and the binder, the particles remain connected to the binder during cycling because the hydrogen bonding enables self-healing, leading to the reformation of the broken hydrogen bonds in each lithiation/delithiation cycle (Bridel, Azaïs, Morcrette, Tarascon, & Larcher, 2011). On the other hand, the native oxide layer on the surface of silicon particles makes the surface layer rich in Si-OH groups in the presence of water. The surface hydroxyl groups have been shown to go through esterification reactions with carboxylic acid groups (-COOH functional groups) of functionalized aliphatic binders (FABs) like polyacrylic acid (PAA), sodium alginate, or sodium carboxymethyl cellulose (CMC) (Mazouzi, Lestriez, Roué, & Guyomard, 2009; Obrovac, 2018). They show a much better mechanical performance with silicon anodes. However, if extra carboxylic acid groups in their structure are not neutralized beforehand, their acidic protons could go through reduction during the first lithiation as follows:



Equation 2.23 shows that such an in-cell reduction can immobilize the mobile Li-ions and also form hydrogen gas that is detrimental for the battery (Hays et al., 2018). Furthermore, neutralization of hydroxyls in polyacids (with LiOH, NaOH, and KOH) has been shown to decrease the unwanted irreversible electrochemical activity of the FABs (Han et al., 2015; J. Li, Le, Ferguson, & Dahn, 2010).

More recently, there have been studies using aromatic binders instead of FABs for the alloying type negative electrode materials. Contrary to the electrochemical neutrality of FABs, aromatic binders, such as polyimides (PIs) and phenolic resin binders, show significant first lithiation capacity and reversible capacity ( $\sim 2000 \text{ mAh g}^{-1}$  and  $\sim 900 \text{ mAh g}^{-1}$  for aromatic PI), which is attributed to electrochemical reduction to hydrogen-containing carbons (Wilkes, Brown, Krause, Triemert, & Obrovac, 2015). The resulting hydrogen-containing carbon that coats the surface of alloying-type active material improves the electronic conductivity and contributes to the reversible cell capacity (Obrovac, 2018). Thermal carbonization has also been applied to aromatic binders to eliminate the need for electrochemical reduction in the first lithiation cycle and hence decrease the irreversible capacity (Hatchard, Fielden, & Obrovac, 2018).

### **2.5.2 Electrolytes**

The electrochemical performance of the electrode materials should first be investigated in half-cell assemblies using lithium metal as the counter-electrode. In this case, regardless of whether the material being tested would eventually be used as a cathode or anode, lithium metal is always the negative electrode of the half-cell because it has the lowest electrode potential (0 vs.  $\text{Li/Li}^+$ ) as illustrated in Figure 2.18 (Winter, Barnett, & Xu, 2018).

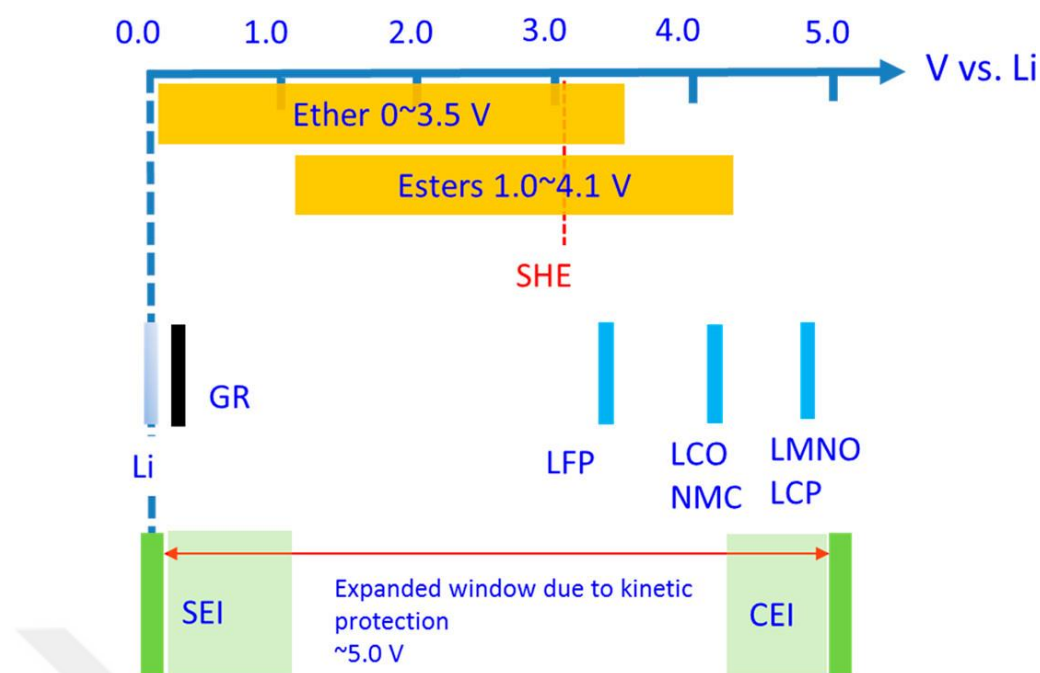
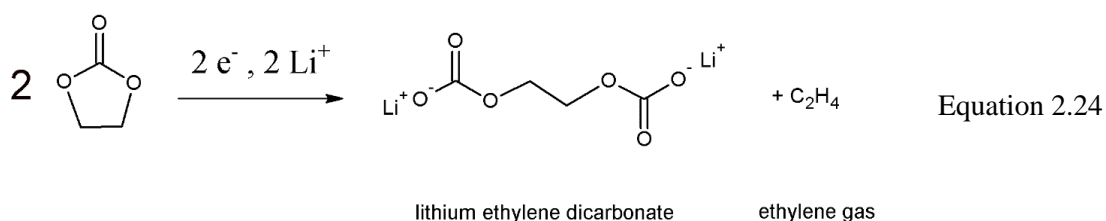


Figure 2.18. Schematic potential diagram showing the mismatch between the electrochemical stabilities of electrolyte and the redox potentials of most anode and cathode materials used in modern LIBs. GR, LFP, LCO, NMC, LMNO, and LCP stand for graphite, lithium iron phosphate, lithium cobalt oxide, lithium nickel manganese cobalt oxide, lithium manganese nickel oxide, and lithium cobalt phosphate, respectively. Adapted with permission from Winter, M., Barnett, B., & Xu, K. (2018). Before Li Ion Batteries. *Chemical Reviews*, 118(23), 11433-11456. doi:<http://dx.doi.org/10.1021/acs.chemrev.8b00422>

The liquid electrolyte is composed of a lithium salt (typically  $\text{LiPF}_6$ ) dissolved in a non-aqueous aprotic solvent. The lithium in the salt is expected to ionize and act as a charge carrier when exposed to the electrochemical potential gradient in the cell (Boettcher et al., 2020; Weiss et al., 2021). The fluorine-containing  $\text{PF}_6^-$  counter-ion of the salt is specifically chosen to protect the surface of aluminum current-collector on the cathode side by forming an  $\text{AlF}_3$  passivating surface layer because the native surface oxide ( $\text{Al}_2\text{O}_3$ ) layer cannot withstand the HF generated in the cell (P. Zhu et al., 2021).

From the Li-electrodepositions studies in 1960s, it was found that the use of non-aqueous aprotic solvents (alkyl ethers and carbonic/carboxylic esters) results in better stability of electrolytes. Those studies were implemented in the early LIB applications (Winter et al., 2018). The choice of the non-aqueous aprotic solvent depends on the type of anode material used (hard carbon, soft carbon, or graphite). Most studies were initially on soft carbon and in the first LIB that Sony commercialized in

1991, a soft carbon (coke) anode was used (Asenbauer et al., 2020; Loeffler, Bresser, Passerini, & Copley, 2015). However since there was a lot of degradation due to exfoliation of it during service (because of PC co-intercalation in it), hard carbon (non-graphitizable carbon) was used for later commercial applications. Back then, there were also studies to investigate using graphite as the anode because it was an abundant material. Still, due to the same reason (the co-intercalation of the organic electrolyte co-solvent used (propylene carbonate (PC)) in graphite), the capacity fading degradation was significant (Figure 2.19) (Pender et al., 2020). The preference of PC over EC was due to the low melting point of PC (-48.8°C) compared to that of EC (36.4°C) (Winter et al., 2018). The issue with the high melting point of EC was solved by mixing it with linear carbonic esters such as dimethyl carbonate (DMC), ethylmethyl carbonate (EMC), and diethyl carbonate (DEC) (probably through the formation of eutectic mixtures). It was found that no exfoliation in soft carbon and graphite happened with EC. The EC-graphite combination has worked commercially ever since. Also after the emergence of ethylene carbonate (EC) as electrolyte co-solvent, the beneficial effect of solid electrolyte interphase (SEI) formation could be observed on the surface of graphite. Briefly, since the lower bound of thermodynamic stability window of the electrolyte components is higher than the working potential of the anode materials (Figure 2.18) (except  $\text{Li}_4\text{Ti}_5\text{O}_{12}$ ), reduction of electrolyte at the anode side during charging is inevitable due to electron transfer. Namely, the reduction products of the EC-based electrolytes are lithium ethylene dicarbonate (LEDC) and ethylene gas (Kitz, Lacey, Novák, & Berg, 2020):



However, it is found that this solid reduction-product acts as an interphase that passivates the anode material (prevents the electron transfer) and, once formed, prevents further reduction of the electrolyte. Moreover, the lithium-ions can diffuse throughs this interphase, which is known as solid electrolyte interphase (SEI) (Peled & Menkin, 2017), and can be considered as a solid electrolyte. The properties of the SEI could be tuned, based on the application of interest, by adding additives to the electrolyte. For

example, fluoroethylene carbonate (FEC) as an electrolyte additive (up to 10 vol.%) forms a more stable SEI and improves the performance of silicon-based batteries. Electrochemical reduction of FEC during lithiation occurs earlier at potentials  $> 1$  V vs.  $\text{Li}^+/\text{Li}$  compared to that of EC (reduction potential), forming a thin layer of  $-\text{CHF}-\text{OCO}_2$ -type compounds that have proven to build more stable SEI composition compared to the decomposition products of EC ( $-\text{CH}_2-\text{OCO}_2$ -type compounds) (C. Xu et al., 2015). For the case of carbon anode materials, vinylene carbonate (VC) additive has shown more promise. Like FEC, VC also gets reduced at potentials  $> 1$  V vs.  $\text{Li}^+/\text{Li}$  and suppresses subsequent EC reduction (Kitz et al., 2020).

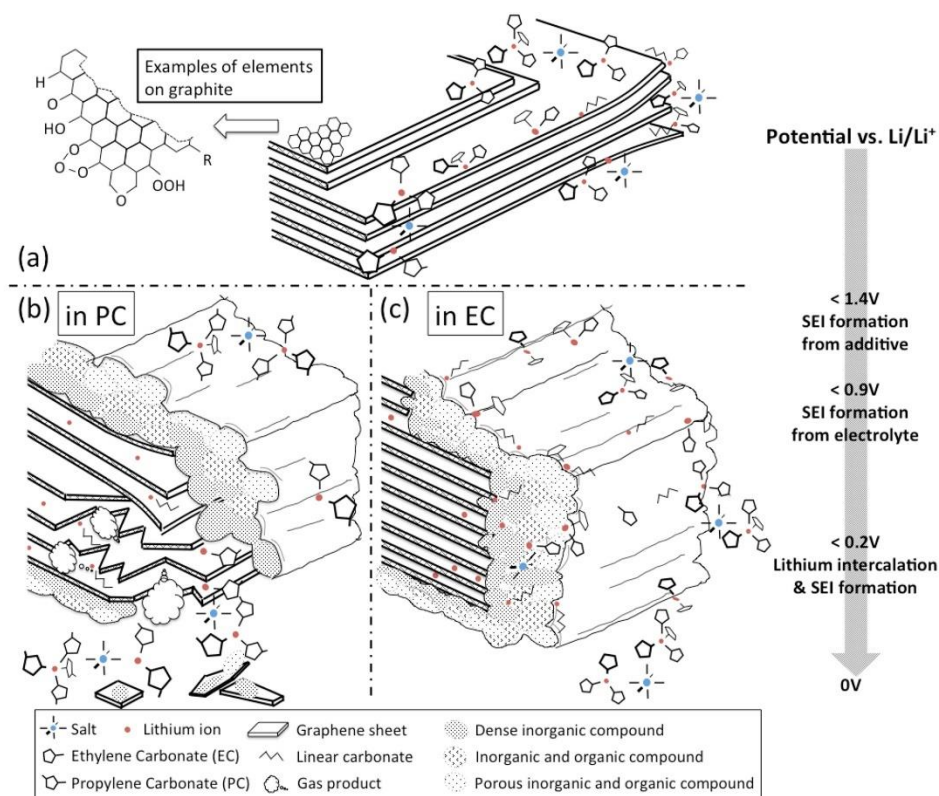


Figure 2.19. Schematic of the anode solid electrolyte interphase (SEI) formation process showing (a) graphene layers surrounded by electrolyte salts and solvents above 1.4 V vs.  $\text{Li}/\text{Li}^+$ , (b) propylene carbonate (PC) intercalation with lithium-ions into graphene layers resulting in exfoliations below 0.9 V vs.  $\text{Li}/\text{Li}^+$  and (c) stable SEI formation in ethylene carbonate (EC)-based electrolyte below 0.9 V vs.  $\text{Li}/\text{Li}^+$ ; plane side with thinner SEI and edge side with thicker SEI. Originally appeared in An, S. J., Li, J., Daniel, C., Mohanty, D., Nagpure, S., & Wood, D. L. (2016). The state of understanding of the LIB graphite solid electrolyte interphase (SEI) and its relationship to formation cycling. Carbon, 105, 52-76. doi:<https://doi.org/10.1016/j.carbon.2016.04.008>

### 2.5.3 Other components and half-cell assembly

When liquid electrolytes are used, there is the need to have a separator to prevent the electrical contact of the electrodes and thereby short-circuiting (Mindemark, Lacey, Bowden, & Brandell, 2018). The separators are typically layered porous films made of polyolefins (polypropylene/ polyethylene/ polypropylene) with a total thickness of  $\sim 25 \mu\text{m}$  (H. Zhang, Zhou, Lin, & Zhu, 2015), allowing liquid electrolyte can pass through. However, the presence of the separator causes an increase in ionic resistance. Therefore, engineering the porosity of the separator to increase the contact area between the electrode and electrolyte and adjusting their tortuosity to decrease the mean free path for ionic conduction are the ways to avoid ionic conductivity loss (Zheng, Song, & Wang, 2016).

The active materials are coated on metallic foils that act as current collectors to transfer the electrons between the electrode and the external circuit (P. Zhu et al., 2021). In almost all commercial lithium-ion batteries, copper foil is the current collector of choice for the anode side. Although its density ( $8.96 \text{ g cm}^{-3}$ ) and cost are less attractive compared to aluminum foil ( $2.70 \text{ g cm}^{-3}$ ), the low working potential of the anode active materials and the undesired alloying reaction of aluminum with lithium at 0.380 V (Obrovac & Chevrier, 2014) make the use of copper foil inevitable. For the cathode materials, the working potential is higher than 2.5 V, the preferred current collector is aluminum foil.

Lithium-ion half-cells are used to study the behavior of electrode materials individually. In a half-cell, there is a limitless supply of lithium ions (Shobukawa, Alvarado, Yang, & Meng, 2017). Therefore the specific capacity of the counter-electrode is not a limiting factor. In addition, Li metal acts as a reference electrode as well as a counter-electrode in a 2-electrode configuration. The characterization of half-cells will be discussed in detail in Chapter 3.

## CHAPTER 3: Characterization Methods

The material characterization is a critical part of research to understand the material structure-property relationship in general and to establish a comprehensive understanding of the energy storage mechanism in lithium-ion batteries. This chapter briefly introduces the characterization methods used in this dissertation. They have been divided into Materials Characterizations Methods and Electrochemical Characterization Methods.

### 3.1 Materials Characterizations Methods

#### 3.1.1 Thermogravimetric and differential thermal analysis (TG-DTA)

Thermogravimetric analysis (TGA) is an analytical technique in which the change in mass of a sample is measured as a function of temperature while the sample is subjected to a controlled heating program. TGA is mostly used to determine the thermal stability and compositional analysis of materials by carefully selecting the temperature program and environment. It is also utilized for the kinetic analysis of processes such as combustion and pyrolysis, as well as for the analysis of the oxidation or corrosion behavior of materials. On the other hand, differential thermal analysis (DTA) is a technique in which the temperature difference between a sample and reference material is measured as a function of temperature under controlled heating in a specified atmosphere. When coupled with TGA, which is called simultaneous thermal analysis (STA), DTA shows whether the thermally-induced transformations or decompositions are endothermic or exothermic. By heating the sample in the presence of oxygen, the organic materials (hydrocarbons) are oxidized to volatile (gaseous) products that leave the system from the exhaust (weight-loss). In contrast, metals and metalloids (such as silicon) are oxidized to form inorganic oxides (weight-gain).

For simultaneous thermal analysis, the sample is placed in a sample crucible made of alumina ( $\text{Al}_2\text{O}_3$ ). An identical empty crucible (reference) is also placed in the heating chamber. The mass of the sample is recorded instantaneously (using a microbalance) as the temperature of the chamber changes according to a predefined program. Also, the difference between the thermocouple signals that touch the bottom of each crucible, known as the DTA signal, is recorded in terms of  $\mu\text{V}$ . The atmosphere in the chamber can be air or nitrogen.

Thermal decomposition profiles, organic/inorganic content and carbon/inorganic ratio of our samples were determined via TG-DTA analyses using NETZSCH Jupiter 449C STA under a temperature increase rate of  $10\text{ K min}^{-1}$  in the air atmosphere. It is explicitly indicated where different atmospheres and heating rates are used. The obtained thermograms were analyzed using Proteus software provided by NETZSCH.

### **3.1.2 Fourier-transformed infrared spectroscopy**

Based on the interactions of electromagnetic waves and matter, a wide range of transitions can be investigated. Depending on the energy levels in the matter and the energy of the incident electromagnetic wave, their interaction can lead to an electronic transition, a vibrational transition, or a rotational transition. For example, as shown in Figure 3.1, the incident beams in the infrared region do not cause electrons to get excited to a higher electronic state. The low energy of an infrared beam can only lead to promotion to a higher vibrational and rotational level (Brisdon, 1998; Duckett & Gilbert, 2000).

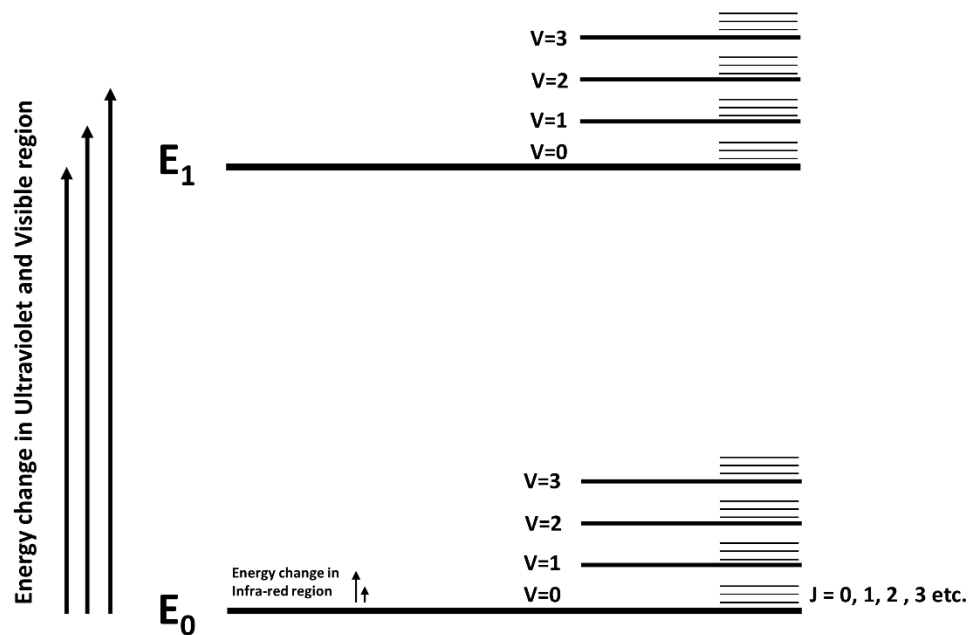


Figure 3.1. Separation of electronic, vibrational, and rotational energy levels for a molecule.

The relative frequency of vibration of two covalently bonded atoms is determined by their mass and bond strength. If they have different electronegativities, there will exist a partial negative charge ( $-\delta$ ) on the more electronegative atom and a partial positive charge ( $+\delta$ ) on the less electronegative one. This separation leads to a permanent electric dipole moment. This electric dipole moment resonates with the same frequency of the bonded atoms. It can absorb infrared vibrations of the same frequency and increase its energy to a higher vibrational level. This way, the frequencies of the absorbed infrared beam can be used to identify the functional groups of the chemical structure.

In this dissertation, Fourier-transformed IR spectroscopy in the attenuated total reflectance (ATR) mode was used to determine the presence or absence of specific functional groups in the synthesized materials or precursors. The instrument used was a Nicolet™ iS™ 10 FTIR Spectrometer equipped with a module with a diamond ATR crystal. Before any analysis, a background was measured. The data acquisition was performed at room temperature between  $600$  and  $4000\text{ cm}^{-1}$  at a resolution of  $2\text{ cm}^{-1}$ , and the data were averaged over 32 scans. The software to analyze the spectra was Omnic™ from Thermo Scientific.

### 3.1.3 Raman spectroscopy

Raman spectroscopy is another common form of vibrational spectroscopy, but it is not based on absorption. Unlike IR spectroscopy, it relies on the light scattering effect. It is known that the internal energy of molecules is quantized based on their vibrational modes. When the energy of the incident light is less than that required to promote the molecule to an excited (higher) electronic state, it can instead lead to promotion to a virtual excited vibrational state. The scattering of the light mostly happens with the same energy as the incident light, which is known as elastic (Rayleigh) scattering (Figure 3.2(a)). In 1928, C.V. Raman found that if elastically scattered light is filtered, the energy of a small fraction of the re-emitted light can be either smaller than (known as Stokes lines (Figure 3.2(b)), or bigger than the incident beam (known as anti-Stokes lines (Figure 3.2(c)) (Brisdon, 1998). The difference between the energy of the scattered light and the energy of the incident beam reveals discrete changes in vibrational modes that are attributed to the transition between quantized internal (vibrational) energy of the molecules. If the vibrational quantum of chemicals is known, this method can be used to identify the molecules.

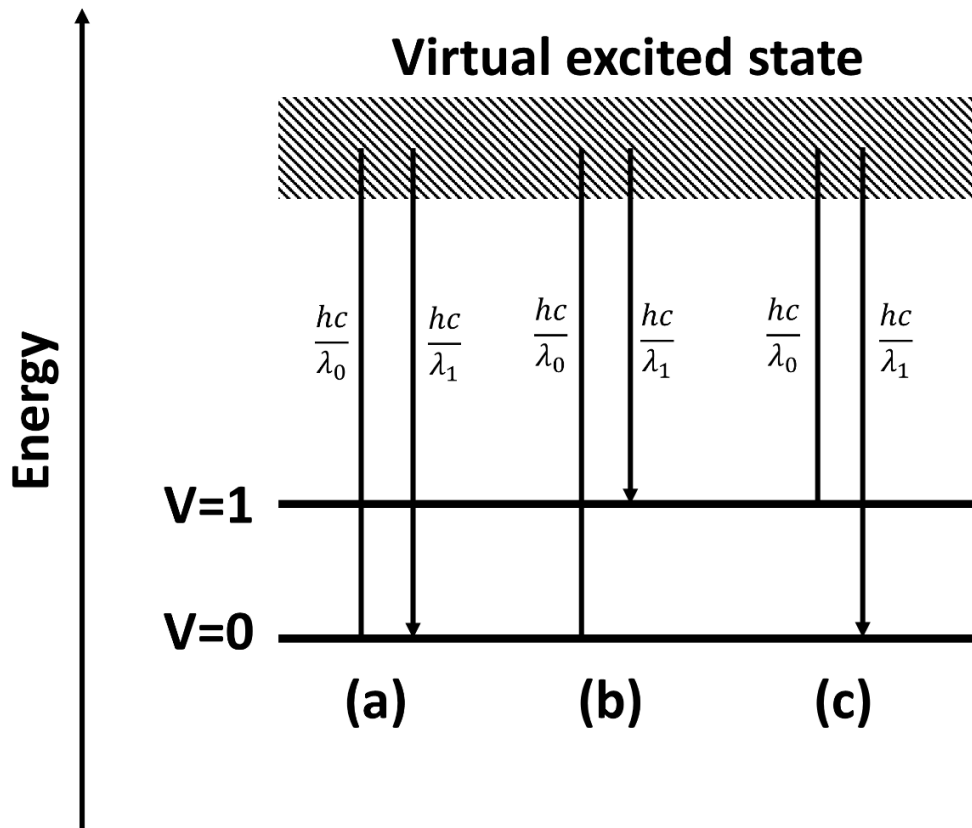


Figure 3.2. Energy levels in Raman spectroscopy that shows (a) Elastic scattering, (b) Stokes scattering (leaving photon with lower energy), and (c) anti-Stokes scattering (leaving photon with higher energy)

The difference in the energy of the vibrational modes can be calculated as:

$$\Delta E = \left( \frac{hc}{\lambda_0} - \frac{hc}{\lambda_1} \right) = hc \left( \frac{1}{\lambda_0} - \frac{1}{\lambda_1} \right) \quad \text{Equation 3.1}$$

where,  $\lambda_0$ ,  $\lambda_1$ ,  $h$ , and  $c$  are the wavelength of the incident and scattered beam, Planck's constant, and speed of light in vacuum, respectively. Using Equation 3.1, the term "Raman shift" is defined as:

$$\Delta\tilde{\nu} = \left( \frac{1}{\lambda_0} - \frac{1}{\lambda_1} \right) \quad \text{Equation 3.2}$$

When the wavelength of the scattered light ( $\lambda_1$ ) is bigger than that of the incident light ( $\lambda_0$ ), the scattering is in the Stokes region, and the Raman shift is positive. Since the probability of Stokes transition is higher than anti-Stokes, Raman spectroscopy is performed in the Stokes region (positive Raman shift) unless otherwise

stated. A Raman spectrometer filters the elastically scattered light and reports the intensity of the scattered lights as a function of their Raman shift.

IR spectroscopy is based on the interaction between the oscillating electric dipole moment in the molecule and the oscillation in the electric field in the incident radiation. So the presence of a permanent electric dipole moment in the molecule is necessary to have IR absorption. It means that symmetry in the molecule can lead to IR-inactive modes of vibration that cannot be detected using IR spectroscopy. However, for a vibrational mode to be observable (active), a change in the polarizability of the molecule during that vibration is required. Polarizability is defined as the ease with which the electron cloud is distorted (polarized) (Brown, 1998).

In this dissertation, we were looking for the identification of amorphous carbon and silicon in the synthesis products. Raman spectra were collected in the Stokes region using a 532 nm monochromatic wavelength ( $\lambda_0$ ) laser of incident beam placed in a Renishaw InVia system at room temperature. The software to analyze the Raman spectra was WiRE 3.4 from Renishaw.

#### **3.1.4 Liquid proton nuclear magnetic resonance ( $^1\text{H}$ NMR) spectroscopy**

Nuclear magnetic resonance is a method that applies electromagnetic radiation to a molecule placed in a magnetic field to study its molecular structure. The hydrogen nuclei (protons) possess a spin quantum number of  $\frac{1}{2}$ . So when placed in an external magnetic field, a hydrogen nucleus can obtain two spin states ( $m = +1/2$ ,  $m = -1/2$ ). The energy of a transition between these 2 spin states is:

$$\Delta E = \frac{\gamma h B_0}{2\pi} \quad \text{Equation 3.3}$$

where  $B_0$  is the strength of the applied magnetic field and  $\gamma$  is the gyromagnetic ratio for the protons ( $26.75 * 10^{-7} \text{ T}^{-1}\text{s}^{-1}$ ). The resonance frequency is defined as the frequency of the radiation that corresponds to this energy and is:

$$2\pi\nu_0 = \gamma B_0 \quad \text{Equation 3.4}$$

The frequency of the transition between 2 spin states corresponds to the radio-frequency region of the electromagnetic spectrum (Brisdon, 1998).

The motion of the electrons surrounding the hydrogen nucleus decreases the strength of the magnetic field experienced by a nucleus. In other words, the electrons surrounding the proton induce a magnetic field that opposes the external magnetic field.

This is called the shielding effect and can be used to differentiate the local environments in which the protons are located, based on the change in the resonance frequency as:

$$2\pi\nu_{eff} = \gamma B_{eff} = B_0(1 - \sigma) \quad \text{Equation 3.5}$$

where  $\sigma$  is defined as the shielding constant and is characteristic of the proton and its local chemical environment, hence, the resonance frequency can be rewritten as:

$$\nu_{eff} = \nu_0(1 - \sigma) \quad \text{Equation 3.6}$$

Equation 3.6 shows that the structure of a molecule can be evaluated based on the resonance frequencies of protons at different local environments. To compare different NMR spectra (from different instruments and magnetic fields), the resonance frequency of unknown protons is compared with tetramethylsilane ( $\nu_{TMS}$ ) and hereby defining the parameter *chemical shift* as:

$$\delta = \frac{\nu_{eff} - \nu_{TMS}}{\nu_0} \cdot 10^6 \quad \text{Equation 3.7}$$

Using the chemical shift instead of frequency and TMS as the reference, the possible effect of change in the magnetic field of different instruments is canceled out. Moreover, the area under each signal can be used to estimate the number of corresponding protons because they are proportional together.

In this dissertation, we used  $^1\text{H}$  NMR spectroscopy to determine the structures of silicon precursor polymers and copolymerization and polymerization of silicon precursor monomers. By integrating the area under the corresponding peaks, we measured the percent incorporation of each moiety in the copolymers. Samples were prepared by dissolving the (co)polymers in corresponding deuterated solvents, and the spectra were recorded using an Oxford Varian Inova 500 spectrometer operating at 500 MHz. The spectra were analyzed using ACD/NMR Processor software (Academic Edition).

### 3.1.5 X-ray diffraction (XRD)

X-ray diffraction analysis was used to identify the crystalline structure of the synthesized materials. Depending on the crystallographic structure of a solid, elastic scattering of X-ray photons by electrons in the solid can cause constructive or destructive interferences. The constructive interference can only occur at certain angles that are defined by Bragg's law (called diffraction angles).

When monochromatic incident X-ray beams with wavelength  $\lambda$  are scattered by atoms in a crystalline solid (as shown in Figure 3.3), the scattered X-rays must be in phase to have constructive interference. However, it can happen only when the difference in the path length taken by the beams is equal to an integer multiple of the beam's wavelength. In other words:

$$\text{Path length difference} = AB + BC = 2d\sin(\theta) = n\lambda \quad \text{Equation 3.8}$$

It means that the diffraction for a set of planes with interplanar spacing  $d$  can only happen at a certain angle  $\theta$  that satisfies Equation 3.8, where  $n$  is an integer. Equation 3.8 is known as Bragg's law (Cullity & Stock, 2001). The diffractograms are generated by measuring the intensity of scattered X-rays at different scattering angles ( $2\theta$ ). At the diffraction angles, their intensity is a measure of the number of diffracted X-rays.

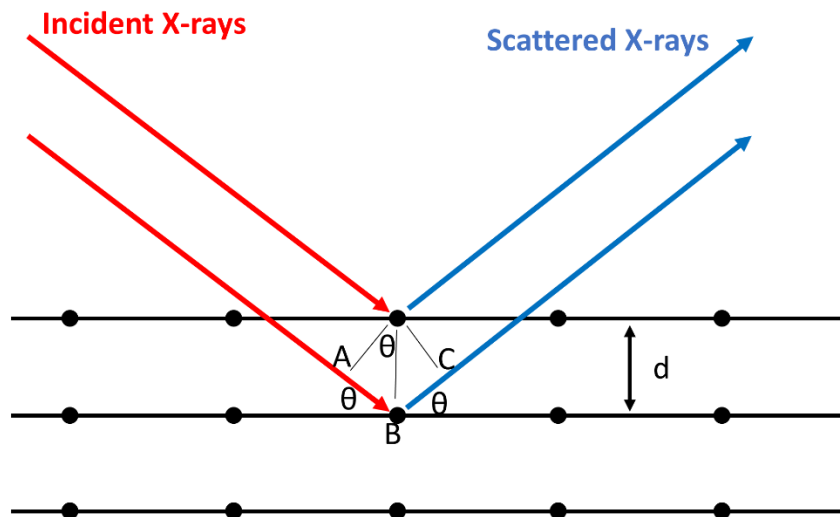


Figure 3.3. Scattering of X-rays by the atoms in a crystalline solid with an interplanar spacing of  $d$

It has been shown that the broadening of each diffraction peak can be due to (1) a decrease in particle size, (2) internal strain in the sample, and (3) instrumental effects. To estimate the crystallite size of the product from the diffractograms, we applied the Scherrer method (Equation 3.9) (Cullity & Stock, 2001):

$$L = \frac{K\lambda}{\beta\cos(\theta)} \quad \text{Equation 3.9}$$

where  $L$  represents the crystallite size,  $K = 0.89$ , and  $\lambda = 1.54060 \text{ \AA}$ .  $\beta$  was the integral breadth of the peaks (in radians) and was determined by fitting a Lorentzian curve to

each peak in the X-ray diffractograms after removal of the instrumental broadening contribution.  $\theta$  was the angle of diffraction for each peak. Because the products were naturally cooled in the furnace, the contribution of strain broadening was neglected.

To determine the percentage of the phases and percent crystallinity, we performed peak profile analysis using Rietveld refinement. Rietveld refinement is a method that fits the experimental diffraction profiles to the known patterns (available crystallographic patterns as CIF files) and finds the fraction of each phase and crystallographic parameters associated with each phase through mathematical algorithms (Doebelin & Kleeberg, 2015).

For this thesis, X-ray diffractometry was performed in a Bruker D2 Phaser diffractometer. The instrument is composed of an X-ray radiation source (Cu target) and an X-ray detector. The X-ray source and the detector are installed on a goniometer (known as Bragg-Brentano geometry) to detect the scattering angles at which diffraction occurs (meet Bragg conditions). A Ni foil filtered Cu  $K_{\beta}$  wavelength in the scattered X-rays. The diffraction patterns were collected in the scattering angle ( $2\theta$ ) range of 5-90° at 0.02° intervals and with a dwelling time of 1 s per step. The software used to analyze the diffraction patterns was DIFFRAC.EVA™ from Bruker. To calculate the percent crystallinity and percentage of phases, Profex freeware was used for Rietveld refinement. It is a graphical user interface (GUI) for the BGMN program (Doebelin & Kleeberg, 2015).

### 3.1.6 Specific surface area by gas adsorption (BET method)

The physical adsorption of a gas on the surface of a solid can be used to measure its specific surface area. Brunauer, Emmett, and Teller further developed Langmuir's theory of the monolayer adsorption to the multilayer adsorption (Brunauer, Emmett, & Teller, 1938) that resulted in the BET equation:

$$\frac{1}{V_a \left( \frac{p_0}{p} - 1 \right)} = \frac{C - 1}{V_m C} \cdot \frac{p}{p_0} + \frac{1}{V_m C} \quad \text{Equation 3.10}$$

where  $p$  and  $p_0$  are the partial pressure and saturation pressure of the adsorbate gas (in our case  $N_2$ ),  $V_a$  volume of the gas adsorbed at room temperature and pressure,  $V_m$  the volume of the gas needed to form an adsorbed monolayer on the solid under measurement, and  $C$  is a dimensionless constant depending on the enthalpy of adsorption of the adsorbate gas (in our case  $N_2$ ) on the solid. From Equation 3.10, the

plot of  $\frac{1}{V_a(\frac{p_0}{p}-1)}$  vs.  $\frac{p}{p_0}$  has a linear form, and the constants  $V_m$  and  $C$  can be estimated by fitting the measurement data to a line. Finding the slope and the y-intercept of the line enables us to find the values of  $V_m$  and  $C$ . We know the molecular cross-sectional area of gases used (For  $N_2$  at 77 K, it is  $0.162 \text{ nm}^2$ ) (Yang et al., 2012), so the surface area of the sample can be estimated. The mass of the samples is also measured after degassing using a weighing scale (with 0.1 mg precision).

In this thesis, the first 15 data points in the adsorption range in each plot were used for the BET linear fitting. The instrument used was Micromeritics, 3Flex. Determination of the specific surface area was done using the Brunauer-Emmett-Teller (BET) model. Before measurements, the samples were degassed at  $150^\circ\text{C}$  for 24 h under vacuum.

### **3.1.7 Field-emission scanning electron microscopy (FE-SEM)**

The scanning electron microscope is used to observe the surface morphology of materials in the micrometer size to a few tens of nanometers. A focused electron beam consisting of accelerated electrons scans the region of interest (ROI) using electromagnetic lenses. While the secondary electrons reveal surface morphology, the back-scattered electrons carry elemental analysis information. The secondary electrons and back-scattered electrons are generated through interactions between the incident electron beam and the sample and are collected in the detectors to form images. The secondary electrons are emitted from the outer shell of atoms from the sample as the electrons from the incident beam remove them. Since the secondary electron detectors are often placed in the corner of the chamber, the contrast of secondary electrons is formed via the relative orientation of the surface of the sample with respect to the detector. This way, the topography of the sample is revealed. The back-scattered electrons are elastically scattered electrons of the beam from the sample. Since the atoms with higher atomic numbers scatter electrons more, the back-scattered electron image can contain atomic number contrast, and phases with higher average atomic numbers appear brighter than phases with lower average atomic numbers. Also, characteristic X-rays are generated if the incident electron beam can remove electrons from the inner shell of the atoms. The result is formations of an X-ray photon with the characteristic energy defined for the atom (e.g., Cu  $K_\alpha$ ). Characteristic X-rays can be used for elemental analysis through energy-dispersive X-ray spectroscopy (EDS).

However, for the case of SEM specimens, as shown in Figure 3.4a, the interaction volume causes the spatial resolution of EDS (determined by beam spread) to be lower than the imaging resolution (determined by the electron probe size).

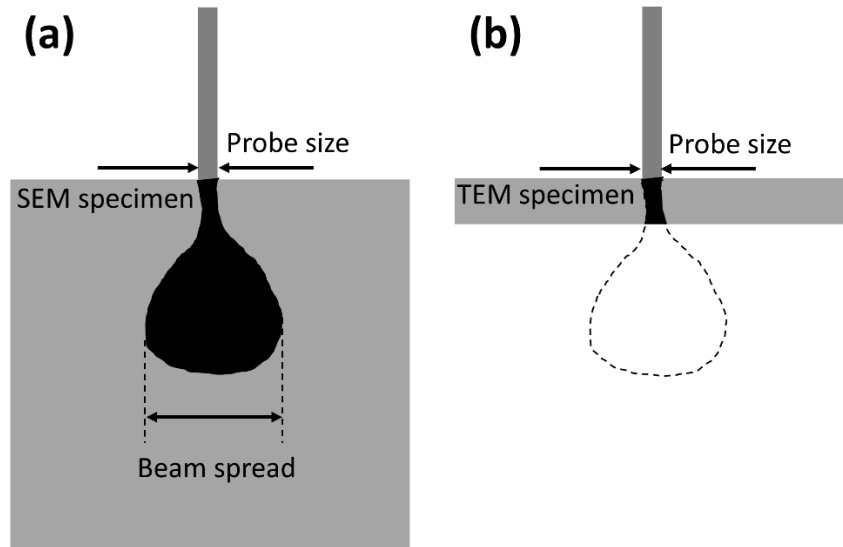


Figure 3.4. (a) An SEM specimen in which the X-ray excitation happens in a spreading volume in the bulk of the specimen, and (b) a thin TEM specimen in which the X-ray excitation region (interaction volume) is of the same size as the probe-size diameter.

The use of field-emission electron sources leads to better resolution because the electron probe diameter has to become narrower to have the image in focus at high magnifications. This narrowing is done by focusing the electron beam through electromagnetic lenses (Goodhew, Humphreys, & Beanland, 2000). The narrower the electrons' energy distribution (wavelength), the lower the chance of having chromatic aberration, and the easier the electron beam's focus is at one point. This is the reason the (cold) electrons from the field-emission source (gun) focus with a higher resolution compared to thermionic-source electrons (Livingston, 1998).

In this dissertation, FE-SEM was performed using a Zeiss LEO-Supra 35 VP FE-SEM. For imaging, mainly the secondary electron signal was used through an in-chamber detector and an in-lens detector. By decreasing the bias voltage of the in-chamber detector, images with atomic number contrast (i.e., observing Si/SiO<sub>x</sub> nanoparticles on the surface of carbon nanofibers) could be achieved due to the increased contribution of back-scattered electrons in the image production. So we assume that the contrast obtained is due to having a mix of secondary electrons and

back-scattered electrons in all cases. EDS mapping analysis was mainly done in the TEM due to the nanostructured morphology and higher spatial resolution of EDS in TEM (Figure 3.4b and section 3.1.8). Before microscopy, samples were mounted on adhesive carbon tapes, placed on microscopy stubs, and the surfaces of the samples were coated with a gold-palladium alloy using a sputtering machine. The images were taken at an electron high-tension of 2-5 kV and a 6-15 mm working distance.

### **3.1.8 Transmission electron microscopy (TEM)**

In a transmission electron microscope, the energy of the incident electron beam is in the range of 150-200 keV, which is ~2 orders of magnitude higher than the energy of the electrons used for imaging in the SEM. This high energy, along with the nanoscale dimensions of the samples, makes the transmission of electrons through the sample possible. Moreover, since the energy of the electron beam is higher than that in SEM, the achievable resolution is also higher. The incident electrons initially move along the optical axis of the microscope, but after interaction with the sample atoms, they get scattered away from this direction. Their scattering angle is proportional to the thickness of the sample and also the mass of the atoms they interact with. Through adjustment of the objective aperture of the microscope, the contribution of electrons scattered at larger angles can be removed from the final formed image, providing thickness contrast and mass contrast.

As discussed in section 3.1.7, for characteristic X-rays formed in the SEM, the large interaction volume leads to a lower spatial resolution for the elemental distribution compared to the imaging resolution. However, as shown in Figure 3.4b, for the case of a TEM specimen, the thickness is so small that the interaction volume does not spread into the thickness. This is the reason that the high-resolution elemental mapping can be obtained in TEM with more accuracy compared to SEM.

In this thesis, high-resolution TEM bright-field imaging in a spherical aberration-corrected scanning TEM (STEM, JEOL JEM-ARM200CF, operated at 200 kV with a probe size of *ca.* 1 Å) was used to evaluate the microstructure and morphology. The elemental distribution was analyzed through energy-dispersive x-ray spectroscopy (EDS) using a JEOL Centurio system mounted on the STEM. The

crystalline nature of the Si nanoparticles was evaluated by fast Fourier transform (FFT) analysis of the high-resolution TEM image.

### 3.1.9 X-ray photoelectron spectroscopy (XPS)

X-ray photoelectron spectroscopy works based on the photoelectric effect (Livingston, 1998). The spectrum of the kinetic energy of electrons removed from a solid placed in an ultra-high vacuum after applying a photon of known energy (incident beam) can be used to determine the spectrum of the binding energies existing in the solid (using a spectrometer as in Figure 3.5a). The kinetic energy of the photoelectrons generated from the sample ( $E_{kin}^{SA}$ ) can be related to the binding energies ( $E_B$ ) as follows:

$$E_{kin}^{SA} = h\nu - E_B - \phi_{SA} \quad \text{Equation 3.11}$$

$$\text{So } E_B = h\nu - (E_{kin}^{SA} + \phi_{SA}) \quad \text{Equation 3.12}$$

where  $h\nu$  is the energy of the incident X-ray beam and  $\phi_{SA}$  is the work function of the sample. Work function is defined as the potential barrier at the surface of a solid for electrons to reach the vacuum level (Greczynski & Hultman, 2020). Based on Equation 3.12, it seems necessary to know the work function of the sample for calculating the binding energy of electrons, but Figure 3.5b shows that when the sample and spectrometer are in electrical contact, their Fermi levels align, and it means that (Figure 3.5b):

$$E_{kin}^{SA} + \phi_{SA} = E_{kin}^{SP} + \phi_{SP} \quad \text{Equation 3.13}$$

where  $E_{kin}^{SA}$  is the kinetic energy measured at the detector and  $\phi_{SP}$  is the work function of the detector. If we substitute Equation 3.13 in Equation 3.12, we have:

$$E_B = h\nu - (E_{kin}^{SP} + \phi_{SP}) \quad \text{Equation 3.14}$$

So the binding energies of photoelectrons can be measured independent of the sample work function.

The binding energy of photoelectrons depends on the oxidation state of the elements in the solid. Hence, in this dissertation, XPS was utilized to comment on the change in the oxidation state of silicon before and after aluminothermic reduction. XPS was used in the range of 0-1150 eV of binding energy using an Al monochromatic X-ray source ( $K_\alpha = 1.487$  keV) operating at 25.1 W (XPS- PHI 5000 VersaProbe).

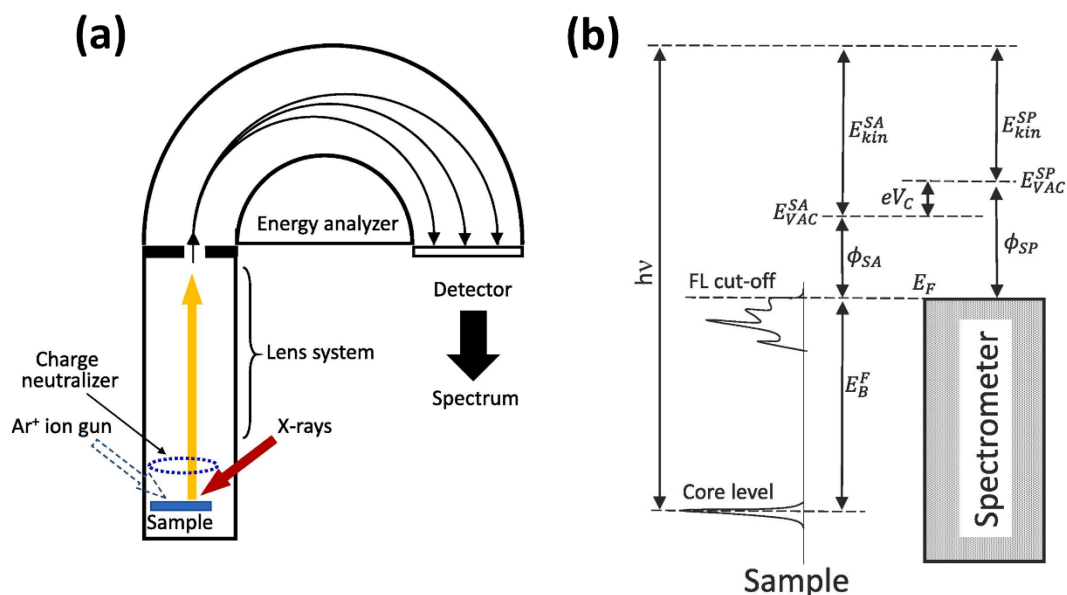


Figure 3.5. (a) The schematic view of the photoelectron spectrometer with a hemispherical electron energy analyzer, (b) energy level diagram for a sample in good electrical contact to the XPS spectrometer. Reprinted with permission from Greczynski, G., & Hultman, L. (2020). X-ray photoelectron spectroscopy: Towards reliable binding energy referencing. *Progress in Materials Science*, 107, 100591. doi:https://doi.org/10.1016/j.pmatsci.2019.100591

## 3.2 Electrochemical Characterization Methods

### 3.2.1 Characterization of a battery half-cell

For electrochemical characterization of battery half-cells, the active material of interest is coated on the current collector metal sheet, and the produced working electrode is assembled into a half-cell, shown as in Figure 3.6. The half-cell is connected to electrochemical workstations in a 2-electrode arrangement.

Since the  $\text{Li}^+$  ions are charged species, their transfer in the half-cell is governed by the gradient in electrochemical potential. The existence of a gradient means that inside the cell, there are overpotentials in the electrochemical potential of  $\text{Li}^+$  ions with respect to the equilibrium state (as shown in Figure 3.7) (Weiss et al., 2021).

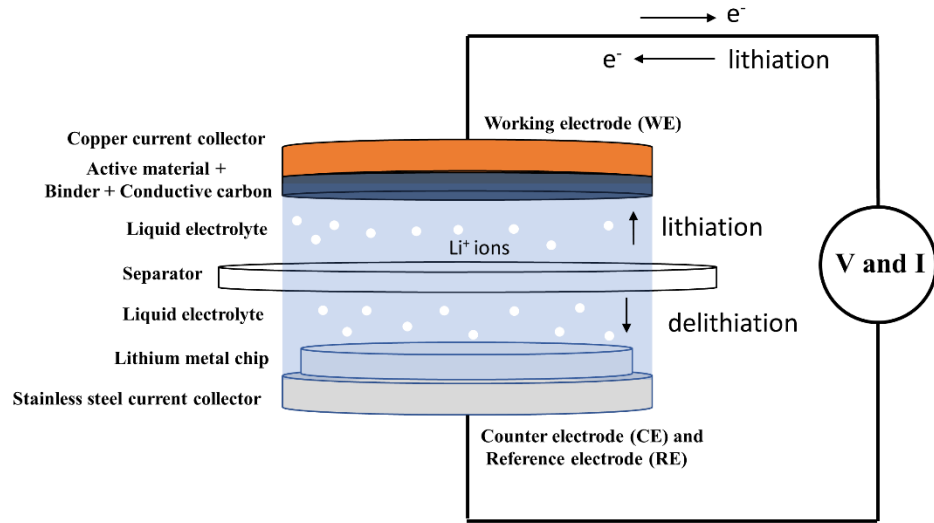


Figure 3.6. The schematic illustration of a half-cell that is used to test the electrochemical performance of the active materials. (The casings are not shown for simplicity).

In the electrochemical characterization of cells, the parameters that we control and measure against time (excitation and response of the system, respectively) are those from the external circuit (typically voltage and current). The difference of the electrochemical potential of electrons (Fermi levels) (Boettcher et al., 2020) in the current collectors connected to the cathode and the anode is related to what we read as cell voltage between the current collectors as:

$$V = -\frac{1}{F}(\tilde{\mu}_{e^-}^c - \tilde{\mu}_{e^-}^a) = V_{OC} + \Delta\phi^c + \Delta\phi^a \quad \text{Equation 3.15}$$

Other than voltage, the control and measurement of the current in the external circuit are also available by adjusting electrochemical workstation parameters. Li-ions within the cell relocate themselves to compensate for the charge due to the transfer of electrons in the external circuit, and thus the mass transfer inside the cell can be governed by adjusting the external circuit parameters.

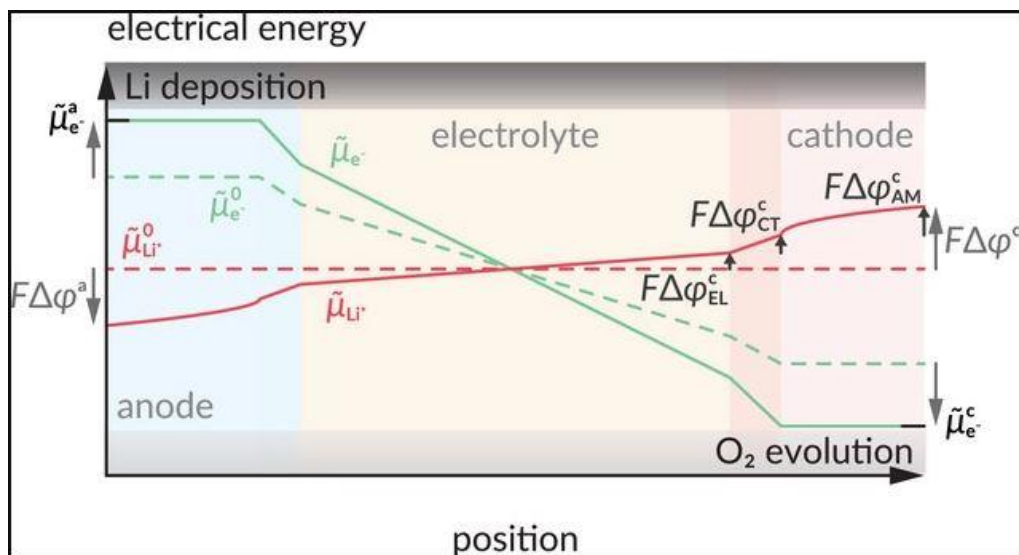


Figure 3.7. Schematic representation of the profiles of the electrochemical potential of electrons and  $Li^+$  ions. It is reprinted with permission. Originally appeared in Weiss, M., Ruess, R., Kasnatscheew, J., Levartovsky, Y., Levy, N. R., Minnmann, P., . . . Janek, J. (2021). Fast Charging of Lithium-Ion Batteries: A Review of Materials Aspects. *Advanced Energy Materials*, 11(33), 2101126. doi:<https://doi.org/10.1002/aenm.202101126>

### 3.2.2 Chronopotentiometry

This method is commonly known as galvanostatic charge-discharge of cells. According to the working potentials of the working electrode, an upper ( $V_2$ ) and a lower ( $V_1$ ) cut-off voltage are used (corresponding to the Fermi level of the delithiated and the lithiated state of the working electrode, respectively, in the half-cell configuration). By applying a constant external electrical current ( $I$ ) between the current-collectors, the fermi level of electrons will change. This change induces a gradient in the electrochemical potential, which is responsible for the transfer of Li-ions in the cell. Each of the cut-off voltages corresponds to a critical surface concentration of Li-ions. The time it takes to reach from  $V_1$  to  $V_2$  is recorded as  $t$  from an initial time  $t_0$ , and the whole charge transferred at any moment will be

$$Q = I * (t - t_0) \quad \text{Equation 3.16}$$

This charge is reported in terms of mAh and normalized by the mass of active material that is applied to the working electrode.

For this dissertation, a battery analyzer system (MTI, BTS8-WA) was used to perform cyclic chronopotentiometry (Galvanostatic charge-discharge).

### 3.2.3 Cyclic Voltammetry

If the potential difference (corresponding to the Fermi level difference) between the terminals of the cell is swept between 2 cut-off values in a linear increase or decrease rate and the changes in the amount of current is recorded, and the current values vs. voltage are plotted, the resulting graph is called cyclic voltammogram. It shows at which potential differences the charge transfer will occur, and it is used to determine whether certain reactions (e.g., lithiation or delithiation of silicon) are taking place. In this dissertation, a potentiostat (Princeton Applied Research PARSTAT MC) was used for cyclic voltammetry, and the scanning rate was  $0.1 \text{ mV s}^{-1}$  if not otherwise stated. The cut-off potentials are stated in each case.

### 3.2.4 Electrochemical Impedance Spectroscopy (EIS)

If an alternating current (AC) signal is applied to an electrochemical cell instead of a direct current (DC), the ratio between the alternating potential signal to alternating current is defined as impedance. The applied signal could be an AC voltage pulse with a given frequency and amplitude. The recorded response could be an AC current with a certain frequency and amplitude. The impedance value has a complex form and is frequency-dependent. Through this frequency dependence, electrochemical phenomena with different frequencies of occurrence can be separately studied. In this dissertation, a potentiostat instrument (Princeton Applied Research PARSTAT MC) was used to record the impedance spectra.

The time-invariance of the spectra was validated according to a Linear Kramers-Kronig tool ("Lin-KK tool") ( $< 1 \%$  residual error). Figure 3.8 shows a representative residual plot. Then the spectra were analyzed using Zview<sup>TM</sup> software to fit hypothetical electrochemical equivalent circuits.

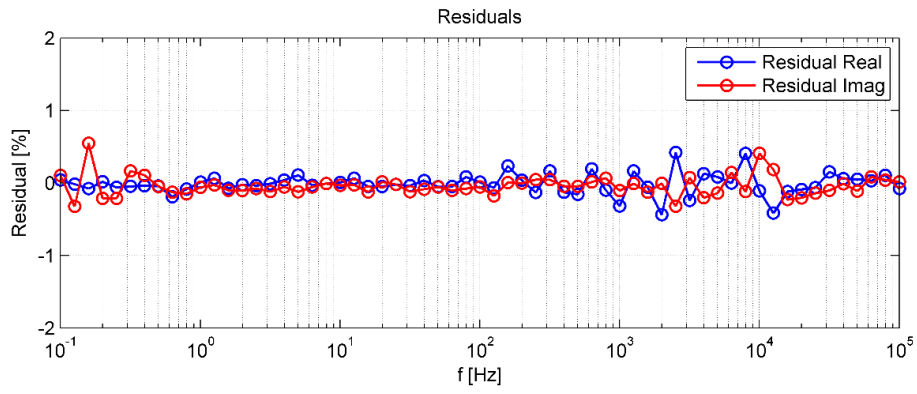


Figure 3.8. Kramers-Kronig fitting residuals are low, and it indicates time-invariance of the conditions and correctness of further proceeding to fit an equivalent circuit model to the spectra.



## Mechanisms of Si Nanoparticle Formation by Molten Salt Magnesiothermic Reduction of Silica for Lithium-ion Battery Anodes<sup>1</sup>

**Abstract:** Molten salt methods enable the synthesis of Si nanostructures by moderating the thermal energy evolved in highly exothermic magnesiothermic reduction reactions (MRR) of silica. Due to their cost-effectiveness and scalability, these techniques are well suited for producing nanoscale Si for a number of applications, including energy storage. To control the microstructure morphology and particle size, it is necessary to understand the formation mechanism of the Si produced. By evaluating the time-resolved phase evolution, when NaCl moderates the thermal energy generated by MRR of SiO<sub>2</sub>, we elucidate the 3 parallel interfacial reaction mechanisms yielding Si nanoparticles—via Mg vapor, an Mg-rich eutectic liquid, and Mg ions dissolved in molten NaCl. These individual Si nanoparticles offer a striking contrast to the typical by-product of MRR of SiO<sub>2</sub> with and without NaCl, which yields a 3-dimensional (3-D) porous network of sintered Si nanoparticles. Lithium-ion battery half-cells with electrodes composed of individual Si nanoparticles showed a greater first-cycle irreversible discharge capacity and faster capacity loss over the first 5 cycles at a current density of 200 mA g<sup>-1</sup> compared to half-cells with electrodes of a porous 3-D Si network—indicative due to thicker solid electrolyte interphase (SEI) formation on individual particles. At a higher current rate of 400 mA g<sup>-1</sup>, once SEI formation and activation of Si are established, both cells exhibit a similar capacity retention rate over 100 cycles.

---

<sup>1</sup> The material in this chapter is from the paper published in <https://doi.org/10.1002/celc.202100683>. The copyright permission has been obtained under License Number 5140790685231 and License date Sep 02, 2021, from John Wiley and Sons.

## 4.1 Introduction

When incorporated into the anode of lithium-ion batteries, silicon (Si) offers a compelling energy storage capacity (Z. Lin, Liu, Ai, & Liang, 2018; Winter et al., 2018), due to a relatively low lithiation potential (0.4 V) and the reversible formation of an amorphous alloy with lithium at room temperature (3579 mAh g<sup>-1</sup> for Li<sub>15</sub>Si<sub>4</sub>) (Obrovac & Chevrier, 2014). In a typical cell stack, replacing graphite with Si in the anode increases energy storage from 726 Wh/L to 976 Wh/L—i.e., ca. 34% improvement (Obrovac & Chevrier, 2014). However, challenges to incorporating Si in lithium-ion battery (LIB) anodes are posed by the large volume expansion and contraction during alloying and dealloying, a low intrinsic electrical conductivity, and instability of the solid electrolyte interphase (SEI) (Ashuri et al., 2015). One solution to controlling fracture resulting from volume expansion is maintaining Si particle sizes below 150 nm (X. H. Liu et al., 2012; M. T. McDowell et al., 2013), while another is to produce a porous microstructure of aggregated Si nanoparticles (Ashuri et al., 2016; Chen et al., 2011). Because the diffusion rate of lithium in Si is slow (Kong et al., 2019), an additional benefit to using Si nanoparticles of a narrow particle size distribution is an increased lithiation rate (Bärmann et al., 2020).

Metallothermic reduction of silica (SiO<sub>2</sub>) has been widely investigated as a scalable solution for low-cost and green production of Si nanoparticles, focusing on magnesium (Mg) as the reducing agent (J. Entwistle et al., 2018; Favors et al., 2014; Rehman, Wang, Manj, Luo, & Yang, 2021; Richman et al., 2008). Although Mg vapor can be used directly to reduce SiO<sub>2</sub> while preserving the structure of the silica raw material (Bao et al., 2007; Sandhage et al., 2002), its use in combination with a molten salt enables better control over morphology and composition at lower temperatures.

The molten salt, an alkali metal halide such as NaCl, performs a dual function—as a solvent for the reducing agent and for thermal moderation. The reducing agent in vapor form is ionized on the liquid surface and dissolved into the liquid. The solubility of the reducing metal species in the liquid salt sets its chemical potential and the nanoparticle yield (Iwadata et al., 2018; X. Liu et al., 2012; Nersisyan, Lee, & Won, 2005; Wypartowicz, Østvold, & Øye, 1980). By using eutectic salt mixtures, such as LiCl-KCl and NaCl-MgCl<sub>2</sub>, the solubility limit can be tuned, while the eutectic

temperature sets the lower bound for selecting processing temperatures. Nanoparticle yield was demonstrated to scale with the solubility limit of Mg for producing Si, as well as Ge, nanoparticles (X. Liu et al., 2012).

As a heat scavenger, the relatively low melting temperature—801°C, in the case of NaCl—moderates self-heating of the product phases due to the massive exothermic energy evolving from the magnesiothermic reduction of silica (Luo et al., 2013; Yermekova, Mansurov, & Mukasyan, 2010). The advantages are control over the growth and sintering of the nanoparticles produced. The degree of thermal moderation is tuned by choice of metal halide salt, determined by the latent heat of melting (Miao et al., 2020).

For magnesiothermic reduction reaction (MRR) of silica with thermal energy moderated by a molten salt, the reaction mechanism is suggested to be the ionization of the Mg vapor atoms at the surface of sessile droplets of molten salt in direct contact with SiO<sub>2</sub> particle surfaces. Mg has a low melting temperature and, in the liquid state, a high vapor pressure. Gas-phase transport is fast and pervasive (Givargizov, 1975), while liquid surfaces are “ideally rough” surfaces (Wagner & Ellis, 1965) that facilitate the ionization of Mg atoms by coordination with Cl ions. The ionization reaction at the molten salt surface is the rate-limiting factor. Mg atoms removed from the vapor are replenished by the liquid-vapor equilibrium. The Mg<sup>2+</sup> ions and their electrons released by ionization are dissolved in the salt (Bockris, Yoshikawa, & Richards, 1964; X. Liu et al., 2012; Nersisyan et al., 2005), up to the solubility limit for the Mg ions. At the SiO<sub>2</sub> surface, electrons attack SiO<sub>2</sub> bonds, reduce Si, and enable the formation of MgO. The SiO<sub>2</sub> surface fragments into Si nanoparticles due to the volumetric changes by departing oxygen ions.

Analysis of an Ellingham diagram shows that most alkali and alkali earth metals can also be used to reduce SiO<sub>2</sub> to Si (G. Zhu, Luo, Wang, Jiang, & Yang, 2019). By choosing a reducing agent of higher valence, such as trivalent Al, Si nanoparticle yield can also be increased (N. Lin, Han, Wang, et al., 2015; N. Lin, Han, Zhou, et al., 2015; Song et al., 2018). However, the use of Al requires choosing a salt that it can dissolve in, such as AlCl<sub>3</sub>, which requires processing in a sealed and closed vessel (X. Lin, Li, Li, Song, & Chen, 2020; D. Wang et al., 2021). Finally, in terms of the starting material, Liu and co-workers have demonstrated that Si nanoparticle formation is independent of

the initial form of SiO<sub>2</sub>—amorphous, quartz, mesoporous silica—, whereas the more critical parameter is the soluble concentration in the molten salt (X. Liu et al., 2012).

Although the mechanism for MRR of silica, exposed to Mg vapor and molten salt, is widely accepted, less clear is the formation mechanism of Si nanoparticles (X. Liu et al., 2012). The presence of the by-product phases, Mg<sub>2</sub>Si and Mg<sub>2</sub>SiO<sub>4</sub>, offered additional clues about the conditions of microstructural evolution during the direct reduction of SiO<sub>2</sub> by Mg vapor (Brindley & Hayami, 1965; Wynnyckyj & Bhogeswara Rao, 1976). In particular, these intermediates formed during reaction between counter-diffusing Mg (g) and SiO (g) species. In addition, the Mg|SiO<sub>2</sub> interface evolution was shown through thermodynamic equilibrium considerations that an initial, thin intermix layer of Mg-Si-O forms at the SiO<sub>2</sub> surface, followed by the formation of MgO and a Si-rich layer at the MgO|SiO<sub>2</sub> interface (Gutman et al., 2006; Gutman, Klinger, Gotman, & Shapiro, 2009).

Herein we report a time-resolved investigation of the microstructural and compositional evolution of NaCl-mediated MRR of cristobalite mineral SiO<sub>2</sub> to elucidate the mechanism by which Si nanoparticles form. We compare the morphology and composition of Si products resulting from MRR with and without NaCl by XRD, SEM, TEM, and BET analyses and consider the thermodynamics consistent with those observations. Finally, we compare the charge storage behavior of the 2 types of Si nanoparticle products.

## 4.2 Experimental Section

### 4.2.1 Materials synthesis

Si nanoparticles were produced by MRR of SiO<sub>2</sub> mineral with and without the addition of NaCl as a heat scavenger (Kong et al., 2019). The as-received mineral was ball-milled for 4 hours followed by immersion in a 2 M HCl solution overnight to remove metallic impurities. It was subsequently washed 3 times with distilled water and once with ethanol. The powder was calcined at 600°C for 4 hours to remove residual organics. To perform MRR, the calcined SiO<sub>2</sub> mineral, Mg powder (Sigma-Aldrich, ≥ 99%), and sodium chloride (NaCl, Sigma-Aldrich, ACS reagent, ≥99.0%), were mixed

at a molar ratio of 1:2.2:10.3 for SiO<sub>2</sub>: Mg: NaCl, using a mortar and pestle for 15 minutes. With a heating rate of 3°C min<sup>-1</sup>, the mixture was heat-treated in an alumina crucible in an Ar atmosphere at 700°C for different dwell times—0 h, 1.5 h, 3 h, and 6 h and then cooling down naturally to room temperature. 0 h corresponds to a heat treatment that includes heating to 700°C and then natural cooling to room temperature (with no dwell time at 700°C). To remove oxygen, the furnace tube was purged with Ar for 15 minutes prior to increasing the temperature. The reduction products were washed and centrifuged in de-ionized water (2 times), a 2 M HCl solution (2 times). The unreacted SiO<sub>2</sub> particles were removed by etching in an aqueous 5 wt% HF solution. After each washing step, the samples were washed with ethanol and dried at 60°C overnight. Each centrifuge process was conducted for 30 minutes under a relative centrifugal force of 3405 x g. The Si nanoparticles produced by MRR of SiO<sub>2</sub> without NaCl served as the reference. Reference samples were processed with the same rinsing procedure, except with the omission of washing with water, which was applied solely to remove residual NaCl.

#### 4.2.2 Materials characterizations

To determine the effect of NaCl on mediating the thermal energy evolved during reduction, we analyzed the thermal behavior of two reactant samples, with and without NaCl, by DTA (NETZSCH Jupiter STA 449C). Samples of ca. 100 mg were heated from room temperature to 900°C under an inert gas atmosphere under a heating rate of 3°C min<sup>-1</sup>. The recorded thermograms were normalized by weight for comparison.

To evaluate the phase composition of the reaction products, we performed XRD analysis (Bruker D2 Phaser), using Cu K $\alpha$  radiation and a Ni filter. The 2 $\theta$  scan range was 15°-90° and the step size 0.02°. By applying the Rietveld refinement (Doebelin & Kleeberg, 2015), we performed quantitative phase analysis on diffractograms obtained from the starting material, the reaction product after reduction, and the product after each washing step—i.e., with water to remove NaCl, with an HCl solution to remove the MgO phase, and with an HF solution to remove residual SiO<sub>2</sub>.

To estimate the crystallite size of the final elemental silicon product from the diffractograms, we applied the Scherrer method (Equation 8) (Cullity & Stock, 2001):

$$L = K\lambda/\beta\cos\theta \quad , \quad (\text{Equation 8})$$

where  $L$  represents the crystallite size,  $K = 0.89$ , and  $\lambda = 1.54060 \text{ \AA}$ .  $\beta$  was determined by fitting a Lorentzian curve to each peak in the X-ray diffractograms— (Figures S1e and S1f), i.e., corresponding to the (111), (220), (311), (400), (331), and (422) crystallographic planes of Si—after removal of the instrumental broadening contribution.  $\theta$  was the angle of diffraction for each peak. The crystallite size was calculated from each of the 6 peaks in the XRD pattern. For each sample, the mean  $\pm$  standard deviation of the 6 calculations is reported here as its crystallite size.

The specific surface area and pore size distribution were determined via  $N_2$  adsorption measurements (Micromeritics, 3Flex). To determine the specific surface area, the Brunauer–Emmett–Teller (BET) model was applied to fit the  $N_2$  adsorption isotherm. Before these measurements were performed, the samples were degassed at  $150^\circ\text{C}$  for 24 h under vacuum.

We evaluated the microstructure morphology by secondary electron imaging in a field-emission scanning electron microscope (SEM; Zeiss Leo Supra 35VP) and by high-resolution bright-field imaging in a spherical aberration-corrected scanning transmission electron microscope (TEM; JEOL JEM-ARM200CF). The crystalline nature of the Si nanoparticles was evaluated by fast Fourier transform (FFT) analysis of the high-resolution TEM image.

#### 4.2.3 Electrochemical characterizations

To validate the charge storage performance of the Si nanoparticle product, we incorporated them into the anode of lithium-ion battery half-cells. The Si nanoparticles were mixed with carbon-black (TIMCAL SUPER C45) and sodium alginate (Sigma-Aldrich), as the binder, in a 60:20:20 weight percent ratio in water to form a slurry. The slurry was cast onto Cu foil of  $10 \mu\text{m}$  thickness, which was then dried in a  $70^\circ\text{C}$  oven overnight. To produce working electrodes, circular discs ( $10 \text{ mm}$  in diameter) were punched from the dried slurry-on-foil. The mass loading of active material was ca.  $0.42 \text{ mg cm}^{-2}$ .

Swagelok half-cells with a Li chip as the counter-electrode were assembled in a glovebox under an Ar environment. The electrolyte was prepared by dissolving 10 wt.% of fluoroethylene carbonate (FEC) (98%, Alfa Aesar) in a 1 M solution of  $\text{LiPF}_6$  dissolved in a mixed solvent of ethylene carbonate (EC)-diethyl carbonate (DEC) (Sigma-Aldrich) with 1:1 volume ratio. Each cell contained  $200 \mu\text{L}$  of the electrolyte.

Celgard™ 2400 of 25  $\mu\text{m}$  thickness was used as the separator. Figure 4.1 shows the half-cell architecture.

Cyclic voltammetry (CV) analysis was performed on the half-cells using a potentiostat (Princeton Applied Research PARSTAT MC) over a voltage range of 0.005-1.5 V (vs. Li/Li<sup>+</sup>) under 0.1 mV s<sup>-1</sup>. The same instrument was used to collect electrochemical impedance spectra (EIS) in the frequency range of 100,000 to 0.1 Hz at the vertex potentials (5 mV and 1.5 V) in each cycle.

To determine the charge storage capacity and stability of charge storage, the half-cells were charged and discharged in a battery analyzer system (MTI, BTS8-WA) over an applied electrical bias range of 0.005-1.5 V. The cells were conditioned for 5 cycles by charging and discharging at 200 mA g<sup>-1</sup>, prior to cycling at a higher current rate, 400 mA g<sup>-1</sup>, to evaluate performance stability. The rate of charge and discharge was determined based on the assumption that 1 C = 4000 mA g<sup>-1</sup>. A C/10 rate of 400 mA g<sup>-1</sup> was chosen for assessing the charge/discharge cycle performance of the half cells.

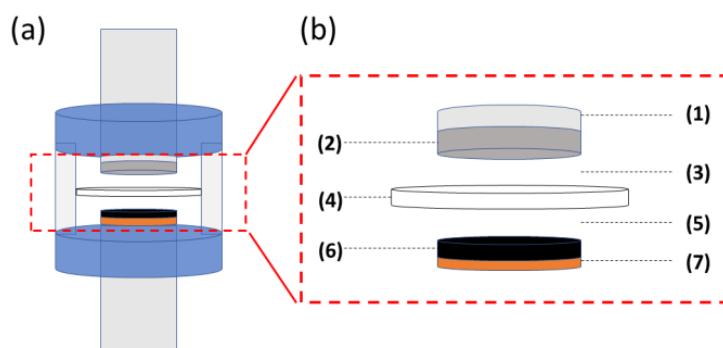


Figure 4.1. Schematic of the LIB half-cell architecture: (a) the entire cell test assembly, (b) inside of the half-cell consisting of (1) stainless steel current collector, (2) lithium metal chip, (3) liquid electrolyte, (4) separator, (5) liquid electrolyte, (6) negative electrode, and (7) copper foil current collector.

## 4.3 Results and Discussion

### 4.3.1 Results

The phase composition of the starting SiO<sub>2</sub> mineral was characterized by XRD. Rietveld analysis of the diffractogram (Figure 4.9a) showed that the mineral was 34.3% cristobalite and 65.7% amorphous.

Through DTA, the amount of heat evolved was compared for MRR of SiO<sub>2</sub> in the presence and the absence of NaCl. As shown in Figure 4.2, NaCl shifted the onset of the exothermic reaction from 493°C to 516°C. The amount of heat released during the reaction without NaCl was six times greater than in the presence of NaCl. Reduction in the presence of NaCl yielded an endothermic peak at ca. 800°C, which corresponded to the melting of NaCl.

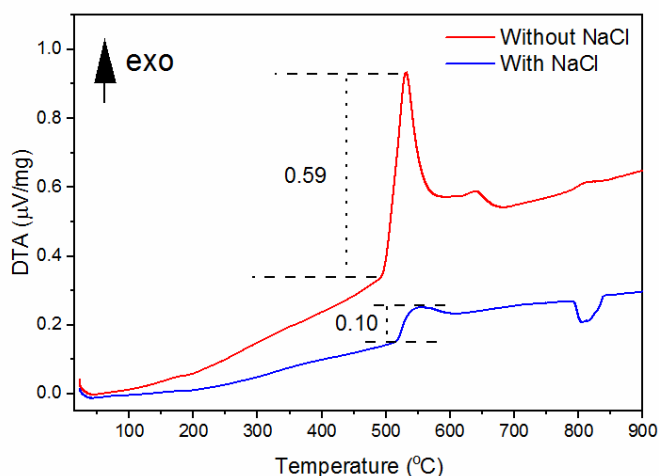


Figure 4.2. Thermograms of the reactants without and with heat moderation.

All samples were heated to 700°C with a heating rate of 3°C min<sup>-1</sup> and held at 700°C for up to 6 h. The samples were described by their dwell time, e.g., 0 h, meaning no dwell duration at 700°C. XRD diffractograms were analyzed to identify the progress of phase development. For the synthesis conducted without NaCl, the diffractograms are shown in Figure 4.3a. In addition to Si, MgO, and Mg<sub>2</sub>Si, and Mg<sub>2</sub>SiO<sub>4</sub> were present.

Figure 4.3b shows XRD patterns of SiO<sub>2</sub> reduced in the presence of NaCl (recorded after NaCl removal by washing with distilled water) under the same synthesis conditions as the MRR of SiO<sub>2</sub> without NaCl. The peak from the residual SiO<sub>2</sub> mineral

at  $2\theta = 22^\circ$  (PDF 82-0512) was observed at 0 h, indicating an incomplete reduction of the mineral into elemental Si during the early stage of the reduction. In contrast to the reduction without NaCl, the formation of  $\text{Mg}(\text{OH})_2$  was observed at 0 h, while no  $\text{Mg}_2\text{SiO}_4$  was present during the entire reaction.

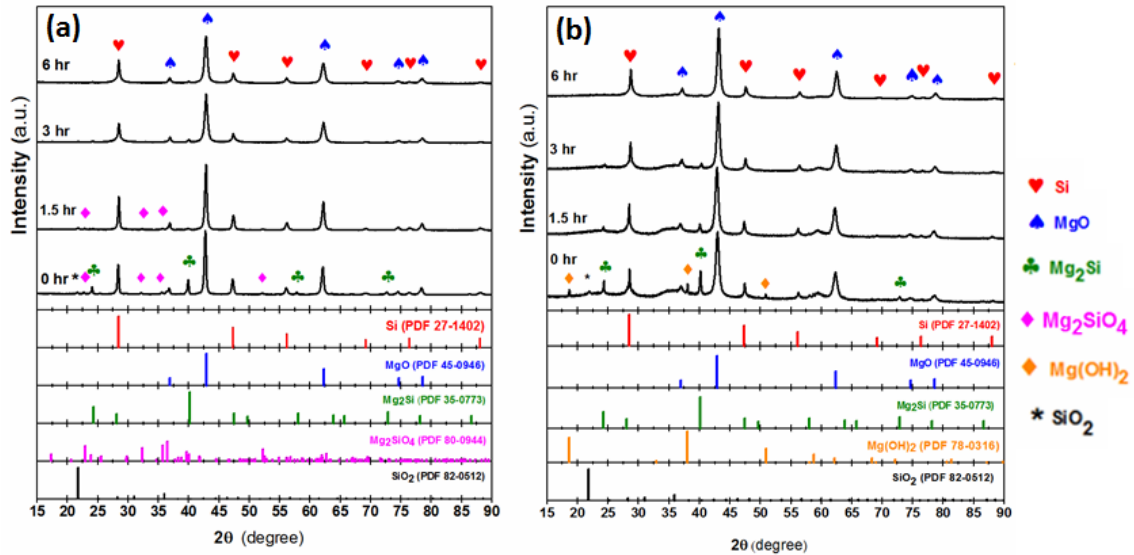


Figure 4.3. XRD patterns of  $\text{SiO}_2$  reduced (a) without the presence of NaCl and (b) in the presence of NaCl.

Table 4.1 summarizes the results of quantitative phase analysis of the diffractograms shown in Figure 4.3. When  $\text{Mg}_2\text{Si}$  or  $\text{Mg}_2\text{SiO}_4$  were initially present, they disappeared with increasing reduction time up to 6 h.

Table 4.1. Quantitative phase analysis of the XRD patterns in Figure 4.3.

Sample	Crystallinity of the mix (%)	Amorphous content (mol%)	Si (mol. %)	MgO (mol. %)	$\text{Mg}_2\text{Si}$ (mol. %)	$\text{SiO}_2$ (mol. %)	$\text{Mg}_2\text{SiO}_4$ (mol. %)	$\text{Mg}(\text{OH})_2$ (mol. %)
no NaCl, 0 h	85.9	9.8	20.9	64.5	3.9	0.6	0.4	0.0
no NaCl, 1.5 h	78.5	14.6	22.5	61.9	0.3	0.6	0.1	0.0
no NaCl, 3 h	86.2	9.0	23.4	67.2	0.0	0.4	0.1	0.0
no NaCl, 6 h	83.1	11.4	16.0	72.1	0.0	0.4	0.0	0.0
NaCl, 0 h	43.5	47.9	5.4	39.9	3.1	1.1	0.0	2.6
NaCl, 1.5 h	42.3	47.3	7.7	43.5	1.5	0.0	0.0	0.0
NaCl, 3 h	59.9	30.3	11.1	57.3	1.3	0.0	0.0	0.0
NaCl, 6 h	69.0	22.1	16.0	61.7	0.3	0.0	0.0	0.0

The diameter of the Si nanocrystals was estimated by applying the Scherrer method to the 6 peaks of Si in the XRD patterns (Figures S1e and S1f), and the results are summarized in Figure 4.4. When NaCl was used, the size of the crystallites formed remained invariant over time, at ca. 21 nm. When reduction was performed without NaCl, crystallites with an average diameter of  $61.3 \pm 4.1$  nm formed immediately and decreased to  $18.8 \pm 5.9$  nm after 6 h.

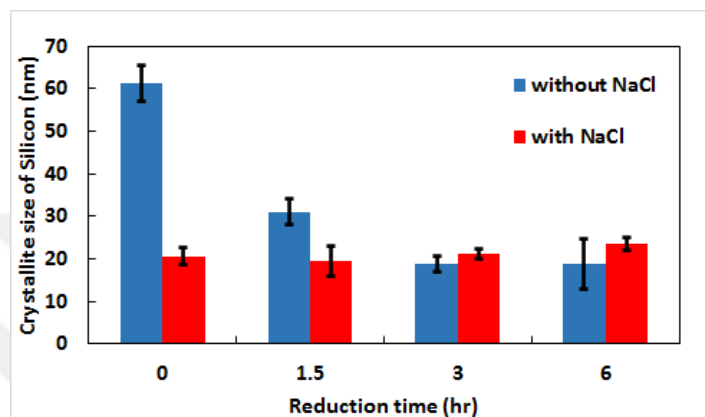


Figure 4.4. Crystallite size of the silicon material obtained under different reduction conditions and duration.

To determine the effect of heat scavenging by NaCl on the specific surface area, we performed N<sub>2</sub> adsorption-desorption analysis. Because the final crystallite size was achieved after 1.5 h of reduction in the presence of NaCl, we proceeded with the comparison of these samples with the control ones (without NaCl). The corresponding isotherms are shown in Figure 4.10. The specific surface area of each sample was calculated using the BET method. As summarized in Table 4.2, the specific surface area was 2.85 times greater in samples reduced with NaCl than those reduced without NaCl and high enough to be suitable for lithium storage (Chen et al., 2011).

The morphology of the starting material (cristobalite SiO<sub>2</sub>) is shown in Figure 4.5a. After reduction for 1.5 h at 700°C, 2 levels of particle size were observed in the agglomerated 3-dimensional (3-D) network product of synthesis without NaCl (Figure 4.5b), by secondary electron SEM imaging: < 250 μm and < 50 nm. However, the product of reduction with NaCl did not show sintering and grain growth (Figure 4.5c). Analysis by bright-field TEM imaging (Figure 4.5d) revealed a well-sintered 3-D mesoporous network of Si particles formed without NaCl. When NaCl was used, we observed non-agglomerated primary particles diameters of 20-30 nm (Figure 4.5e).

Most of these particles had a shell layer, which is most likely a form of native oxide. Fast Fourier transform analysis of the HRTEM images (insets in Figure 4.5d and Figure 4.5e) revealed polycrystalline pseudo-diffraction patterns that were indexed to the crystallographic planes of Si.

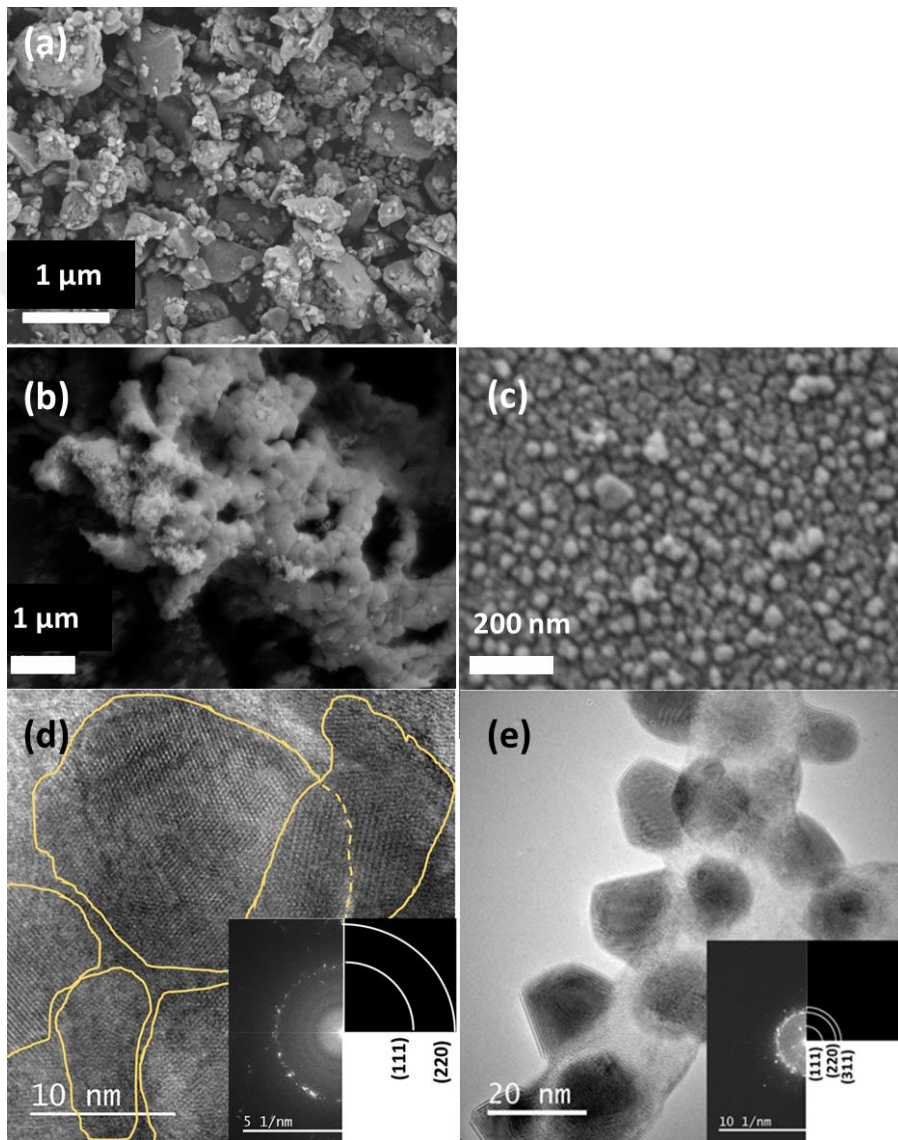


Figure 4.5. Morphology revealed by SEM imaging of (a) the mineral  $\text{SiO}_2$ , (b) the product of synthesis without  $\text{NaCl}$ , and (c) the product of synthesis with  $\text{NaCl}$ . Representative bright-field TEM micrographs of the Si particles synthesized (d) without  $\text{NaCl}$  and (e) with the presence of  $\text{NaCl}$ . The insets in (d) and (e) are FFT analyses of the corresponding images.

Table 4.2. Nanoparticle properties extracted from N<sub>2</sub> adsorption-desorption and microscopy data.

Sample	BET specific surface area (m <sup>2</sup> g <sup>-1</sup> )	Total free volume (BJH) (cm <sup>3</sup> g <sup>-1</sup> )	Estimated equivalent spherical particle size (nm)	Observed particle size (TEM, SEM) (nm)
SiO <sub>2</sub> mineral	21.6	0.019	-	2610
Si (without NaCl)	47.8	0.271	53.9	NA
Si (with NaCl)	136.5	0.860	18.9	20

Both individual Si nanoparticles and porous 3-D Si network produced by MRR for 1.5 h were tested as active material in Si|electrolyte|Li half-cells to investigate the effect of the microstructure on electrochemical performance. The cycling capacity of both anodes was tested over 100 cycles of charge-discharge at a rate of 400 mA g<sup>-1</sup> (Figure 4.6a). The initial 5 cycles were run at a rate of 200 mA g<sup>-1</sup> to establish a stable solid electrolyte interphase (SEI) on the surface of Si particles. The delithiation capacity of the 1<sup>st</sup> and the 100<sup>th</sup> cycle (at 400 mA g<sup>-1</sup>) for the half-cell with porous 3-D Si network was 2466 mAh g<sup>-1</sup> and 1287 mAh g<sup>-1</sup>, respectively, corresponding to a 52% capacity retention. Electrodes with individual Si nanoparticles had corresponding values of 2023 mAh g<sup>-1</sup> and 960 mAh g<sup>-1</sup>, consistent with 47% capacity retention. Coulombic efficiencies of the electrodes are plotted in Figure 4.6a (secondary y-axis). The electrode with the porous 3-D Si network yielded higher Coulombic efficiencies for all cycles. The initial irreversible capacity loss (at 200 mA g<sup>-1</sup>) of the electrode containing individual Si nanoparticles was much larger compared to that of the electrode with the porous 3-D Si network (Figure 4.6b). The Coulombic efficiencies of the corresponding first cycles were 47% and 74%, respectively, indicating that lithiation and delithiation in the Si in the porous 3-D network electrode were more reversible in character, possibly due to thicker SEI formation on the individual Si nanoparticles. In both samples, the fluoroethylene carbonate (FEC) reduction was observed at ca. 1 V vs. Li/Li<sup>+</sup>. Voltage drop during lithiation was less steep in the electrodes with individual Si nanoparticles, suggesting more charge transfer during irreversible SEI formation (Kitz et al., 2020).

Reversible lithiation and delithiation of Si in the electrodes were also revealed by CV by the presence of the characteristic peaks (Figure 4.6c and Figure 4.6d). During

the cathodic scan from 1.5 V electrode potential to 5 mV,  $\text{Li}^+$  was inserted into the electrode.

The reduction of the electrolyte additive (FEC) was observed within the first cathodic scan under an electrode potential of ca. 1 V in the cyclic voltammograms shown in Figure 4.6e (C. Xu et al., 2015). The peak appearing at 0.18 V corresponds to an initial alloying reaction that formed  $\text{LiSi}$ , which was superimposed on the subsequent formation of alloys of elevated Li. These alloys were further lithiated to  $\text{Li}_{3.16}\text{Si}$ , as characterized by the peak at 0.02 V (Reyes Jiménez et al., 2017). The dealloying reaction occurred in 2 steps. The anodic peak observed at 0.37 V corresponds to the formation of  $\text{Li}_7\text{Si}_3$  from  $\text{Li}_{3.16}\text{Si}$ , and the one at 0.52 V to complete dealloying of Si. The relative size of the peak at 0.37 V is larger in Figure 4.6c, indicating that deep lithiation of the Si material was achieved more easily in Si synthesized without NaCl—i.e., the porous 3-D Si network. Except for the first cathodic scan (Figure 4.6e), the specific currents for the electrode without NaCl were larger than the ones with NaCl (Figure 4.6c and Figure 4.6d). The larger charge-transfer currents observed for the first cathodic scan of the half-cell with individual particles indicates reduction of more electrolyte co-solvent and formation of thicker SEI per unit mass of the individual Si nanoparticles (Kitz et al., 2020).

Figure 4.6f shows the rate-performance of the half-cells after undergoing 10 cycles of cyclic voltammetry at  $0.1 \text{ mV s}^{-1}$ . The specific capacities decreased with increasing rate. Electrodes of the porous 3-D Si network showed higher specific capacities compared to electrodes of individual Si nanoparticles. Both half-cells partially recovered their specific capacities after reducing the current to  $400 \text{ mA g}^{-1}$ .

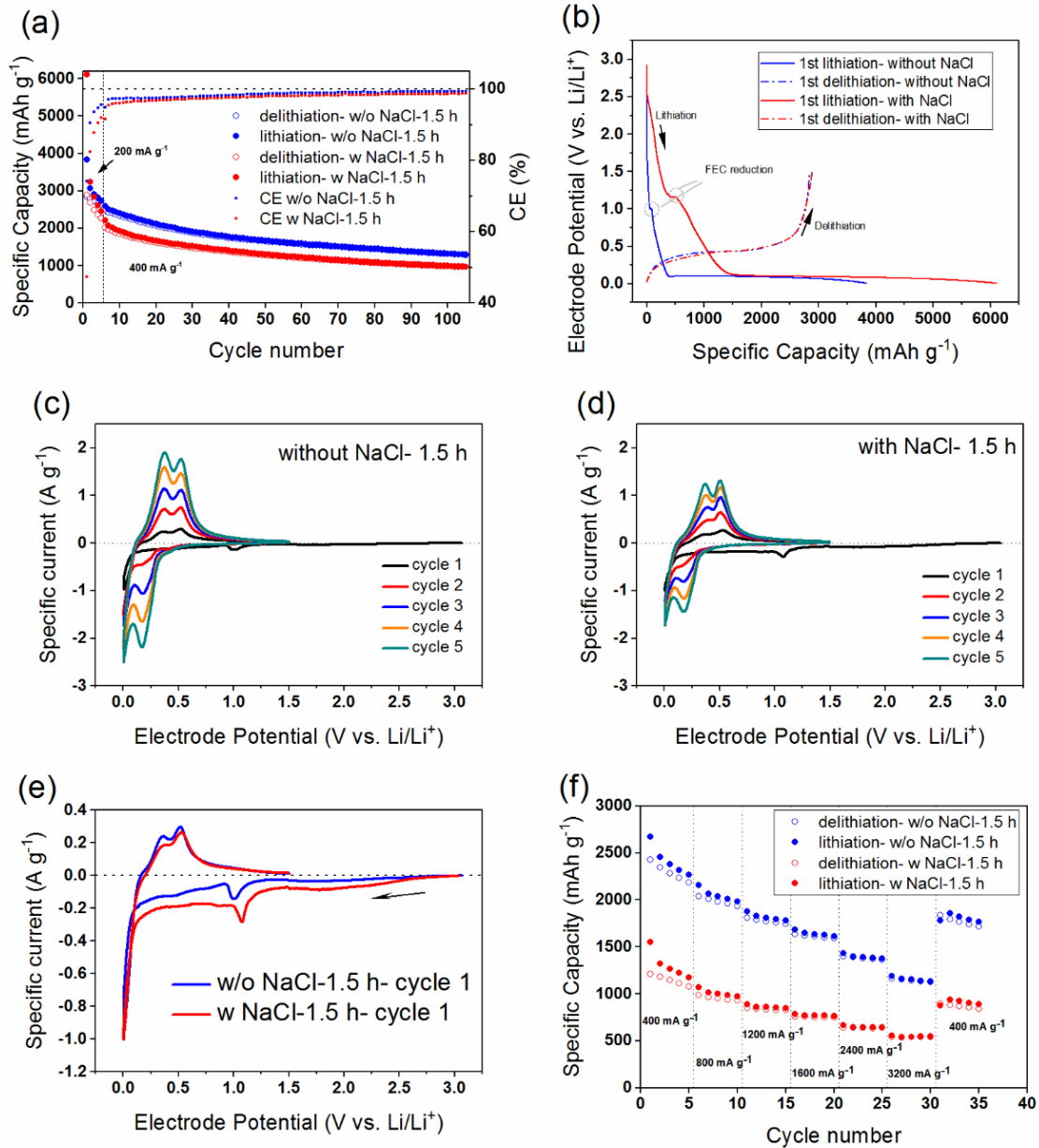


Figure 4.6. (a) Cycling performance of the two types of half-cells; (b) potential profile of the first cycles; cyclic voltammetry of the Si|electrolyte|Li half-cells (under 0.1 mV s<sup>-1</sup> scan rate) (c) for the porous Si network, and (d) for individual particles; (e) first cyclic voltammograms of the Si|electrolyte|Li half-cells, and (f) the rate performance of half-cells after undergoing 10 CV cycles.

Electrochemical impedance spectroscopy was performed at the vertex potentials of the cyclic voltammograms. The corresponding Nyquist plots of the half-cells in the lithiated state (at 5 mV) are shown in Figure 4.7. The size of the suppressed semi-circle decreased with cycling, indicating a decrease in overall impedance throughout cycling. Comparison of Figure 4.7a and Figure 4.7c reveals that the impedance of isolated Si particles is larger compared to that of the porous 3-D network, which suggests the formation of a thicker SEI layer on individual Si particles (Figure 4.6e).

In Figure 4.7b and Figure 4.7d, we show the resistance variation with cycling in the half-cells. In the half-cell with the porous 3-D network of Si, the Nyquist plot of the EIS spectrum only showed a suppressed semi-circle. By contrast, the half-cell with individual Si nanoparticles in the electrode yielded EIS spectra with 3 semi-circles. The corresponding equivalent circuit models are shown in the inset (Figure 4.7b and Figure 4.7d).

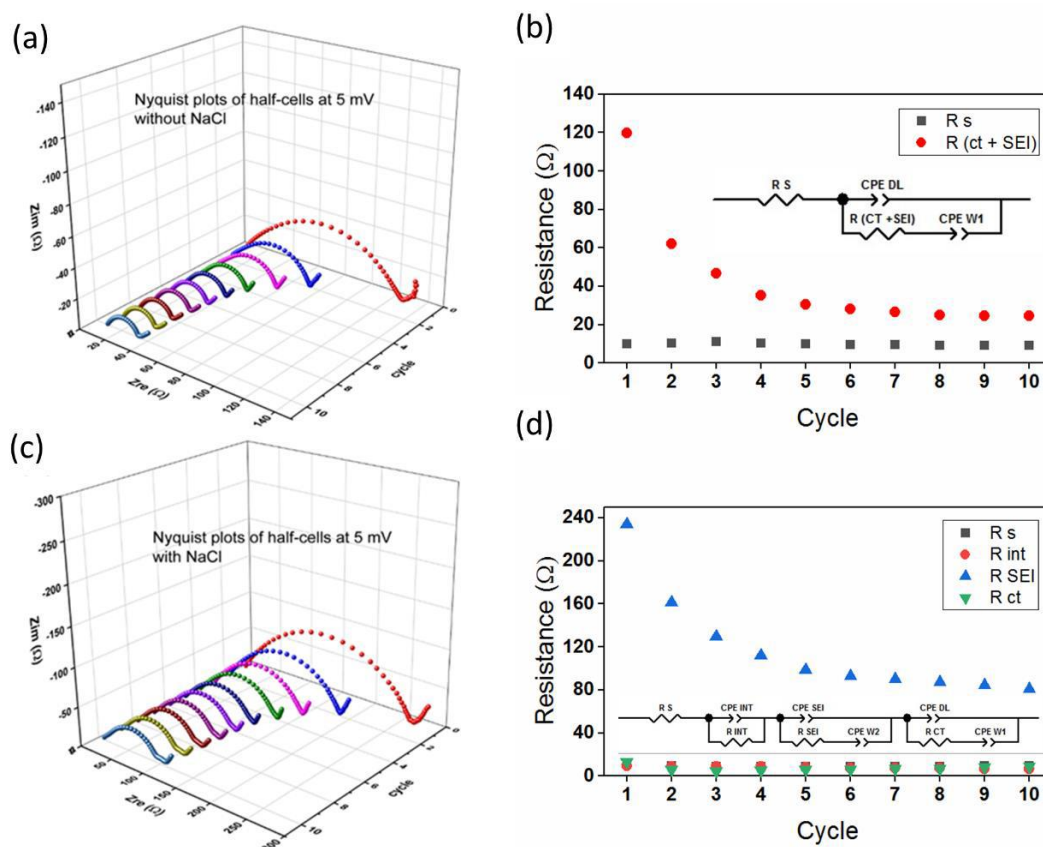


Figure 4.7. Nyquist plots of the half-cells in the lithiated state (5 mV) with active material synthesized (a) without NaCl (active material with a porous network) and (c) with NaCl (individual particles) along with their corresponding resistance values, respectively (b), (d); corresponding equivalent circuits in the inset figures.

### 4.3.2 Discussion

When SiO<sub>2</sub> and Mg are heated to  $T > 516^{\circ}\text{C}$ , analysis of the thermochemical data reveals a strong driving force for MRR of SiO<sub>2</sub> due to the highly exothermic nature of the reaction (Equation 1).



Under adiabatic conditions, the maximum temperature attainable by the material phases is  $< 3088^{\circ}\text{C}$ , via self-heating resulting from the exothermicity of the reaction (Supporting Information). The addition of NaCl, at a NaCl:SiO<sub>2</sub> molar ratio of 10.28:1, reduces this upper bound temperature to  $885^{\circ}\text{C}$ . Such a decrease in total heat evolved (Figure 4.2) is due to the latent heat of melting of NaCl at  $801^{\circ}\text{C}$ , during which 289 kJ — based on 28.16 kJ/mol for melting of NaCl (Chase, 1998) — is absorbed by the transforming salt.

In our work, we performed MRR in an open crucible, i.e., under non-adiabatic conditions. While the reference (no NaCl) Si product consisted of well-sintered aggregates (Figure 4.5d), the Si nanoparticles produced with NaCl heat moderation were individual nanoparticles (Figure 4.5e). This striking difference in morphology suggests that without NaCl, the reacting materials reached sufficiently high temperatures by self-heating that enabled sintering, albeit without melting of the Si particles—i.e.,  $801^{\circ}\text{C} < T < 1414^{\circ}\text{C}$ . In addition, the presence of Mg<sub>2</sub>SiO<sub>4</sub> in samples undergoing reduction up to 3 h indicates that the temperature achieved by self-heating exceeded  $1000^{\circ}\text{C}$  (Brindley & Hayami, 1965). However, with NaCl, the results were consistent with the findings of Liu and co-workers (X. Liu et al., 2012) i.e., highly crystalline Si primary nanoparticles were produced by MRR at melting temperatures set by the molten salt, and their size set by the degree of thermal moderation via the molar ratio of the inert salt.

Although the efficacy of NaCl as a heat scavenger and its role in the reduction reaction during synthesis of Si nanoparticles by MRR of different forms of SiO<sub>2</sub> are well known, we sought to elucidate a formation mechanism of the Si nanoparticles that is consistent with the microstructural and compositional evolution observed. Liu and co-workers demonstrated the synthesis of Si NPs at  $353^{\circ}\text{C}$  by using a solution of LiCl and KCl, which forms a binary eutectic liquid stable at temperatures well below the pure compounds. As our analyses demonstrate, the use of NaCl as a single component also

offers an effective “solvent”, one that is simpler. When heated to 700°C in a furnace, the melting of NaCl can also be achieved through self-propagating heating from the exothermic reaction. Although the Mg concentration was lower in pure NaCl than in a 1:1 mixture of MgCl<sub>2</sub>:NaCl, the Si nanoparticles were of comparable size to those formed in the molten salt mixture by reduction at 600°C (X. Liu et al., 2012), as a result of the 10.28 moles of NaCl used.

One consequence of the relatively low processing temperatures was limited growth due to limited diffusion. At the high temperatures reached via self-heating from exothermic MRR without NaCl present, the surface diffusivity of Si was sufficiently high to enable growth. In contrast, heat scavenging by melting of NaCl restricted the product phases to lower temperatures, suppressing the growth of Si nanoparticles due to the more limited diffusivity of Si. The Si nanoparticles produced were ca. 20 nm in diameter with a yield of ca. 36%, which can be improved through further optimization of process parameters, such as more effective separation processing (Zhiliang Liu et al., 2017) and tuning the molar ratio of NaCl to minimize the maximum temperature of self-heating.

Based on the materials characterization results (summarized in Table 4.3), we propose a physical model for the microstructural evolution of NaCl-mediated MRR of SiO<sub>2</sub>. During MRR, the mixture of Mg powder, NaCl, and calcined, ball-milled SiO<sub>2</sub> powders were heated to 973 K, which exceeded the melting temperature of elemental Mg. As the system underwent heating, the Mg and NaCl particles melted and formed (separate) sessile droplets, with SiO<sub>2</sub> particles and Mg droplets supported by the NaCl liquid. The SiO<sub>2</sub> particles (2.61 ± 0.68 μm diameter, 6.8 vol%) and the Mg particles (184 ± 47 μm diameter, 9.5 vol%) were supported by NaCl particles (437 ± 49 μm diameter, 83.7 vol%).

Table 4.3. Summary of particle characteristics for generating the physical model.

Powder	Particle Size (μm)	Molar %	Weight %	Density (g cm <sup>-3</sup> )	Volume %
SiO <sub>2</sub> mineral (cristobalite)	2.61 ± 0.68	7.4	8.4	2.65	6.8
Mg powder	184 ± 47	16.3	7.6	1.738	9.5
NaCl	437 ± 49	76.3	84.0	2.16	83.7

Because Mg liquid has a high vapor pressure, the surface of the Mg droplets served as the source Mg gas atoms, which underwent fast transport to all surfaces of the material system. Mg atoms contacting the NaCl liquid surface were ionized, and the  $\text{Mg}^{2+}$  ions were dissolved into the NaCl liquid up to a limited solubility (X. Liu et al., 2012; Nersisyan et al., 2005). In addition, the liquid contacts the  $\text{SiO}_2$  particles and facilitates the diffusion of Mg ions to the reaction interface (X. Liu et al., 2012).

As shown in Figure 4.8, there were 3 reaction paths for Mg to reduce  $\text{SiO}_2$  particles—via gas-phase transport to the  $\text{SiO}_2$  particle surface, at the  $\text{Mg}(l)|\text{SiO}_2$  interface, or diffusing through the molten NaCl.

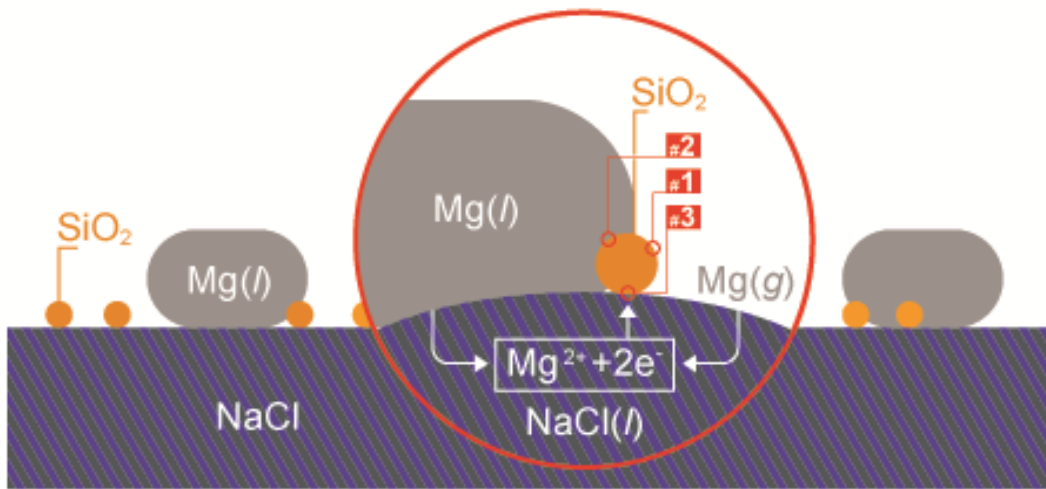
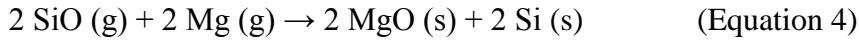
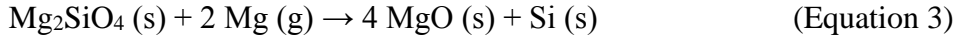


Figure 4.8. Physical model of NaCl-mediated MRR of  $\text{SiO}_2$  to produce Si nanoparticles, with the 3 reaction pathways indicated described in detail in the text.

**Path 1:** consists of Mg vapor adsorbing onto the  $\text{SiO}_2$  surface resulted in MRR due to the higher oxidation potential of Mg than that of Si. The absence of  $\text{Mg}_2\text{SiO}_4$  suggests that the reaction proceeded in 3 sequential reactions via counter-diffusing Mg (g) and SiO (g) (Wynnyckyj & Bhogeswara Rao, 1976):



**Path 2:** Reaction at the Mg (l)|SiO<sub>2</sub> interface proceeded via formation of a eutectic liquid interlayer, of Mg with 1.16 at% Si, at 638°C (Massalski, Okamoto, International, Subramanian, & Kacprzak, 1990), i.e. during heating of the system. As Mg and Si ions form the eutectic liquid, the Si-O bonds are destabilized, forming a thin intermix layer of Mg-Si-O ions on the SiO<sub>2</sub> interface (Gutman et al., 2006). Oxidation of the Mg ions formed MgO, initiating MRR already at the eutectic temperature and leading to melting of the NaCl supporting particles via self-heating from the thermal energy released. Because Si has very low diffusivity in MgO, a Si-rich layer would have formed at the SiO<sub>2</sub>|MgO interface (Gutman et al., 2006). Subsequent diffusion of Mg to the SiO<sub>2</sub> surface led to MRR with the reaction front of the Si-rich layer moving into the SiO<sub>2</sub> (Gutman et al., 2006). Nucleation of Si nanoparticles in this surface layer fragments the SiO<sub>2</sub> underneath, resulting in MgO and Si particles supported on NaCl surfaces.

While the system is at 1073 K, the Mg-rich liquid formed an interface with SiO<sub>2</sub> with the morphology, SiO<sub>2</sub>|Si|MgO|Mg-rich liquid. Upon cooling of the system to room temperature, Mg<sub>2</sub>Si (s) precipitated out during the eutectic reaction. Because it does not form a stable interface with SiO<sub>2</sub>, it must have nucleated at the MgO|Mg-rich liquid interface. Up to 1.5 h of reduction, the amount of Mg<sub>2</sub>Si phase decreased with a correlated increase in Si and MgO, indicating that less Mg was available for forming Mg<sub>2</sub>Si, due to participation in MRR of the remaining SiO<sub>2</sub>. Further prolonged reduction yielded precipitation of Si nanoparticles in the Mg-rich liquid without Mg<sub>2</sub>Si formation.

**Path 3:** When Mg<sup>2+</sup> diffused through liquid NaCl to the SiO<sub>2</sub> surface, MRR with the SiO<sub>2</sub> surface produced MgO and Si phases. The strong driving force for MRR suggested that the interface reaction was limited only by the diffusivity of Mg<sup>2+</sup> through the liquid NaCl due to low solubility. In addition, the Gibbs free energy of formation for MgO is ca. 410 kJ/mol lower than that of Mg<sub>2</sub>Si, suggesting that Mg<sub>2</sub>Si was less likely

to form via a reaction path of limited  $\text{Mg}^{2+}$  flux (Chase, 1998). The absence of  $\text{Mg}_2\text{SiO}_4$  further validates the heat scavenging role of NaCl.

During prolonged MRR, sessile NaCl liquid droplets containing dissolved Mg ions supported  $\text{SiO}_2$ , Si, and MgO particles, as well as  $\text{Mg}_2\text{Si}$ , if present. MgO is not soluble in  $\text{SiO}_2$  nor in molten NaCl.  $\text{Mg}_2\text{Si}$  eutectic liquids may be present in the system but supported on either the NaCl surface or the MgO particle surface, i.e., not in direct contact with the  $\text{SiO}_2$  surfaces (Gutman et al., 2006). The amount of  $\text{Mg}_2\text{Si}$  in the reaction products decreased as the reaction proceeded from 1.5 h to 6 h, consistent with the increase in MgO and Si. In contact with the SiO gas,  $\text{Mg}_2\text{Si}$  reacts to form MgO and Si (Equation 5).

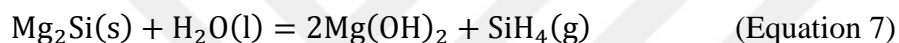


When NaCl is present, the maximum temperature reached can be estimated by considering the morphology of the product microstructure. The formation of the undesired  $\text{Mg}_2\text{SiO}_4$  phase was suppressed. In the absence of NaCl, the reduction reaction proceeds via diffusion of Mg vapor and SiO vapor, which is stable at temperatures exceeding  $1280^\circ\text{C}$  and disproportionates into  $\text{SiO}_2$  and Si at lower temperatures (Toguri & Pidgeon, 1961). Although  $\text{Mg}_2\text{SiO}_4$  may form by the solid-state reaction of MgO and  $\text{SiO}_2$  between  $1100\text{-}1400^\circ\text{C}$  (Brindley & Hayami, 1965), the more likely reaction is the fast transport of Mg vapor through the initial MgO interfacial layer, meeting and reacting with the counter diffusing SiO vapor to form  $\text{Mg}_2\text{SiO}_4$  and Si, both of which condenses on the surface of  $\text{SiO}_2$  (Wynnyckyj & Bhogeswara Rao, 1976). The silicate phase can react further with excess Mg vapor to yield MgO and Si, which is consistent with the evolution in phase composition at reduction times exceeding 3 h. However, in the presence of molten NaCl, MRR at the  $\text{SiO}_2$  surface (Equation 6)



is the rate-limiting step, when Mg ions are dissolved up to their solubility limit in the NaCl liquid and diffuse rapidly to the SiO<sub>2</sub> reaction interface. Without thermal moderation by molten NaCl, the presence of Mg<sub>2</sub>SiO<sub>4</sub> suggests that the exothermic heating of the reaction products in the open crucible reached 1100-1400°C; by contrast, when NaCl absorbed 289 kJ of thermal energy, the reduction products remain below 1100°C.

Mg(OH)<sub>2</sub> had also appeared in the initial MRR products when NaCl was present. It is likely to have evolved from Mg<sub>2</sub>Si reacting with water, according to Equation 7, which has a reaction enthalpy of -593.877 kJ/mol at room temperature. In fact, the spontaneous sparks that arise with the introduction of water and the subsequent bubbling both confirm the formation of SiH<sub>4</sub> (Iwodate et al., 2018; X. Liu et al., 2012).



The ensuing reaction of SiH<sub>4</sub> with the oxygen in ambient air was shown by Iwodate and co-workers to yield amorphous SiO<sub>2</sub> (Iwodate et al., 2018).

Capacity, cycle life, and Coulombic efficiencies of both individual Si particles and porous 3-D Si network were determined without any further surface coating or modification. When fresh cells of Si electrodes undergo lithiation, the liquid electrolyte is reduced on their surface, resulting in the formation of SEI (Kitz et al., 2020; C. Xu et al., 2015). During the first cathodic scan from the open-circuit voltage (OCV), a larger current was observed for the half-cell containing individual Si particles, suggesting the reduction of more electrolyte. The higher specific surface area of the individual Si nanoparticles facilitates the electrochemical reduction kinetics, promoting the formation of a thicker SEI layer on their surface. Similarly, the electrolyte additive (FEC) was reduced at a higher potential (ca. 1 V in Figure 4.6e) in the case of individual Si nanoparticles, indicative of early-onset SEI formation.

When the cycling performance of the individual Si nanoparticles and the porous 3-D Si network were compared at a high current rate (400 mA g<sup>-1</sup>), after establishing SEI formation and activation of Si, we observed a similar capacity retention rate over 100 cycles. However, due to the much higher initial capacity loss and faster capacity

reduction over the first 5 cycles at  $200 \text{ mA g}^{-1}$ , the individual Si nanoparticles showed lower capacity compared to the porous 3-D Si network. To understand the capacity-fading mechanism, we compared the EIS evolution and total battery impedance of these two materials. The size of the suppressed semi-circle for both systems decreased over the first 10 cycles, indicating that the stabilization of the SEI layer over the electrode surface occurred slowly over the first 10 cycles (Guo, Sun, Chen, Wang, & Manivannan, 2011). However, we observed the higher  $R_{\text{SEI}}$  for individual Si nanoparticles after the first lithiation, which is consistent with thicker SEI formed over the nanoparticles. In addition to the semi-circle associated with the impedance due to SEI formation, a second one grew gradually over the first 10 cycles in the case of the individual Si nanoparticles, identified as  $R_{\text{CT}}$ . This observation suggests that electronic contact between the porous network and the conductive additives/binders remained intact throughout those cycles, but the individual nanoparticles suffered from disconnection from the additives or the current collector, resulting in an increase in charge-transfer resistance. Overall, the electrochemical performance suggests that although the size of individual Si nanoparticles is small enough to compensate for the mechanical strain induced by volume changes during repeated lithiation/delithiation, the porous structure and interconnected nature of the 3-D Si network more effectively accommodate the volume change and allow strain relaxation without detrimental mechanical stress. It has been shown that the crystal size of Si also plays an important role in the cycle stability (Domi, Usui, Sugimoto, & Sakaguchi, 2019; D. Wang et al., 2021). Although the sample prepared with NaCl possessed a smaller crystal size than the one prepared without NaCl, and their crystal size must have affected the cycle stability, their differences in particle size and morphology contributed more strongly. The electrochemical performance of both materials can be further improved with device fabrication strategies, such as carbon coating and preparation of composites with materials of high electrical conductivity (Xiang et al., 2021).

Extensive work has been reported in the literature on molten salt-mediated MRR of silica to produce porous 3-D networks of nanostructured Si, for which processing parameters have been explored—closed vs. open reactor vessels, furnace temperature, heating rate, and reactant stoichiometry (J. Entwistle et al., 2018; Favors et al., 2014; X. Liu et al., 2012). In our approach, we focused on blending the powders in an open crucible—NaCl (ca.  $437 \mu\text{m}$ ), Mg (ca.  $184 \mu\text{m}$ ), and  $\text{SiO}_2$  mineral (ca.  $2.6 \mu\text{m}$ )—giving

rise to 3 simultaneous interfacial reactions during silica reduction. Putting such large NaCl crystals in direct contact with the much smaller Mg and SiO<sub>2</sub> micron-sized particles offers a heat sink that limits the maximum temperature that the product Si nanoparticles are exposed to. The reduced diffusivity at temperatures below 885°C results in a loose powder of 20 nm-diameter Si particles, produced by a low-cost, scalable process. The reactant blend configuration is independent of the reactor vessel geometry, ensuring the presence of the 3 interfacial reaction paths. Moreover, because these Si nanoparticles are in a form that is more versatile than a porous scaffold, they are easily incorporated into a wider variety of production strategies for LIB anodes—e.g., electrospinning and being wrapped by graphene (Ashuri et al., 2016; Favors et al., 2014; Kong et al., 2019).

#### 4.4 Conclusion

By analyzing the evolving phase composition over time, we show that NaCl-mediated MRR of SiO<sub>2</sub> yields isolated Si nanoparticles via 3 parallel reaction pathways. Si nanoparticles of 20 nm can be size-tuned according to the size of NaCl particles providing heat scavenging. The electrochemical performance of these Si nanoparticles compared to that of 3-D Si networks revealed thicker SEI formation by their incorporation into half-cells—via the first-cycle irreversible discharge capacity of half-cells, faster capacity loss over the first 5 cycles at 200 mA g<sup>-1</sup>, and via larger impedance. However, at higher cycling current rates of 400 mA g<sup>-1</sup>, that is, once SEI formation and the activation of Si were established, both types of electrodes offered similar capacity retention rates over 100 cycles in half-cells.

## 4.5 Supporting Information

### 4.5.1 XRD patterns

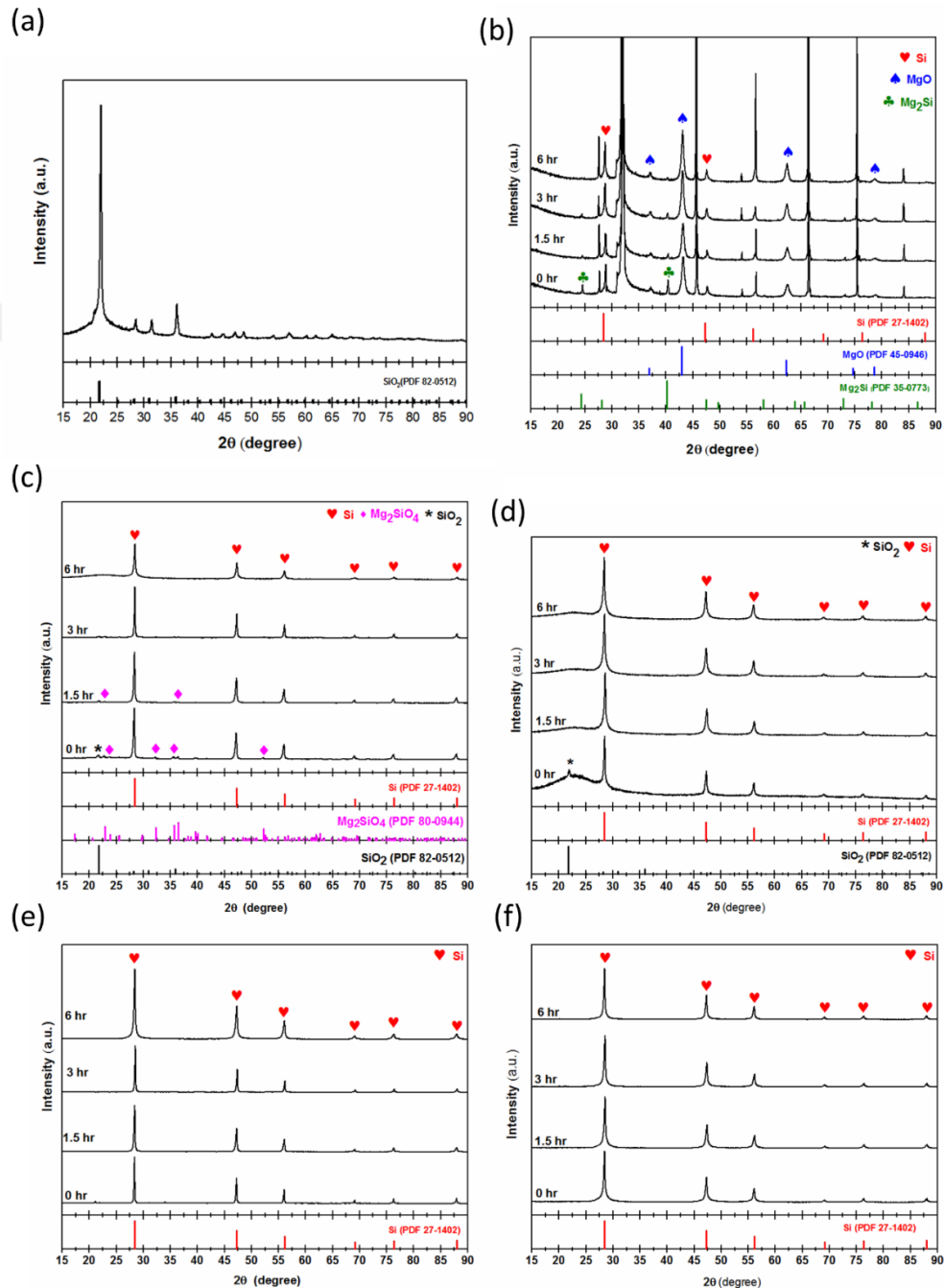


Figure 4.9. (a) The XRD pattern of the ball-milled and cleaned SiO<sub>2</sub> mineral used as the silicon source. Phase analysis shows the single crystalline phase of cristobalite (PDF 82-0512). The crystallinity of this powder was calculated to be 34.3%. (b) XRD patterns of as reduced samples synthesized with NaCl. The non-indexed sharp peaks represent NaCl (PDF 88-2300). To observe the peaks, we had to zoom the vertical axis.

(c), (d) XRD patterns of the samples synthesized after HCl washing step for no NaCl and NaCl-containing samples respectively. (e), and (f) XRD patterns of the samples synthesized after HF washing step for no NaCl and NaCl-containing samples respectively.

#### 4.5.2 N<sub>2</sub> adsorption-desorption

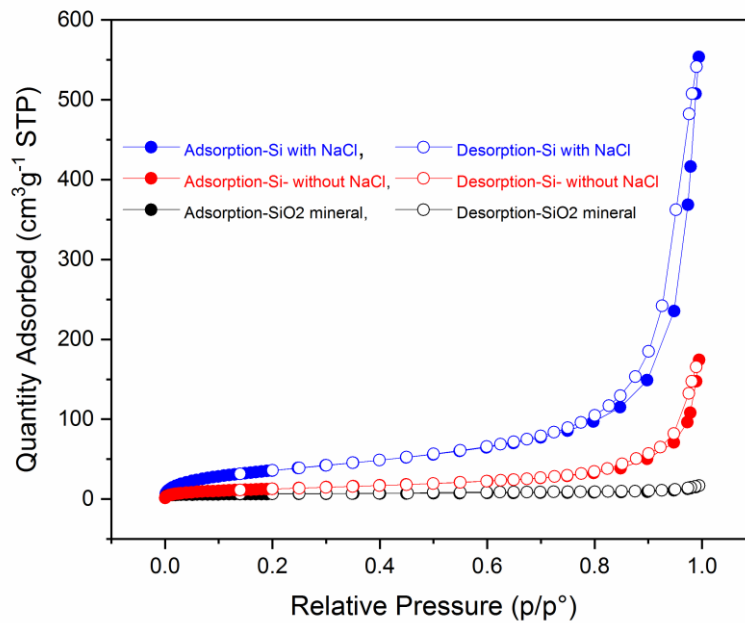


Figure 4.10. N<sub>2</sub> adsorption-desorption isotherms for the Si products and the starting SiO<sub>2</sub> mineral

### 4.5.3 Estimation of equivalent spherical particle size

In Table 4.2 (column 4), we have estimated an equivalent particle size based on the BET-derived specific surface area values. Assuming we have spherical particles, their specific surface area (SSA) can be calculated as:

$$SSA = \frac{4\pi R^2}{(d)\left(\frac{4}{3}\pi R^3\right)} = \frac{3}{(d)(R)} = \frac{6}{(d)(D)}$$

where;

d: density of the material

R: radius of spheres

D: Diameter of spheres.

So, the equivalent spherical particle size can be estimated as:

$$D = \frac{6}{(d)(SSA)}$$

In the case of silicon, we have assumed that  $d = 2.33 \text{ g cm}^{-3}$ .

#### 4.5.4 Supplementary micrographs

We present other transmission electron micrographs (lower in magnification) from same product samples shown in Fig. 4 that are representative of particles distributed over the entire TEM grid.

The synthesis without NaCl led to formation 3-D porous network. Below is a TEM (Fig. S3a) and from the same sample as in Fig. 4b and Fig. 4d. However, in the sample synthesized with NaCl, the electron micrographs as Fig. 4c and Fig. 4e showed individual nanoparticles. In Fig. S3b, we show lower-magnification TEM micrographs from the same sample as in Fig. 4c and Fig. 4e:

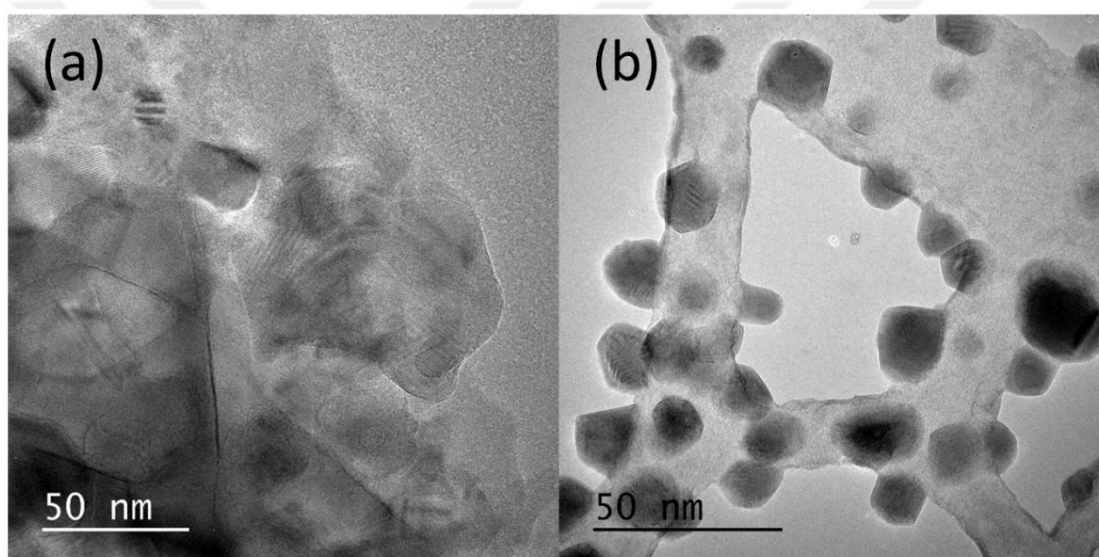
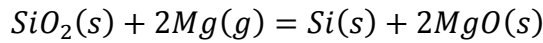


Figure 4.11. Bright-field TEM micrographs of the silicon particles synthesized (a) without NaCl and (e) with the presence of NaCl (lower magnification compared to Figure 4.5).

#### 4.5.5 Maximum temperature calculation without NaCl

To estimate the theoretical maximum temperature that would be reached by the product phases under adiabatic conditions, we performed the calculation for the magnesiothermic reduction reaction (MRR) for SiO<sub>2</sub> and Mg vapor in an adiabatic container at 493°C (766.15 K), which is the temperature revealed by TG-DTA to be the onset of MRR (see Figure 4.2).



From the thermochemical database, the molar enthalpy is determined according to

$$H_{\text{SiO}_2,766.15} = H_{\text{SiO}_2,298} + \int_{298}^{766.15} C_{p,\text{SiO}_2} dT$$

$$H_{\text{SiO}_2(s),766.15} = -882.623 \frac{\text{kJ}}{\text{mol}} \text{ (Barin 89)}$$

$$H_{\text{Mg}(g),766.15} = 156.836 \frac{\text{kJ}}{\text{mol}} \text{ (Landolt 99, Bard 85)}$$

$$H_{\text{Si}(s),766.15} = 10.917 \frac{\text{kJ}}{\text{mol}} \text{ (Knacke 91)}$$

$$H_{\text{MgO}(s),766.15} = -580.376 \frac{\text{kJ}}{\text{mol}} \text{ (Knacke 91, Glushko 94, Landolt 99)}$$

The heat released by the MRR at 766.15 K is

$$\begin{aligned} \Delta H_{766.15} &= H_{\text{Si}(s),766.15} + 2(H_{\text{MgO}(s),766.15}) - H_{\text{SiO}_2(s),766.15} - 2(H_{\text{Mg}(g),766.15}) \\ &= (10.917) + 2(-580.376) - (-882.623) - 2(156.836) = -580.884 \text{ kJ} \end{aligned}$$

Under adiabatic conditions, this thermal energy self-heats the reaction products:

$$\Delta H_{\text{rxn}@766.15} = \Delta H_{\text{heating Si}} + \Delta H_{\text{heating MgO}}$$

up to the maximum adiabatic temperature.

$$\Delta H_{\text{rxn}@766.15} = \int_{766.15}^{T_{\text{max}}} (n_{\text{Si}})(C_{p(\text{Si})})dT + \int_{766.15}^{T_{\text{max}}} (n_{\text{MgO}})(C_{p(\text{MgO})})dT$$

To solve this equation, it is necessary to identify phase transformations that may occur during heating of MgO and Si, to account for changes in heat capacity and absorption of latent heats of transformation.

$\Delta H_{\text{rxn}@766.15}$  is the thermal energy available for self-heating of the reaction products—*i.e.*, 1 mol Si and 2 mols MgO. The thermochemical data needed to perform the calculations are summarized in Table 4.4.

The constant-pressure molar heat capacities are presented as:

$$C_p = A + (B * 10^{-3})T + (C * 10^5)T^{-2} + (D * 10^{-6})T^2 \frac{J}{\text{mol.K}}$$

The coefficients valid for the range of temperatures specified are summarized in Table 4.4.

Table 4.4. Specific heat capacity coefficients for Si and MgO

Phase	A	B	C	D	Range (K)	Reference
Si (s)	22.824	3.858	-3.540	0	298.15-1685	Knacke 91
Si (l)	27.196	0	0	0	1685-3504	Knacke 91
MgO (s)	47.485	4.648	-10.34	-0.268	298.15-1700	Knacke 91, Glushko 94, Landolt 99
MgO (s)	78.297	-19.425	-171.035	5.156	1700-3100	Barin 93, Glushko 94, Landolt 99
MgO(l)	84.000	0	0	0	3100-5100	Glushko 94, Landolt 99

$$\text{For Si (s)} \rightarrow \text{Si (l)}, \Delta H_m = 50.208 \frac{\text{kJ}}{\text{mol}} \text{ at } 1685\text{K}$$

$$\text{For MgO (s)} \rightarrow \text{MgO (l)}, \Delta H_m = 77.000 \frac{\text{kJ}}{\text{mol}} \text{ at } 3100\text{K}$$

The heat required to raise the temperature of 1 mol of Si from 766.15 to 1685 K

is

$$\begin{aligned} \Delta H_1 &= \int_{766.15}^{1685} (n_{\text{Si}})(C_{p(\text{Si})})dT \\ &= \int_{766.15}^{1685} (1)(22.824 + (3.858 * 10^{-3})T - (3.540 * 10^{-5})T^{-2})dT \\ &= 25.06 \text{ kJ} \end{aligned}$$

And the heat required to raise the temperature of 2 mols of MgO from 766.15 to 1685 K is

$$\begin{aligned}\Delta H_2 &= \int_{766.15}^{1685} (n_{\text{MgO}})(C_{p(\text{MgO})})dT \\ &= \int_{766.15}^{1685} (2)(47.485 + (4.648 * 10^{-3})T + (-10.34 * 10^5)T^{-2} \\ &\quad + (-0.268 * 10^{-6})T^2 )dT = 95.49 \text{ kJ}\end{aligned}$$

The total heat required becomes

$$\Delta H_1 + \Delta H_2 = 25.06 + 95.49 = 120.55 \text{ kJ}$$

The remaining thermal energy available for self-heating is  $580.884 - 120.55 = 460.33 \text{ kJ}$ .

Because 1 mol of Si undergoes melting at 1685 K, the heat required to melt 1 mol of Si is determined as

$$\Delta H_3 = (n_{\text{Si}})(\Delta H_{m,\text{Si}}) = (1)(50.208) = 50.208 \text{ kJ}$$

The remaining available heat is  $460.33 - 50.208 = 410.13 \text{ kJ}$ .

The heat required to raise the temperature of 1 mol of liquid Si and 2 mols of MgO from 1685 to 1700 K are, respectively:

$$\Delta H_4 = \int_{1685}^{1700} (n_{\text{Si,l}})(C_{p(\text{Si,l})})dT = \int_{1685}^{1700} (1)(27.196) dT = 0.41 \text{ kJ}$$

$$\begin{aligned}\Delta H_5 &= \int_{1685}^{1700} (n_{\text{MgO}})(C_{p(\text{MgO})})dT \\ &= \int_{1685}^{1700} (2)(47.485 + (4.648 * 10^{-3})T - (10.34 * 10^5)T^{-2} \\ &\quad - (0.268 * 10^{-6})T^2 )dT = 1.63 \text{ kJ}\end{aligned}$$

The total heat required becomes

$$\Delta H_4 + \Delta H_5 = 0.41 + 1.63 = 2.04 \text{ kJ}$$

The remaining thermal energy available for self-heating is  $410.13 - 2.04 = 408.09 \text{ kJ}$ .<sup>2</sup>

This residual thermal energy propagates in raising the temperature of 1 mol of liquid Si and 2 mols of MgO from 1700 K to 3100 K

$$\Delta H_6 = \int_{1700}^{3100} (n_{\text{Si,l}})(C_{\text{p(Si,l)}})dT = \int_{1700}^{3100} (1)(27.196) dT = 38.07 \text{ kJ}$$

$$\begin{aligned} \Delta H_7 &= \int_{1700}^{3100} (n_{\text{MgO}})(C_{\text{p(MgO)}})dT \\ &= \int_{1700}^{3100} (2)(78.297 + (-19.425 * 10^{-3})T + (-171.035 * 10^5)T^{-2} \\ &\quad + (5.156 * 10^{-6})T^2) dT = 165.12 \text{ kJ} \end{aligned}$$

$$\Delta H_6 + \Delta H_7 = 38.07 + 165.12 = 203.19 \text{ kJ}$$

The remaining available thermal energy is  $408.09 - 203.19 = 204.90 \text{ kJ}$ .

To melt 2 mol of MgO, the thermal energy required is

$$\Delta H_8 = (n_{\text{MgO}})(\Delta H_{\text{m,MgO}}) = (2)(77.000) = 154.00 \text{ kJ}$$

Because the available heat is larger than this amount, it is consumed in melting 2 mols of MgO completely. The remaining available thermal energy is  $204.90 - 154.00 = 50.90 \text{ kJ}$ .

---

<sup>2</sup> There is no phase transformation occurring at 1700 K. Only the temperature-dependent heat capacity behavior of MgO changes.

This amount of thermal energy will increase the temperature of 1 mol of liquid Si and 2 mols of liquid MgO from 3100 K to the unknown temperature,  $T_{\max}$ .

$$50.90 \text{ kJ} = \Delta H_9 + \Delta H_{10}$$

The heat required to raise the temperature of 1 mol of liquid Si from 3100 K to  $T_{\max}$  is

$$\begin{aligned} \Delta H_9 &= \int_{3100}^{T_{\max}} (n_{\text{Si,l}})(C_{p(\text{Si,l})})dT \\ &= \int_{3100}^{T_{\max}} (1)(27.196) dT = (27.196 * 10^{-3})(T_{\max} - 3100)\text{kJ} \end{aligned}$$

And the heat required to raise the temperature of 2 mols of liquid MgO from 3100 K to  $T_{\max}$  is

$$\begin{aligned} \Delta H_{10} &= \int_{3100}^{T_{\max}} (n_{\text{MgO,l}})(C_{p(\text{MgO,l})})dT \\ &= \int_{3100}^{T_{\max}} (2)(84.000) dT = (168.00 * 10^{-3})(T_{\max} - 3100)\text{kJ} \end{aligned}$$

$$50.90 = (27.196 * 10^{-3})(T_{\max} - 3100) + (168.00 * 10^{-3})(T_{\max} - 3100)$$

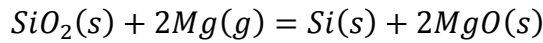
$$50.90 = (195.196 * 10^{-3})(T_{\max} - 3100)$$

Solving this equation reveals the theoretical maximum adiabatic temperature, i.e., the upper bound of the temperature reached by self-heating:

$$T_{\max} = 3360.73 \text{ K (3087.58}^\circ\text{C)}$$

#### 4.5.6 Maximum temperature calculation with NaCl

To estimate the theoretical maximum temperature that would be reached by the product phases under adiabatic conditions when NaCl is present, we performed the calculation for the magnesiothermic reduction reaction (MRR) for SiO<sub>2</sub> and Mg vapor in an adiabatic container at 516°C (789.15 K), which is the temperature revealed by TG-DTA to be the onset of MRR in the presence of NaCl (see Figure 4.2).



From the thermochemical database, the molar enthalpy is determined according to

$$H_{\text{SiO}_2,789.15} = H_{\text{SiO}_2,298} + \int_{298}^{789.15} C_{p,\text{SiO}_2} dT$$

$$H_{\text{SiO}_2(s),789.15} = -880.949 \frac{\text{kJ}}{\text{mol}} \text{ (Barin 89)}$$

$$H_{\text{Mg}(g),789.15} = 157.314 \frac{\text{kJ}}{\text{mol}} \text{ (Landolt 99, Bard 85)}$$

$$H_{\text{Si}(s),789.15} = 11.498 \frac{\text{kJ}}{\text{mol}} \text{ (Knacke 91)}$$

$$H_{\text{MgO}(s),789.15} = -579.244 \frac{\text{kJ}}{\text{mol}} \text{ (Knacke 91, Glushko 94, Landolt 99)}$$

The heat released by MRR at 789.15 K is

$$\begin{aligned} \Delta H_{789.15} &= H_{\text{Si}(s),789.15} + 2(H_{\text{MgO}(s),789.15}) - H_{\text{SiO}_2(s),789.15} - 2(H_{\text{Mg}(g),789.15}) \\ &= (11.498) + 2(-579.244) - (-880.949) - 2(157.314) = -580.669 \text{ kJ} \end{aligned}$$

Under adiabatic conditions, this thermal energy self-heats the reaction products and the NaCl heat moderator:

$$\Delta H_{\text{rxn}@789.15} = \Delta H_{\text{heating Si}} + \Delta H_{\text{heating MgO}} + \Delta H_{\text{heating NaCl}}$$

up to the maximum adiabatic temperature.

$$\begin{aligned} \Delta H_{\text{rxn}@789.15} = & \int_{789.15}^{T_{\text{max}}} (n_{\text{Si}})(C_{p(\text{Si})})dT \\ & + \int_{789.15}^{T_{\text{max}}} (n_{\text{MgO}})(C_{p(\text{MgO})})dT + \int_{789.15}^{T_{\text{max}}} (n_{\text{NaCl}})(C_{p(\text{NaCl})})dT \end{aligned}$$

To solve this equation, it is necessary to identify phase transformations that may occur during heating of MgO, Si, and NaCl, to account for changes in heat capacity and absorption of latent heats of transformation.

We used 10.28 mols of NaCl and 2 mols MgO for every 1 mol of SiO<sub>2</sub><sup>3</sup>.

To determine the energy balance for self-heating, the thermochemical data used is summarized in Table 4.4 and Table 4.5. The constant-pressure molar heat capacities depended on temperature according to the relationship:

$$C_p = A + (B * 10^{-3})T + (C * 10^5)T^{-2} + (D * 10^{-6})T^2 \frac{J}{\text{mol.K}}$$

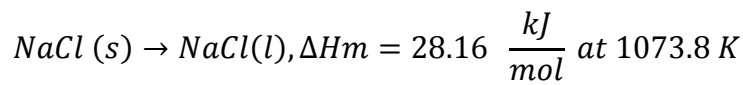
Table 4.5 includes the coefficients valid for the range of temperatures specified.

---

<sup>3</sup> This ratio corresponds to a weight ratio of SiO<sub>2</sub>: NaCl of 1:10.

Table 4.5. Specific heat capacity coefficients for NaCl

Phase	A	B	C	D	Range (K)	Reference
NaCl (s)	56.297	-13.015	-3.423	21.862	298.15-900	Barin 93, Landolt 99
NaCl (s)	58.637	-17.832	-4.893	24.549	900-1073.8	Landolt 99
NaCl (l)	-25.312	76.203	398.013	-17.661	1073.8-1500	Barin 93, Landolt 99
NaCl (l)	66.944	0	0	0	1500-2500	Landolt 99



The heat required to raise the temperature of 1 mol of Si from 789.15 to 900 K is

$$\begin{aligned} \Delta H_1 &= \int_{789.15}^{900} (n_{Si})(C_{p(Si)})dT \\ &= \int_{973.15}^{1073.8} (1)(22.824 + (3.858 * 10^{-3})T - (3.540 * 10^5)T^{-2})dT \\ &= 2.84 \text{ kJ} \end{aligned}$$

The heat required to raise the temperature of 2 mols of MgO from 789.15 to 900 K is

$$\begin{aligned} \Delta H_2 &= \int_{789.15}^{900} (n_{MgO})(C_{p(MgO)})dT \\ &= \int_{789.15}^{900} (2)(47.485 + (4.648 * 10^{-3})T - (10.34 * 10^5)T^{-2} \\ &\quad - (0.268 * 10^{-6})T^2)dT = 11.03 \text{ kJ} \end{aligned}$$

The heat required to raise the temperature of 10.28 mols of NaCl from 789.15 to 900 K is

$$\begin{aligned}\Delta H_3 &= \int_{789.15}^{900} (n_{NaCl})(C_{p(NaCl)})dT \\ &= \int_{789.15}^{900} (10.28)(56.297 - (13.015 * 10^{-3})T - (3.423 * 10^5)T^{-2} \\ &\quad + (21.862 * 10^{-6})T^2 )dT = 68.87 \text{ kJ}\end{aligned}$$

The total heat required becomes

$$\Delta H_1 + \Delta H_2 + \Delta H_3 = 2.84 + 11.03 + 68.87 = 82.74 \text{ kJ}$$

The remaining thermal energy available for self-heating is  $580.669 - 82.74 = 497.93 \text{ kJ}$ .

The heat required to raise the temperature of 1 mol of Si from 900 K to 1073.8 K is

$$\begin{aligned}\Delta H_4 &= \int_{900}^{1073.8} (n_{Si})(C_{p(Si)})dT \\ &= \int_{900}^{1073.8} (1)(22.824 + (3.858 * 10^{-3})T - (3.540 * 10^5)T^{-2} )dT \\ &= 4.56 \text{ kJ}\end{aligned}$$

The heat required to raise the temperature of 2 mols of MgO from 900 K to 1073.8 K is

$$\begin{aligned}\Delta H_5 &= \int_{900}^{1073.8} (n_{MgO})(C_{p(MgO)})dT \\ &= \int_{900}^{1073.8} (2)(47.485 + (4.648 * 10^{-3})T - (10.34 * 10^5)T^{-2} \\ &\quad - (0.268 * 10^{-6})T^2 )dT = 17.64 \text{ kJ}\end{aligned}$$

The heat required to raise the temperature of 10.28 mols of NaCl from 789.15 to 900 K is

$$\begin{aligned}\Delta H_6 &= \int_{900}^{1073.8} (n_{NaCl})(C_{p(NaCl)})dT \\ &= \int_{900}^{1073.8} (10.28)(58.637 - (17.832 * 10^{-3})T - (4.893 * 10^5)T^{-2} \\ &\quad + (24.549 * 10^{-6})T^2 )dT = 115.25 \text{ kJ}\end{aligned}$$

The total thermal energy required for heating all phases from 900 to 1073.4 K is

$$\Delta H_4 + \Delta H_5 + \Delta H_6 = 4.56 + 17.64 + 115.25 = 137.45 \text{ kJ}$$

The remaining thermal energy available for self-heat is  $497.93 - 137.45 = 360.48 \text{ kJ}$ .

The remaining thermal energy first melts 10.28 mols of NaCl at 1073.8 K.

The heat required to melt 10.28 mols of NaCl is

$$\Delta H_7 = (n_{NaCl})(\Delta H_{m,NaCl}) = (10.28)(28.16) = 289.48 \text{ kJ}$$

The residual available heat is  $360.48 - 289.48 = 71.00 \text{ kJ}$ .

This thermal energy heats the temperature of 1 mol of Si, 2 mols of MgO and 10.28 mols of liquid NaCl from 1073.8 K to the unknown temperature of  $T_{max}$ .

$$71.00 \text{ kJ} = \Delta H_8 + \Delta H_9 + \Delta H_{10}$$

$$\begin{aligned}
\Delta H_8 &= \int_{1073.8}^{T_{max}} (n_{Si})(C_{p(Si)})dT \\
&= \int_{1073.8}^{T_{max}} (1)(22.824 + (3.858 * 10^{-3})T - (3.540 * 10^5)T^{-2})dT \text{ J} \\
&= (1 \\
&\quad * 1 * 10^{-3})((1.929 * 10^{-3})T^2 + 22.824T + (3.540 \\
&\quad * 10^5)T^{-1})_{1073.8}^{T_{max}} \text{ kJ}
\end{aligned}$$

$$\begin{aligned}
\Delta H_9 &= \int_{1073.8}^{T_{max}} (n_{MgO})(C_{p(MgO)})dT \\
&= \int_{1073.8}^{T_{max}} (2)(47.485 + (4.648 * 10^{-3})T - (10.34 * 10^5)T^{-2} \\
&\quad - (0.268 * 10^{-6})T^2)dT \text{ J} \\
&= (2 \\
&\quad * 1 * 10^{-3})((-8.933 * 10^{-8})T^3 + (2.324 * 10^{-3})T^2 + 47.485T \\
&\quad + 1.034T^{-1})_{1073.8}^{T_{max}} \text{ kJ}
\end{aligned}$$

$$\begin{aligned}
\Delta H_{10} &= \int_{1073.8}^{T_{max}} (n_{NaCl})(C_{p(NaCl)})dT \\
&= \int_{1073.8}^{T_{max}} (10.28)(-25.312 + (76.203 * 10^{-3})T \\
&\quad + (398.013 * 10^5)T^{-2}) - (17.661 * 10^{-6})T^2)dT \text{ J} \\
&= (10.28 * 1 * 10^{-3})((-5.887 * 10^{-6})T^3 + (3.810 * 10^{-2})T^2 \\
&\quad - 25.312T - (3.980 * 10^7)T^{-1})_{1073.8}^{T_{max}} \text{ kJ}
\end{aligned}$$

$$\begin{aligned}
&71.00 * 1 * 10^3 \\
&= ((-6.07 * 10^{-5})T^3 + (3.98 * 10^{-1})T^2 - (1.42 * 10^2)T \\
&\quad - (4.09 * 10^8)T^{-1})_{1073.8}^{T_{max}}
\end{aligned}$$

$$71.00 * 10^3 = (-6.07 * 10^{-5})T_{max}^3 + (3.98 * 10^{-1})T_{max}^2 - (1.42 * 10^2)T_{max} - (4.09 * 10^8)T_{max}^{-1} + 149612.5879$$

The solution to this equation is

$$T_{max} = 1157.65 \text{ K } (884.50^\circ \text{ C})$$

This value represents the upper bound for the maximum temperature reached by the reaction products and inert NaCl under adiabatic conditions.

Thus, by mixing the reactants with NaCl as a thermal moderator, we show here that the upper bound of the reaction is decreased from 3088°C to 885°C.

#### **4.5.7 References of Supporting Information**

Barin I: Thermochemical Data of Pure Substances, VCH Verlags Gesellschaft, Weinheim, 1989.

Barin I: Thermochemical Data of Pure Substances, Part I, VCH Verlags Gesellschaft, Weinheim, 1993.

Bard A. J., Parsons R., Jordan J., Standard potentials in aqueous solution, Marcel Dekker Inc., New York, 1985.

Glushko Thermocenter of the Russian Academy of Sciences, IVTAN Association, Izhorskaya 13/19, 127412 Moscow, Russia, 1994.

Knacke O., Kubaschewski O., Hesselman K., Thermochemical properties of inorganic substances, 2nd ed., Springer-Verlag, Berlin, pp.1-1113, 1991.

Landolt-Börnstein: Thermodynamic Properties of Inorganic Material, Scientific Group Thermodata Europe (SGTE), Springer-Verlag, Berlin-Heidelberg, 1999.

## CHAPTER 5: Synthesis of Carbon-SiO<sub>2</sub> Composite Fibers

### 5.1 Introduction

In this chapter, we demonstrate the routes by which we produced carbon-silicon oxide (C-SiO<sub>2</sub>) fibers. We started with the synthesis and characterization of copolymers containing carbon and silicon precursors. Then we synthesized silicon-precursor homopolymers and blended them with commercial polyacrylonitrile as the carbon precursor. Polymeric fibers that contained carbon and silicon precursors were fabricated using both copolymers and homopolymer/PAN blends. In addition, hybrid fibers were synthesized via electrospinning of a hybrid solution prepared using acid-catalyzed hydrolysis and partial condensation of tetraethoxysilane (TEOS) in N,N-Dimethylformamide (DMF) followed by mixing with a polyacrylonitrile solution. The properties of the resulting fibers were investigated and compared.

### 5.2 Experimental

#### 5.2.1 Copolymer nanofibers

A copolymer is a polymer formed by linking two or more different kinds of monomers together in the same polymer chain. Two types of silicon containing monomer were copolymerized with acrylonitrile (AN): vinyl-triethoxysilane (VTES) and 3-(triethoxysilyl)propyl methacrylate (TMSPMA), shown in Figure 5.1. The copolymers –poly(AN-*co*-VTES) and poly(AN-*co*-TMSPMA), in which AN moiety and the second monomer served as carbon and silicon precursors, respectively, were synthesized via free radical polymerization (FRP). The molar ratio of the AN: TMSPMA and AN: VTES were both set to 95:5. The solvent was toluene, and the initiator used was a 1 M solution of Azobisisobutyronitrile (AIBN) in toluene. The

molar ratio of monomer: initiator was set to 1000, and the synthesis temperature was 65°C.

Since the silicon incorporation was directly related to the amount of inorganic content, the synthesis had to be done using lower AN: TMSPMA and AN: VTES molar ratios than 95:5. However, all our synthesis trials using lower molar ratios led to gelation of the copolymer. One possible explanation could be condensation between adjacent SiOR groups in TMSPMA and VTES in a copolymer chain.

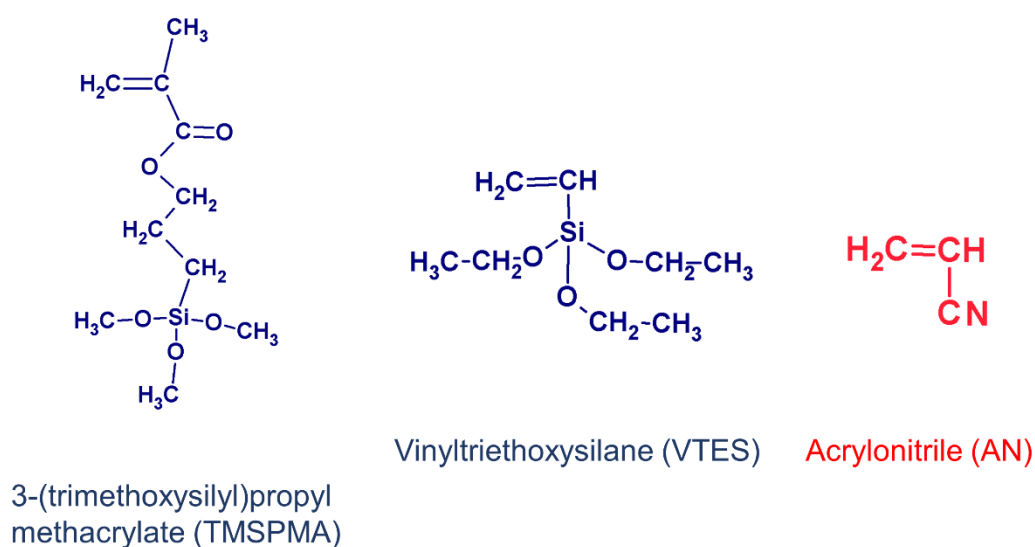


Figure 5.1. The monomers used for copolymerization

The synthesized copolymers were dissolved in DMF to obtain 7 wt.% solution which was electrospun into fibers under a high-voltage of 13 kV, spinneret tip to collector distance of 20 cm, and dispensing rate of ~ 0.5 ml hr<sup>-1</sup>.

### 5.2.2 Homopolymers and producing blend nanofibers

In this section, we show the homopolymerization of the VTES and TMSPMA monomers. After polymerization, the polymers were dissolved in stock solutions and mixed with commercial polyacrylonitrile (PAN) (M<sub>w</sub> 150 kDa) solution to form a blend. Nanofibers were produced through subsequent electrospinning.

Homopolymerization of VTES was done in bulk. In solution polymerization the inherent tendency of propagating VTES radical to undergo chain-transfer reactions with itself made its separation from the solvent difficult (Mori et al., 2013). For the synthesis

of polyvinyltriethoxysilane (PVTES), VTES monomer and 1,1'-Azobis(cyclohexanecarbonitrile) (VAZO initiator) were mixed in monomer: initiator ratio of 100:1. The temperature was set to 92°C and the bulk FRP was run for 26 hours. The reaction proceeded as in Figure 5.2.

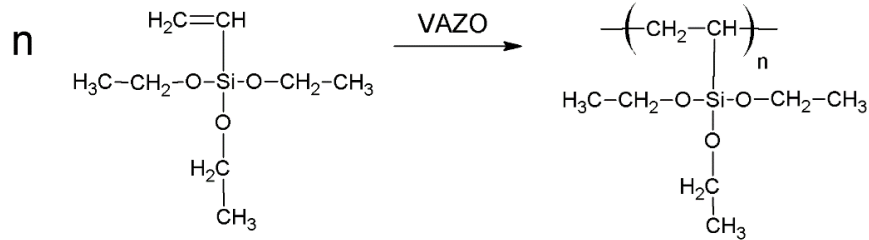


Figure 5.2. Homopolymerization of VTES

The synthesized PVTES was dissolved in toluene as a stock solution. This solution was added to a solution of 8 wt.% commercial PAN ( $M_w$  150 kDa) in DMF to have a PAN: PVTES ratio of 1: 1. The solution was electrospun under a high-voltage of 13 kV, the spinneret tip to collector distance of 20 cm, and the dispensing rate of  $\sim 0.5$  ml  $\text{hr}^{-1}$  to obtain a fiber mat. The stabilization was done under air at 280°C for 2 hours with  $2^\circ\text{C min}^{-1}$  heating rate. Then the carbonization was performed under argon atmosphere at 700°C for 1 hour with a heating rate of  $5^\circ\text{C min}^{-1}$ .

The synthesis of pTMSPMA was carried out through modification of an original synthesis by Maçon (Maçon et al., 2015). The free-radical polymerization (FRP) was performed in toluene at 65°C using AIBN as initiator. To reduce the possibility of gelation, thioglycerol (TG) was added as a chain-transfer agent in molar ratio:

$$R_0 = \frac{n_{\text{chain transfer agent}}}{n_{\text{monomer}}} = 0.05 \quad \text{Equation 5.1}$$

The molar ratio of initiator to monomer was kept constant as:

$$C_0 = \frac{n_{\text{initiator}}}{n_{\text{monomer}}} = 0.05 \quad \text{Equation 5.2}$$

The total concentration of monomer in the solvent was 1 mol  $\text{L}^{-1}$ . The FRP was carried out in a round-bottom flask and under a positive relative pressure of nitrogen gas. After 48 h of reaction with stirring at 300 rpm, the reaction product was precipitated in n-hexane, dissolved in tetrahydrofuran (THF) as the stock solution, and

stored at 4°C to prevent hydrolysis and polycondensation of alkoxy silane groups (gelation).

To incorporate pTMSPMA in the fibers, a solution of 8 wt.% PAN was mixed with the stock solution of pTMSPMA in THF to have 1:1 weight ratio of PAN:pTMSPMA. The electrospinning was performed using a high-voltage of 13 kV, the spinneret tip to collector distance of 20 cm, and the solution dispensing rate of ~ 0.5 ml hr<sup>-1</sup>. The resulting fiber mat was stabilized at 280°C (2°C min<sup>-1</sup> heating rate) under air for 4 hours and carbonized under Ar at 800°C for 6 hours (5°C min<sup>-1</sup> heating rate).

### 5.2.3 Hybrid nanofibers

In this project, since the polyacrylonitrile (the polymer of choice) was insoluble in water, the acid-catalyzed hydrolysis and condensation of TEOS was done in the solvent of PAN, which is DMF. Through simple calculations as in Equation 5.3, solutions with different nominal inorganic contents (10 wt.%, 15 wt.%, 20 wt.%, and 30 wt.%) were prepared by using PAN and TEOS as precursors and DMF as the solvent. A 1 mol L<sup>-1</sup> HCl solution was used as the acid catalyst, and the volume of the acid was calculated according to R<sub>HCl</sub> in Equation 5.3.

$$I_h = \frac{m_I}{m_I + m_O}$$

$$m_I = \frac{m_{TEOS}}{M_{w,TEOS}} \times M_{w,SiO_2}$$

$$m_I = m_{SiO_2}, m_O = m_{PAN}$$

$$R_{HCl} = \frac{n_{HCl}}{n_{SiOR}} = 0.01$$

Equation 5.3

The amount of PAN was adjusted to have a final concentration of 7 wt.% PAN in the hybrid solutions. After complete dissolution of all materials, the resulting transparent solutions were electrospun under a high-voltage of 13 kV and a distance of 20 cm between the tip of the spinneret and the collector. The dispensing rate for each solution had to be optimized separately.

The hybrid materials went through stabilization under air with 2°C min<sup>-1</sup> heating rate at 280°C for 4 hours. Then they were carbonized under argon with 5°C min<sup>-1</sup> heating rate at 800°C for 6 hours.

## 5.3 Results

### 5.3.1 Copolymer nanofibers

The IR spectra of the synthesized poly(AN-*co*-TMSPMA) and poly(AN-*co*-VTES) copolymers are shown in Figure 5.3. The C=C associated absorptions disappear as the free radical polymerization (FRP) occurs.

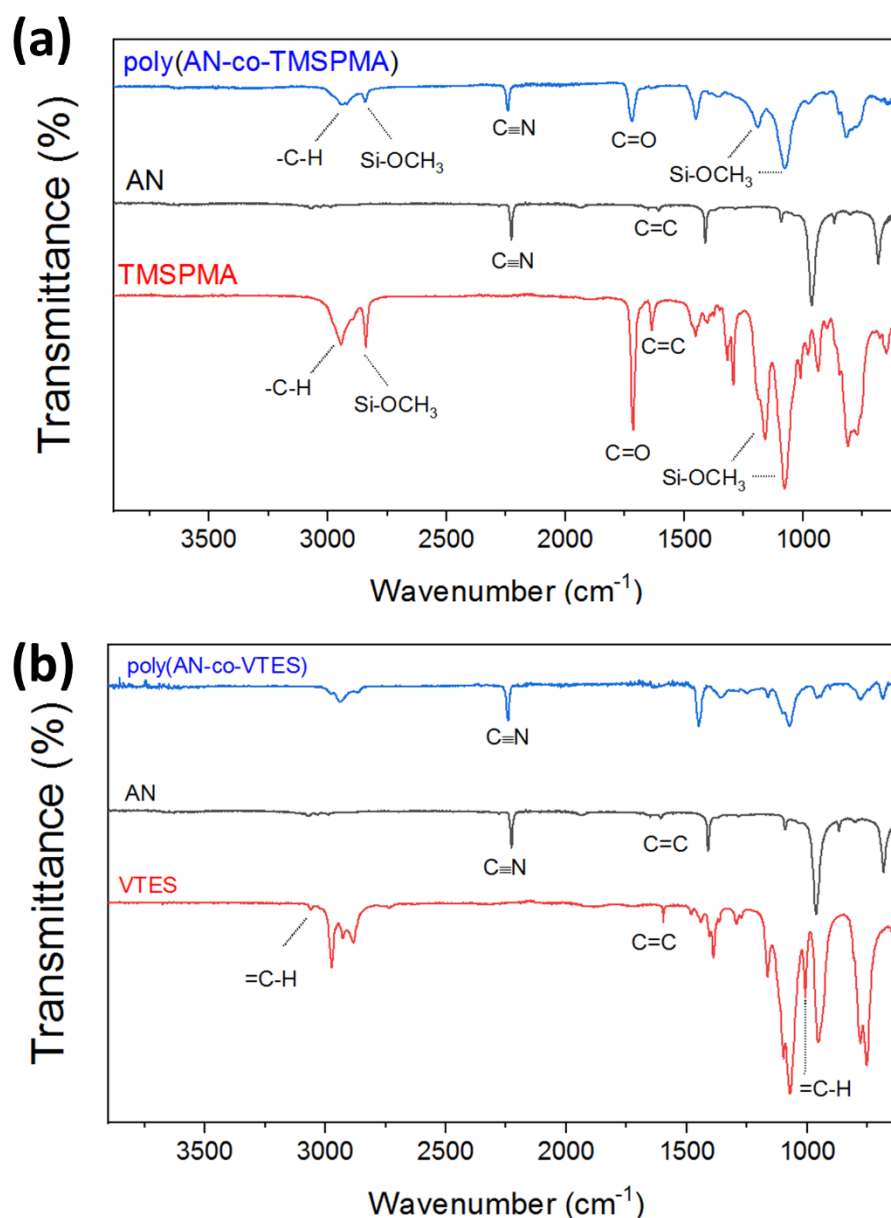


Figure 5.3. IR spectra of the synthesized (a) poly(AN-*co*-TMSPMA) and (b) poly(AN-*co*-VTES) copolymers.

The  $^1\text{H}$  NMR spectra of the synthesized copolymers are shown in Figure 5.4. Based on the shielding effect of the electrons, the protons covered with less electron density (connected to an electronegative atom) have a higher resonance frequency (i.e., higher chemical shift). Also, the integration values of the peaks were used as a guide to assign the peaks to each proton properly (Figure 5.4). In Figure 5.4a, if we assume that  $m = 1$ , then there should exist 2 type A protons. This way, the integration of peak G (assigned to acrylonitrile moiety) gives 11.56 type G protons. The incorporation of TMSPMA moiety in the poly(AN-*co*-TMSPMA) is calculated as:

$$\text{mol\% TMSPMA} = \frac{1}{1 + 11.56} \times 100 = 7.96 \quad \text{Equation 5.4}$$

Similarly, in Figure 5.4b, by assuming  $m = 1$ , the integration of A-type protons is 9. Then the integration of E-type protons is 67.02. The share of VTES moiety in poly(AN-*co*-VTES) is then calculated as:

$$\text{mol\% VTES} = \frac{1}{1 + 67.02} \times 100 = 1.47 \quad \text{Equation 5.5}$$

The fiber diameter in both cases was in the 200-400 nm range, as shown in Figure 5.5. The subsequent thermogravimetric analysis under air showed 5.93 wt.% inorganic content for poly(AN-*co*-TMSPMA) and 2.94 wt.% inorganic content for poly(AN-*co*-VTES). Since the inorganic content incorporated in the copolymers was low, they were not subjected to carbonization.

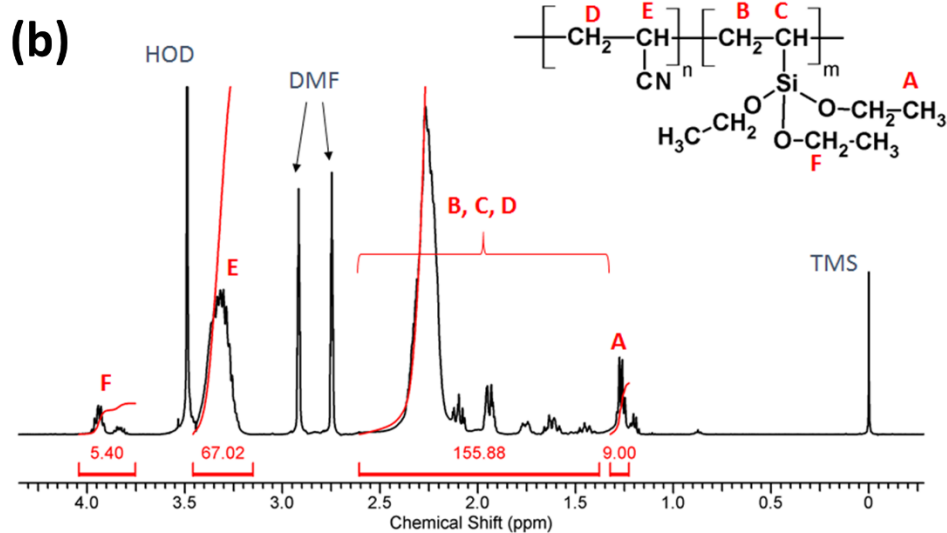
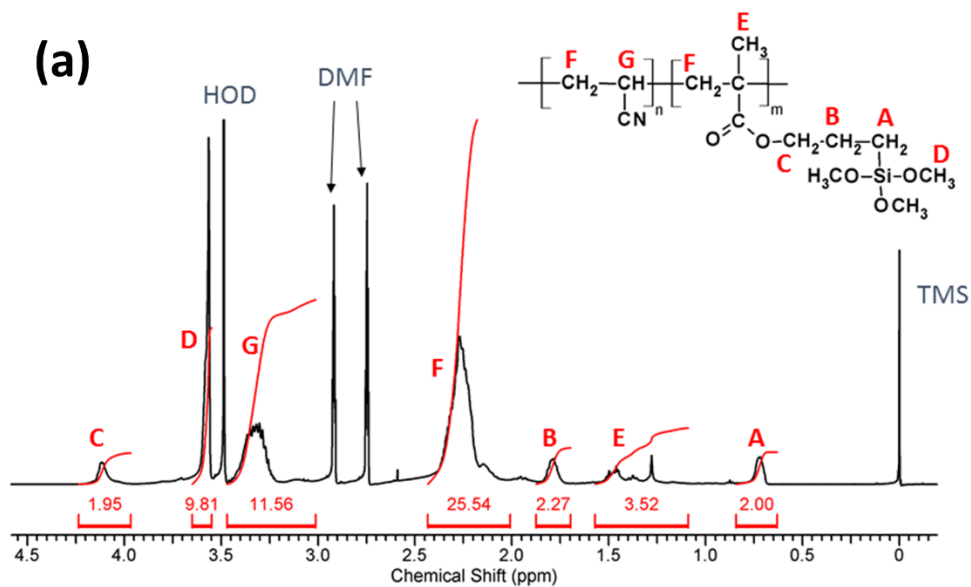


Figure 5.4.  $^1\text{H}$  NMR spectra of the synthesized (a) poly(AN-*co*-TMSPMA) and (b) poly(AN-*co*-VTES) copolymers.

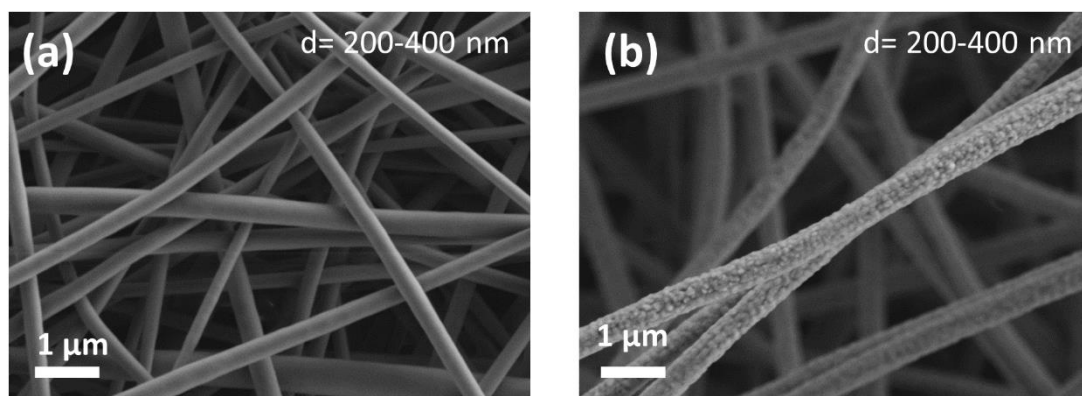


Figure 5.5. Morphology of the fibermats made from (a) poly(AN-*co*-TMSPMA) and (b) poly(AN-*co*-VTES) copolymers.

### 5.3.2 Homopolymers and producing blend nanofibers

Figure 5.6 shows the comparison between the IR spectra of VTES and PVTES. We observe the disappearance of C=C-associated absorptions after the polymerization reaction. Although the C=C absorptions are disappeared according to the FTIR spectra, the presence of left-over monomer VTES was confirmed according to the  $^1\text{H}$  NMR spectrum of the homopolymer and its comparison with that of the monomer (Figure 5.7). We observe a decrease in the ratio of olefinic protons (C and D) accompanied by forming of secondary and tertiary protons. Tertiary protons (C') are shielded by electropositive atoms (Si), so they appear at lower chemical shifts compared to secondary protons (D'). Bulk polymerization is prone to contain left-over monomers.

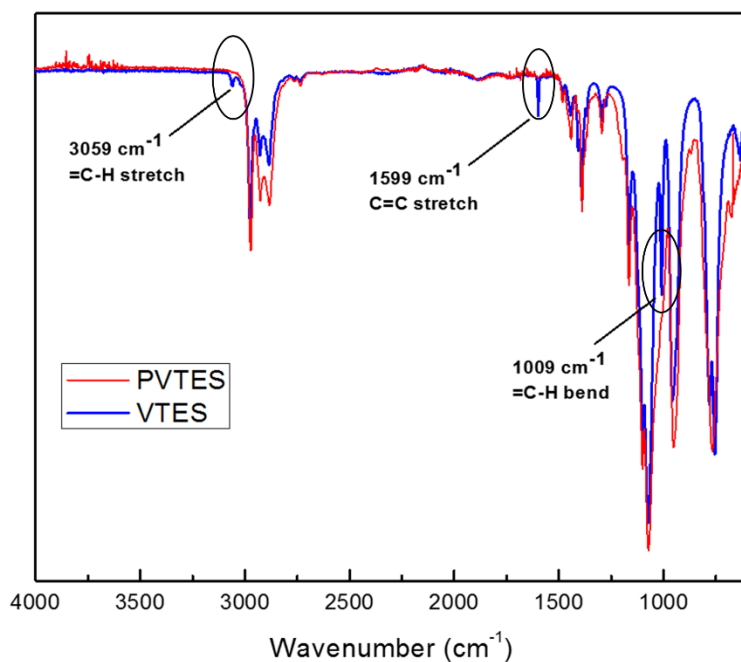


Figure 5.6. The IR spectra of VTES and PVTES

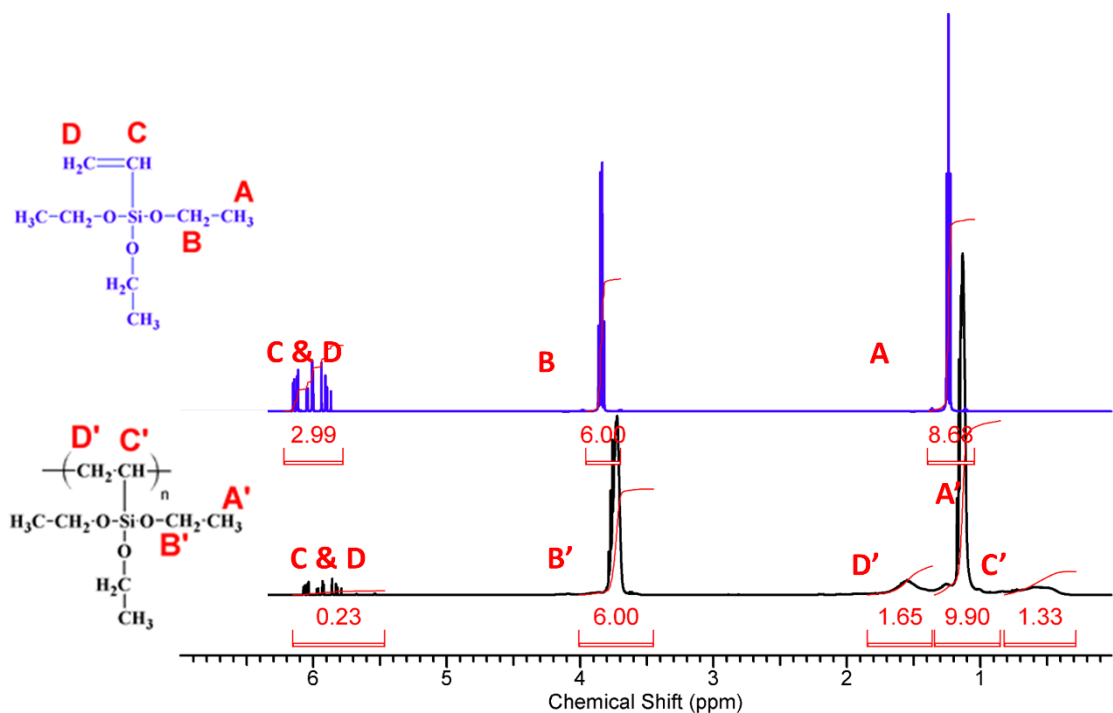


Figure 5.7.  $^1\text{H}$  NMR spectra of the VTES and (bulk-polymerized) PVTES

The polymeric fibers of PAN-PVTES had a diameter of less than 1  $\mu\text{m}$  (Figure 5.8 (a)). The resulting carbonized fibers contained  $\sim 7.6$  wt.% of inorganic content ( $\text{SiO}_x$ ) that was distributed evenly in the fiber, as shown in Figure 5.8. The low inorganic content showed that probably the amount of PVTES in the stock solution was not as much as predicted. This can be due to the presence of left-over monomer in the synthesis.

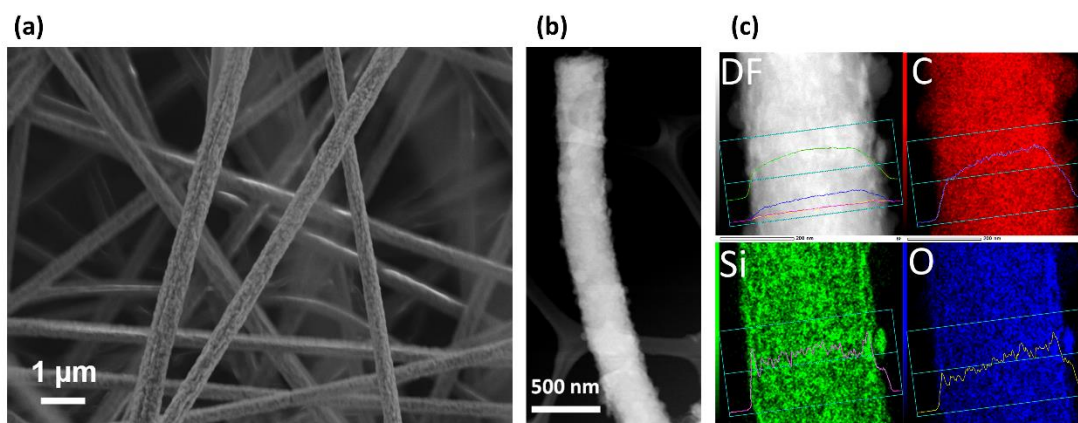


Figure 5.8. (a) Electrospun PAN-PVTES 1:1 fiber mat and, (b) its dark-field TEM micrograph after carbonization ,and (c) its corresponding elemental maps for carbon, silicon, and oxygen (scale bars show 200 nm).

Figure 5.9 shows the comparison between the IR spectra of TMSPMA and pTMSPMA. The disappearance of C=C absorption can be seen in the case of pTMSPMA. Also, in Figure 5.10, the disappearance of olefinic protons that appear above 5.5 ppm region and formation of secondary and tertiary protons below 2 ppm region. Unlike bulk polymerization of PVTES, for this synthesis, the pTMSPMA does not contain any residual monomer.

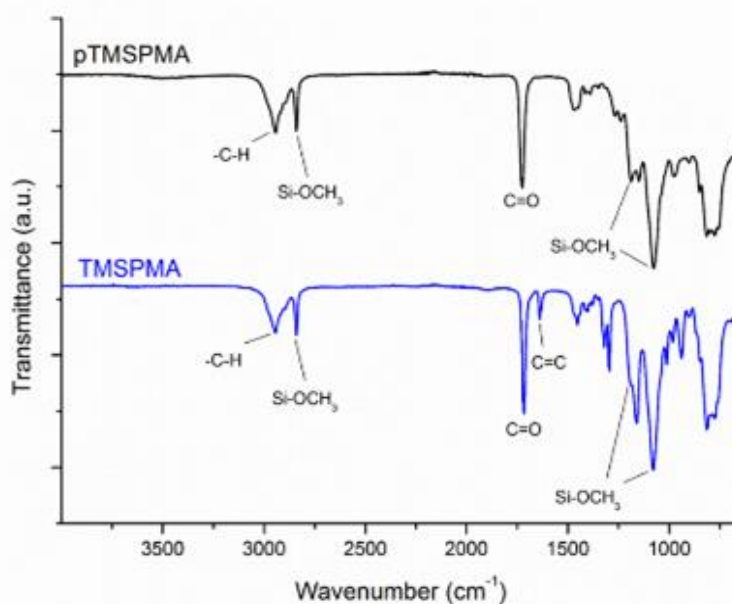


Figure 5.9. The IR spectra of TMSPMA and pTMSPMA

The morphology of the resulting fiber mat is shown in Figure 5.11a. The STEM-EDS elemental map of carbonized fibers (Figure 5.11) shows a fine spatial distribution of carbon, silicon, and oxygen. The thermogravimetric analysis (TGA) under air showed that this carbonized fiber mat contained 32.3 wt.% inorganic content. In addition, the IR spectrum of TGA residue resembled that of SiO<sub>2</sub>. The Raman spectrum of this sample did not show the presence of any elemental silicon (Figure 5.12). Only D-band and G-band attributed to the amorphous carbon contents were present.

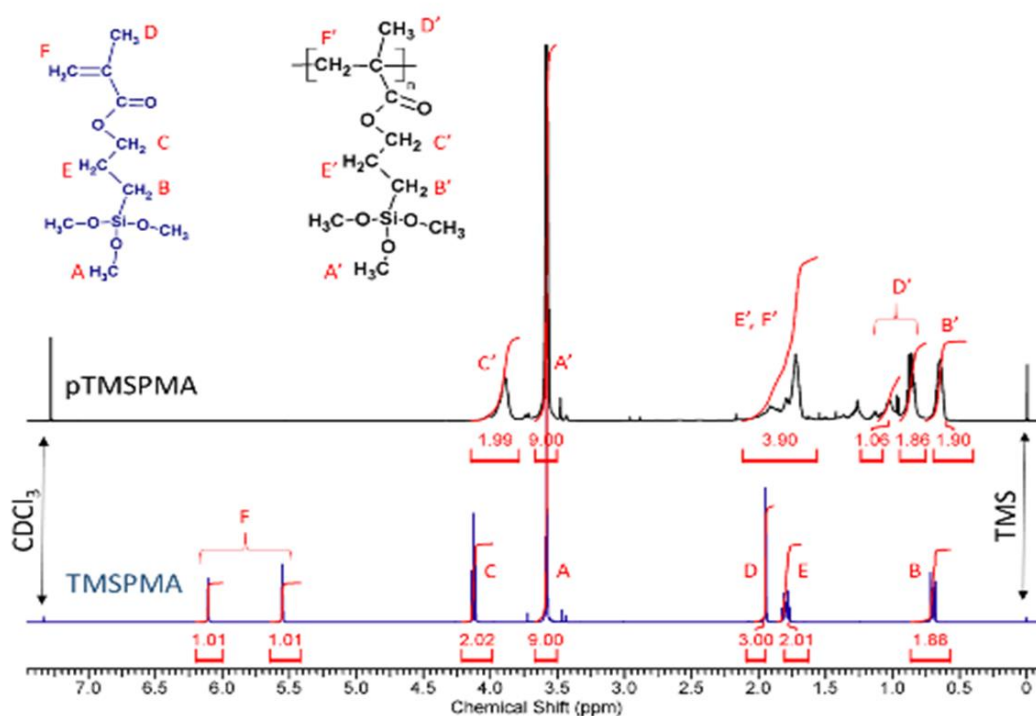


Figure 5.10. <sup>1</sup>H NMR of TMSPMA and pTMSPMA (NMR in deuterated chloroform).

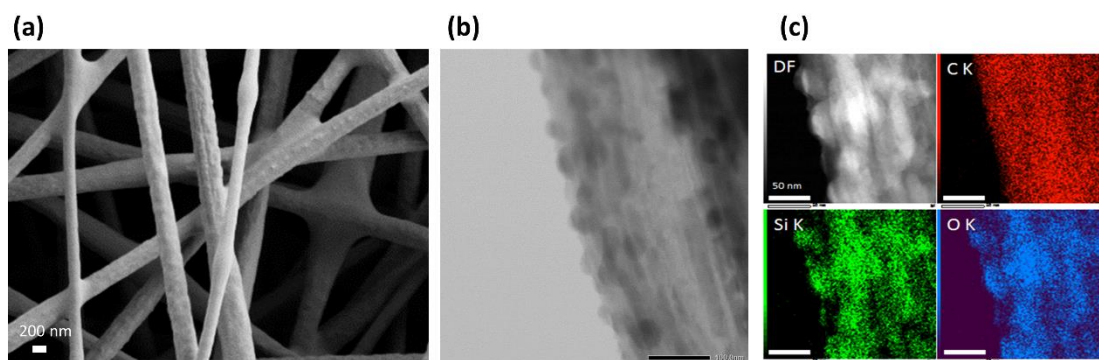


Figure 5.11. (a) Electrospun PAN-pTMSPMA 1:1 fiber mat, and (b) its TEM micrograph after carbonization (scale bar shows 100 nm), and (c) its STEM-EDS elemental distribution maps of carbon, silicon, and oxygen (scale bar shows 50 nm).

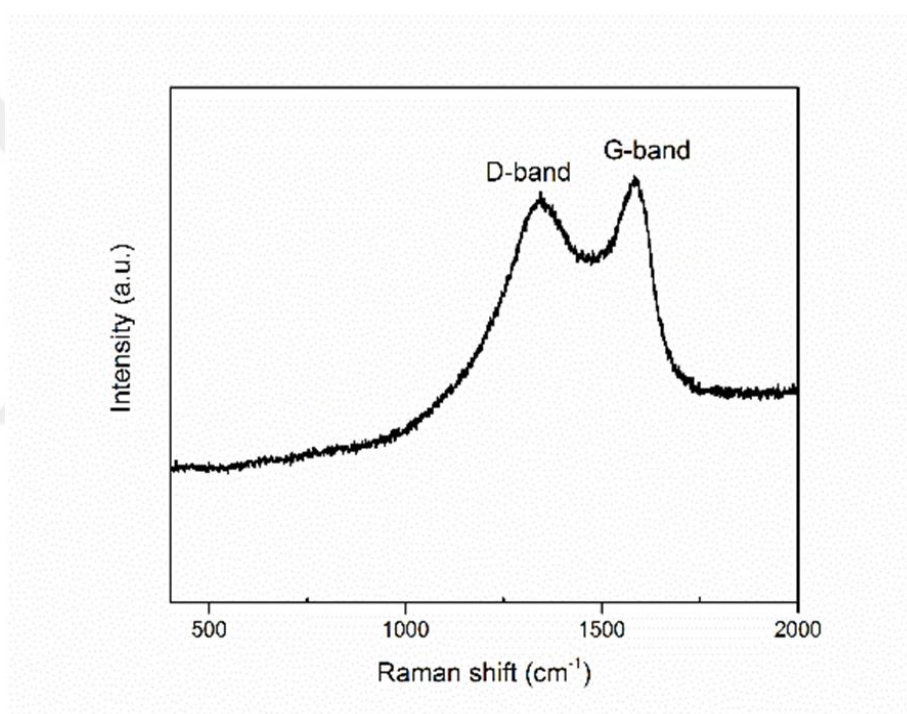


Figure 5.12. Raman spectrum of carbonized fiber mat synthesized from electrospun PAN-pTMSPMA 1:1

Since the inorganic content of this composite fiber sample was significant (32.3 wt.%), we tested it in a half-cell. The free-standing carbonized fiber mats were applied as the working electrodes in half-cells, with Li chip as the counter (and reference electrode). The electrolyte used was a 1 M solution of  $\text{LiPF}_6$  in a mixed EC:DEC (1:1) solvent. The cyclic voltammogram (in 0.005- 3V cut-off voltage window) is shown in Figure 5.13 and shows that no lithiation-delithiation of silicon/silicon oxide has taken place. The galvanostatic charge-discharge also showed low specific capacities, confirming that silicon oxide that was incorporated in the fibers could not go through alloying-dealloying with lithium.

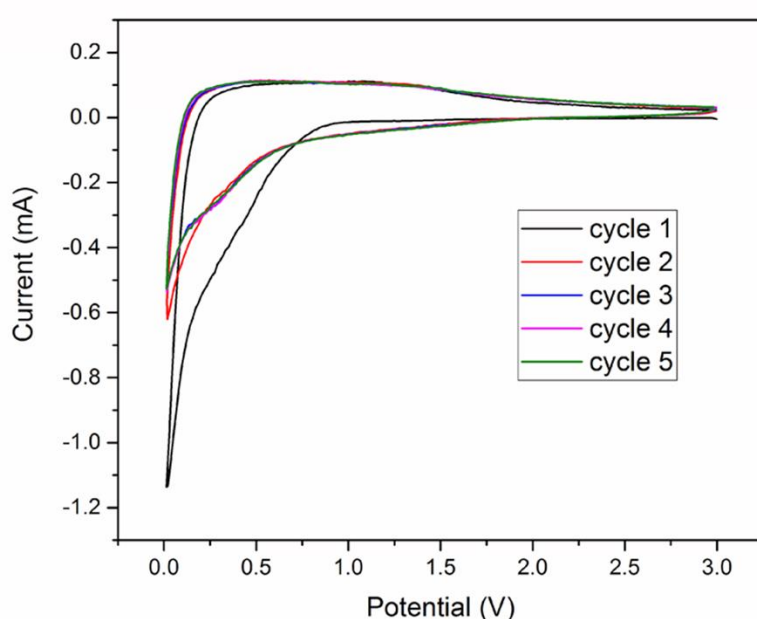


Figure 5.13. Cyclic voltammogram (under  $0.1 \text{ mV s}^{-1}$ ) of the half-cell made of C- $\text{SiO}_2$  derived from PAN-pTMSPMA mixture (in 0.005- 3V cut-off voltage window)

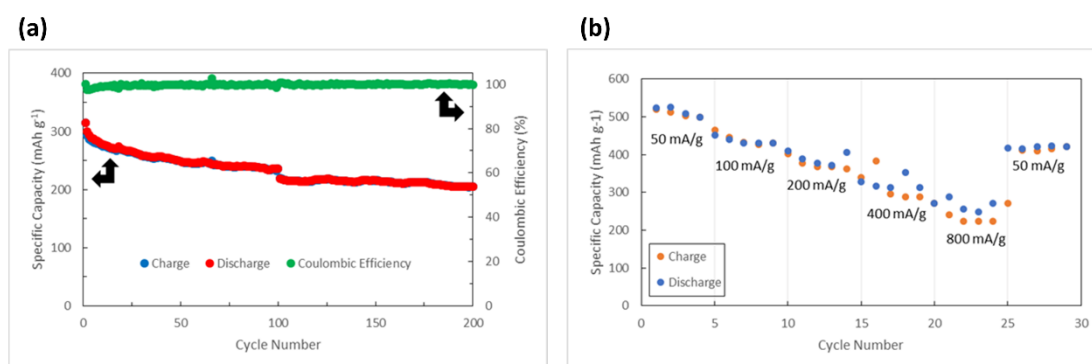


Figure 5.14. (a) The galvanostatic charge-discharge (under  $500 \text{ mA g}^{-1}$ ) and (b) the rate performance of the half-cell made of C- $\text{SiO}_2$  derived from PAN-pTMSPMA mixture (in 0.005- 3V cut-off voltage window)

### 5.3.3 Hybrid nanofibers

Electrospinning of the solution of TEOS-sol and PAN successfully yielded hybrid PAN-SiO<sub>2</sub> fibers without significant bead formation. (Figure 5.15). A small amount of spindle-shaped beads were observed when the solution with the highest SiO<sub>2</sub> content was used.

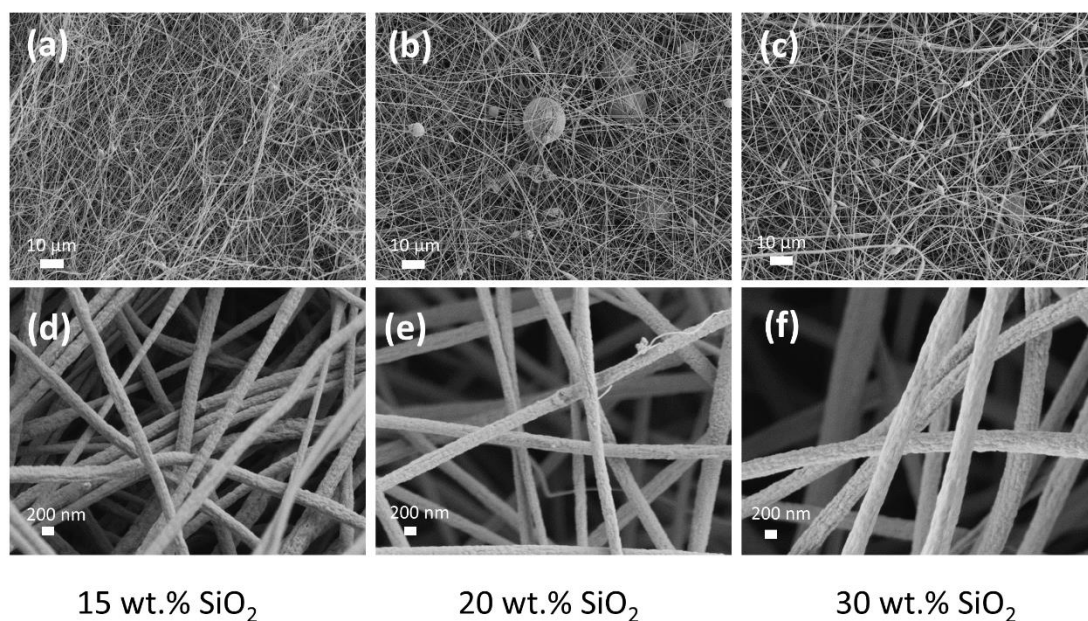


Figure 5.15. Micrograph of the fibers produced through different PAN-SiO<sub>2</sub> hybrids

Comparison of the IR spectra of the prepared hybrid materials (Figure 5.16) showed that fibermats with higher theoretical inorganic content show higher absorption associated with Si-O-Si. Moreover, thermogravimetric analysis of hybrid PAN-SiO<sub>2</sub> materials showed that the theoretical amount of inorganic content correlated well with the amount of residual mass measured after heating under air (Figure 5.17). Namely, we observed a residual mass of 10.19, 14.65, 19.94, and 26.79 wt.% for the theoretical SiO<sub>2</sub> content of 10, 15, 20, and 30 wt.%, respectively. These measurements indicated that we have control over the amount of SiO<sub>2</sub> incorporated through hybrid synthesis.

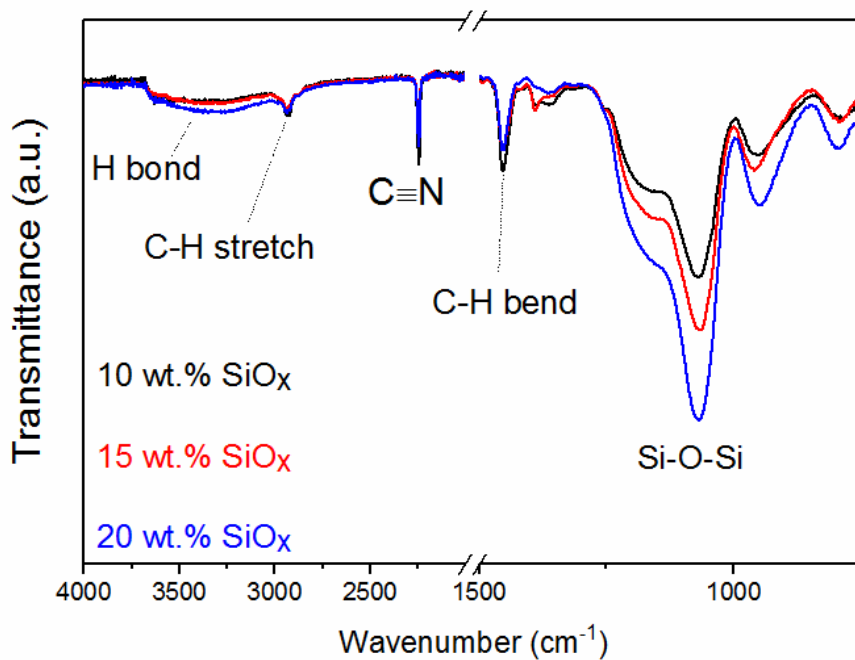


Figure 5.16. The comparison between the IR spectra of the different PAN-SiO<sub>2</sub> hybrids with different nominal SiO<sub>2</sub> content

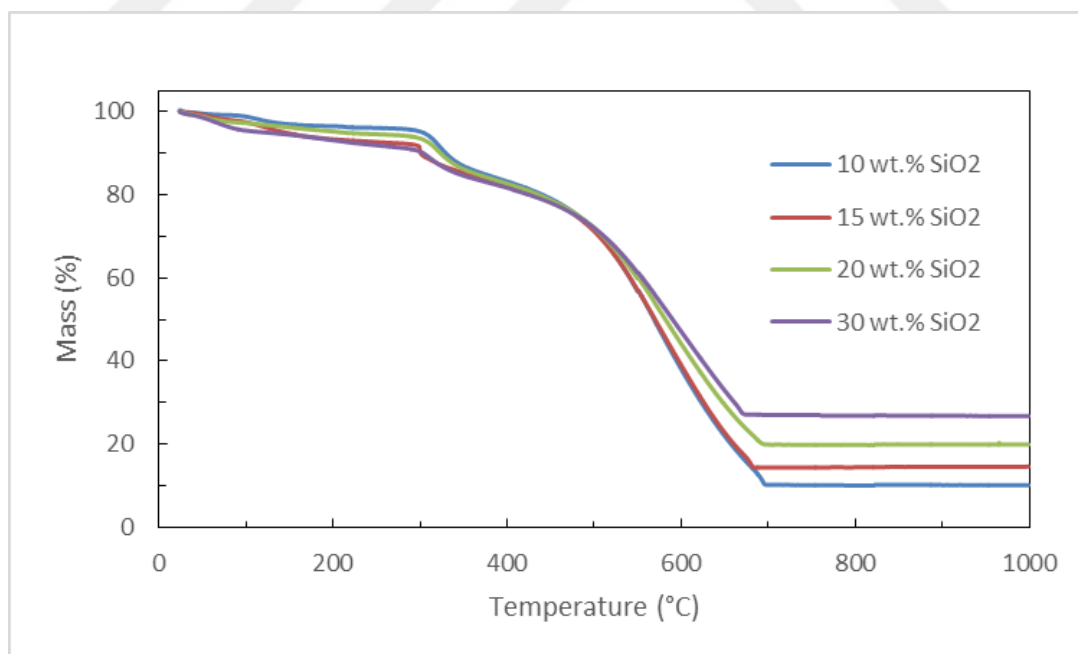


Figure 5.17. Thermogravimetric analysis of the hybrid PAN-SiO<sub>2</sub> materials under air (10 K min<sup>-1</sup> heating rate)

The resulting carbonized fiber mats contained 38 wt.%, 46 wt.%, and 52 wt.% of SiO<sub>2</sub> according to the thermogravimetric analysis. X-ray diffraction patterns of the

carbonized fibermats showed completely amorphous structures (Figure 5.18a). In addition, Raman spectroscopy showed the presence of D-band at  $1342\text{ cm}^{-1}$  and G-band at  $1587\text{ cm}^{-1}$  (with equal intensity), indicative of the presence of amorphous carbon. The  $I_D/I_G$  ratio did not show any correlation with  $\text{SiO}_2$  content. It means that the inorganic  $\text{SiO}_2$  content did not affect the carbonization and long-range order of the amorphous carbon. No sign of elemental silicon was observed in the Raman spectra (Figure 5.18b).

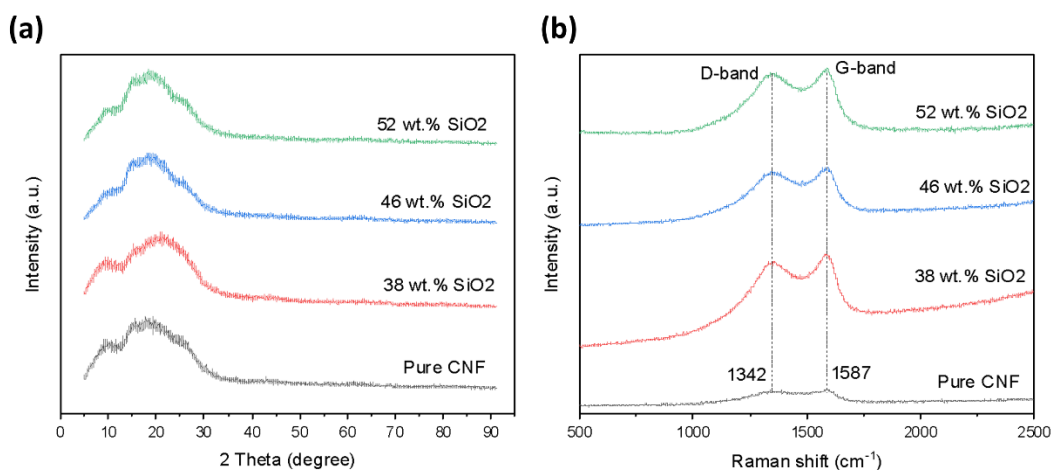


Figure 5.18. The X-ray diffraction pattern and Raman spectra of the carbonized hybrid structures

Free-standing electrodes were punched from carbonized fiber mat and used as the working electrodes against Li foil in a half-cell. Except for the first cycle, that is related to SEI formation (Kitz et al., 2020), the cyclic voltammogram (Figure 5.19) did not show any peaks indicating the reaction of  $\text{SiO}_2$  with lithium. In addition, the specific capacity values (Figure 5.20) were also low, confirming that  $\text{SiO}_2$  did not undergo an alloying-dealloying reaction with Li.

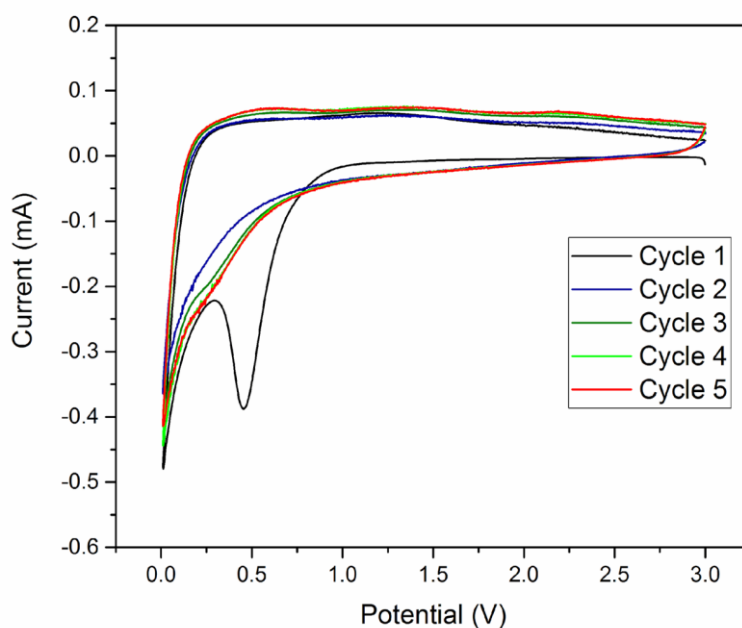


Figure 5.19. Cyclic voltammogram (under  $0.1 \text{ mV s}^{-1}$ ) of the half-cell made of C-SiO<sub>2</sub> derived from PAN-SiO<sub>2</sub> with nominal 30wt.% SiO<sub>2</sub> (in 0.005- 3V cut-off voltage window)

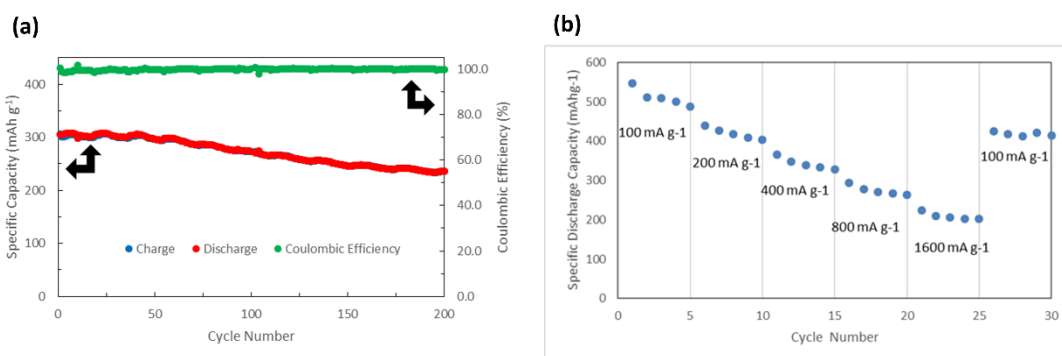


Figure 5.20. (a) The galvanostatic charge-discharge (under  $500 \text{ mA g}^{-1}$ ) and (b) the rate performance of the half-cell made of C-SiO<sub>2</sub> derived from PAN-SiO<sub>2</sub> with nominal 30wt.% SiO<sub>2</sub> (in 0.005- 3V cut-off voltage window)

A comparison of the long-term retention of specific capacities of lithiation (discharge) for free-standing C-SiO<sub>2</sub> fibermats from different hybrid PAN-SiO<sub>2</sub> compositions is shown in Figure 5.21. The specific capacity increased with the increase of SiO<sub>2</sub> content. However, none of the compositions showed superior specific capacity compared to the reference sample that was carbon nanofiber mat without any SiO<sub>2</sub> content.

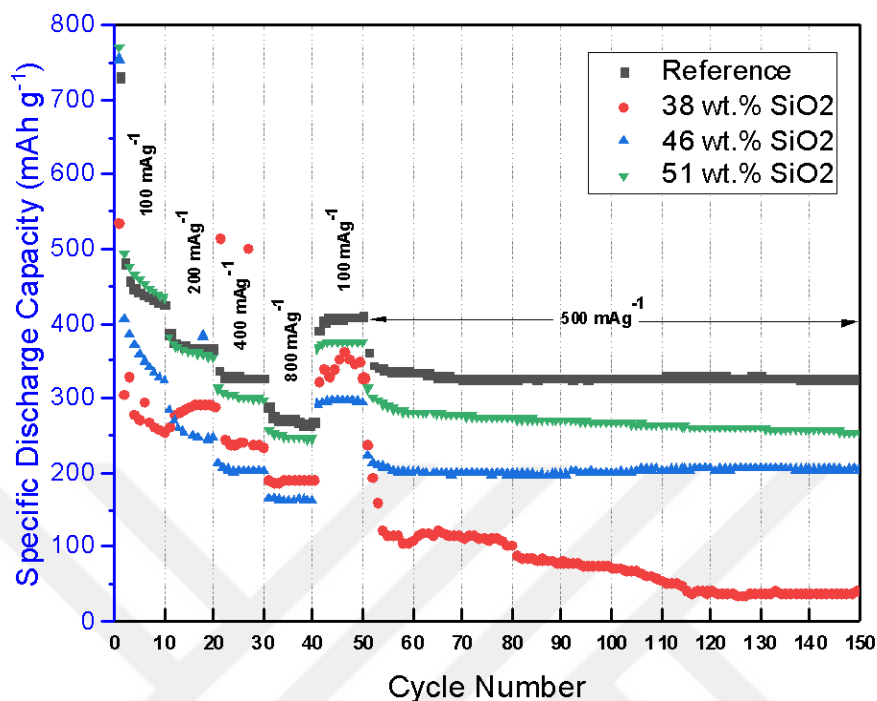


Figure 5.21. Comparison of the long-term retention of specific capacities of lithiation (discharge) for free-standing C-SiO<sub>2</sub> fibermats from different hybrid PAN-SiO<sub>2</sub> compositions (in 0.005- 3V cut-off voltage window). The current rates are shown on the plot.

## 5.4 Discussion

We incorporated silicon in polyacrylonitrile fibers through 3 different routes: (1) synthesis of copolymers of acrylonitrile and silicon-containing monomers, (2) blending of silicon-containing homopolymers with polyacrylonitrile, and (3) synthesis of hybrids of siloxane oligomers and polyacrylonitrile.

The stock solutions of pTMSPMA and PVTES, even if stored in the fridge, were prone to gelation. This was the main reason that we sought simpler methods for preparing the electrospinning solutions.

Synthesis of SiO<sub>2</sub> sol from organometallic molecules such as tetraethylorthosilicate (TEOS) has typically been carried out in aqueous solutions

(Novak, 1993). With acid catalysis, the sol will gradually turn into a gel if heated. However, if the sol is added to a preformed organic polymer solution (as we demonstrated for the case of PAN), gelation can be further slowed down. This is the principle of the synthesis of Type I hybrid materials that include “carrying out the inorganic hydrolysis and condensation reactions in the presence of a preformed organic polymer” (Novak, 1993). We have applied this principle to fabricate hybrid electrospun nanofibers. Acid-catalyzed and polycondensed TEOS formed in-situ SiO<sub>2</sub> nanodomains directly inside a polymer matrix during electrospinning. A well-blended mixture of C and SiO<sub>x</sub> through a fine mix of their precursors was obtained after carbonization of the polymeric fibers.

Comparison of the electrochemical properties of different carbonized C-SiO<sub>x</sub> fibermats (Figure 5.14 and Figure 5.21) showed that the reference sample without SiO<sub>x</sub> shows superior specific capacities compared to all other compositions. It indicates that the silicon phase in the fibers is relatively inactive with respect to lithium. The silicon suboxides (SiO<sub>x</sub>), depending on the value of x (0 < x < 2), can react (alloy-dealloy) with Li-ions in a reversible (for x = 0) or irreversible (for x = 2) way (Takezawa, Iwamoto, Ito, & Yoshizawa, 2013). This is because SiO<sub>x</sub> can be described by thermodynamically stable phases of Si and SiO<sub>2</sub>, which react with Li reversibly and irreversibly respectively as:



SiO<sub>x</sub> in C-SiO<sub>x</sub> nanofibers described in this chapter were synthesized from VTES, TMSPMA, and TEOS. TEOS is known to be condensed into a network of amorphous SiO<sub>4</sub> tetrahedra. The other two monomers also contain 3 alkoxy groups bonded to the silicon, which can be condensed similarly to TEOS. The high-temperature processing (stabilization of fibermats at 280°C under air) could have led to the formation of SiO<sub>2</sub> in the carbonized fibers. Therefore, the SiO<sub>2</sub> phase in carbon fibers that were derived from PAN-PVTES and PAN-pTMSPMA blend fibermats could not undergo electrochemical alloying-dealloying of the C-SiO<sub>x</sub> fibermats.

The hybrid synthesis route offered more experimental convenience to synthesize C-SiO<sub>2</sub> fibers, and since the inorganic phase was SiO<sub>2</sub>, the lithium storage capacity of the C-SiO<sub>2</sub> sample was also low. The cycling experiments of the C-SiO<sub>2</sub> fibers (Figure 5.21) showed an increase in the specific capacity with increasing SiO<sub>2</sub> content although

it is expected to observe a decrease in the specific capacity since  $\text{SiO}_2$  is an inactive phase. , It is speculated that the  $\text{SiO}_2$  could have been reduced in the cell at low-current (slow) lithiation rates as reported elsewhere (Lepoivre et al., 2016). Nonetheless, the  $\text{SiO}_2$  in these composite fibers must be reduced to silicon using chemical routes to obtain high-capacity electrode materials.



## Silicon Nanocrystals-embedded Carbon Nanofibers from Hybrid Polyacrylonitrile – TEOS Precursor as High-performance Lithium-ion Battery Anodes

**Abstract:** The high capacity of silicon (Si) for lithium intake has made it a promising anode material for lithium-ion batteries; however, pulverization of Si due to huge volume change during lithiation/delithiation leads to drastic capacity loss during cycling. Nanostructured Si and its nanocomposites with carbon have been shown to be effective in addressing low cyclability. In this study, we report an efficient method for the synthesis of a nanocomposite containing Si nanodomains homogeneously embedded in an electrically conductive carbon nanofiber (CNF) network. Electrospinning of polyacrylonitrile (PAN) solution containing hydrolyzed tetraethoxysilane (TEOS), as a Si precursor, and subsequent carbonization of hybrid nanofibers yielded a composite of SiO<sub>2</sub> ultrafine nano-domains in carbon network (C-SiO<sub>2</sub>). Low temperature molten salt-assisted aluminothermic reduction of C-SiO<sub>2</sub> nanofibers allowed us to obtain C-Si/SiO<sub>x</sub> nanocomposite without forming SiC, which is thermodynamically favorable at high temperatures in a system with a high interfacial surface area between the carbon and SiO<sub>2</sub> phases. Nanocomposite C-Si/SiO<sub>x</sub> anode showed a reversible capacity of 860 mAh g<sup>-1</sup> at a current rate of 200 mA g<sup>-1</sup> retaining its capacity of 680 mAh g<sup>-1</sup> after 100 cycles. In addition, the nanocomposite anode delivered a reversible capacity of 569 mAh g<sup>-1</sup> at a current rate of 400 mA g<sup>-1</sup> and maintained 95% of its capacity after the subsequent 100 cycles. This study demonstrates the capability of designing nanocomposite anodes from precursors and the use of low-temperature aluminothermic reduction that results in a material with small-sized Si nanodomains uniformly dispersed in the carbon matrix, which could address the cyclability issue of the silicon-based anodes.

## 6.1 Introduction

Silicon is an attractive material for the anode in lithium-ion batteries (LIBs) due to its low delithiation potential (0.4 V), high gravimetric and volumetric capacity, and abundance in nature (Ashuri et al., 2015; Obrovac & Chevrier, 2014). However, its use for storage of lithium ions poses limitations to long-term reliable performance. In service, lithiation/delithiation cycles induce volume expansion/contraction of silicon that generate high mechanical stress and leads to pulverization (Matthew T. McDowell et al., 2013; Zuo et al., 2017). Solid electrolyte interphase (SEI), an inevitable by-product of reduction of electrolyte on the newly exposed silicon surface, undergoes breaking and regrowth during cycling (Peled & Menkin, 2017). The consumption of mobile Li ions in the SEI leads to capacity loss and a degradation in capacity retention (Obrovac, 2018; L. Wang et al., 2020; H. Wu et al., 2012). Moreover, the low intrinsic electrical conductivity of silicon contributes to the sluggish kinetics of its lithiation (Ashuri et al., 2015; Zuo et al., 2017).

To mitigate Si electrode degradation, nanoscale silicon and its encapsulation in a carbon matrix offer a possible solution. Nano-sized particles are less prone to pulverization, compared to micron-sized particles, due to the lower density of defects in their structure (M. T. McDowell et al., 2013; Z.-L. Xu, Liu, Luo, Zhou, & Kim, 2017). Encapsulation in a mechanically strong and conductive carbon matrix, meanwhile, protects the electrolyte from decomposition on the Si surface and the consequent decrease in interparticle electrical resistance (Ashuri et al., 2016; N. Liu et al., 2014).

Because the SEI formed on carbon through contact with state-of-the-art electrolytes is known to be stable (Peled & Menkin, 2017), there is compelling motivation to prepare silicon nanoparticles embedded in a carbon matrix (Kitz et al., 2020). Carbon nanofibers (CNFs) have been widely preferred carbon materials for fabricating composite anodes due to their large surface area, excellent electrical conductivity, and structural stability, as well as the ease of incorporating nanoparticles. Composite nanofiber scaffolding is commonly produced via electrospinning of carbon precursors containing Si—either in the form of commercial Si nanoparticles or Si-containing chemicals, such as TEOS (T. H. Hwang, Y. M. Lee, B. S. Kong, J. S. Seo, & J. W. Choi, 2012; B. Zhang et al., 2016). The direct addition of Si nanoparticles into the

polymer solution before electrospinning generally results in agglomerated particles in the carbon nanofiber (CNF) matrix or even on the surface of the CNFs, exposing the Si directly to reaction with the electrolyte (Ji & Zhang, 2009; Y. Li et al., 2013). It was shown that functionalizing the Si surface ensured uniform dispersion of Si nanoparticles in the CNF matrix, which in turn improved cycle stability (Z.-L. Xu et al., 2014). Alternatively, by initially forming the hybrid nanocomposite structure as a precursor (Novak, 1993), the uniform distribution of silicon was ensured across the CNF matrix.

To this end, acid-catalyzed hydrolysis and polycondensation of TEOS have been used in the in-situ formation SiO<sub>2</sub> nanodomains directly inside a polymer matrix, which can serve as a carbon precursor (Cengiz, Ansari Hamedani, Hayat Soytas, & Demir-Cakan, 2019; Maçon et al., 2015; Owens et al., 2016). Initially, there were no particles, but instead, short Si-O-Si oligomer chains had formed as a well-blended mixture of C and Si through a fine mix of their precursors. Subsequent metallothermic reduction of such finely mixed composite precursor of C-SiO<sub>2</sub> would produce a homogenous dispersion of Si in a C matrix.

Thermodynamic analysis reveals that during high-temperature metallothermic, e.g. magnesiothermic, reduction of C-SiO<sub>2</sub> compounds, SiC formation has a significantly larger driving force, compared to the SiO<sub>2</sub> reduction (Ahn et al., 2016). However, SiC does not interact with lithium ions, and its presence solely leads to a decrease in specific capacity (Kannan et al., 2016; Timmons et al., 2007). The development of temperature-control during metallothermic reduction of SiO<sub>2</sub> using heat scavenging salts (Ansari Hamedani, Ow-Yang, & Hayat Soytas, 2021; Favors et al., 2014; X. Liu et al., 2012; Miao et al., 2020), and low-temperature aluminothermic reduction with AlCl<sub>3</sub> (Jia et al., 2020; Song et al., 2018), allows for better control over the temperature and consequent phase evolution (N. Lin, Han, Wang, et al., 2015; N. Lin, Han, Zhou, et al., 2015).

In this study, we used a combination of acid-catalyzed polycondensation and electrospinning to obtain the polyacrylonitrile-silica (PAN-SiO<sub>x</sub>) nanofiber precursor. The nanofibers obtained were stabilized by dehydrogenation and cyclization of PAN (B. Zhang et al., 2016) and carbonized to form CNF mats with a uniform and fine dispersion of silica nanodomains. To increase the lithium-storage capacity, we reduced the SiO<sub>2</sub> to Si through a low-temperature aluminothermic reduction with AlCl<sub>3</sub>. We

validated the electrochemical performance of the material in lithium-ion battery (LIB) half-cells, via cyclic voltammetry (CV), galvanostatic charge-discharge, and impedance spectroscopy analyses.

## 6.2 Materials and Methods

### 6.2.1 Synthesis of Active Materials

Precursor fibers were synthesized by electrospinning from a DMF solution containing PAN and TEOS. Specifically, we added 0.87 g TEOS to 11.4 g of N,N-dimethylformamide (DMF) under stirring. We then added 83  $\mu\text{L}$  of a 1 M HCl solution to the mixture as a condensation reaction catalyst. After 30 minutes of stirring under 500 rpm, we added 1 g of polyacrylonitrile (PAN Mw: 150,000) to the mixture and left it under stirring at 80°C for 24 hours until complete dissolution. Electrospinning of this PAN-SiO<sub>x</sub> solution was under 12 kV, with a tip to collector distance of 20 cm and a solution feeding rate of 0.800 ml hr<sup>-1</sup>.

To stabilize the electrospun fibermats, we performed heat treatment at 200°C for 2 hours under air, followed by carbonization at 800°C under an Ar atmosphere, to produce C fibers decorated by silica particles (C-SiO<sub>2</sub>). For aluminothermic reduction, we mixed 0.5 g of C-SiO<sub>2</sub> with 0.9 g of Al and 3 g of AlCl<sub>3</sub> in a mortar and pestle for 30 minutes and heated the mixture at 350°C for 15 hours under an Ar atmosphere (65 ml-MTI super-alloy high-pressure hydro-thermal reactor). The reduction product (C-Si/SiO<sub>x</sub>) was immersed in distilled water and 2 M of HCl solution, filtered and dried at 60°C. It should be noted that we did not use any form of pre-synthesized silicon nanoparticles, nor did we perform hydrofluoric acid etching of the final product. To compare the synthesis, we also performed magnesiothermic reduction. To this end C-SiO<sub>2</sub>, Mg powder (Sigma-Aldrich,  $\geq 99\%$ ), and sodium chloride (NaCl, Sigma-Aldrich, ACS reagent,  $\geq 99.0\%$ ), were mixed at a weight ratio of 1:0.8:10 for C-SiO<sub>2</sub>: Mg: NaCl, in a mortar for 15 minutes. The mixture was placed in a furnace with Ar atmosphere and with a heating rate of 3°C min<sup>-1</sup>, the it was heat-treated in an alumina crucible at 700°C

for 1.5 hours. Washing the byproducts and separation steps were the same as aluminothermic reduction.

### 6.2.2 Materials Characterizations

To characterize the synthesis products, we performed analyses of the molecular structure, mass change, electrospun mat morphology, and phase composition. Fourier-transform infrared (FTIR) spectra were recorded using a Nicolet iS10 FT-IR spectrometer operated in the ATR mode to investigate the formation of SiO<sub>2</sub> structure in hybrid PAN-SiO<sub>x</sub> electrospun fibers. Thermogravimetric analysis (TGA) was performed on a NETZSCH STA Jupiter 449 C instrument to quantify the total amount of inorganic contents (Si or SiO<sub>2</sub>) in the composite fibermats. The heating rate was set to 10°C min<sup>-1</sup> from room temperature up to 1000°C. The atmosphere used was dry air with a flow rate of 40 sccm.

The morphology of the fibers in each step of synthesis was observed under a field-emission scanning electron microscope (SEM; Zeiss LEO Supra 35 VP). To monitor the phase composition of the reduction reaction products, we performed XRD analysis (Bruker D2 Phaser), using Cu K $\alpha$  radiation and a Ni filter. The 2 $\theta$  scan range was 5°-90° and the step size 0.02°. Raman spectra were recorded using a 532 nm wavelength laser in a Renishaw InVia system to assess long-range order in C-Si/SiO<sub>x</sub> and C-SiO<sub>2</sub> fibers. To confirm the homogeneity of dispersion of Si NPs in the C-Si/SiO<sub>x</sub> fibers, the elemental distribution was assessed through energy-dispersive spectroscopy (EDS) using a JEOL Centurio system mounted on a spherical aberration-corrected scanning transmission electron microscope (STEM; JEOL JEM-ARM200CF) operated at 200 kV with a probe size of *ca.* 1 Å.

To determine the chemical oxidation state of Si in the fibers before and after reduction, X-ray Photoelectron Spectroscopy (XPS) was used in the range of 0-1150 eV of binding energy using an Al monochromatic X-ray source operating at 25.1 W (XPS-PHI 5000 VersaProbe).

### 6.2.3 Electrochemical Characterizations

To assess the electrochemical performance of the C-Si/SiO<sub>x</sub> fibers, we incorporated the fiber mats into the anode of lithium-ion battery half-cells. We mixed the C-Si/SiO<sub>x</sub> active material with carbon-black (TIMCAL SUPER C45- MTI) and carboxymethyl cellulose (CMC- MTI), as the binder, in a 1:1:1 weight percent ratio in water to form a slurry. The slurry was cast onto Cu foil of 10 μm thickness and then dried in a 70°C oven overnight. Circular discs of the working electrode (10 mm in diameter) were punched from the dried coated foils. The mass loading of active material was ca. ~0.31 mg cm<sup>-2</sup>.

We assembled half-cells in the Swagelok reactor vessel with a lithium chip as the reference and counter-electrode (in a 2-electrode configuration) in a glovebox under Ar environment (O<sub>2</sub> and H<sub>2</sub>O < 0.1 ppm). The electrolyte was prepared by dissolving 10 wt.% of fluoroethylene carbonate (FEC) (98%, Alfa Aesar) in a 1 M solution of LiPF<sub>6</sub> dissolved in a solvent mixture of ethylene carbonate (EC)-diethyl carbonate (DEC) (Sigma-Aldrich) with a 1:1 volume ratio. Each cell contained 100 μL of electrolyte. Celgard™ 2400 of 25 μm thickness was used as the separator. The half-cells assembled were characterized by cyclic voltammetry (CV) analysis, to evaluate the charge storage activity of silicon. We performed CV under 0.1 mV s<sup>-1</sup> under cut-off potentials of 1.5 V and 5 mV using PARSTAT-MC. To understand the ease of charge transfer in the working electrode, electrochemical impedance spectroscopy (EIS) was conducted in the same instrument at the specified cut-off potentials, between 100 kHz and 100 mHz with 10 mV of AC amplitude. Spectral analysis was performed using a linear Kramers-Kronig transformation tool ("Lin-KK tool"), and the Zview software to extract the equivalent circuit fit. The galvanostatic discharge-charge (lithiation-delithiation) of the half-cells was conducted between 1.5 V and 5 mV to assess capacity retention. C-SiO<sub>2</sub> nanofibers was also subjected to galvanostatic discharge-charge cycles as a reference.

### 6.3 Results

Figure 6.1(a) shows SEM images of the as-spun fibers, with diameter in the submicron range ( $962 \pm 131$  nm) and the absence of individual particles. FTIR spectra of the PAN-SiO<sub>x</sub> fibers (Figure 6.1b) revealed that Si-O-Si groups were present, in contrast to the pure PAN polymer (shown in red dashline). TGA (Figure 6.1c) revealed that at ca. 300°C, the thermal degradation of polyacrylonitrile started through dehydrogenation and cyclization of the polymer (Huang, Wei, Peng, & Lee, 2019). Further heating in air resulted in complete oxidative degradation of the polymer. From the thermogravimetric mass values, the inorganic content of the fibers was calculated to be  $\frac{16.6}{92.6}(100) = 17.9$  wt. %.

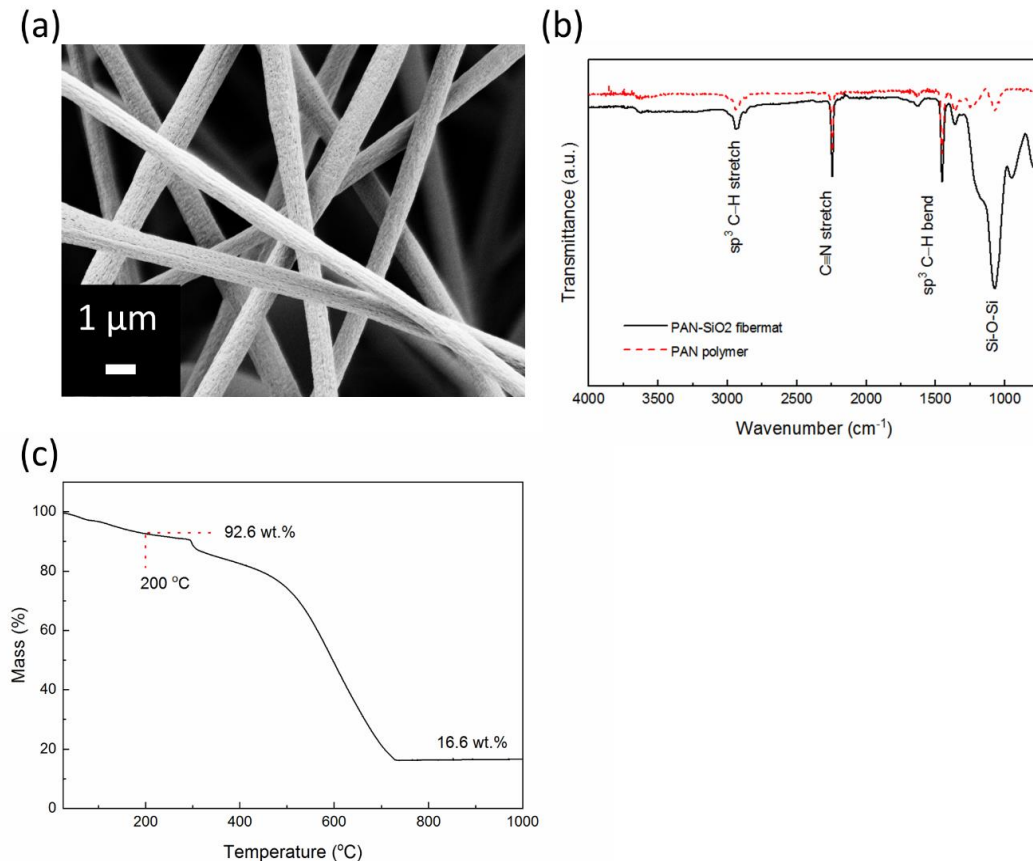


Figure 6.1. (a) SEM micrograph of PAN-SiO<sub>x</sub> hybrid nanofibers, (b) FTIR spectrum of PAN-SiO<sub>x</sub> nanofibers and pure PAN, and (c) TGA of PAN-SiO<sub>x</sub> nanofibers under air.

After undergoing stabilization and carbonization, the fiber diameter shrank to  $882 \pm 119$  nm (Figure 6.2a). No crystalline phase was observed in the C-SiO<sub>2</sub> product. In the X-ray diffractograms, only 2 broad peaks were observed at 22° and 43°, which were consistent with amorphous carbon {002} and {100} planes (Figure 6.2b). Thermograms (Figure 6.2c) of the carbonized fibers did not show a weight-loss step at ca. 300°C, as expected since the material cannot undergo further dehydrogenation and carbonization (B. Zhang et al., 2016). Calculation of the inorganic content indicated that the amount of SiO<sub>2</sub> in the C-SiO<sub>2</sub> fibermats was  $\frac{22.0}{91.2}(100) = 24.1$  wt. %. Analysis of the Raman shift spectra (Figure 6.2d) revealed the G-band and D-band scatterings of amorphous carbon at 1592 cm<sup>-1</sup> and at 1342 cm<sup>-1</sup>, respectively. The ratio of the intensity of the aforementioned peaks was used to assess the state of long-range order in the C-SiO<sub>2</sub> product. A ratio value close to 1 revealed that the carbon material was amorphous and had only short-range order (Blanco, Renman, Zhu, Vullum-Bruer, & Svensson, 2021). No additional scattering peaks aside from carbon were observed.

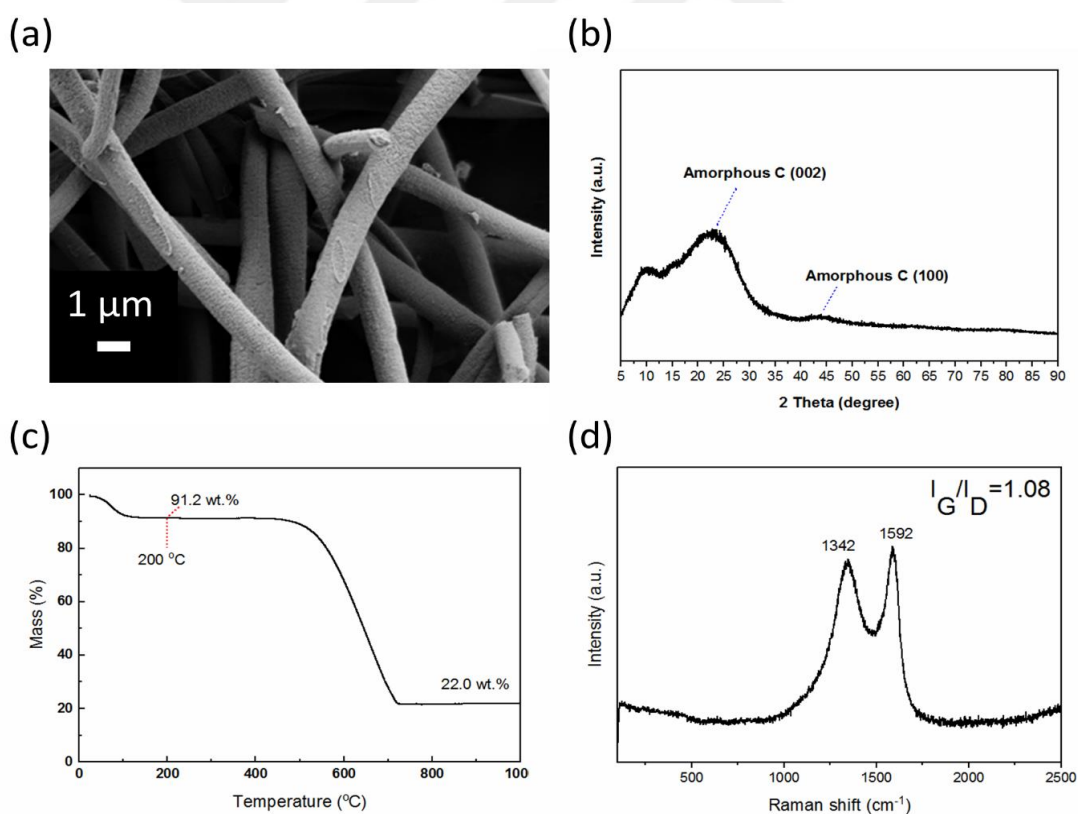


Figure 6.2. (a) SEM micrograph, (b) XRD pattern, (c) TGA (under air atmosphere), and (d) Raman spectrum of carbonized C-SiO<sub>2</sub> fibers.

After undergoing aluminothermic reduction in the presence of  $\text{AlCl}_3$ , the crystalline phases present were unreacted Al and  $\text{AlCl}_3$ ,  $\text{AlOCl}$  as the byproduct, and crystalline silicon, as shown in Figure 6.7a. Washing the product with distilled water removed  $\text{AlCl}_3$  and  $\text{AlOCl}$  (Figure 6.7b).

The morphology of the product after HCl treatment was revealed by secondary electron imaging, as shown in Figure 6.3(a). We obtained short fibers of carbon decorated with fine silicon particles. XRD analysis of the product (Figure 6.3b) showed elemental silicon peaks with a background of amorphous carbon resembling that shown in Figure 6.2b. To estimate the amount of silicon in the composite, we performed TGA under an air atmosphere. Because the dynamic step ( $10^\circ\text{C min}^{-1}$ ) was insufficient for complete oxidation of Si, we added an isothermal step of 4 hours at  $1400^\circ\text{C}$ . The thermogram (shown in Figure 6.3c) revealed an inorganic content of 25.6 wt.% at  $800^\circ\text{C}$ , which was increased to 32.7% after the isothermal holding step. The Raman spectrum (Figure 6.3d) of the composite material showed the same peaks associated with amorphous carbon (G-band peak at  $1592\text{ cm}^{-1}$  and D-band peak at  $1364\text{ cm}^{-1}$ ). However, the  $\frac{I_G}{I_D}$  ratio had increased slightly. The Si peak at  $512\text{ cm}^{-1}$  was also present. The distinguishable functional groups in the FTIR spectra of carbonized fibers and reduced carbonized fibers are shown in Figure 6.8. The stretching vibration of C=N in the ring at  $1580\text{ cm}^{-1}$  appeared in both samples. The Si-O-Si stretching vibration was also observed at  $1075\text{ cm}^{-1}$ , the intensity of which had decreased after aluminothermic reduction (Ashuri et al., 2016; Cengiz et al., 2019). STEM-EDS mapping of the fibers after aluminothermic reduction (Figure 6.9) revealed the elemental distribution in a composite fiber. The carbon distribution was uniform in the fiber, while silicon and oxygen appeared finely distributed in more localized domains.

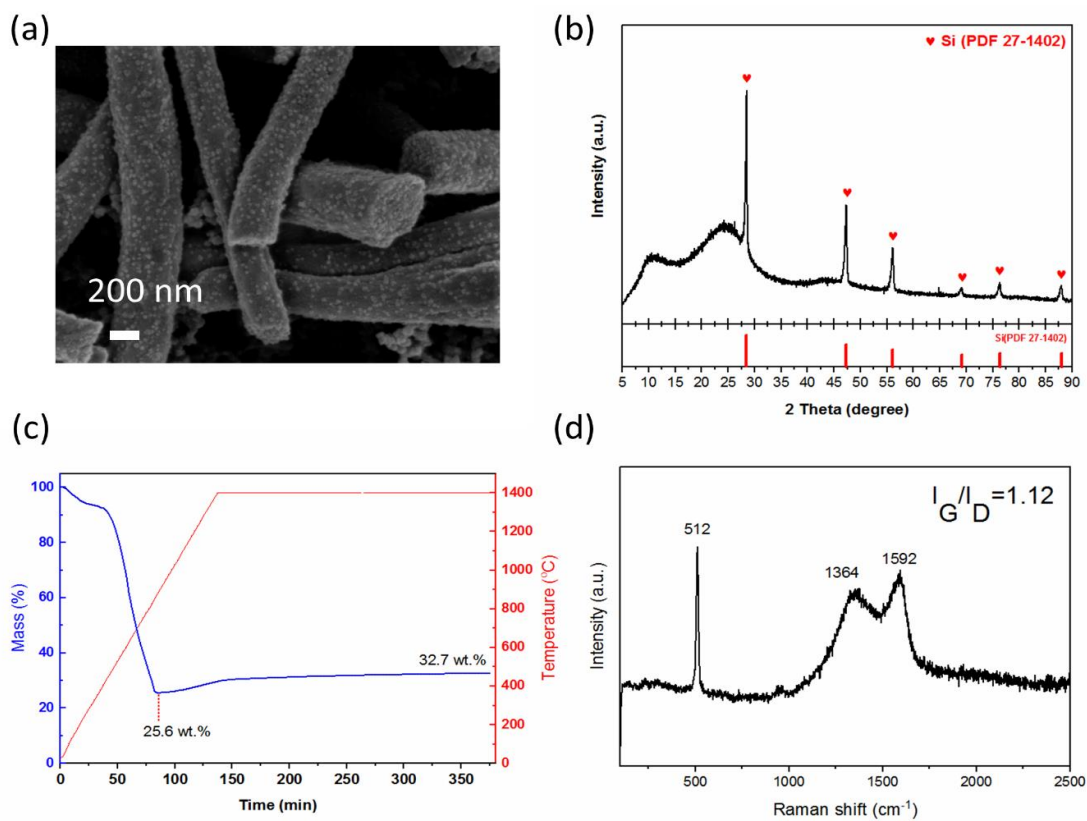


Figure 6.3. (a) SEM micrograph, (b) XRD pattern, (c) TGA (under air atmosphere), and (d) Raman spectrum of reduced C-Si/SiO<sub>x</sub> fibers.

Because SiC is known to form during the reduction of SiO<sub>2</sub> in the presence of C, magnesiothermic reduction of the same precursor composite fibers was also performed, to ascertain its absence in the aluminothermally reduced samples. Figure 6.4 shows the comparison of the XRD patterns of the reduced fibers of C-Si/SiO<sub>x</sub> through aluminothermic reduction (with Al-AlCl<sub>3</sub>) and the ones with magnesiothermic reduction (Mg-NaCl (as a reference)). This comparison revealed that in the case of magnesiothermic reduction, even in the presence of NaCl as a heat scavenger, an amorphous SiC phase was present.

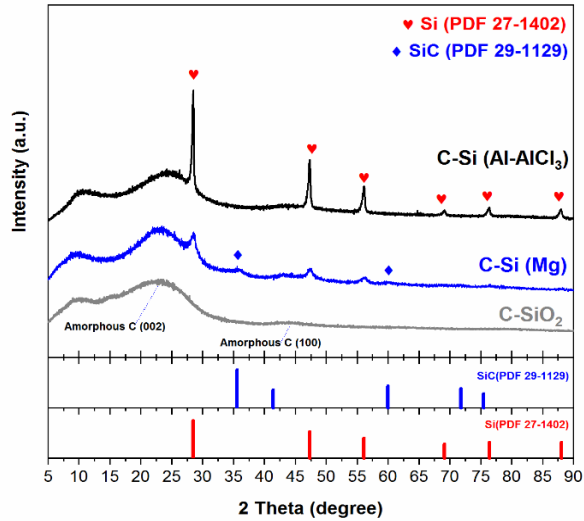


Figure 6.4. XRD patterns of carbonized fibers and the ones reduced via magnesiothermic and aluminothermic reduction.

Figure 6.5 shows the XPS O1s and Si2p region spectra of the carbonized fibers before and after aluminothermic reduction. Based on the known binding energies of tetrahedral structures  $\text{Si}(\text{O}_4)$ ,  $\text{Si}(\text{SiO}_3)$ ,  $\text{Si}(\text{Si}_2\text{O}_2)$ ,  $\text{Si}(\text{Si}_3\text{O})$ , and  $\text{Si}(\text{Si}_4)$ , the Si2p spectra of the carbonized fibers showed a single peak at  $\sim 103$  eV that corresponded to  $\text{Si}(\text{O}_4)$  structure. This fact indicated that before reduction, the non-carbon phase mainly consisted of  $\text{SiO}_2$  (Takezawa et al., 2013). However, after aluminothermic reduction as the Si-Si bonds formed, the prevalent binding energies shifted towards  $\text{Si}(\text{Si}_2\text{O}_2)$  and  $\text{Si}(\text{Si}_4)$  structures. This is also consistent with Figure 6.8, which shows a decrease in the absorption intensity associated with polar Si-O bonds. The full spectrum of the XPS is shown in Figure 6.10.

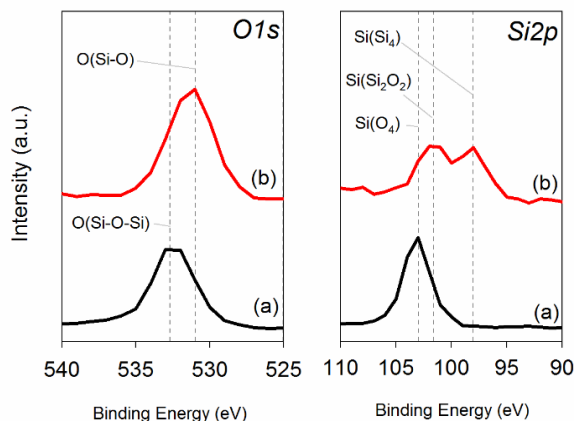


Figure 6.5. XPS spectra of O1s and Si2p of carbonized hybrid nanofibers (a) before and (b) after aluminothermic reduction.

Figure 6.6a summarizes the interaction of the C-Si/SiO<sub>x</sub> composite with lithium during cyclic voltammetry. The formation of a peak during lithiation at 0.19 V vs. Li<sup>+</sup> after the 1st cycle was observed. The delithiation was stepwise, and 2 significant peaks were observed at 0.33 V and 0.49 V. The active material and lithium reactivity increased after a few cycles. After the 5<sup>th</sup> cycle (the measurement was done for 10 cycles), the peak heights were stabilized. Figure 6.6b shows the Nyquist plots of the half-cell under cyclic voltammetry at 5 mV (lithiated state). The size of the semi-circles decreased as the cycle numbers increased. In Figure 6.6c, we present the quantification of the resistances corresponding to the equivalent circuit model (shown in the inset). The charge-transfer resistance decreased upon cycling. In Figure 6.6d, we show the voltage profiles of selected charging-discharging during cycling. The initial delithiation capacity at a current rate of 200 mA g<sup>-1</sup> was 860 mAh g<sup>-1</sup>, which decreased to 680 mAh g<sup>-1</sup> after 100 cycles, resulting in a capacity retention of 79%. During further cycling at 400 mA g<sup>-1</sup>, the initial delithiation capacity was 569 mAh g<sup>-1</sup> and sustained at 539 mAh g<sup>-1</sup> after 100 cycles, retaining 95% of its capacity. Because carbon-black (amorphous carbon) was active in the 5 mV-1.5 V range of voltage, we have excluded the contribution of carbon-black (Lepoivre et al., 2016). The capacity values for long cycling (Figure 6.6e) were reported after the carbon contribution was subtracted. C-SiO<sub>2</sub> composite fibers showed an initial delithiation capacity of only 239 mAh g<sup>-1</sup> and reversible capacity of 144 mAh g<sup>-1</sup> at a current of 100 mA g<sup>-1</sup> after 100 cycles (Figure 6.11).

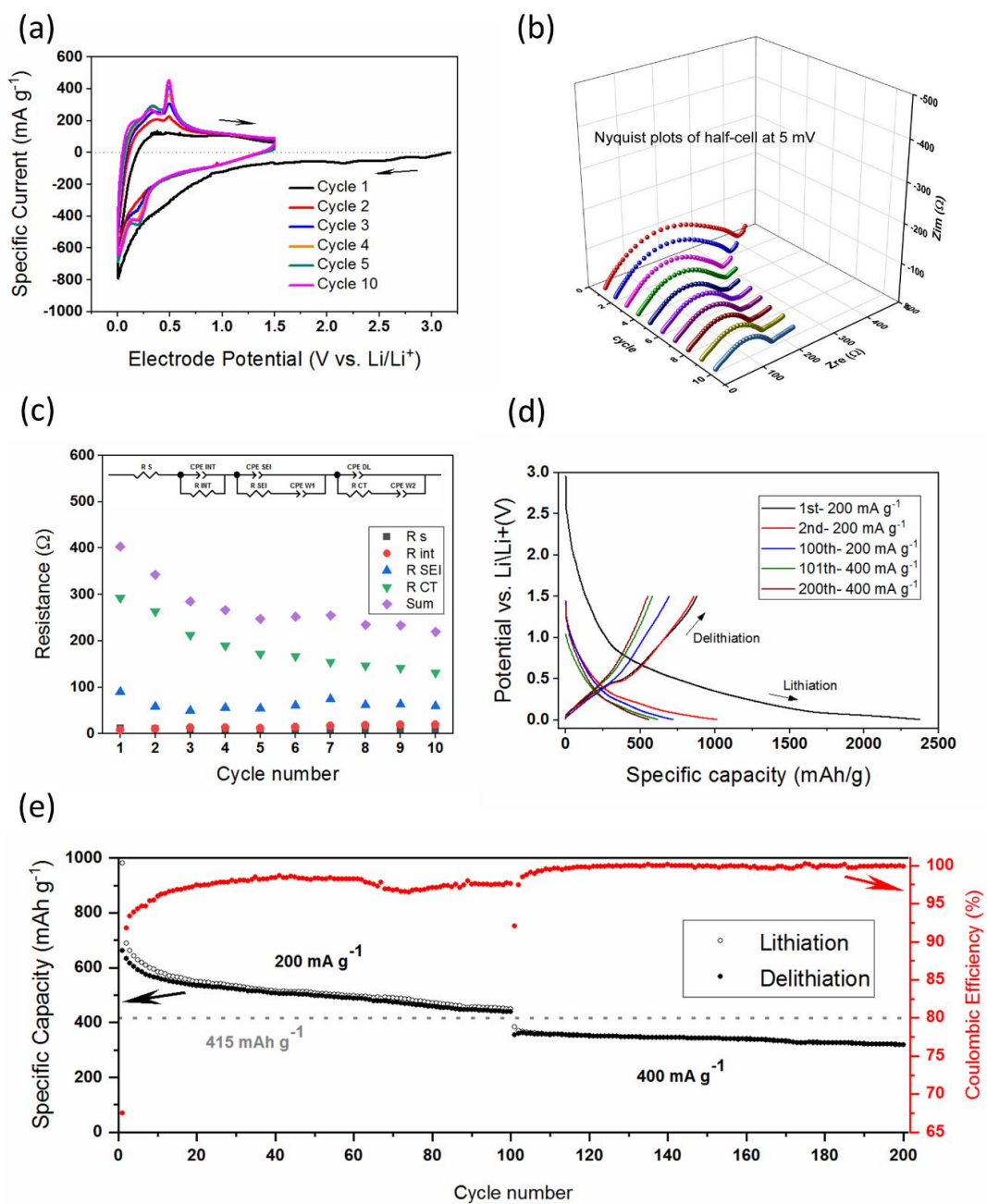


Figure 6.6. (a) Cyclic voltammograms (CV), (b) Nyquist plots vs. cycle numbers of CV, (c) the resistances extracted from fitting an equivalent circuit model (inset) vs. cycle numbers of CV ( $R_s$ : equivalent series resistance,  $R_{int}$ : interfacial resistance,  $R_{SEI}$ : SEI resistance,  $R_{CT}$ : charge-transfer resistance), (d) the voltage profiles of the selected cycles, and (e) cycling performance of the C-Si/SiO<sub>x</sub> material as the working electrode.

## 6.4 Discussion

Precursor fibers of the PAN-SiO<sub>x</sub> composite were produced through hydrolysis and polycondensation of TEOS and subsequent electrospinning of PAN-TEOS solution. The fibers were hybrid structures of PAN and siloxane oligomers, which were transformed into an intermixed structure of amorphous carbon and SiO<sub>2</sub> via a stabilization-carbonization process at 200°C and 800°C, respectively. Low-temperature reduction of C-SiO<sub>2</sub> using Al-AlCl<sub>3</sub> at 350°C led to the in-situ formation of Si particles at a nanoscale size in the CNF matrix, which was validated by STEM-EDS mapping showing the elemental distribution of Si and O-rich fine domains in the C matrix (Figure 6.9). Aluminothermic reduction of C-SiO<sub>2</sub> hybrid structure in the presence of AlCl<sub>3</sub> was specifically preferred to prevent the formation of SiC, which was possible in higher temperature processes, such as magnesiothermic reduction, especially when the contact area between silica and carbon is large (Ahn et al., 2016). From a thermodynamic point of view, in the magnesiothermic reduction of a C-SiO<sub>2</sub> composite, the formation of SiC at the interface of SiO<sub>2</sub> and C has a larger driving force (more negative  $\Delta G$ ) compared to the formation of Si and C phases (Ahn et al., 2016). Formation of the amorphous SiC phase was shown to be responsible for a significant drop in specific capacity of C-Si composites, because it is an inactive material for Li<sup>+</sup> ions (Timmons et al., 2007). Hence its formation should be avoided by choosing appropriate reduction conditions, such as temperature via the use of salts as heat-scavenger (Ansari Hamedani et al., 2021; X. Liu et al., 2012; Miao et al., 2020). Our C-SiO<sub>2</sub> nanocomposite was a finely mixed hybrid of carbon and SiO<sub>2</sub> with a large interface; so the formation of amorphous SiC was thermodynamically and kinetically favored. In fact, the presence of amorphous SiC phase was observed in the sample produced using magnesiothermic reduction in the presence of NaCl as a heat scavenger (Figure 6.4).

The electrochemical performance of C-Si/SiO<sub>x</sub> as a LIB anode was evaluated by means of CV, EIS and galvanostatic charge-discharge. Alloying and dealloying of Li with Si/SiO<sub>x</sub> were revealed by the characteristic peaks observed in CV of the half-cell. The magnitude of the peaks increased in the first few cycles and stabilized after 5 cycles, which indicated a further degree of alloying with the increasing number of cycles likely due to slow wetting of the electrode and/or activation of silicon. As the cell

potential was swept, the  $\text{Li}^+$  ions were transferred due to the gradient in electrochemical potential (Boettcher et al., 2020), but once their surface concentration reached the highest value (corresponding to the lowest potential), the direction of the sweep was reversed. Therefore, it took a few cycles (in CV) to observe the full activity of silicon. However, in the constant-current measurements, the specific capacity values decreased monotonically. The first onset in reduced current was at 0.9 V, corresponding to SEI formation, and was observed only in the first cycle. The overlapped cathodic peaks in the following cycles demonstrate the completion of SEI formation. The initial alloying reaction was evident by the presence of the peak at 0.19 V, consistent with the formation of  $\text{LiSi}$  (Reyes Jiménez et al., 2017), which was further lithiated as indicated by the peak at the lowest cut-off voltage (0.005 V). A 2-step delithiation had occurred, as demonstrated by the two characteristic peaks in the anodic branch. The peak at 0.33 V was attributed to dealloying of higher Li-containing Li-Si alloy ( $\text{Li}_{x+y}\text{Si}$ ), while the peak at 0.49 V was the dealloying of a lower Li-containing Li-Si alloy ( $\text{Li}_x\text{Si}$ ) (Bärmann et al., 2020). The EIS results showed that the overall internal resistance decreased during the first 10 CV cycles, which was more pronounced during the first 5 cycles and was indicative of slow stabilization of the SEI layer on the electrode surface (Guo et al., 2011).

The C-Si/ $\text{SiO}_x$  anode showed a reversible capacity of 439 mAh  $\text{g}^{-1}$  (excluding the contribution of carbon black) at a current rate of 200 mA  $\text{g}^{-1}$  ( $\sim C/2$ ) after 100 cycles, and 319 mAh  $\text{g}^{-1}$  at a current rate of 400 mA  $\text{g}^{-1}$  ( $\sim 1C$  rate) after subsequent 100 cycles with a capacity retention of 90%. It has been shown that for any value of  $x$ ,  $\text{SiO}_x$  can be written as  $\text{SiO}_x = (1-x/2) \text{Si} + (x/2) \text{SiO}_2$  (Takezawa et al., 2013). Through the TGA measurement under air (Figure 6.3c), the amount of each component in the C-Si/ $\text{SiO}_x$  composite was estimated. Complete oxidation of pure Si to  $\text{SiO}_2$  ( $\text{Si} + \text{O}_2 \rightarrow \text{SiO}_2$ ) was expected to lead to a  $\frac{32}{28} = 114 \text{ wt. \%}$  gain in mass (Lepoivre et al., 2016). Due to the weight increase of  $\frac{32.7-25.6}{25.6}(100) = \sim 28 \text{ wt. \%}$ , we concluded that the inorganic content in the composite contained  $\sim 25 \text{ wt. \%}$  Si and  $\sim 75 \text{ wt. \%}$  unreduced  $\text{SiO}_2$ . Accordingly, the composite will contain 74.4 wt.% amorphous carbon, 6.4 wt.% Si, and 19.2 wt.%  $\text{SiO}_2$ . The theoretical specific capacity was estimated, based on these calculated percentages of each component as:  $(0.744)(250 \text{ mAh/ g c}) + (0.064)(3579 \text{ mAh/ g si}) + (0.192)(0 \text{ mAh/ g siO}_2) = 415 \text{ mAh g}^{-1}$  (Lepoivre et al., 2016; Takezawa et al., 2013). Because we could not claim complete oxidation of the composite material

even after 4 hours of dwelling at 1400°C, the theoretical specific capacity value obtained was considered to be a lower-bound estimate. By comparing the measured specific capacity results (Figure 6.6e) to this value, we conclude that the inactive SiC phase was not present in the developed C-Si/SiO<sub>x</sub> composite that performed at its full potential as an anode active material (Timmons et al., 2007). In addition, the difference between the measured specific capacities of C-Si/SiO<sub>x</sub> and C-SiO<sub>2</sub> proves the successful reduction of SiO<sub>2</sub>, producing active Si for lithium-ion battery anodes. In this regard, the low-temperature aluminothermic reduction of SiO<sub>2</sub> embedded in CNF matrix showed promise for producing carbon-silicon hybrid anode materials without forming the inactive SiC phase. We attribute the high retention capacity retention of the C-Si/SiO<sub>x</sub> nanocomposite anode to the small size of the Si nanodomains, the homogeneity of their dispersion, and the ability of the carbon matrix to buffer the volumetric changes due to expansion and contraction of Si. As a comparison, for silicon nanoparticles of ~ 20 nm diameter (cycling data in the Figure 6.12), a 22% decrease in capacity was observed in only 5 cycles, when charged-discharged at a current rate of 200 mA g<sup>-1</sup>. The capacity-loss per cycle was 4.4% and 0.33% for silicon nanoparticles and C-Si/SiO<sub>x</sub>, respectively, proving the effective performance of the composite structure as a LIB anode material.

## 6.5 Conclusions

We investigated the production of finely mixed C-Si/SiO<sub>x</sub> nanocomposite fiber mats via acid-catalyzed polycondensation and electrospinning of the precursor followed by aluminothermic reduction in the presence of AlCl<sub>3</sub> and validation of their electrochemical performance as an anode active material in LIB half-cells. By starting with a Si precursor in a polymer solution, a homogeneous distribution of the Si/SiO<sub>x</sub> phase in the carbon matrix was achieved. The relatively lower temperature of aluminothermic reduction of C-SiO<sub>2</sub> in the presence of AlCl<sub>3</sub> enabled the production of C-Si/SiO<sub>x</sub> without forming SiC – an inactive phase for LIBs. The nanocomposite anode showed a reversible capacity of 860 mAh g<sup>-1</sup> (439 mAh g<sup>-1</sup> excluding the contribution of carbon black) after 100 cycles at a current rate of 200 mA g<sup>-1</sup>. At a higher current rate

of  $400 \text{ mA g}^{-1}$ , a reversible capacity of  $539 \text{ mAh g}^{-1}$  ( $319 \text{ mAh g}^{-1}$  excluding the contribution of carbon black) was observed after subsequent 100 cycles with a higher than 90% capacity retention, which was attributed to the small size of the Si nanodomains, the homogeneity of their dispersion, and the ability of the carbon matrix to buffer the expansion-contraction of Si.

## 6.6 Supporting Information

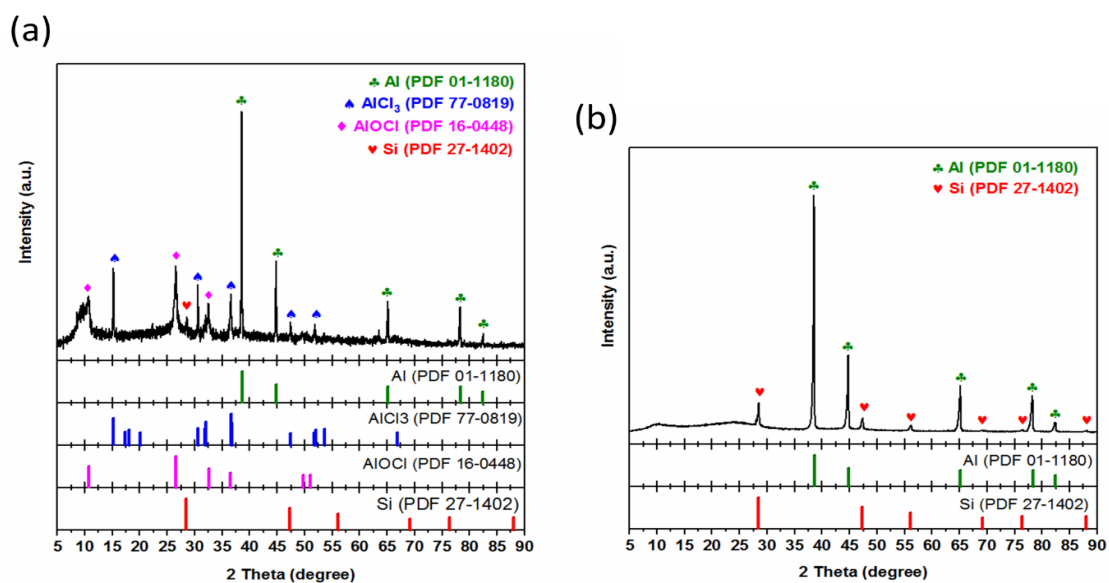


Figure 6.7. XRD phase analysis of (a) as-reduced powder, and (b) after washing with distilled water.

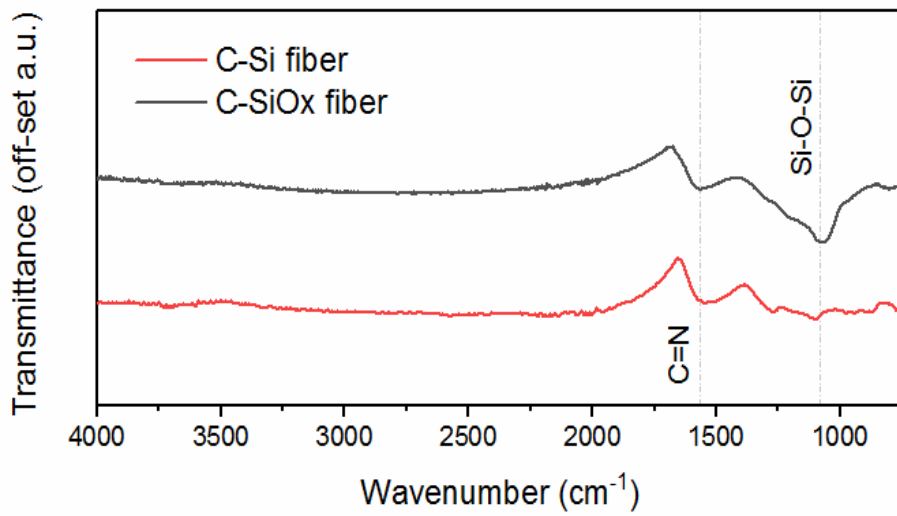


Figure 6.8. FTIR spectra of carbonized fibers before and after aluminothermic reduction.

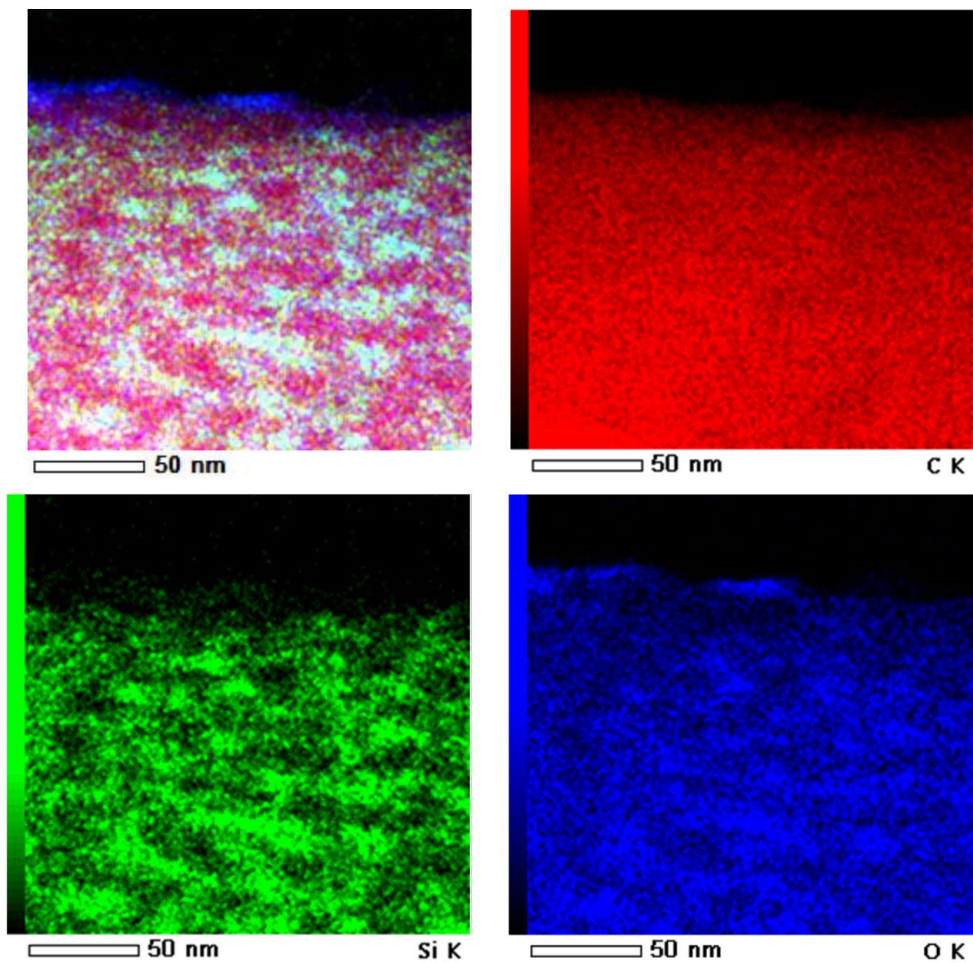


Figure 6.9. STEM-EDS mapping of elemental distribution on a C/Si short fiber.

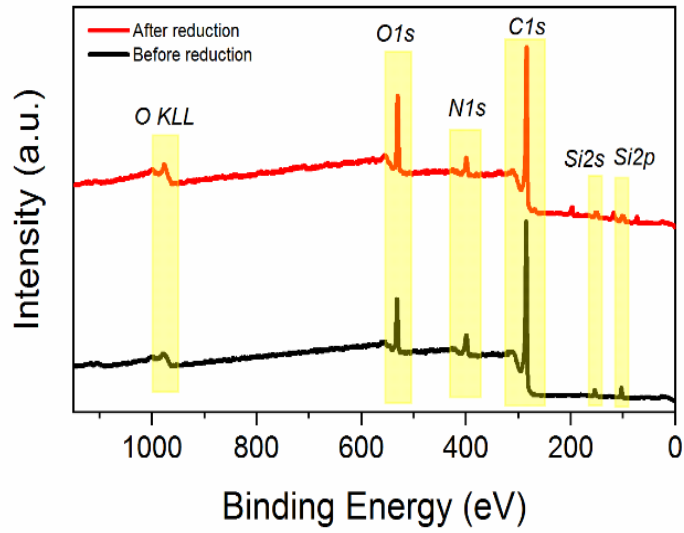


Figure 6.10. XPS survey spectra of carbonized fibers and their spectra after aluminothermic reduction.

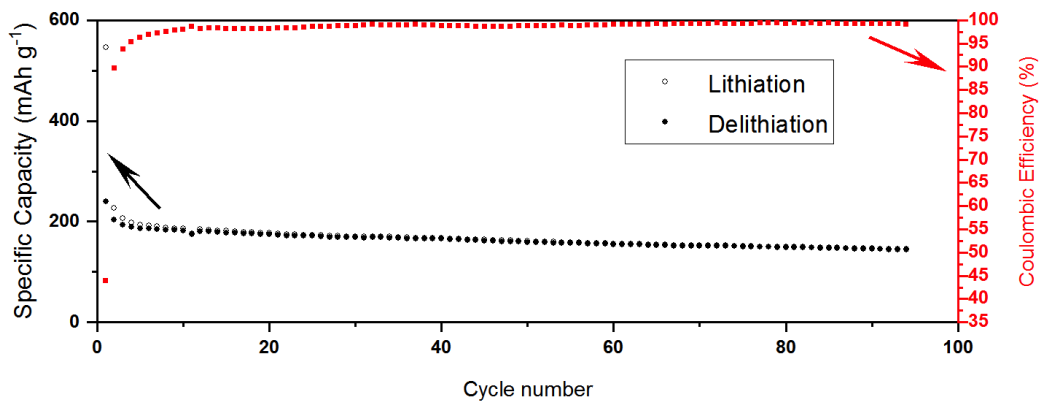


Figure 6.11. The galvanostatic charge-discharge cycling of the C-SiO<sub>2</sub> (before aluminothermic reduction)

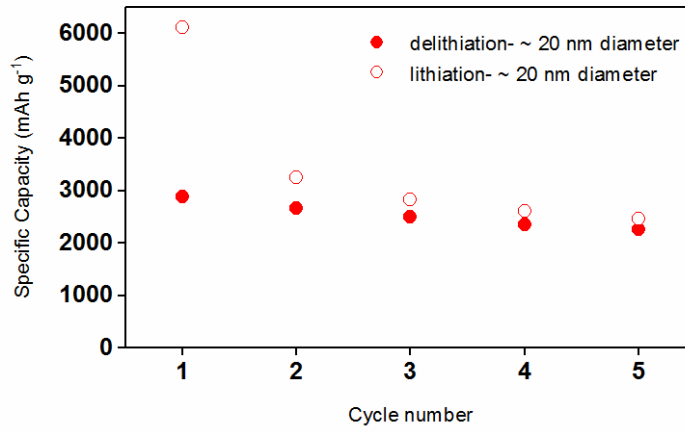


Figure 6.12. The first 5 cycles of an electrode containing Si nanoparticles at 200 mA g<sup>-1</sup> current rate.

## CHAPTER 7: Summary and Further Studies

The objective of this dissertation is to study the scalable synthesis and electrochemical behavior of Si and Si@C nanostructures as lithium-storage materials.

Our study in the synthesis of silicon showed:

- Through thermodynamic calculations, we estimated the upper bound for the temperatures of the products of magnesiothermic reduction reaction (using the adiabatic temperature estimation) in the presence and absence of NaCl as a heat scavenger. We showed that this upper bound temperature of the products decreases to 885°C with a NaCl: SiO<sub>2</sub> molar ratio of 10.28:1, while in its absence, it is 3088°C.
- For the synthesis of individual silicon nanoparticles through NaCl-mediated magnesiothermic reduction reaction (Mg-MRR), the time-resolved analysis of the phases showed the coexistence of 3 different simultaneous interfacial reaction pathways.
- Individual silicon nanoparticles compared to the 3-D Si networks (synthesized without heat-scavenging) showed higher impedance values. It is speculated that thicker SEI formation in the first 5 cycles (at 200 mA g<sup>-1</sup>) has led to faster lithium storage capacity fading in them.

Our study on the silicon incorporated into carbon nanofibers showed:

- We incorporated silicon in polyacrylonitrile through 3 different routes: (1) Synthesis of copolymers of acrylonitrile with silicon-containing moieties, (2) Blending silicon-containing homopolymers with polyacrylonitrile and (3) synthesis of hybrids made of siloxane oligomers and polyacrylonitrile.
- The hybrid synthesis route offered more control over the SiO<sub>x</sub> incorporation into the precursor C-SiO<sub>x</sub> fibers.
- Homogeneous distribution of the Si/SiO<sub>x</sub> phase in the carbon matrix was achieved by starting with a silicon precursor in a polymer solution.

- The hybrids nanocomposites C-SiO<sub>2</sub> could be reduced using NaCl-mediated magnesiothermic reduction reaction (Mg-MRR) and AlCl<sub>3</sub>-mediated low-temperature aluminothermic reduction reaction (LTARR). However, the lower temperature of AlCl<sub>3</sub>- mediated LTAAR of C-SiO<sub>2</sub> enabled the production of C-Si/SiO<sub>x</sub> without forming SiC – an inactive phase for LIBs.
- The small size of the Si nanoparticles, the homogeneity of their dispersion, and the ability of the carbon matrix to buffer the expansion-contraction of Si led to 90% capacity retention between 100<sup>th</sup> and 200<sup>th</sup> cycles.

Chapter 2 (section 2.1.2) gives a chronicle perspective of the current state-of-the-art silicon-based anode materials. Based on the current trends after 2016, the multi-step synthesis procedures should be simplified to economically justify the production of the nanomaterials and lead to their practical application. In this dissertation, we investigated a scalable approach to producing Si nanoparticles by NaCl-mediated magnesiothermic reduction (MR) of silica and simple and effective approaches to fabricate nanocomposites of Si nanocrystals evenly embedded in a carbon nanofiber network, starting from carbon and Si precursors. Through these investigations, this work contributes to the understanding of the formation of silicon nanoparticles via 3 simultaneous pathways during the NaCl-mediated magnesiothermic reduction of SiO<sub>2</sub>, which was achieved through a study on time-resolved compositional and microstructural evolution of the magnesiothermic reduction reaction. In addition, this study demonstrates the capability of designing nanocomposite anodes from simple precursors and the use of low-temperature aluminothermic reduction that results in a material with small-sized Si nanoparticles uniformly dispersed in the carbon matrix, which could address the cyclability issue of the silicon-based anodes.

Further studies include increasing the SiO<sub>2</sub> loading in the carbon nanofibers through the selection of precursors and processing conditions and increasing the aluminothermic reduction yield to obtain materials with higher specific capacity for lithium ion batteries. AlCl<sub>3</sub>-mediated low-temperature aluminothermic reduction reaction can also be applied to other structures in which homogeneously-dispersed SiO<sub>2</sub> nanodomains are embedded in a carbon matrix. Moreover, the combination of salts

which form eutectic mixtures with lower melting points used in metallothermic reduction reactions can be further studied.



## References

- Adelhelm, P. (2018). Editorial: The Energy Challenge, Batteries, and Why Simple Math Matters. *Angewandte Chemie International Edition*, 57(23), 6710-6711. doi:<https://doi.org/10.1002/anie.201803221>
- Ahn, J., Kim, H. S., Pyo, J., Lee, J.-K., & Yoo, W. C. (2016). Variation in Crystalline Phases: Controlling the Selectivity between Silicon and Silicon Carbide via Magnesiothermic Reduction using Silica/Carbon Composites. *Chemistry of Materials*, 28(5), 1526-1536. doi:<http://doi.org/10.1021/acs.chemmater.5b05037>
- Andersen, H. F., Filtvedt, W., Maehlen, J. P., Mongstad, T. T., Kirkengen, M., & Holt, A. (2014). Production of Silicon Particles for High-Capacity Anode Material Yielding Outstanding Production Capacity. *ECS Transactions*, 62(1), 97-105. doi:10.1149/06201.0097ecst
- Ansari Hamedani, A., Ow-Yang, C. W., & Hayat Soytas, S. (2021). Mechanisms of Si Nanoparticle Formation by Molten Salt Magnesiothermic Reduction of Silica for Lithium-ion Battery Anodes. *ChemElectroChem*, 8(16), 3181-3191. doi:<https://doi.org/10.1002/celec.202100683>
- Asenbauer, J., Eisenmann, T., Kuenzel, M., Kazzazi, A., Chen, Z., & Bresser, D. (2020). The success story of graphite as a lithium-ion anode material – fundamentals, remaining challenges, and recent developments including silicon (oxide) composites. *Sustainable Energy & Fuels*, 4(11), 5387-5416. doi:10.1039/D0SE00175A
- Ashuri, M., He, Q., Liu, Y., Zhang, K., Emani, S., Sawicki, M. S., . . . Shaw, L. L. (2016). Hollow Silicon Nanospheres Encapsulated with a Thin Carbon Shell: An Electrochemical Study. *Electrochimica Acta*, 215, 126-141. doi:<http://dx.doi.org/10.1016/j.electacta.2016.08.059>
- Ashuri, M., He, Q., & Shaw, L. L. (2015). Silicon as a potential anode material for Li-ion batteries: where size, geometry and structure matter. *Nanoscale*, 8(1), 74-103. doi:<http://dx.doi.org/10.1039/C5NR05116A>
- Bao, Z., Weatherspoon, M. R., Shian, S., Cai, Y., Graham, P. D., Allan, S. M., . . . Sandhage, K. H. (2007). Chemical reduction of three-dimensional silica micro-assemblies into microporous silicon replicas. *Nature*, 446(7132), 172-175. doi:<http://doi.org/10.1038/nature05570>
- Bärmann, P., Diehl, M., Göbel, L., Rutttert, M., Nowak, S., Winter, M., & Placke, T. (2020). Impact of the silicon particle size on the pre-lithiation behavior of silicon/carbon composite materials for lithium ion batteries. *Journal of Power Sources*, 464, 228224. doi:<http://doi.org/10.1016/j.jpowsour.2020.228224>
- Blanco, M. V., Renman, V., Vullum-Bruer, F., & Svensson, A. M. (2020). Nanostructured diatom earth SiO<sub>2</sub> negative electrodes with superior electrochemical performance for lithium ion batteries. *RSC Advances*, 10(55), 33490-33498. doi:10.1039/D0RA05749E
- Blanco, M. V., Renman, V., Zhu, J., Vullum-Bruer, F., & Svensson, A. M. (2021). Optimizing carbon coating parameters for obtaining SiO<sub>2</sub>/C anodes with improved electrochemical performance. *Journal of Solid State Electrochemistry*, 25(4), 1339-1351. doi:<http://doi.org/10.1007/s10008-021-04912-2>

- Bockris, J. O. M., Yoshikawa, S., & Richards, S. R. (1964). Diffusion of Unlike Ions into Liquid Sodium Chloride. *The Journal of Physical Chemistry*, 68(7), 1838-1841. doi:<http://doi.org/10.1021/j100789a028>
- Boettcher, S. W., Oener, S. Z., Lonergan, M. C., Surendranath, Y., Ardo, S., Brozek, C., & Kempler, P. A. (2020). Potentially Confusing: Potentials in Electrochemistry. *ACS Energy Letters*, 261-266. doi:<http://doi.org/10.1021/acseenergylett.0c02443>
- Bridel, J. S., Azaïs, T., Morcrette, M., Tarascon, J. M., & Larcher, D. (2011). In Situ Observation and Long-Term Reactivity of Si/C/CMC Composites Electrodes for Li-Ion Batteries. *Journal of the Electrochemical Society*, 158(6), A750-A759. doi:10.1149/1.3581024
- Brindley, G. W., & Hayami, R. (1965). Kinetics and mechanism of formation of forsterite (Mg<sub>2</sub>SiO<sub>4</sub>) by solid state reaction of MgO and SiO<sub>2</sub>. *Philosophical Magazine* (1798-1977), 12(117), 505-514. doi:<http://doi.org/10.1080/14786436508218896>
- Brisdon, A. K. (1998). *Inorganic spectroscopic methods*: Oxford University Press New York.
- Brown, J. M. (1998). Molecular spectroscopy. *Oxford Chemistry Primers*, 55(1), ALL-ALL.
- Brunauer, S., Emmett, P. H., & Teller, E. (1938). Adsorption of Gases in Multimolecular Layers. *Journal of the American Chemical Society*, 60(2), 309-319. doi:10.1021/ja01269a023
- Cengiz, E. C., Ansari Hamedani, A., Hayat Soytaş, S., & Demir-Cakan, R. (2019). The adsorption effect of freestanding SiO<sub>x</sub>-decorated stabilized polyacrylonitrile interlayers in lithium-sulfur batteries. *Dalton Transactions*, 48(13), 4353-4361. doi:<http://doi.org/10.1039/C8DT04674C>
- Chan, C. K., Peng, H., Liu, G., McIlwrath, K., Zhang, X. F., Huggins, R. A., & Cui, Y. (2008). High-performance lithium battery anodes using silicon nanowires. *Nature Nanotechnology*, 3(1), 31-35. doi:10.1038/nnano.2007.411
- Chase, M. W. J. (1998). *NIST-JANAF Thermochemical Tables*: American Inst. of Physics.
- Chen, W., Fan, Z., Dhanabalan, A., Chen, C., & Wang, C. (2011). Mesoporous Silicon Anodes Prepared by Magnesiothermic Reduction for Lithium Ion Batteries. *Journal of the Electrochemical Society*, 158(9), A1055-A1059. doi:<http://doi.org/10.1149/1.3611433>
- Cullity, B. D., & Stock, S. R. (2001). *Elements of X-ray Diffraction* (Vol. 3): Prentice-Hall, New Jersey.
- Doebelin, N., & Kleeberg, R. (2015). Profex: a graphical user interface for the Rietveld refinement program BGMN. *Journal of Applied Crystallography*, 48(5), 1573-1580. doi:<http://doi.org/10.1107/S1600576715014685>
- Domi, Y., Usui, H., Sugimoto, K., & Sakaguchi, H. (2019). Effect of Silicon Crystallite Size on Its Electrochemical Performance for Lithium-Ion Batteries. *Energy Technology*, 7(5), 1800946. doi:<https://doi.org/10.1002/ente.201800946>
- Duckett, S. B., & Gilbert, B. C. (2000). *Foundations of Spectroscopy*: Oxford University Press, Incorporated.
- Entwistle, J., Rennie, A., & Patwardhan, S. (2018). A review of magnesiothermic reduction of silica to porous silicon for lithium-ion battery applications and beyond. *Journal of Materials Chemistry A*, 6(38), 18344-18356. doi:<http://doi.org/10.1039/c8ta06370b>
- Entwistle, J. E., Booth, S. G., Keeble, D. S., Ayub, F., Yan, M., Corr, S. A., . . . Patwardhan, S. V. Insights into the Electrochemical Reduction Products and

- Processes in Silica Anodes for Next-Generation Lithium-Ion Batteries. *Advanced Energy Materials*, n/a(n/a), 2001826. doi:10.1002/aenm.202001826
- Entwistle, J. E., Booth, S. G., Keeble, D. S., Ayub, F., Yan, M., Corr, S. A., . . . Patwardhan, S. V. (2020). Insights into the Electrochemical Reduction Products and Processes in Silica Anodes for Next-Generation Lithium-Ion Batteries. *Advanced Energy Materials*, 10(43), 2001826. doi:<https://doi.org/10.1002/aenm.202001826>
- Favors, Z., Wang, W., Bay, H. H., Mutlu, Z., Ahmed, K., Liu, C., . . . Ozkan, C. S. (2014). Scalable Synthesis of Nano-Silicon from Beach Sand for Long Cycle Life Li-ion Batteries. *Scientific Reports*, 4, 5623. doi:<http://doi.org/10.1038/srep05623>
- Gao, P., Huang, X., Zhao, Y., Hu, X., Cen, D., Gao, G., . . . Wu, G. (2018). Formation of Si Hollow Structures as Promising Anode Materials through Reduction of Silica in AlCl<sub>3</sub>-NaCl Molten Salt. *ACS Nano*, 12(11), 11481-11490. doi:10.1021/acsnano.8b06528
- Givargizov, E. I. (1975). Fundamental aspects of VLS growth. *Journal of Crystal Growth*, 31, 20-30. doi:[http://doi.org/10.1016/0022-0248\(75\)90105-0](http://doi.org/10.1016/0022-0248(75)90105-0)
- Goodhew, P. J., Humphreys, J., & Beanland, R. (2000). *Electron microscopy and analysis*: CRC Press.
- Greczynski, G., & Hultman, L. (2020). X-ray photoelectron spectroscopy: Towards reliable binding energy referencing. *Progress in Materials Science*, 107, 100591. doi:<https://doi.org/10.1016/j.pmatsci.2019.100591>
- Guo, J., Sun, A., Chen, X., Wang, C., & Manivannan, A. (2011). Cyclability study of silicon-carbon composite anodes for lithium-ion batteries using electrochemical impedance spectroscopy. *Electrochimica Acta*, 56(11), 3981-3987. doi:<https://doi.org/10.1016/j.electacta.2011.02.014>
- Gutman, I., Gotman, I., & Shapiro, M. (2006). Kinetics and mechanism of periodic structure formation at SiO<sub>2</sub>/Mg interface. *Acta Materialia*, 54(18), 4677-4684. doi:<http://doi.org/10.1016/j.actamat.2006.05.048>
- Gutman, I., Klinger, L., Gotman, I., & Shapiro, M. (2009). Model for evolution of periodic layered structure in the SiO<sub>2</sub>/Mg system. *Solid State Ionics*, 180(26), 1350-1355. doi:<http://doi.org/10.1016/j.ssi.2009.08.015>
- Hai, N. H., Grigoriants, I., & Gedanken, A. (2009). Converting Stöber Silica and Mediterranean Sand to High Surface Area Silicon by a Reaction under Autogenic Pressure at Elevated Temperatures. *The Journal of Physical Chemistry C*, 113(24), 10521-10526. doi:10.1021/jp809432t
- Han, Z.-J., Yamagiwa, K., Yabuuchi, N., Son, J.-Y., Cui, Y.-T., Oji, H., . . . Komaba, S. (2015). Electrochemical lithiation performance and characterization of silicon-graphite composites with lithium, sodium, potassium, and ammonium polyacrylate binders. *Physical Chemistry Chemical Physics*, 17(5), 3783-3795. doi:10.1039/C4CP04939J
- Hatchard, T. D., Fielden, R. A., & Obrovac, M. N. (2018). Sintered polymeric binders for Li-ion battery alloy anodes. *Canadian Journal of Chemistry*, 96(7), 765-770. doi:10.1139/cjc-2017-0728
- Hays, K. A., Ruther, R. E., Kukay, A. J., Cao, P., Saito, T., Wood, D. L., & Li, J. (2018). What makes lithium substituted polyacrylic acid a better binder than polyacrylic acid for silicon-graphite composite anodes? *Journal of Power Sources*, 384, 136-144. doi:<https://doi.org/10.1016/j.jpowsour.2018.02.085>
- Huang, C.-L., Wei, T.-H., Peng, S.-Y., & Lee, K.-M. (2019). Study of electrospun polyacrylonitrile fibers with porous and ultrafine nanofibril structures: Effect of

- stabilization treatment on the resulting carbonized structure. *Journal of Applied Polymer Science*, 136(46), 48218. doi:<https://doi.org/10.1002/app.48218>
- Hwang, T. H., Lee, Y. M., Kong, B.-S., Seo, J.-S., & Choi, J. W. (2012). Electrospun Core-Shell Fibers for Robust Silicon Nanoparticle-Based Lithium Ion Battery Anodes. *Nano Letters*, 12(2), 802-807. doi:<http://doi.org/10.1021/nl203817r>
- Hwang, T. H., Lee, Y. M., Kong, B. S., Seo, J. S., & Choi, J. W. (2012). Electrospun Core-Shell Fibers for Robust Silicon Nanoparticle-Based Lithium Ion Battery Anodes. *Nano Letters*, 12(2), 802-807. doi:<http://doi.org/10.1021/nl203817r>
- Iwodate, Y., Ohgane, K., & Ohkubo, T. (2018). Magnesiothermic Reduction of Silicon Dioxide to Obtain Fine Silicon Powder in Molten Salt Media: Analysis of Reduction Mechanism. *Electrochemistry*, 86(4), 198-201. doi:<http://dx.doi.org/10.5796/electrochemistry.17-00090>
- Ji, L., Jung, K.-H., Medford, A. J., & Zhang, X. (2009). Electrospun polyacrylonitrile fibers with dispersed Si nanoparticles and their electrochemical behaviors after carbonization. *Journal of Materials Chemistry*, 19(28), 4992-4997. doi:10.1039/B903165K
- Ji, L., & Zhang, X. (2009). Electrospun carbon nanofibers containing silicon particles as an energy-storage medium. *Carbon*, 47(14), 3219-3226. doi:<https://doi.org/10.1016/j.carbon.2009.07.039>
- Jia, H., Li, X., Song, J., Zhang, X., Luo, L., He, Y., . . . Zhang, J.-G. (2020). Hierarchical porous silicon structures with extraordinary mechanical strength as high-performance lithium-ion battery anodes. *Nature Communications*, 11(1), 1474. doi:<http://doi.org/10.1038/s41467-020-15217-9>
- Kannan, A. G., Kim, S. H., Yang, H. S., & Kim, D.-W. (2016). Silicon nanoparticles grown on a reduced graphene oxide surface as high-performance anode materials for lithium-ion batteries. *RSC Advances*, 6(30), 25159-25166. doi:<http://doi.org/10.1039/C5RA27877E>
- Kitz, P. G., Lacey, M. J., Novák, P., & Berg, E. J. (2020). Operando investigation of the solid electrolyte interphase mechanical and transport properties formed from vinylene carbonate and fluoroethylene carbonate. *Journal of Power Sources*, 477, 228567. doi:<http://doi.org/10.1016/j.jpowsour.2020.228567>
- Kong, X., Zheng, Y., Wang, Y., Liang, S., Cao, G., & Pan, A. (2019). Necklace-like Si@C nanofibers as robust anode materials for high performance lithium ion batteries. *Science Bulletin*, 64(4), 261-269. doi:<http://doi.org/10.1016/j.scib.2019.01.015>
- Lee, D. J., Lee, H., Ryou, M.-H., Han, G.-B., Lee, J.-N., Song, J., . . . Park, J.-K. (2013). Electrospun Three-Dimensional Mesoporous Silicon Nanofibers as an Anode Material for High-Performance Lithium Secondary Batteries. *ACS Applied Materials & Interfaces*, 5(22), 12005-12010. doi:10.1021/am403798a
- Lepoivre, F., Larcher, D., & Tarascon, J.-M. (2016). Electrochemical Activation of Silica for Enhanced Performances of Si-Based Electrodes. *Journal of the Electrochemical Society*, 163(13), A2791-A2796. doi:<http://doi.org/10.1149/2.1221613jes>
- Li, J., Le, D.-B., Ferguson, P. P., & Dahn, J. R. (2010). Lithium polyacrylate as a binder for tin-cobalt-carbon negative electrodes in lithium-ion batteries. *Electrochimica Acta*, 55(8), 2991-2995. doi:<https://doi.org/10.1016/j.electacta.2010.01.011>
- Li, Y., Guo, B., Ji, L., Lin, Z., Xu, G., Liang, Y., . . . Zhang, X. (2013). Structure control and performance improvement of carbon nanofibers containing a

- dispersion of silicon nanoparticles for energy storage. *Carbon*, 51, 185-194. doi:<https://doi.org/10.1016/j.carbon.2012.08.027>
- Lin-KK tool. Retrieved from <https://www.iam.kit.edu/et/Lin-KK.php>
- Lin, N., Han, Y., Wang, L., Zhou, J., Zhou, J., Zhu, Y., & Qian, Y. (2015). Preparation of Nanocrystalline Silicon from SiCl<sub>4</sub> at 200°C in Molten Salt for High-Performance Anodes for Lithium Ion Batteries. *Angewandte Chemie International Edition*, 54(12), 3822-3825. doi:<http://doi.org/10.1002/anie.201411830>
- Lin, N., Han, Y., Zhou, J., Zhang, K., Xu, T., Zhu, Y., & Qian, Y. (2015). A low temperature molten salt process for aluminothermic reduction of silicon oxides to crystalline Si for Li-ion batteries. *Energy & Environmental Science*, 8(11), 3187-3191. doi:<http://doi.org/10.1039/C5EE02487K>
- Lin, X., Li, A., Li, D., Song, H., & Chen, X. (2020). Facile Fabrication of High-Performance Si/C Anode Materials via AlCl<sub>3</sub>-Assisted Magnesiothermic Reduction of Phenyl-Rich Polyhedral Silsesquioxanes. *ACS Applied Materials & Interfaces*, 12(13), 15202-15210. doi:10.1021/acsami.0c00152
- Lin, Z., Liu, T., Ai, X., & Liang, C. (2018). Aligning academia and industry for unified battery performance metrics. *Nature Communications*, 9(1), 5262. doi:<http://dx.doi.org/10.1038/s41467-018-07599-8>
- Liu, N., Huo, K., McDowell, M. T., Zhao, J., & Cui, Y. (2013). Rice husks as a sustainable source of nanostructured silicon for high performance Li-ion battery anodes. *Scientific Reports*, 3, 1919. doi:10.1038/srep01919
- Liu, N., Lu, Z., Zhao, J., McDowell, M. T., Lee, H.-W., Zhao, W., & Cui, Y. (2014). A pomegranate-inspired nanoscale design for large-volume-change lithium battery anodes. *Nature Nanotechnology*, 9(3), 187-192. doi:<http://doi.org/10.1038/nnano.2014.6>
- Liu, N., Wu, H., McDowell, M. T., Yao, Y., Wang, C. M., & Cui, Y. (2012). A Yolk-Shell Design for Stabilized and Scalable Li-Ion Battery Alloy Anodes. *Nano Letters*, 12(6), 3315-3321. doi:10.1021/nl3014814
- Liu, X., Giordano, C., & Antonietti, M. (2012). A molten-salt route for synthesis of Si and Ge nanoparticles: chemical reduction of oxides by electrons solvated in salt melt. *Journal of Materials Chemistry*, 22(12), 5454-5459. doi:<http://dx.doi.org/10.1039/C2JM15453F>
- Liu, X. H., Zhong, L., Huang, S., Mao, S. X., Zhu, T., & Huang, J. Y. (2012). Size-Dependent Fracture of Silicon Nanoparticles During Lithiation. *ACS Nano*, 6(2), 1522-1531. doi:10.1021/nn204476h
- Liu, Z., Chang, X., Wang, T., Li, W., Ju, H., Zheng, X., . . . Li, X. (2017). Silica-Derived Hydrophobic Colloidal Nano-Si for Lithium-Ion Batteries. *ACS Nano*, 11(6), 6065-6073. doi:<http://doi.org/10.1021/acsnano.7b02021>
- Liu, Z., Guan, D., Yu, Q., Xu, L., Zhuang, Z., Zhu, T., . . . Mai, L. (2018). Monodisperse and Homogeneous SiO<sub>x</sub>/C Microspheres: A Promising High-Capacity and Durable Anode Material for Lithium-Ion Batteries. *Energy Storage Materials*. doi:<https://doi.org/10.1016/j.ensm.2018.01.004>
- Livingston, J. D. (1998). *Electronic Properties of Engineering Materials*: Wiley.
- Loeffler, B. N., Bresser, D., Passerini, S., & Copley, M. (2015). Secondary Lithium-Ion Battery Anodes: From First Commercial Batteries to Recent Research Activities. *Johnson Matthey Technology Review*, 59(1), 34-44. doi:10.1595/205651314X685824

- Lu, J., Chen, Z., Pan, F., Cui, Y., & Amine, K. (2018). High-Performance Anode Materials for Rechargeable Lithium-Ion Batteries. *Electrochemical Energy Reviews*, 1(1), 35-53. doi:10.1007/s41918-018-0001-4
- Luo, W., Wang, X., Meyers, C., Wannemacher, N., Sirisaksoontorn, W., Lerner, M. M., & Ji, X. (2013). Efficient fabrication of nanoporous Si and Si/Ge enabled by a heat scavenger in magnesiothermic reactions. *Scientific Reports*, 3, 2222. doi:<http://dx.doi.org/10.1038/srep02222>
- Maçon, A. L., Page, S. J., Chung, J. J., Amdursky, N., Stevens, M. M., Weaver, J. V., . . . Jones, J. R. (2015). A structural and physical study of sol–gel methacrylate–silica hybrids: intermolecular spacing dictates the mechanical properties. *Physical Chemistry Chemical Physics*, 17(43), 29124-29133. doi:<http://doi.org/10.1039/c5cp04656d>
- Magasinski, A., Zdyrko, B., Kovalenko, I., Hertzberg, B., Burtovyy, R., Huebner, C. F., . . . Yushin, G. (2010). Toward Efficient Binders for Li-Ion Battery Si-Based Anodes: Polyacrylic Acid. *ACS Applied Materials & Interfaces*, 2(11), 3004-3010. doi:10.1021/am100871y
- Massalski, T. B., Okamoto, H., International, A., Subramanian, P. R., & Kacprzak, L. (1990). *Binary Alloy Phase Diagrams*: ASM International.
- Mazouzi, D., Lestriez, B., Roué, L., & Guyomard, D. (2009). Silicon Composite Electrode with High Capacity and Long Cycle Life. *Electrochemical and Solid-State Letters*, 12(11), A215. doi:10.1149/1.3212894
- McDowell, M. T., Lee, S. W., Harris, J. T., Korgel, B. A., Wang, C., Nix, W. D., & Cui, Y. (2013). In Situ TEM of Two-Phase Lithiation of Amorphous Silicon Nanospheres. *Nano Letters*, 13(2), 758-764. doi:<http://doi.org/10.1021/nl3044508>
- McDowell, M. T., Lee, S. W., Harris, J. T., Korgel, B. A., Wang, C. M., Nix, W. D., & Cui, Y. (2013). In Situ TEM of Two-Phase Lithiation of Amorphous Silicon Nanospheres. *Nano Letters*, 13(2), 758-764. doi:<http://doi.org/10.1021/nl3044508>
- Meyers, M. A., & Chawla, K. K. (2008). *Mechanical behavior of materials*: Cambridge university press.
- Miao, R., Kang, S., Liao, W., Wang, Y., Liu, J., Zhong, G., . . . Zhang, J. (2020). Heat-regulating effects of inert salts on magnesiothermic reduction preparation of silicon nanopowder for lithium storage. *Ionics*, 26(3), 1249-1259. doi:<http://doi.org/10.1007/s11581-019-03256-2>
- Mindemark, J., Lacey, M. J., Bowden, T., & Brandell, D. (2018). Beyond PEO—Alternative host materials for Li+-conducting solid polymer electrolytes. *Progress in Polymer Science*, 81, 114-143. doi:<https://doi.org/10.1016/j.progpolymsci.2017.12.004>
- Mori, H., Saito, Y., Takahashi, E., Nakabayashi, K., Onuma, A., & Morishima, M. (2013). Synthesis of sulfonated organic–inorganic hybrids through the radical copolymerization of vinyl sulfonate esters and vinyl trialkoxysilanes. *Reactive and Functional Polymers*, 73(4), 658-667. doi:<http://dx.doi.org/10.1016/j.reactfunctpolym.2013.02.001>
- Nersisyan, H. H., Lee, J. H., & Won, C. W. (2005). A study of tungsten nanopowder formation by self-propagating high-temperature synthesis. *Combustion and Flame*, 142(3), 241-248. doi:<http://doi.org/10.1016/j.combustflame.2005.03.012>
- Novak, B. M. (1993). Hybrid Nanocomposite Materials—between inorganic glasses and organic polymers. *Advanced Materials*, 5(6), 422-433. doi:<http://doi.org/10.1002/adma.19930050603>

- Obrovac, M. N. (2018). Si-alloy negative electrodes for Li-ion batteries. *Current Opinion in Electrochemistry*, 9, 8-17. doi:<https://doi.org/10.1016/j.coelec.2018.02.002>
- Obrovac, M. N., & Chevrier, V. L. (2014). Alloy Negative Electrodes for Li-Ion Batteries. *Chemical Reviews*, 114(23), 11444-11502. doi:<http://dx.doi.org/10.1021/cr500207g>
- Obrovac, M. N., & Christensen, L. (2004). Structural Changes in Silicon Anodes during Lithium Insertion/Extraction. *Electrochemical and Solid-State Letters*, 7(5), A93. doi:10.1149/1.1652421
- Owens, G. J., Singh, R. K., Foroutan, F., Alqaysi, M., Han, C.-M., Mahapatra, C., . . . Knowles, J. C. (2016). Sol-gel based materials for biomedical applications. *Progress in Materials Science*, 77, 1-79. doi:<http://dx.doi.org/10.1016/j.pmatsci.2015.12.001>
- Peled, E., & Menkin, S. (2017). Review-SEI: Past, Present and Future. *Journal of the Electrochemical Society*, 164(7), A1703-A1719. doi:<http://doi.org/10.1149/2.1441707jes>
- Pender, J. P., Jha, G., Youn, D. H., Ziegler, J. M., Andoni, I., Choi, E. J., . . . Mullins, C. B. (2020). Electrode Degradation in Lithium-Ion Batteries. *ACS Nano*, 14(2), 1243-1295. doi:10.1021/acsnano.9b04365
- Pirzada, T., Arvidson, S. A., Saquing, C. D., Shah, S. S., & Khan, S. A. (2012). Hybrid Silica-PVA Nanofibers via Sol-Gel Electrospinning. *Langmuir*, 28(13), 5834-5844. doi:10.1021/la300049j
- Pirzada, T., Arvidson, S. A., Saquing, C. D., Shah, S. S., & Khan, S. A. (2014). Hybrid Carbon Silica Nanofibers through Sol-Gel Electrospinning. *Langmuir*, 30(51), 15504-15513. doi:10.1021/la503290n
- Placke, T., Kloepsch, R., Dühnen, S., & Winter, M. (2017). Lithium ion, lithium metal, and alternative rechargeable battery technologies: the odyssey for high energy density. *Journal of Solid State Electrochemistry*, 21(7), 1939-1964. doi:10.1007/s10008-017-3610-7
- Rahaman, M. S. A., Ismail, A. F., & Mustafa, A. (2007). A review of heat treatment on polyacrylonitrile fiber. *Polymer Degradation and Stability*, 92(8), 1421-1432. doi:<https://doi.org/10.1016/j.polymdegradstab.2007.03.023>
- Rehman, W. U., Wang, H., Manj, R. Z. A., Luo, W., & Yang, J. (2021). When Silicon Materials Meet Natural Sources: Opportunities and Challenges for Low-Cost Lithium Storage. *Small*, 17(9), 1904508. doi:<https://doi.org/10.1002/sml.201904508>
- Reyes Jiménez, A., Klöpsch, R., Wagner, R., Rodehorst, U. C., Kolek, M., Nölle, R., . . . Placke, T. (2017). A Step toward High-Energy Silicon-Based Thin Film Lithium Ion Batteries. *ACS Nano*, 11(5), 4731-4744. doi:<http://doi.org/10.1021/acsnano.7b00922>
- Richman, E. K., Kang, C. B., Brezesinski, T., & Tolbert, S. H. (2008). Ordered Mesoporous Silicon through Magnesium Reduction of Polymer Templated Silica Thin Films. *Nano Letters*, 8(9), 3075-3079. doi:<http://doi.org/10.1021/nl801759x>
- Sandhage, K. H., Dickerson, M. B., Huseman, P. M., Caranna, M. A., Clifton, J. D., Bull, T. A., . . . Schoenwaelder, M. E. A. (2002). Novel, Bioclastic Route to Self-Assembled, 3D, Chemically Tailored Meso/Nanostructures: Shape-Preserving Reactive Conversion of Biosilica (Diatom) Microshells. *Advanced Materials*, 14(6), 429-433. doi:[http://doi.org/10.1002/1521-4095\(20020318\)14:6<429::AID-ADMA429>3.0.CO;2-C](http://doi.org/10.1002/1521-4095(20020318)14:6<429::AID-ADMA429>3.0.CO;2-C)

- Shobukawa, H., Alvarado, J., Yang, Y., & Meng, Y. S. (2017). Electrochemical performance and interfacial investigation on Si composite anode for lithium ion batteries in full cell. *Journal of Power Sources*, 359, 173-181. doi:<https://doi.org/10.1016/j.jpowsour.2017.05.044>
- Song, G., Ryu, J., Kim, J. C., Lee, J. H., Kim, S., Wang, C., . . . Park, S. (2018). Revealing salt-expedited reduction mechanism for hollow silicon microsphere formation in bi-functional halide melts. *Communications Chemistry*, 1(1), 42. doi:<http://doi.org/10.1038/s42004-018-0041-z>
- Tai, M. H., Gao, P., Tan, B. Y. L., Sun, D. D., & Leckie, J. O. (2014). Highly Efficient and Flexible Electrospun Carbon–Silica Nanofibrous Membrane for Ultrafast Gravity-Driven Oil–Water Separation. *ACS Applied Materials & Interfaces*, 6(12), 9393-9401. doi:10.1021/am501758c
- Takezawa, H., Iwamoto, K., Ito, S., & Yoshizawa, H. (2013). Electrochemical behaviors of nonstoichiometric silicon suboxides (SiO<sub>x</sub>) film prepared by reactive evaporation for lithium rechargeable batteries. *Journal of Power Sources*, 244, 149-157. doi:<https://doi.org/10.1016/j.jpowsour.2013.02.077>
- Tan, Y., Jiang, T., & Chen, G. Z. (2021). Mechanisms and Product Options of Magnesiothermic Reduction of Silica to Silicon for Lithium-Ion Battery Applications. *Frontiers in Energy Research*, 9(98). doi:10.3389/fenrg.2021.651386
- Teo, W. (2015). *Introduction to Electrospinning Parameters and Fiber Control*.
- Timmons, A., Todd, A. D. W., Mead, S. D., Carey, G. H., Sanderson, R. J., Mar, R. E., & Dahn, J. R. (2007). Studies of Si<sub>1-x</sub>C<sub>x</sub> Electrode Materials Prepared by High-Energy Mechanical Milling and Combinatorial Sputter Deposition. *Journal of the Electrochemical Society*, 154(9), A865-A874. doi:<http://doi.org/10.1149/1.2755782>
- Tjong, S. C., & Chen, H. (2004). Nanocrystalline materials and coatings. *Materials Science and Engineering: R: Reports*, 45(1), 1-88. doi:<https://doi.org/10.1016/j.mser.2004.07.001>
- Toguri, J. M., & Pidgeon, L. M. (1961). HIGH-TEMPERATURE STUDIES OF METALLURGICAL PROCESSES: PART I. THE THERMAL REDUCTION OF MAGNESIUM OXIDE WITH SILICON. *Canadian Journal of Chemistry*, 39(3), 540-547. doi:<http://doi.org/10.1139/v61-065>
- Ulvestad, A., Reksten, A. H., Andersen, H. F., Carvalho, P. A., Jensen, I. J. T., Nagell, M. U., . . . Kuposov, A. Y. (2020). Crystallinity of Silicon Nanoparticles: Direct Influence on the Electrochemical Performance of Lithium Ion Battery Anodes. *ChemElectroChem*, 7(21), 4349-4353. doi:<https://doi.org/10.1002/celec.202001108>
- Wagner, R. S., & Ellis, W. C. (1965). *Vapor-liquid-solid Mechanism of Crystal Growth and Its Application to Silicon*: Bell Telephone Laboratories.
- Wang, D., Zhang, D., Dong, Y., Lin, X., Liu, R., Li, A., . . . Song, H. (2021). Reconstructed Nano-Si Assembled Microsphere via Molten Salt-Assisted Low-Temperature Aluminothermic Reduction of Diatomite as High-Performance Anodes for Lithium-Ion Batteries. *ACS Applied Energy Materials*, 4(6), 6146-6153. doi:10.1021/acsaem.1c00938
- Wang, L., Lin, Y., DeCarlo, S., Wang, Y., Leung, K., Qi, Y., . . . Eichhorn, B. W. (2020). Compositions and Formation Mechanisms of Solid-Electrolyte Interphase on Microporous Carbon/Sulfur Cathodes. *Chemistry of Materials*, 32(9), 3765-3775. doi:<http://doi.org/10.1021/acs.chemmater.9b05027>

- Wang, M.-S., Song, W.-L., Wang, J., & Fan, L.-Z. (2015). Highly uniform silicon nanoparticle/porous carbon nanofiber hybrids towards free-standing high-performance anodes for lithium-ion batteries. *Carbon*, 82, 337-345. doi:<https://doi.org/10.1016/j.carbon.2014.10.078>
- Weihan, L., Linchao, Z., Ying, W., & Yan, Y. (2016). Nanostructured electrode materials for lithium-ion and sodium-ion batteries via electrospinning. *Science China Materials*, 59(4), 287-321.
- Weiss, M., Ruess, R., Kasnatscheew, J., Levartovsky, Y., Levy, N. R., Minnmann, P., . . . Janek, J. (2021). Fast Charging of Lithium-Ion Batteries: A Review of Materials Aspects. *Advanced Energy Materials*, 11(33), 2101126. doi:<https://doi.org/10.1002/aenm.202101126>
- Wilkes, B. N., Brown, Z. L., Krause, L. J., Triemert, M., & Obrovac, M. N. (2015). The Electrochemical Behavior of Polyimide Binders in Li and Na Cells. *Journal of the Electrochemical Society*, 163(3), A364-A372. doi:10.1149/2.0061603jes
- Wilson, A. M., Way, B. M., Dahn, J. R., & Buuren, T. v. (1995). Nanodispersed silicon in pregraphitic carbons. *Journal of Applied Physics*, 77(6), 2363-2369. doi:10.1063/1.358759
- Winter, M., Barnett, B., & Xu, K. (2018). Before Li Ion Batteries. *Chemical Reviews*, 118(23), 11433-11456. doi:<http://dx.doi.org/10.1021/acs.chemrev.8b00422>
- Wu, H., Chan, G., Choi, J. W., Ryu, I., Yao, Y., McDowell, M. T., . . . Cui, Y. (2012). Stable cycling of double-walled silicon nanotube battery anodes through solid-electrolyte interphase control. *Nature Nanotechnology*, 7(5), 309-314. doi:<http://doi.org/10.1038/nnano.2012.35>
- Wu, H., & Cui, Y. (2012). Designing nanostructured Si anodes for high energy lithium ion batteries. *Nano Today*, 7(5), 414-429. doi:<http://dx.doi.org/10.1016/j.nantod.2012.08.004>
- Wyller, G. M., Preston, T., Mongstad, T., Klette, H., Nordseth, Ø., Lindholm, D., . . . Marstein, E. (2016). *THERMAL DECOMPOSITION OF MONOSILANE OBSERVED IN A FREE SPACE REACTOR*.
- Wynnyckyj, J., & Bhogeswara Rao, D. (1976). THE MECHANISM OF REDUCTION OF SILICA BY MAGNESIUM VAPOR. *High Temperature Science*, 8(3), 203-217.
- Wygartowicz, J., Østvold, T., & Øye, H. A. (1980). The solubility of magnesium metal and the recombination reaction in the industrial magnesium electrolysis. *Electrochimica Acta*, 25(2), 151-156. doi:[http://doi.org/10.1016/0013-4686\(80\)80036-3](http://doi.org/10.1016/0013-4686(80)80036-3)
- Xiang, B., An, W.-L., Fu, J.-J., Mei, S.-X., Guo, S.-G., Zhang, X.-M., . . . Chu, P. K. (2021). Graphene-encapsulated blackberry-like porous silicon nanospheres prepared by modest magnesiothermic reduction for high-performance lithium-ion battery anode. *Rare Metals*, 40(2), 383-392. doi:10.1007/s12598-020-01528-9
- Xie, J., Wang, G., Huo, Y., Zhang, S., Cao, G., & Zhao, X. (2014). Nanostructured silicon spheres prepared by a controllable magnesiothermic reduction as anode for lithium ion batteries. *Electrochimica Acta*, 135, 94-100. doi:<http://dx.doi.org/10.1016/j.electacta.2014.05.012>
- Xu, C., Lindgren, F., Philippe, B., Gorgoi, M., Björefors, F., Edström, K., & Gustafsson, T. (2015). Improved Performance of the Silicon Anode for Li-Ion Batteries: Understanding the Surface Modification Mechanism of Fluoroethylene Carbonate as an Effective Electrolyte Additive. *Chemistry of Materials*, 27(7), 2591-2599. doi:<http://doi.org/10.1021/acs.chemmater.5b00339>

- Xu, Z.-L., Liu, X., Luo, Y., Zhou, L., & Kim, J.-K. (2017). Nanosilicon anodes for high performance rechargeable batteries. *Progress in Materials Science*, 90, 1-44. doi:<https://doi.org/10.1016/j.pmatsci.2017.07.003>
- Xu, Z.-L., Zhang, B., & Kim, J.-K. (2014). Electrospun carbon nanofiber anodes containing monodispersed Si nanoparticles and graphene oxide with exceptional high rate capacities. *Nano Energy*, 6, 27-35. doi:<http://dx.doi.org/10.1016/j.nanoen.2014.03.003>
- Yang, W., Davies, A. J., Lin, X., Suyetin, M., Matsuda, R., Blake, A. J., . . . Schröder, M. (2012). Selective CO<sub>2</sub> uptake and inverse CO<sub>2</sub>/C<sub>2</sub>H<sub>2</sub> selectivity in a dynamic bifunctional metal–organic framework. *Chemical Science*, 3(10), 2993-2999. doi:10.1039/C2SC20443F
- Yao, Y., McDowell, M. T., Ryu, I., Wu, H., Liu, N. A., Hu, L. B., . . . Cui, Y. (2011). Interconnected Silicon Hollow Nanospheres for Lithium-Ion Battery Anodes with Long Cycle Life. *Nano Letters*, 11(7), 2949-2954. doi:10.1021/nl201470j
- Yasuda, K., Nohira, T., Kobayashi, K., Kani, N., Tsuda, T., & Hagiwara, R. (2013). Improving Purity and Process Volume During Direct Electrolytic Reduction of Solid SiO<sub>2</sub> in Molten CaCl<sub>2</sub> for the Production of Solar-Grade Silicon. *Energy Technology*, 1(4), 245-252. doi:10.1002/ente.201300001
- Yermekova, Z., Mansurov, Z., & Mukasyan, A. S. (2010). Combustion synthesis of silicon nanopowders. *International Journal of Self-Propagating High-Temperature Synthesis*, 19(2), 94-101. doi:<http://doi.org/10.3103/S1061386210020032>
- Yördem, O. S., Papila, M., & Menciloğlu, Y. Z. (2008). Effects of electrospinning parameters on polyacrylonitrile nanofiber diameter: An investigation by response surface methodology. *Materials & Design*, 29(1), 34-44. doi:<http://dx.doi.org/10.1016/j.matdes.2006.12.013>
- Zhang, B., Kang, F., Tarascon, J.-M., & Kim, J.-K. (2016). Recent advances in electrospun carbon nanofibers and their application in electrochemical energy storage. *Progress in Materials Science*, 76(Supplement C), 319-380. doi:<https://doi.org/10.1016/j.pmatsci.2015.08.002>
- Zhang, H., Zhou, M.-Y., Lin, C.-E., & Zhu, B.-K. (2015). Progress in polymeric separators for lithium ion batteries. *RSC Advances*, 5(109), 89848-89860. doi:10.1039/C5RA14087K
- Zhang, S., Du, Z., Lin, R., Jiang, T., Liu, G., Wu, X., & Weng, D. (2010). Nickel Nanocone-Array Supported Silicon Anode for High-Performance Lithium-Ion Batteries. *Advanced Materials*, 22(47), 5378-5382. doi:10.1002/adma.201003017
- Zheng, Z., Song, S., & Wang, Y. (2016). Sol-gel-processed amorphous lithium ion electrolyte thin films: Structural evolution, theoretical considerations, and ion transport processes. *Solid State Ionics*, 287, 60-70. doi:<https://doi.org/10.1016/j.ssi.2016.02.006>
- Zhou, X., Wan, L.-J., & Guo, Y.-G. (2013). Electrospun Silicon Nanoparticle/Porous Carbon Hybrid Nanofibers for Lithium-Ion Batteries. *Small*, 9(16), 2684-2688. doi:10.1002/sml.201202071
- Zhu, G., Chao, D., Xu, W., Wu, M., & Zhang, H. (2021). Microscale Silicon-Based Anodes: Fundamental Understanding and Industrial Prospects for Practical High-Energy Lithium-Ion Batteries. *ACS Nano*. doi:10.1021/acsnano.1c05898
- Zhu, G., Luo, W., Wang, L., Jiang, W., & Yang, J. (2019). Silicon: toward eco-friendly reduction techniques for lithium-ion battery applications. *Journal of Materials Chemistry A*, 7(43), 24715-24737. doi:10.1039/C9TA08554H

- Zhu, J., Wang, T., Fan, F., Mei, L., & Lu, B. (2016). Atomic-Scale Control of Silicon Expansion Space as Ultrastable Battery Anodes. *ACS Nano*, *10*(9), 8243-8251. doi:10.1021/acsnano.6b04522
- Zhu, P., Gastol, D., Marshall, J., Sommerville, R., Goodship, V., & Kendrick, E. (2021). A review of current collectors for lithium-ion batteries. *Journal of Power Sources*, *485*, 229321. doi:<https://doi.org/10.1016/j.jpowsour.2020.229321>
- Zuo, X., Zhu, J., Müller-Buschbaum, P., & Cheng, Y.-J. (2017). Silicon based lithium-ion battery anodes: A chronicle perspective review. *Nano Energy*, *31*, 113-143. doi:<http://doi.org/10.1016/j.nanoen.2016.11.013>

